Inaugural dissertation

for

obtaining the doctoral degree

of the

Combined Faculty of Mathematics, Engineering and Natural Sciences

of the

Ruprecht – Karls – University

Heidelberg

Presented by

M.Sc. Robert Engel (ne Pilz)

born in: Mannheim-Neckarau

Oral Examination: 04.10.2022

Globo-series glycosphingolipid-protein interactions in immortalized proximal tubular epithelial cells and formation of keto-type ceramides in the skin of KDSR patients

Referees: Prof. Dr. Britta Brügger

PD Dr. Roger Sandhoff

Table of Contents

Table of Figures

Table of Tables

Abbreviations

Abbreviation	
A4GALT	Alpha-1,4-galactosyltransferase
ABCA12	ATP-binding cassette sub-family A member 12
ABCB4	ATP-binding cassette sub-family B member 4
AD	Atopic dermatitis
AEE	Apical early endosomes
AH	Alkaline hydrolysis
AKT	Proteinkinase B
ALDH3A2	Aldehyde dehydrogenase 3A2
ALOX12B	12R-lipoxygenase
ALOXE3	Lipoxygenase-3
AMN	Amnionless
ANOVA	Analysis of variance
ARCI	Autosomal recessive congenital ichthyosis
ASM/SMPD1	Acid sphingomyelinase
ATP9A	Probable phospholipid-transporting ATPase IIA
AUTS2	Activator of transcription and developmental regulator AUTS2
AV	Apical vacuoles
BSA	Bovine serum albumin
BSA	Body surface area
CAV1	Caveolin-1
CDS	Coding sequence
Cer	Ceramide
CerS	Ceramide synthase
CERT	Ceramide transport protein
CID	Collision-induced dissociation
CoA	Coenzyme-A
CPM	Carboxypeptidase M
CRISPR	Clustered Regularly Interspaced Short Palindromic Repeats
CuAAC	Copper azide-alkyne-cycloaddition
DAPI	4',6-Diamidino-2-phenylindol
DAT	Dense apical tubules
DDQ	2,3-dichlor-5,6-dicyano-1,4-benzoquinone
DEAE	Diethylaminoethyl
DES1	Sphingolipid Δ^4-desaturase
DES2	Sphingolipid Δ^4-desaturase/C4-monooxygenase
DMEM	Dulbecco’s modified eagle medium
DMSO	Dimethyl sulfoxide
DPP4	Dipeptidyl peptidase 4
EASI	Eczema area and severity index
EGF	Epidermal growth factor
EGFR	Epidermal growth factor receptor

EKVP4	Erythrokeratodermia variabilis et progressiva 4
ELOVL1/4	Elongation of very long chain fatty acids protein
EMT	Epithelial-to-Mesenchymal Transition
EPCAM	Epithelial cell adhesion molecule
ER	Endoplasmic Reticulum
ERK	Extracellular signal-regulated kinase
FAK	Focal adhesion kinase
FAPP2	Pleckstrin homology domain containing A8
FAS	Fatty acid synthase
FC	Fold Change
FCS	Fetal calf serum
FGF	Fibroblast growth factor
FGFR	Fibroblast growth factor receptor
FITC	Fluorescein isothiocyanate
GalCerS	Galactosylceramide synthase
Gb3Cer	Globotriaosylceramide
Gb3S	Gb3 synthase
GBA	Beta-Glucocerebrosidase
GCS	Glucosylceramide synthase
GEM	Glycosphingolipid-enriched membrane
Genta-TR	Gentamicin-TexasRed
GLA	Alpha-Galactosidase A
GlcCer	Glucosylceramide
GLP-1	Glucagon-like peptide 1
gRNA	Guide RNA
GSH	Glutathione
GSL	Glycosphingolipid
H&E	Hematoxylin and eosin
HeLa	Henrietta Lacks cells
HexCer	Hexosylceramide
HGF	Hepatocyte growth factor
HGFAC	HGF activator protein
HPTLC	High-performance thin layer chromatography
HPV	Human papilloma virus
HSAN1	Hereditary sensory and autonomic neuropathy type 1
IMDM	Iscove’s modified eagle medium
ITGA3	Integrin alpha-3
KD1/2	Kunitz-type domain 1/2
KDS	3-Ketodihydrosphingosine
KDSR	3-Ketodihydrosphingosine reductase
LacCer	Lactosylceramide
LAPTM4A	Lysosomal-associated transmembrane protein 4A
LC-FA	Long chain fatty acid (C13 – C21)
LC-MS/MS	Liquid chromatography-coupled tandem mass spectrometry

LCS	Lactosylceramide synthase
LDLR	Low-density lipoprotein receptor
LMWP	Low-molecular weight protein
LRP2	Megalin
m/z	Mass-to-charge ratio
McL	McLafferty
MDCK	Madin Darby Canine Kidney cells
MRM	Multiple reaction monitoring
mRNA	Messenger RNA
mtCDase	Mitochondrial ceramidase
NaOH	Sodium hydroxide
NHEJ	Non-homologous end joining
NRK	Normal rat kidney cells
OA	Oleic acid
OK	Opposum kidney cells
P5P	Pyridoxal-5-Phosphate
pacSph	Photoactivatable, bifunctional sphingosine
PAM	Protospace adjacent motif
PASI	Psoriasis activity index
PBS	Phosphate-buffered saline
PC	Phosphatidylcholine
PCR	Polymerase chain reaction
Pd/C	Palladium on charcoal
PERIOPTER	Periorifical and ptchyotropic erythrokeratoderma
PFA	Paraformaldehyde
PLA	Proximity ligation assay
POM	Postnatal microcephaly
Pso	Psoriasis vulgaris
PTEC	Proximal tubular epithelial cells
RIP	Receptor-interacting protein kinase
ROS	Reactive oxygen species
RPTEC	Renal proximal tubular epithelial cells
S1P	Sphingosine-1-Phosphate
S1PL	Sphingosine-1-Phosphate Lyase
S1PL-I	S1PL inhibitor
Sa	Sphinganine
SAP-C	Saposin-C
SB	Stratum Basale / Sphingoid Base
SC	Stratum Corneum
SCCPDH	Saccharopine dehydrogenase-like oxidoreductase
SDS-PAGE	Sodium dodecyl sulphate polyacrylamide gel electrophoresis
SG	Stratum granulosum
SM	Sphingomyelin
SNP	Single nucleotide polymorphism

So	Sphingosine
SP3	Single-Pot Solid-Phase-enhanced Sample Preparation
SpCas9	Streptococcus pyogenes Cas9
SPHK1/2	Sphingosine kinase ½
SPINT1	Kunitz-type inhibitor of serine peptidases
SPT	Serine palmitoyl-CoA transferase complex
SPTLC1/2/3	Serine palmitoyl-CoA transferase long chain 1/2/3
SPTssa/SPTssb	SPT small subunit a/b
SRM	Single reaction monitoring
SS	Stratum spinosum
SSEA3	Stage-specific early antigen-3
SSEA4	Stage-specific early antigen 4
ST14	Matriptase
STD	Standard
STGD3	Stargardt disease type 3
StxB	Shiga Toxin B-subunit
TBTA	Tris[(1-benzyl-1H-1,2,3-triazol-4-yl)methyl]amin
TEWL	Transepidermal water loss
TGN	Trans-Golgi network
THPTA	Tris(3-hydroxypropyltriazolylmethyl)amine
TIDE	Tracking of Indels by Decomposition
TLC	Thin layer chromatography
TLR4	Toll-like receptor 4
TM9SF2	Transmembrane 9 superfamily member 2 precursor
TMD	Transmembrane domain
TMT	Tandem mass tag
TTSP	Transmembrane serine protease
UDP	Uridindiphosphate
ULC-FA	Ultra long chain fatty acid
UPLC	Ultra-performance liquid chromatography
UTR	Untranslated region
UV	Ultraviolet
VA	Volar forearm
v-ATPase	Vacuolar-type ATPase
VCAM1	Vascular cell adhesion molecule 1
VLC-FA	Very long chain fatty acid
VLC-SB	Very long chain sphingoid base

1 Summary

Sphingolipids have important physiological functions and a tightly regulated and spatially distributed anabolic and catabolic enzymatic network. Dysfunction within this enzymatic network is associated with many diseases. The exact mechanisms how these metabolic dysregulations cause pathological alterations are often unknown and an in-depth investigation of these mechanisms may provide novel therapeutic targets for treatments. Therefore, I investigated biochemical consequences of dysfunction for two enzymes of the sphingolipid metabolic network – 3-ketodihydrosphingosine reductase (**KDSR**) and Gb3 synthase (**Gb3S**). Dysfunction of both is associated with a specific organ pathology in mammals.

(I) Loss of globo-series glycosphingolipids by knockout of **Gb3S** was associated with albuminuria but was also shown to convey renoprotective effects in models of glycerol-induced and gentamicin-induced acute kidney injury in mice. How globo-series glycosphingolipids mediate these effects remains unexplained. I used the immortalized proximal tubular epithelial cell line HK-2 as an *in vitro* model to identify – after introducing genetic modifications with the CRISPR/Cas9 system - protein interaction partners of globo-series glycosphingolipids using a bifunctional, metabolic sphingolipid probe (pacSph). I found indications of an interaction of Gb3Cer with the Kunitz-type serine-protease inhibitor SPINT1, an inhibitor of HGF activator (HGFAC) and therefore modulator of MET signalling. Interestingly, activation of MET signalling was shown before to mediate renoprotective effects in models of acute kidney injury. Although the presented data is not comprehensive, it may stimulate further investigations of the role of globo-series glycosphingolipids in signalling in this context. Establishing a link between Gb3Cer and the regulation of MET signalling may help to identify strategies to reduce acute kidney damage in CRUSH syndrome, during pharmacological interventions, or with diabetes, but could also provide novel targets for cancer treatment.

(II) Furthermore, I examined the role of the sphingolipid *de novo* synthesis enzyme **KDSR** in skin of two patients with biallelic mutations in KDSR

and symptomatic palmoplantar keratoderma. Following analysis of stratum corneum by LC-MS/MS and chemical synthesis of keto-type ceramides, I revealed the biochemical consequences of KDSR dysfunction and found that significant amounts of a novel, yet undescribed, class of sphingolipids - 3-ketodihydroceramide - are formed in the skin of both patients. Analysis of skin biopsies and blood samples further revealed that 3-ketodihydroceramides are exclusively formed in the epidermis and cannot be detected in the dermis or blood indicating a close link to the observed skin pathologies. Further analysis revealed a significant reduction in the length of epidermal sphingoid bases and ceramides, not only in KDSR patients, but also in *atopic dermatitis* and *psoriasis vulgaris* indicating dysfunctional keratinocyte differentiation. A mechanistic link between the presence of pathological keto-type compounds and pathogenesis in KDSR patients remains to be established. It may be speculated, that reactive 3-ketosphingolipids have a negative impact on reactive oxygen species (ROS) scavenging systems in the epidermis, but this remains to be further addressed. If a mechanistic link can be established, a careful reduction of serine-palmitoyl-CoA transferase (SPT) activity to match the reduced activity of KDSR or pharmacological targeting of the oxidative stress response may be a feasible strategy to improve the burden of these patients. Reduction of SPT activity may be achieved with inhibitors like myriocin.

Concluding, these findings demonstrate the relevance of sphingolipid metabolism for physiology and pathology and provide a foundation for further research.

Zusammenfassung

Sphingolipide haben wichtige physiologische Funktionen und ein eng reguliertes, räumlich getrenntes anaboles und kataboles enzymatisches Netzwerk. Fehlfunktionen innerhalb dieses enzymatischen Netzes sind mit vielen Krankheiten assoziiert. Die genauen Mechanismen, wie Fehlregulierungen des metabolischen Netzwerks zu pathologischen Veränderungen führen, sind oft unbekannt. Eine Untersuchung dieser Mechanismen könnte neue Ansatzpunkte für die Behandlung und Therapie dieser Krankheiten liefern. Diese Arbeit beschäftigt sich mit den biochemischen Konsequenzen der Dysfunktion zweier dieser Enzyme im Sphingolipid Metabolismus – 3-ketodihydrosphingosine reductase (**KDSR**) und Gb3 synthase (**Gb3S**). Die Dysfunktion beider Enzyme ist mit einer jeweils spezifischen Organpathologie verbunden.

(I) Der Verlust von Glykosphingolipiden der globo-Serie durch Knockout von **Gb3S** führte zu milder Albuminurie, wurde aber auch für nierenschützende Eigenschaften in Modellen für Glycerol- und Gentamicin-induziertes akutes Nierenversagen in Mäusen verantwortlich gemacht. Wie dieser Effekt durch globo-Serie Glykosphingolipide vermittelt wird, ist unklar. Ich verwendete die immortalisierte, proximale epitheliale Tubulus Zelllinie HK-2 als ein *in vitro* Modell, um – nach genetischer Modifikation mit CRISPR/Cas9 Technik - Protein-Interaktionspartner von globo-Series Glykosphingolipiden durch Nutzung einer bifunktionellen, metabolischen Sphingolipid-Sonde (pacSph) zu ermitteln. Dabei fand ich Anzeichen für eine Interaktion von Gb3Cer mit dem Kunitz-Typ Serin-Protease Inhibitor SPINT1, einem Inhibitor von HGF activator protein (HGFAC), und daher auch ein Regulator von Signaling über den MET Rezeptor. Interessanterweise wurde in früheren Studien gezeigt, dass MET Rezeptor Signaling nierenschützende Wirkungen in Modellen von akutem Nierenversagen vermittelt. Obwohl die gezeigten Daten noch kein vollständiges Bild vermitteln, hoffe ich, dass sie weitere Untersuchungen zur Verknüpfung zwischen globo-Serie Glykosphingolipiden und MET Signalling in diesem Kontext anregen können. Falls sich ein Zusammenhang etablieren lässt, könnte das helfen Strategien zur Vermeidung von akutem

Nierenversagen bei CRUSH Syndrom, pharmakologischer Behandlung oder auch Krankheiten wie Diabetes und Krebs zu entwickeln.

(II) Des Weiteren habe ich die Rolle des Enzyms **KDSR**, einem wichtigen Bestandteil des Sphingolipid *de novo* Synthesewegs, in der Haut von zwei Patienten mit Mutationen in diesem Enzym untersucht, die Symptome einer palmo-plantaren Keratodermie zeigten. Durch die Analyse von Stratum Corneum durch LC-MS/MS und chemische Synthese von Keto-Typ Ceramid-Standards, klärte ich die biochemischen Konsequenzen der KDSR Dysfunktion auf und fand heraus, dass sich in der Haut dieser Patienten signifikante Mengen einer neuen und bisher nicht beschriebenen Lipidklasse, sogenannte 3-Ketodihydroceramide, befinden. Weitere Analysen von Hautbiopsien und Blutproben zeigten, dass 3-Ketodihydroceramide nur in der Epidermis, nicht aber in Dermis Proben oder Blut der Patienten nachgewiesen werden können, was auf eine enge Verknüpfung zu den pathologischen Veränderungen in der Epidermis hindeutet. Bei weiteren Analysen fand ich außerdem heraus, dass Sphingoid Basen und Ceramide eine signifikante Reduktion ihrer Länge aufweisen. Ähnliche Beobachtungen machte ich mit Proben von Patienten mit atopischer Dermatitis und Psoriasis vulgaris was auf eine Dysfunktion in der Differenzierung von Keratinozyten hindeutet. Ein mechanistischer Zusammenhang zwischen der Präsenz der pathologischen Keto-Typ-Lipide und Pathogenese in KDSR Patienten muss noch etabliert werden. Man könnte spekulieren, dass reaktive 3-Ketosphingolipide einen negativen Effekt auf den Schutz vor reaktiven Sauerstoffspezies in der Epidermis haben. Falls sich ein kausaler Zusammenhang bestätigen lässt, könnte eine vorsichtige Reduktion der Aktivität der Serin-Palmitoyl-CoA Transferase (SPT) oder pharmakologische Modulation der oxidativen Stress Antwort eine mögliche Strategie darstellen, um die Krankheitslast der Patienten zu reduzieren. Inhibition der SPT Aktivität sollte dabei bis auf eine Stufe, die der reduzierten katalytischen Kapazität von KDSR entspricht, beispielsweise durch Inhibitoren wie Myriocin, erfolgen.

Zusammenfassend demonstrieren diese Befunde die Relevanz des Sphingolipid Metabolismus im Kontext von Physiologie und Pathologie und bieten eine Grundlage für weitere Untersuchungen.

2 Introduction

2.1 Sphingolipid Metabolism

Cellular lipids are essential for the compartmentalization of life in cells and organisms and as part of cellular membranes, lipids form a barrier that separates distinct biological compartments and provide a hub for specialized biological functions. Lipids are also direct mediators in cellular signalling as active signalling molecules. The complex body of known lipids is vastly growing, and the abundance range of single lipid species can cover more than nine orders of magnitude (1–3).

The sphingolipid metabolic network

Sphingolipids are a structurally distinct class of lipid metabolites with functions in many cellular processes, including growth, differentiation, cell-cell contacts, apoptosis, and inflammation (4, 5). As membrane-bound members of lipid microdomains, sphingolipids influence protein function and signalling processes. Soluble sphingolipids like sphingosine-1-phosphate (S1P) are direct mediators of cellular signalling. Furthermore, sphingolipids are structural components of cellular membranes and extracellular lipid barriers, as seen in myelin sheets and the skin barrier. Most sphingolipids are expressed in a cell- and tissue-specific manner (6). The sphingolipid core motif (Figure 1) characterizes this distinct class of lipids. Modifications of the sphingolipid motif yield sphingolipid subclasses with their own unique properties including ceramides, sphingomyelins, and glycosphingolipids (1).

All sphingolipids are synthesized within a metabolic network that is framed by two gate-keeping metabolic reactions. On the one hand, sphingolipid *de novo* biosynthesis generates new sphingoid bases and is the single metabolic entry point for the complete sphingolipid metabolic network (Figure 2) (7). On the other hand, almost all degradation of sphingoid bases is irreversibly channelled through the sphingosine-1-phosphate lyase (S1PL) pathway (Figure 3) (8). The highly complex, compartmentalized, and interconnected metabolic network between these two metabolic pathways provides the biochemical foundation for the synthesis of all sphingolipids. Interestingly, the essential enzymes of these pathways, the serine palmitoyl-CoA transferase (SPT) complex and S1PL, are both dependent on pyridoxal-5’-phosphate (P5P) (9, 10). Within the sphingolipid

metabolic network sphingoid bases may be recycled via the salvage and sphingomyelinase pathway from complex sphingolipids or from extracellular and dietary sources (11).

Sphingolipid biosynthesis

Sphingolipid *de novo* biosynthesis is initiated in the endoplasmic reticulum (ER) with the condensation of *L*-serine and an acyl-CoA (primarily palmitoyl-CoA) by the serine-palmitoyl-CoA transferase complex (SPT). This P5P-dependent reaction yields the first sphingoid base 3-ketodihydrosphingosine (KDS) (in case of palmitoyl-CoA with a C18 sphingoid base backbone) and is considered the rate-limiting step of de novo sphingolipid synthesis (9, 10, 12, 13). The heterodimeric SPT complex consist of two large subunits SPTLC1/SPTLC2 or SPTLC1/SPTLC3 (14–16) and a small subunit (SPTssa or SPTssb) that confers specificity towards the acyl-CoA substrate (17, 18). Availability of the acyl-CoA substrate and subunit composition are key determinants for the length of the resulting sphingoid bases (17). In most tissues the C18 sphingoid base is most abundant ("C+number" refers to the number of carbon atoms in the aliphatic chain). Accumulation of C20 sphingoid bases in the brain was associated with neurodegeneration (19) and a broad spectrum of sphingoid base length can be observed in the skin ranging from

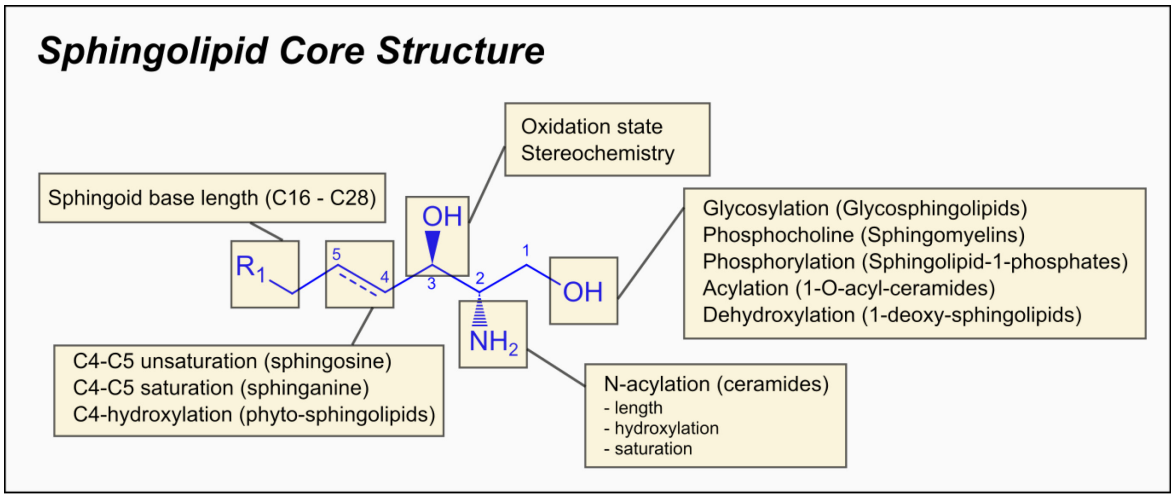

Figure 1 The sphingolipid core motif.

The sphingoid base core motif is characterized by an aliphatic chain of varying length with polar modifications by hydroxylation of C1 and C3 and amination at C2. Sphingosine-based sphingolipids carry a characteristic trans-double bond between C4 and C5. Further modifications of this core motif include acylation of the C2-amino group to yield ceramides. Attachment of polar headgroups to the C1-hydroxyl group may yield glycosphingolipids, sphingomyelins, and sphingolipid-1-phosphates.

C12 to C28 length (20–22). Although *L*-serine is the primary amino acid substrate for the SPT complex, the alternative amino acid substrates *L*-glycine and *L*-alanine may also be utilized. This is especially observed in hereditary sensory and autonomic neuropathy type 1 (HSAN1) patients, where it is associated with the formation of 1-deoxy- and 1-deoxymethyl-sphingolipids (23, 24). In a NADPH-dependent reaction the 3-keto group of the SPT product KDS is rapidly reduced to a 3-hydroxy group by 3-ketodihydrosphingosine reductase (KDSR) and yields the sphinganine base (25). Sphinganine is a substrate for ceramide synthases (CerS) (26, 27). CerS are characterized by their preference towards acyl-CoA substrates and tissue-specific distribution (Table 1). Ceramide is considered a key intermediate of sphingolipid metabolism, providing the core structure for several metabolic paths, and is derived from dihydroceramide by desaturation through sphingolipid Δ^4-desaturase (DES1) (28, 29). DES2 was shown to have Δ^4-desaturase/C4-monooxygenase activity which results in the formation of phytoceramides (30–33) (Figure 2).

Ceramides may be modified at the C1-hydroxyl group to yield glycosphingolipids, sphingomyelins, 1O-acyl-ceramides, or ceramide-1-phosphates (1, 34). Compartmentalization and the conjuncture of enzymes and substrates is a key determinant in the metabolic fate of single sphingolipid species (35). Due to variations in the sphingoid base, acyl-CoA substrate, and additional modifications thousands of sphingolipid species can be derived by combinatorial biochemistry.

Most anabolic reactions of sphingolipid metabolism are associated with a catabolic counterpart, that ensures degradation of synthesized lipids and prevents potentially toxic lipid accumulation and storage. Defects in sphingolipid catabolism are often associated with lysosomal storage diseases (36). Degradation by S1PL is the final catabolic step for the degradation of the sphingoid base backbone. S1PL is promiscuous regarding its substrate and can utilize sphingosine-1-phoshate, sphinganine-1-phosphate, and phytosphingosine-1-phosphate (37, 38). Sphingoid base degradation generates hexadecenal (or the respective metabolite for the other sphingoid bases (Figure 3)) and phosphoethanolamine. Hexadecenal is converted to palmitic acid by aldehyde dehydrogenase ALDH3A2 and activated palmitoyl-CoA may be reused as a substrate in glycerolipid and sphingolipid metabolism (Figure 3) (39).

Table 1 Proposed substrate affinities for ceramide synthases.

Isoform	Acyl-CoA preference	Tissue distribution	Reference
CerS1	C18	Brain	(40)
CerS2	C20 – C26	Ubiquitous	(41)
CerS3	C18 -C38 + polyunsaturated species	Epidermis and Testis	(42–44)
CerS4	C18-C22 (+C24 – C26)	Sebaceous glands, lung, etc.	(45)
CerS5	C16	Ubiquitous	(45)
CerS6	C16	Ubiquitous	(46)

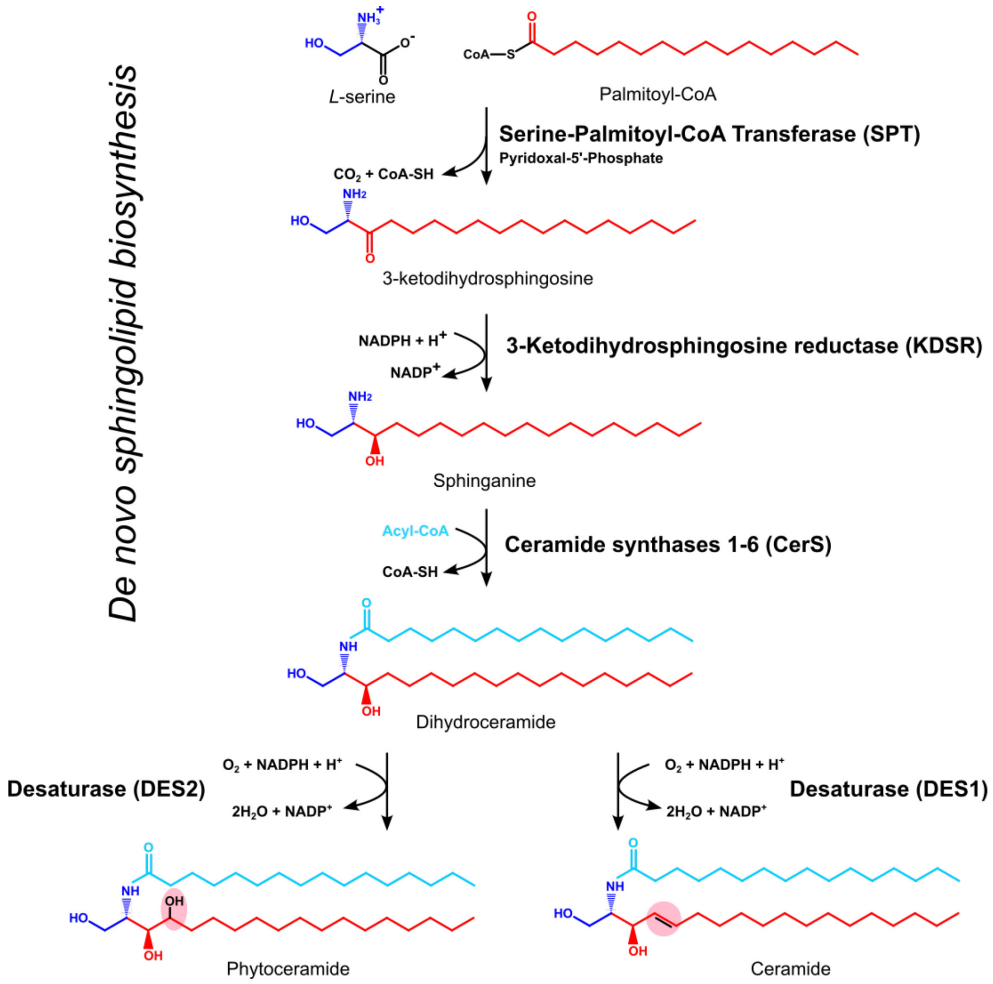

Figure 2 Sphingolipid de novo biosynthesis pathway.

Sphingolipid de novo biosynthesis is initiated by the condensation of acyl-CoA with L-serine. The product 3-ketodihydrosphingosine (KDS) is reduced by 3-ketodihydrosphingosine reductase (KDSR) to sphinganine in a $NADPH^+$-dependent manner. Ceramide synthases N-acylate sphinganine to produce dihydroceramide, which is a substrate for several metabolic pathways. Desaturation via DES1 yields ceramides and hydroxylation via DES2 yields phytoceramides. Modified from Rabionet et al. (2014).

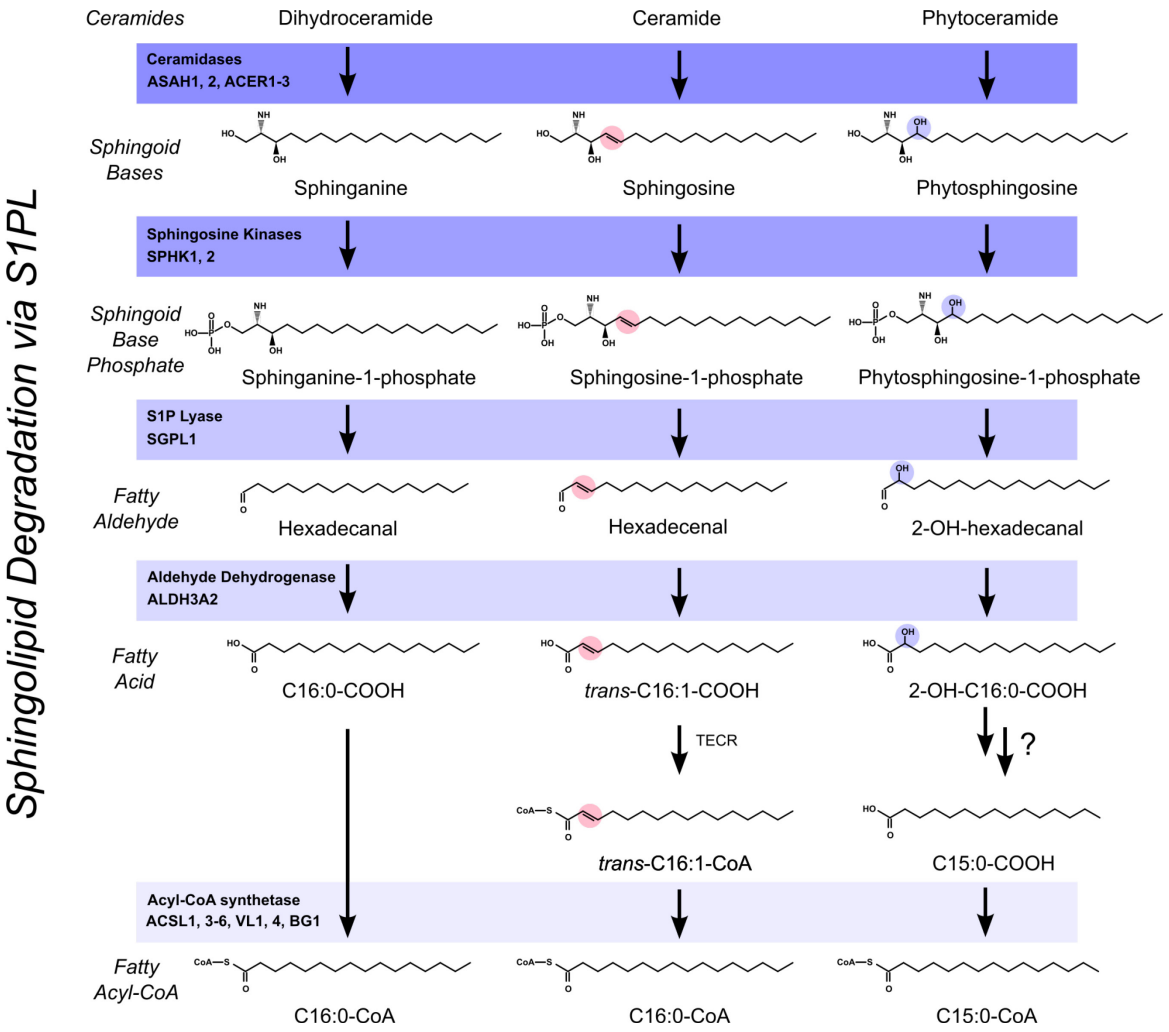

Figure 3 Sphingolipid degradation pathway (modified from Kihara, 2016).

Sphingoid bases are degraded via the S1P lyase pathway. Phosphorylation of sphingoid bases by sphingosine kinase (SPHK1 and SPHK2) yields sphingoid base phosphates. S1PL irreversibly converts sphingoid base phosphates to aliphatic aldehydes. Aldehyde dehydrogenase ALDH3A2 converts fatty aldehydes to fatty acids. Activation by CoA allows the integration of these products into glycerolipid or sphingolipid metabolism.

2.2 Metabolism and Function of globo-series Glycosphingolipids

Glycosphingolipids (GSL) form a major sphingolipid subclass and are characterized by their hydrophobic ceramide membrane-anchor and a diverse set of glycan structures that is attached to the C1-hydroxyl group by a β-glycosidic bond and provides each glycosphingolipid species with often unique functional properties in signalling, cell-cell communication, and development (48, 49).

GSL are classified based on their core glycan structures with the ganglio-, the globo- and the (neo)lacto-series being most abundant in mammalian cells (Figure 4) (48). Glycosphingolipid synthesizing enzymes are distributed across the ER and the Golgi cisternae (50) The spatial segregation of these enzymes is a determinant in the synthesis of specific glycan structures in different tissues and cell types. The delivery of lipid substrates to their specific location occurs via vesicular transport or requires dedicated lipid transport proteins and lipid flippases (51, 52). Transport of ceramide to the trans-Golgi network via ceramide transport protein (CERT) targets ceramide to sphingomyelin synthesis (52). After biosynthesis of the glycan moiety within the Golgi-network, mature glycosphingolipids are transported to the plasma membrane with membrane-bound transport carriers where they reside on the outer leaflet of the membrane (2). Degradation of glycosphingolipids is initiated by internalization and mediated by the action of a set of specialized lysosomal glycosidases and co-factors that hydrolyse terminal carbohydrate moieties. Finally, free sphingoid bases are released due to the action of acid ceramidase and, after transport to the ER, can be reutilized for the synthesis of complex sphingolipids (salvage pathway) (36).

Globo-series GSL biosynthesis

Galactosylceramide and glucosylceramide are common precursors for all glycosphingolipids (48). Glucosylceramide is synthesized by glucosylceramide synthase (GCS) after vesicular trafficking of ceramide from the ER to cytosolic leaflet of cis-Golgi membranes. Transbilayer flipping makes GlcCer accessible for further glycosylating enzymes. Galactosylation of GlcCer by lactosylceramide synthase (LCS) on the lumenal side yields lactosylceramide (LacCer) which is a central branching point for the synthesis of different glycosphingolipid core structures (48, 53). The synthesis of globo-series GSL is dependent on the

transport of glucosylceramide from the cytosolic side of the cis-Golgi to the trans-Golgi network via the lipid transfer protein FAPP2 (54, 55). A trans-Golgi lipid flippase (possibly ABCB4 or ABCA12 (56) translocates GlcCer to the lumenal side of the trans-Golgi, where it can be converted to lactosylceramide (LacCer) and subsequently globotriaosylceramide (Gb3Cer) by addition of UDP-galactose. Gb3Cer is the core structure for glycosphingolipids of the globo-series. Gb3Cer synthesis is mediated by an alpha-1,4-galactosyl transferase (Gb3 synthase/CD77 synthase, encoded by the A4GALT gene) (48, 57, 58). Metabolically downstream globo-series GSL, including Gb4Cer, Forssman antigen, stage-specific embryonic antigen-3 (SSEA3, Gb5Cer), Globo-H and stage-specific embryonic antigen-4 (SSEA4, sialyl-Gb5Cer) are synthesized by subsequent glycosylation reactions. Genome-wide CRISPR-based knockout screenings using Shiga toxin-induced cell death identified LAPTM4A and TM9SF2 as required for the synthesis of Gb3Cer. LAPTM4A is thought to regulate post-transcriptional Gb3 synthase activity and TM9SF2 to regulate the subcellular localization of Gb3 synthase (59–61). Gb3Cer is catabolized in the lysosome by α-galactosidase A (GLA). Mutations in GLA are associated with Fabry disease, which is characterized by lysosomal accumulation of Gb3Cer and lyso-Gb3Cer (62–64).

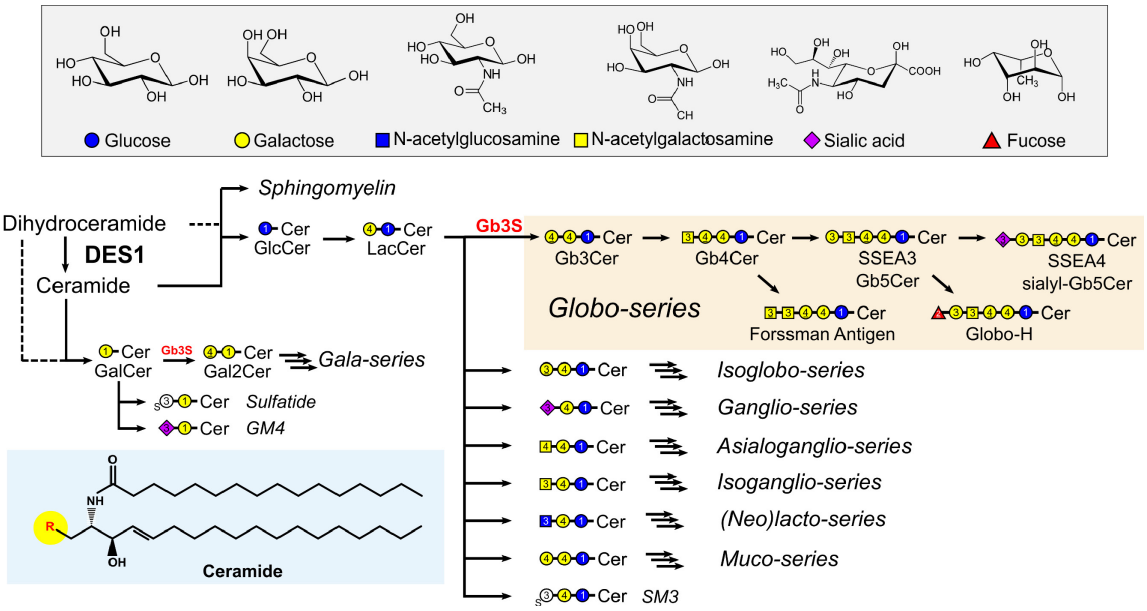

Figure 4 Glycosphingolipid biosynthesis and carbohydrate structures.

For GSL biosynthesis (dihydro)ceramides are glycosylated at the C1-hydroxyl group. All GSL are based on GlcCer and GalCer. LacCer is a central metabolic intermediate and precursor for several GSL series, based on core glycan motifs. This scheme does not account for the topological separation of different LacCer pools and highlight only the most prominent globo-series glycan structures.

Biological functions of globo-series GSL

Glycosphingolipids are localized to glycosphingolipid-enriched microdomains (GEM). They are involved in a variety of functions including cell-cell communication, cell adhesion, signalling receptor modulation, and apoptosis induction. Furthermore, GSL are important for cellular growth and differentiation (65–71).

Although cultured cells can grow in absence of glycosphingolipids, on an organismal level abnormal glycosphingolipid expression is often associated with physiological deficiencies. To elucidate the biological functions of certain glycosphingolipid subclasses, mouse knockout models of the respective enzymes have been studied in detail. While a loss of GCS and LCS expression was associated with embryonic lethality (72–74), more specific knockouts revealed a variety of phenotypes. GM3 synthase knockout mice exhibited enhanced insulin sensitivity (75). The loss of galactosylceramide synthase (GalCerS) was associated with neurological phenotypes (76). Depletion of the (neo)lacto-series revealed multiple phenotypes including early death, growth inhibition, fur loss, obesity, B-cell abnormalities, and reproductive problems (48, 77). Initially, Gb3S depletion did not result in an apparent phenotype, apart from a resistance against Shiga toxin, for which Gb3Cer is the cellular receptor (78). A recent study discovered an attenuation of bone formation due to a decrease in osteoblasts in Gb3S knockout mice (79).

Gb3S is an important enzyme of the p^k blood group system and responsible for the synthesis of different lipid-based antigens including P^k antigen (Gb3Cer), P antigen (Gb4Cer) and P1 antigen (a lacto-series GSL). In rare cases, the p phenotype can be observed in humans (worldwide prevalence: $5.8{:}10^6$ (80)) and is associated with a lack of these antigens. Pregnant women with a p phenotype often suffer from miscarriages, which is linked to the expression of anti-P^kPP1 antibodies. No other apparent phenotypes have been described in these individuals (81–83).

The biological functions of globo-series GSL are still debated, and several *in vitro* studies provide further insight in the context of neural differentiation. Stemness factors are often linked to the expression of globo-series GSL (84). The differentiation of stem cells into neuronal cells is associated with a switch

glycosphingolipid expression from globo-series to ganglio-series (85, 86). Russo et al. (2018) identified a globo-series GSL-dependent, self-contained circuit that regulates neuronal development and differentiation. Globo-series GSL were shown to repress the epigenetic regulator of neuronal gene expression AUTS2, which also controls GM3 synthase expression. Thereby, the expression of globo-series GSL inhibits the expression of ganglio-series GSL requiring a decrease of globo-series GSL for the differentiation of stem cells into neuronal cells (87). The exact mechanism of epigenetic regulation by globo-series GSL is yet unsolved.

A recent study on cell-to-cell heterogeneity in skin fibroblasts demonstrated that the sphingolipid compositional state influences cell identity, cellular responses, and cell-specific transcriptional programs (88). Manipulations of sphingolipid metabolism were sufficient to reprogram the respective cells, which was attributed to a connection between lipid composition and signalling pathways. The globo-series GSL Gb4Cer was shown to positively regulate signalling of fibroblast growth factor 2 (FGF2) through fibroblast growth factor receptor (FGFR), while ganglioside GM1 acted as a negative regulator (88).

A modulation of growth factor receptors by globo-series GSL was also demonstrated for Gb4Cer and epidermal growth factor receptor (EGFR), which results in an activation of extracellular signal-regulated kinase (ERK) signalling (89). Critical roles in the regulation of apoptosis and survival in breast cancer were attributed to the globo-series GSLs SSEA3, SSEA4 and Globo H through the formation of a complex with caveolin-1(CAV1)/focal adhesion kinase (FAK)/AKT/receptor-interacting protein kinase (RIP) in membrane microdomains that prevents the initiation of CD95/Fas-dependent apoptotic signalling (90). Furthermore, depletion of globo-series GSL through deletion of Gb3S has been shown to induce epithelial-to-mesenchymal transition (EMT) in epithelial cancer cells and Gb3S contributes to the maintenance of an epithelial cell state (91). Globo-series GSL may also modulate inflammatory processes. TLR4-mediated macrophage activation is positively regulated by Gb3Cer and Gb4Cer at low concentrations (92), while at higher concentrations the inflammatory response is suppressed (93).

Globo-series GSL were found to be upregulated in several cancer types, including leukaemia, Burkitt's lymphoma, pancreas, and colon cancer (94, 95) and a role of Globo H and SSEA-4 in the development and progression of cancer and as potential therapeutic target is discussed (96).

Recently, another role for globo-series GSL was described in renal physiology (97). Loss of globo-series GSL in Gb3S knockout mice was associated with an increase in albumin excretion in absence of apparent changes to glomerular filtration. These effects were enhanced by a western-type diet, that was found to increase Gb3S expression. The observed effects were attributed to a reduced uptake of compounds from the glomerular filtrate in renal proximal tubular epithelial cells (Figure 5). Furthermore, Gb3S mice were protected in a model of glycerol- and gentamicin-induced acute kidney injury. These results point to a modulatory effect of globo-series GSL within the proximal tubular endolysosomal network, but the underlying mechanisms remain unknown. A clathrin-independent and glycosphingolipid-dependent endocytic mechanism, that requires GSL for clustering, membrane bending, and vesicle biogenesis was described and highlights a role for glycosphingolipids in endocytosis (98).

In summary, these studies indicate, that globo-series GSL and glycosphingolipids in general may play a role in the diversification of cellular responses and cell fate decisions. Although globo-series GSL are not essential for life, they may be important to finetune cellular responses, interactions, and activities, like endocytosis in specialized environments.

The proximal tubular endolysosomal network

The main function of the proximal tubules is the reabsorption of essential nutrients and macromolecules, including albumin, transferrin, and low-molecular weight proteins (LMWPs), from the glomerular filtrate to sustain homeostasis (99). Dysfunction of the endolysosomal network in proximal tubular cells is associated with a massive loss of solutes and proteins through the urine (100). Proximal tubules are divided into S1, S2 and S3 segments based on cellular morphology, mRNA expression, protein expression, ultrastructure and endolysosomal network (101, 102). Most proteins from the glomerular filtrate are cleared in the S1 segment with the highest expression of the endolysosomal machinery through receptor-mediated, clathrin-dependent endocytosis (101, 103, 104).

The two multiligand receptors lipoprotein receptor-related protein 2 (LRP2)/megalin and cubilin are located at the brush border of proximal tubular epithelial cells and have an essential function in the binding and uptake of proteins and compounds from the glomerular filtrate (103, 104). For membrane-anchorage cubilin interacts

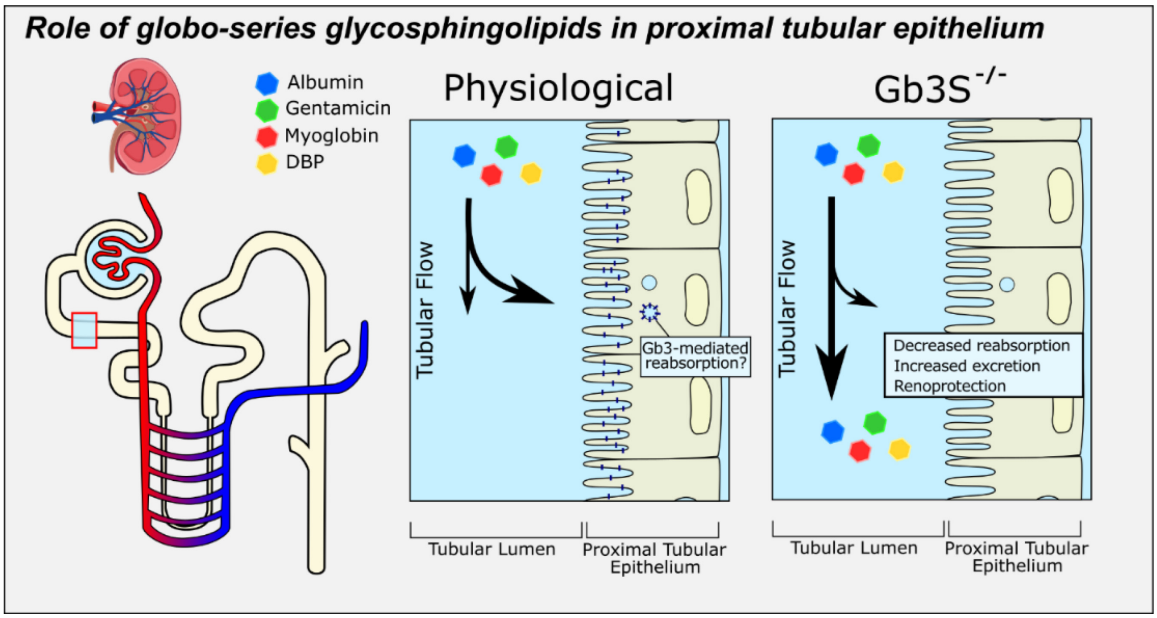

Figure 5 Hypothesized role of globo-series GSL in the proximal tubulus.

Proposed model for the effects of Gb3 synthase knockout on renal reabsorption. Under physiological conditions most protein in the ultrafiltrate is reabsorbed in the S1 and S2 segments of the proximal tubules through receptor-mediated endocytosis in a specialized endolysosomal network. Gb3Cer is proposed to have a positive modulatory function on endocytosis of filtered proteins and xenobiotics. Lack of Gb3Cer is associated with an increase in urinary excretion of filtered compounds. In models of glycerol- and gentamicin-induced acute kidney injury, the reduced reabsorption of myoglobin or gentamicin in proximal tubular epithelial cells decreased the cytotoxic burden on these cells.

with amnionless (AMN) to form the CUBAM complex, which may also be important for the apical sorting of cubilin (105). Receptor recruitment to clathrin coated pits is facilitated by interaction with Dab2 endocytic adaptor (106). Receptor-ligand complexes are internalized within clathrin-coated vesicles. In apical early endosomes (AEE) ligands are released from the receptors by vesicular acidification through vacuolar H^+ ATPase (v-ATPase) (107, 108). Ligand containing AEE mature into apical vacuoles (AV) and ligands are degraded in lysosomes. Receptors are recycled to the apical surface through Rab11-positive dense apical tubules (DAT) (109). Impaired recycling of receptors as seen in patients with mutations in chloride-proton exchanger ClC-5 is associated with a loss of ligands in the glomerular filtrate (110). Some studies point to a compensatory role for megalin-dependent fluid phase uptake in the recovery of supranormal albumin levels under nephrotic conditions (99, 111, 112).

2.3 Skin sphingolipid metabolism and diseases

Skin structure and layers of the epidermis

The second part of this work will focus on skin sphingolipid metabolism and the role of KDSR mutations for the development of palmoplantar keratoderma.

The skin is the largest organ of the human body and provides an essential barrier between organisms and their environment. Dermis and epidermis are two major structures in the skin. The dermis consists of papillary and reticular fibroblasts and is supplied by blood vessels. The basal membrane separates dermal from epidermal cells. The epidermis is a highly polarized, stratified epithelium and is supported by the basal membrane. The epidermis is subdivided into several cell layers with specific characteristics and functions including the stratum basale (SB), stratum spinosum (SS), stratum granulosum (SG) and stratum corneum (SC). The primary barrier between organisms and their environment is formed in the upper layer of the epidermis, the stratum corneum, while the lower layers (SB, SS, SG) ensure a constant renewal of this barrier. Important functions of the epidermis include the prevention of water loss, exclusion of toxins, resistance to mechanical stress, antimicrobial effects, and a participation in immune responses (Reviewed in (113, 114)).

The basal membrane provides support for a layer of epidermal stem cells, the stratum basale (SB) (115). Epidermal stem cell-derived progeny undergoes several cycles of replication and finally enters terminal differentiation into corneocytes (116). The balance between proliferation and terminal differentiation is tightly controlled (117). The stratum spinosum is characterized by a reinforcement of the cytoskeleton by a keratin filament network and desmosomes are formed between cells. Lipid biosynthesis is highly increased at the interface between stratum spinosum and stratum granulosum (SG) to meet the demand for the formation of the lipid barrier and late differentiation markers of keratinocytes like loricrin and (pro)filaggrin are expressed (47). This is in line with an increase in expression of enzymes of the sphingolipid metabolic machinery (118). Lipids are stored in lamellar bodies (119–121). Keratinocytes start to flatten but are still nucleated in the SG. The SG/SC interface is characterized by an extrusion of synthesized lipids into the extracellular space where they form the hydrophobic lipid lamellae, which

surround the cornified lipid envelope (120, 122). Keratinocytes are further flattened during cornification and lose cellular organelles and nuclei. Mature corneocytes are strongly interconnected by corneodesmosomes and water impermeability is ensured by the intercellular lipid lamellae and the cornified lipid envelope (123, 124). Corneodesmosomes between aging corneocyte layers are slowly degraded and finally dead corneocytes are shed in a process called desquamation to ensure a constant renewal of the stratum corneum and the skin barrier with an estimated turnover of 40-56 days in humans (117, 125, 126).

The terminal differentiation of keratinocytes involves complex signalling processes and changes in cellular physiology. This introduction will emphasize changes in sphingolipid metabolism as they are observed during cornification and formation of the skin lipid barrier.

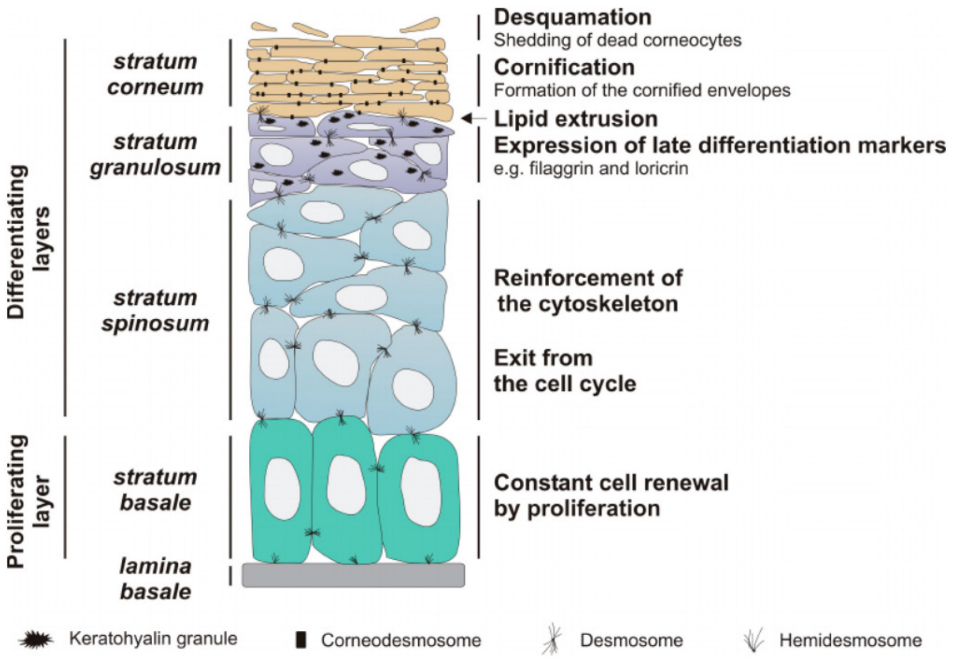

Figure 6 Epidermal structure and terminal differentiation of keratinocytes.

The epidermis is a stratified and polarized epithelium and characterized by the maturation and terminal differentiation of keratinocytes. Epidermal stem cells in the stratum basale are supported by the lamina basale. Progeny cells enter terminal differentiation in the stratum spinosum, which is linked to a loss of proliferative capacity and a reinforcement of the cytoskeleton. The stratum granulosum is characterized by an increase in lipid synthesis, corneocyte envelope proteins and the formation of lamellar bodies. At the interface to the stratum corneum lamellar body contents are extruded into the intercellular space for the formation of lipid lamellae and the cornified lipid envelope. Keratinocytes flatten, lose cellular organelles, and become corneocytes. Renewal of the epidermis is ensured by constant shedding of the outer corneocytes. Figure taken from (127).

Sphingolipid diversity in the skin

Sphingolipid metabolism in the skin differs from other tissues and has unique properties due to the specialized function of ceramides in the skin as components of the lipid lamellae. Lipid lamellae are part of the skin lipid barrier composed of ceramides, free fatty acids, and cholesterol in approximately equimolar ratio (128). Keratinocyte differentiation is associated with a marked increase in ceramide production and Ceramides are estimated to amount for 50% of total lipid in stratum corneum by weight (119). In the epidermis sphingolipids may have physiological functions as membrane lipids, signalling lipids, and barrier lipids. Regulatory functions of sphingolipids include cell cycle arrest, differentiation, and apoptosis (129).

The diversity of sphingolipid species observed in the skin is unique compared to other tissues. Epidermal sphingoid bases are synthesized via *de novo* synthesis by the SPT complex. In contrast to other tissues where the majority of sphingoid bases are composed of aliphatic chains with 18 carbon atoms epidermal sphingoid bases can reach a length of up to 28 carbon atoms (20, 130–132). The mechanisms leading to, and the functions associated with this broad length distribution are not well established. Subunit composition of the SPT complex may play a major role in the determination of sphingoid base length. SPTLC3 is highly expressed in skin tissue (14, 15). Although SPTLC3 was shown to be involved in the production of shorter C16 sphingoid bases (133), the SPTLC1/SPTLC3 complex is promiscuous towards other substrates (14) and may be involved in the production of sphingoid bases >C22. Furthermore, the availability of elongated acyl-CoA substrates as they are observed with the expression of elongation of very long chain fatty acids protein 1 and 4 (ELOVL1 and ELOVL4) in the epidermis (134, 135) could favour a synthesis of longer sphingoid bases.

Besides differences in length distribution, a high structural diversity can be observed for epidermal sphingoid bases. Sphingosine, sphinganine, phytosphingosine and 6-hydroxy-sphingosine, a structural variant observed exclusively in the epidermis, have been reported (47). The biosynthetic mechanism for the synthesis of 6-OH-sphingosine bases is not yet established.

This diversity in sphingoid bases is complemented by a variety of substrates for N-acylation of sphingoid bases. Acyl-CoAs cover an increased length, several degrees of saturation, hydroxylation, and methyl-branching and compared to other tissues a high amount of α-hydroxylated C16- – C26-FA (LC- and VLC-FA) ceramide species is present in the epidermis (136). Sphingoid bases may be N-acylated with ultra-long chain fatty acids (ULC-FA) (C28 - C38) (43). These ULC-FA-ceramides may also be ω-hydroxylated (137) and ω-esterified (138). In addition, ω-esterified ceramides may be bound to proteins of the cornified envelope (139). Furthermore, 1-O-acyl-ceramides can be found in the skin (140).

Motta et al. (1993) proposed a systematic, letter-based nomenclature system to group ceramide species with common structural features, which is presented in an extended form in Figure 7. The last letter describes the structural features of the sphingoid base (S – sphingosine, dS – sphinganine, P – phytosphingosine, H – 6-OH-sphingosine). The first letter describes the modification at the N-acyl terminus (N – non-hydroxylated, A – α-hydroxylated, O - ω-hydroxylated, EO – esterified ω-hydroxylated, PO – protein-bound ω-hydroxylated). For the presented thesis I further extended the described nomenclature system to describe ceramides with 3-ketodihydrosphingosine base (dK) and 3-ketosphingosine base (K).

N-acyl FA / SB	**N** non-hydroxy	**A** α-hydroxy	**O** ω-hydroxy	**EO** esterified ω-hydroxy	**PO** protein-bound
dS Sphinganine	NdS	AdS	OdS	EOdS	POdS
S Sphingosine	NS	AS	OS	EOS	POS
P Phyto-Sph	NP	AP	OP	EOP	POP
H 6OH-Sph	NH	AH	OH	EOH	POH
(d)K 3-Keto-(dh)Sph	N(d)K	A(d)K	O(d)K	EO(d)K	PO(d)K

Figure 7 Nomenclature system for skin ceramides (modified from (141)).

Formation of the skin barrier

The biosynthetic pathways for the synthesis of this high variety of sphingolipid species are highly specialized and often unique to epidermis. The synthesis of intercellular barrier ceramides is initiated in the lower SS layers and increased in SG due to an upregulation of *de novo* sphingolipid synthesis in the ER. The increase in sphingolipid levels and diversity is highly correlated with keratinocyte differentiation (142).

Synthesized ceramides are transported to the Golgi-network, where they are converted to GlcCer and SM and packed into lamellar bodies, which is thought to protect differentiating keratinocytes from cytotoxic effects of ceramide accumulation (143). At the SG-SC interface, lamellar bodies fuse with the apical membrane and release their contents into the extracellular space. This is accompanied by the secretion of the catabolic enzymes β-glucocerebrosidase (GBA) and acidic sphingomyelinase (ASM/SMPD1) as well as corresponding sphingolipid activator proteins saposin A-D (144) and the hydrolysis of most of these complex sphingolipids to ceramides (145, 146). GlcCer was shown to be a precursor for NS, NH, NP, AS, AH, AP, EOS; EOH, EOP, POS, POH ceramides (147), while SM yield NS and AS ceramides (148).

While Cers2, Cers3, Cers4, and Cers5 were found to be expressed in murine skin biopsies (43), a strong induction of CerS3 activity was observed upon differentiation of human cultured keratinocytes (149), that replaces CerS2 activity in differentiating layers of the epidermis (135). CerS3 is responsible for the synthesis of ULC-FA-ceramides (43). ULC-FA substrates for CerS3 are provided by de novo fatty acid synthesis through cytosolic FAS and subsequent elongation of the resulting fatty acids by the ER-associated ELOVL1- and ELOVL4-associated elongase complex to ULC-FAs (>28 carbons) (134, 135). ELOVL4 was shown to be coregulated with CerS3 (150) and the ELOVL complex may directly interact with CerS3 (Rabionet et al., 2014). Phytoceramides are synthesized through hydroxylation of dihydroceramide. Desaturase DES2 is upregulated during keratinocyte differentiation and contributes to the production of phytosphingosine-based ceramides (33).

For the formation of the cornified lipid envelope, the generation of ω-OH-ULC-FA-ceramides and their glycosylation is essential. The ω-OH group is introduced to ULC-FA-ceramides by oxidation through CYP4F22 (137). ω-OH-ceramides are esterified with (primarily) linoleic acid by PNPLA1 using triglycerides as linoleic acid donors (138) a process substantially activated by ABDH5 (151). It is unclear at which step glycosylation occurs. The cornified envelope is formed around anuclear corneocytes by protein crosslinking through transglutaminases. ω-esterified-glucosylceramides are covalently linked to proteins of the cornified envelope (139). Evidence for a non-enzymatic mechanism for protein-binding of linoleic acid-ω-

esterified-glucosylceramides was recently presented (152). ω-esterified-glucosylceramides are successively oxygenated by 12*R*-lipoxygenase (ALOX12B) to form 9*R*-hydroperoxy-EOS-glucosylceramides and epidermal lipoxygenase-3 (ALOXE3) converts this intermediate to EpOH-EOS-glucosylceramides (47, 153), which can be oxidized by SDR9C7 to Ep-keto-EOS-glucosylceramides (epoxy-enone-EOS-GlcCer). The resulting epoxy-enones are reactive and undergo non-enzymatic Michael addition or Schiff base and pyrrole formation resulting in covalent linkage to proteins of the cornified envelope (152). Hydrolysis of the glucosyl moiety by GBA occurs after covalent linkage to the cornified envelope and requires sphingolipid activator protein saposin-C (SAP-C) as a cofactor. This novel mechanism contrasts with predicted mechanisms that require successive oxygenation of esterified-linoleic acid for esterase-catalysed hydrolysis of the oxidized ω-linoleic acid followed by crosslinking of the exposed ω-OH group to proteins of the cornified envelope. Protein-bound ω-OH-ceramides can be further hydrolysed by acidic ceramidase or alkaline ceramidase 1 resulting in release of the sphingoid base moiety and a protein-bound ω-OH-ULC-FA (34, 154)

Skin diseases related to sphingolipid metabolism

Defects in enzymes involved in the synthesis and hydrolysis of barrier sphingolipids are often associated with a reduction of barrier function and severe skin disorders. GCS (155), GBA (156, 157) and ASM (158) were associated with severe barrier defects. Furthermore, the activator protein saposin-C (SAP-C) was shown to be essential for establishment of the skin barrier (159). Deletion of Sptlc2 in mice was associated with psoriasiform skin lesions (160). Deficiency of CerS3 in humans was linked to autosomal recessive congenital ichthyosis (ARCI) (161) and lethal skin barrier defects in mice (43). Mutation of ELOVL4 were found to be causative for Stargardt diseases type 3 (STGD3) (162). CYP4F22 deficiency was linked to ARCI and ichthyosis (137, 163, 164). DGAT2-deficiency was shown to reduce linoleic acid levels and result in a depletion of ω-acyl-ceramides accompanied by skin barrier defects (165). Defective transport of GlcCer into lamellar bodies by ABCA12 was found to cause severe skin barrier defects and Harlequin ichthyosis (166, 167). Furthermore, mutations in ALOX12B and ALOXE3, which are essential for the oxygenation of esterified linoleic acids were found to cause ARCI in humans and skin barrier defects in mice (153, 168–170).

Pathological changes in the skin are tightly linked to alterations in epidermal lipid metabolism. Changes in epidermal lipid profiles were described for skin pathologies like atopic dermatitis, psoriasis and xerosis (171). Furthermore, a decrease in epidermal ceramides is often associated with increased trans-epidermal water loss, barrier dysfunction and loss of microbial protection (34).

In atopic dermatitis (AD), considered a disease of immunological pathogenesis, it is unclear whether changes in skin barrier permeability are consequence of inflammation (“inside-outside” hypothesis) or if they contribute to disease activity (“outside-inside” hypothesis) (172–174). Total ceramide levels are reduced (175) and ceramide composition is altered in lesional AD skin (175–177). Several ceramide classes are depleted including EOS, EOH, EOP, NH, and NP ceramides (177). The distribution of species within ceramide classes is changed, favouring shorter ceramide species (177–179). An elevation of CerS4 expression was described in lesional atopic dermatitis skin, that may explain changes in the N-acylation pattern (180).

In *psoriasis vulgaris* (Pso) patients changes in epidermal lipid composition were observed. Psoriasis vulgaris is characterized as an immune-inflammatory disease that involves the skin. Skin lesions exhibit a decrease in NDS, NH, AH, EOH, EOP and EOS ceramides (141, 181) and reduced levels of phytoceramides (176). NS and AS ceramides are significantly increased.

Recently, biallelic mutations in *KDSR* were linked to skin disorders of the erythrokeratoderma spectrum (182–184). The mutations in these patients did not confer a complete loss of enzymatic function, which would result in a complete lack of sphingolipids and is predicted to be incompatible with life. Although a reduced percentage of esterified ceramides was observed in KDSR patients, sphingolipid levels were rather normal (183) and the causative mechanisms for the pathogenesis of KDSR-associated skin disorders is under investigation.

In summary, these studies highlight the essential function of each metabolic step during synthesis of skin barrier ceramides and demonstrate the critical issues that are associated with a perturbation of epidermal sphingolipid metabolism.

3 Aim of the thesis

The two chapters of this thesis are about different enzymes of sphingolipid metabolism in their specific contexts of physiology and pathology.

(I) Gb3S, a glycosphingolipid synthesizing enzyme, was described to be involved in kidney function of mice, specifically the reuptake of compounds from the glomerular filtrate. A reduction of reuptake was associated with protective effects in glycerol- and gentamicin-induced models of acute kidney injury. The underlying mechanisms are unknown. My aim is to investigate, whether and how globo-series GSL – protein interactions may mediate the reuptake and renoprotective effects. I will establish the necessary cell culture models and assay conditions for the identification of protein interaction candidates with globo-series GSL using a bifunctional sphingosine probe (pacSph). The identification of protein candidates for an interaction with globo-series GSL may provide a foundation for future investigations of the underlying mechanisms. An understanding of the underlying mechanisms could result in strategies to avoid renotoxicity of common pharmacological compounds or during cancer treatments.

(II) Biallelic mutations in KDSR, an enzyme of the sphingolipid *de novo* synthesis pathway, were shown to cause skin pathologies of the erythrokeratoderma spectrum. Sphingolipid synthesis and composition are important determinants of skin maintenance. My aim is to analyse the consequences of KDSR mutations regarding ceramide and sphingoid base metabolism by liquid chromatography-based tandem mass spectrometry (LC-MS/MS). Of special interest is the question whether there is an accumulation of the KDSR substrate KDS and if this can be an alternative substrate for ceramide synthases to generate non-physiological ceramides. Furthermore, I want to compare observations from KDSR patients to atopic dermatitis and psoriasis vulgaris patients. A detailed understanding of the metabolic effects of KDSR mutation may help to develop treatment strategies for these patients.

4 Chapter 1 - Identification of globo-series GSL-interacting proteins

4.1 Results

In a model of rhabdomyolysis, Gb3 synthase knockout was shown to protect mice from acute kidney injury. The aim of this chapter is to provide a foundation for a future investigation of the physiological and pathophysiological effects of globo-series GSL in the context of renal proximal tubular epithelial cells and how the lack of these lipids can contribute to renoprotection. A special emphasis was laid on the identification of specific protein interactions of globo-series GSL using a bifunctional lipid probe (pacSph) for proximity crosslinking and protein enrichment.

4.1.1 HK-2 - a proximal tubular epithelial cell line

The immortalized human proximal tubular epithelial cell line HK-2 (185) is derived from a single cell of adult human kidney. It was immortalized using the E6/E7 genes from human papilloma virus (HPV). Compared to other cell lines that are often derived from tumours, from animals or are of embryonic origin, HK-2 retains some characteristics of primary and renal proximal tubular epithelial cells (RPTECs). The dependence on epidermal growth factor (EGF) indicates a regulatory control of growth processes (185). HK-2 expresses alkaline phosphatase, γ-glutamyl peptidase, leucine aminopeptidase, acid phosphates, cytokeratin, α3β1 integrin and fibronectin, which are epithelial markers and brush border associated enzymes (185). The mesenchymal markers factor VIII-related antigen, 6.19 antigen and CALLA endopeptidase are not expressed in HK-2. Functional characteristics include Na^+-dependent/phlorizin-sensitive sugar transport, which is unique to the apical membrane of proximal tubular epithelial cells and indicates that brush border membrane transport systems are retained in this cell line. Adenylate cyclase is responsive to parathyroid, but not antidiuretic, hormone. HK-2 is also a suitable model to study injury response and injury repair in proximal tubular epithelial cells, and it was shown that the respective mechanisms of H_2O_2 response are retained (185). HK-2 forms monolayers during growth with a cuboidal morphology. Dome formation and contact inhibition can be observed. Junctional complexes and microvilli that are reminiscent of brush border are present (185). At lower

confluence levels fibroblast-like protrusions can be observed in individual cells (Figure 8B).

HK-2 cells express globo-series GSL

I examined glycosphingolipid expression in HK-2 cells by high-performance thin layer chromatography (HPTLC) and liquid chromatography-coupled tandem mass spectrometry (LC-MS/MS).

For this, I grew the cells to 80% confluence in either DMEM/F-12 (1:1) (Dulbecco's modified eagle medium/F-12) supplemented with 10% fetal calf serum (FCS) or keratinocyte serum-free medium supplemented with EGF and bovine pituitary extract. For comparison a normal rat kidney (NRK) cell line was grown under the same conditions. The cells were harvested by scraping and lipids were extracted, phospholipids were removed by alkaline hydrolysis and samples were fractionated into neutral and acidic glycosphingolipids by anion exchange. Separation of the lipids on a HPTLC plate and carbohydrate-sensitive orcinol staining revealed the specific glycosphingolipid expression patterns (Figure 8A).

The major neutral glycosphingolipids observed in HK-2 were of the globo-series, namely Gb3Cer and Gb4Cer. Globo-series GSL levels were comparable under both media conditions. I found hexosylceramide in both media conditions and I observed a slightly increased level of lactosylceramide in DMEM/F-12 (10% FCS). Acidic glycosphingolipids of the GM- and GD-series were present in HK-2 at a low level. In NRK cells I only found moderate amounts of GM3 (Figure 8A). The expression of Gb3Cer was further confirmed by treatment of HK-2 with the Cy3-labeled B-subunit of shigella toxin (StxB-Cy3) and subsequent confocal fluorescence microscopy. The binding of the StxB-subunit to Gb3Cer is a crucial step in shiga toxin uptake and indicates the presence of Gb3Cer (Figure 8C). Furthermore, I confirmed Gb3 expression by immunostaining with chicken anti-Gb3Cer antibody (JM06/298-2) (Figure 8D). Permeabilization of the cells with 0.1% Triton X-100 led to a more particulate staining compared to non-permeabilized samples. The even distribution of the staining likely resembles physiological Gb3Cer localization more closely. On cellular level I observed differences in staining intensity between individual cells indicating heterogenous Gb3Cer expression within the population.

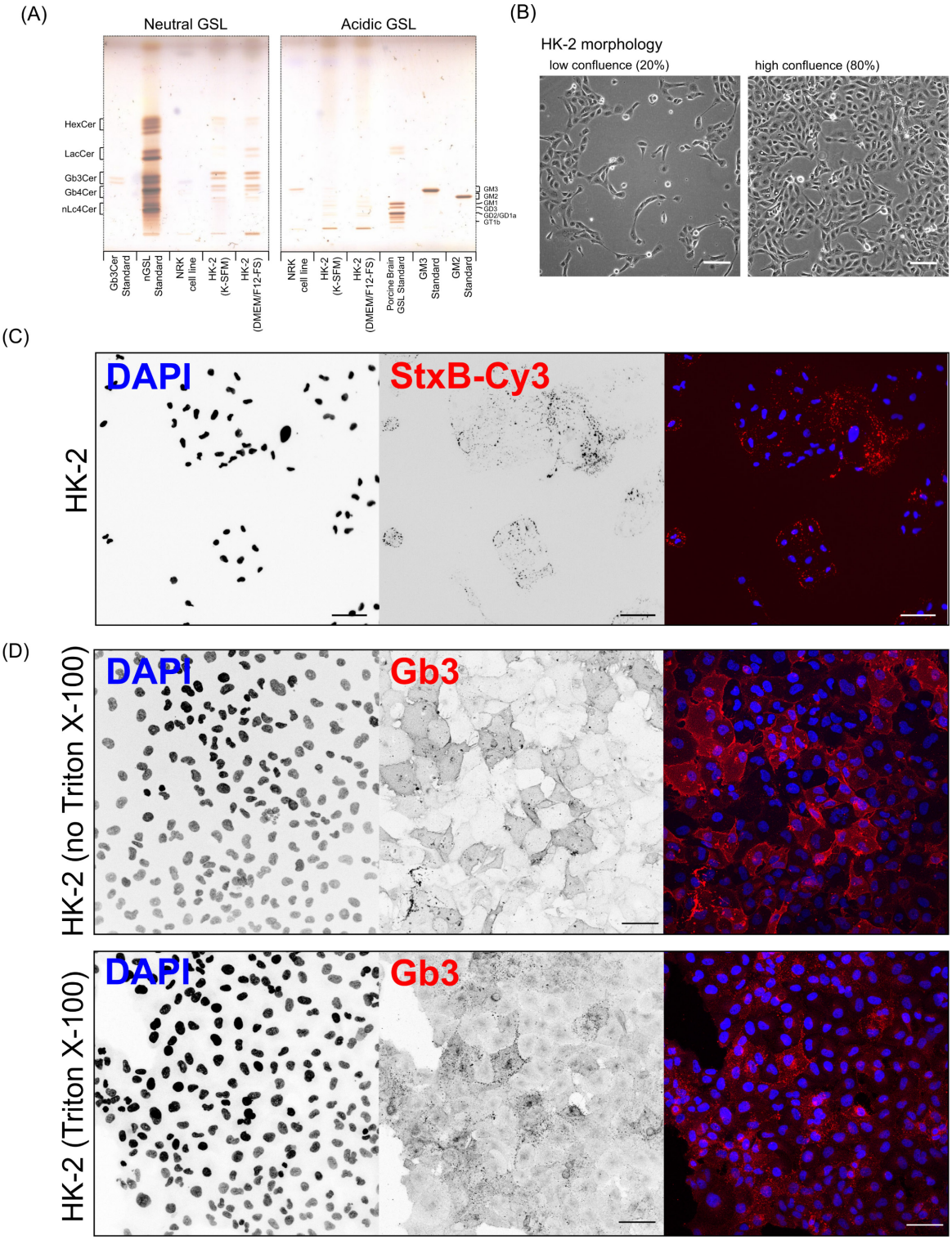

Figure 8 Characterization of the human PTEC line HK-2.

Glycosphingolipid expression in human proximal tubular epithelial HK-2 cells was examined with various methods. (A) High-performance thin layer chromatography (HPTLC) of fractionated lipid extracts was performed. The lipid extract equivalent to 100 µg protein was applied to the plates. Plates were developed in chloroform/acetone (1:1) and chloroform/methanol/0.2% $CaCl_2$ (60:35:8) subsequently over the full length. Glycosphingolipids were stained with orcinol solution. For evaluation of neutral GSLs a neutral GSL (nGSL) standard containing GlcCer, LacCer, Gb3Cer, Gb4Cer and

nLc4Cer and Gb3Cer standard were applied. For acidic GSL a porcine brain ganglioside mix (including GM1, GD3, GD2, GD1a and GT1b) and GM3 and GM2 standards were applied. (B) HK-2 cells were grown under standard growth conditions (DMEM/F-12 + 10% FCS) to the desired density and brightfield images were obtained. (C) HK-2 cells were treated with 0.5 µg/mL StxB-Cy3 and StxB binding was confirmed by confocal microscopy. Nuclei were counterstained with DAPI. (D) Permeabilized (Triton X-100) and non-permeabilized (no Triton X-100) HK-2 cells were stained with chicken anti-Gb3Cer antibody (JM06/298) (dilution 1:100). Antibody binding was detected with secondary goat anti-chicken Alexa594™ antibody conjugate (1:200). Scale bars indicate 50 µm.

I evaluated the expression of lipid species by mass spectrometry. A parent scan of m/z 264 by direct injection of HK-2 lipid extract from a subconfluent culture revealed the palmitic acid (C16) and nervonic acid (C24:1) N-conjugated lipids as the primarily expressed species in ceramides (Cer), hexosylceramide (HexCer), lactosylceramide (LacCer) and globotriaosylceramide (Gb3Cer) (Figure 9A). This was further confirmed by liquid chromatography-coupled mass spectrometric analysis. C18-, C20-, C22-, and C24-N-conjugated species of Gb3Cer were observed in minor amounts (Figure 9B).

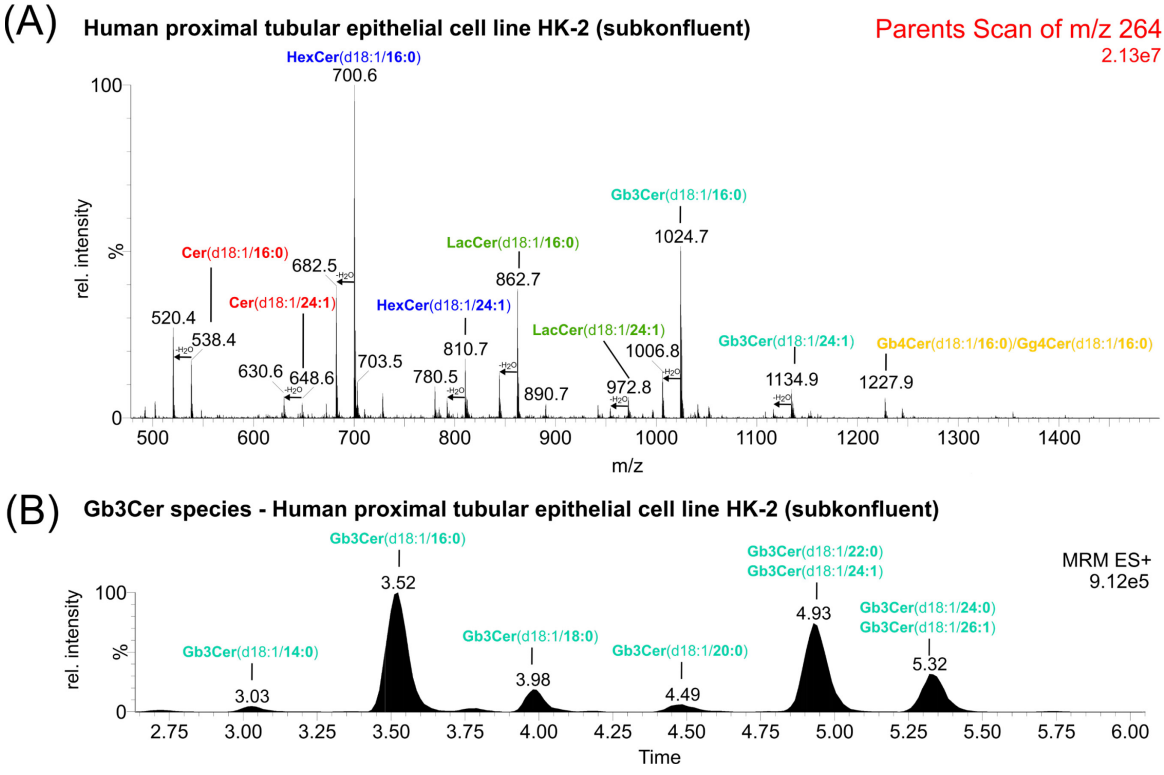

Figure 9 Mass spectrometric characterisation of neutral GSL expression.

Mass spectrometric characterization of the expression of sphingolipid species. (A) Parent scan of m/z 264 @ 28 eV collision energy from m/z 500 – m/z 1500. Lipid extract from a subconfluent HK-2 culture was injected. Major species of the observed sphingolipid classes are annotated. (B) Relative LC-MS/MS analysis of Gb3Cer species from a subconfluent HK-2 culture.

4.1.2 Metabolic labelling of GSL with pacSph

The application of a bifunctional sphingosine (pacSph) probe to interrogate protein-sphingolipid interaction was demonstrated by metabolic labelling (Haberkant 2015). Due to the additional metabolic steps, labelling of glycosphingolipids may require an adjustment of labelling parameters. For labelling of globo-series GSL several metabolic steps have to be passed after metabolic conversion to ceramide and glucosylceramide including the transport by FAPP2 to the trans-Golgi network, ABCB1-mediated flipping, conversion to lactosylceramide, and conversion by Gb3 synthase to Gb3Cer.

I established a LC-MS/MS method to examine changes in pacSph-labelling of sphingolipid and degradation of the probe into phospholipids, investigated the use of a S1PL inhibitor as an alternative to S1PL knockout to prevent degradation of the probe into glycerolipids, and optimized labelling parameters, like labelling time and cell culture state, for an increase in specific labelling of globo-series GSL. Further modification of lipid labelling on species level was proven to be possible by treatment with oleic acid.

LC-MS/MS for evaluation of pacSph labelling

For the evaluation of analytical conditions of pac-sphingolipids and pac-phospholipids, I treated HK-2 cells with pacSph (6 µM, 4h) and extracted the lipids without further UV crosslinking or click reaction. A parent scan of m/z 264 revealed HexCer(d18:1/16:0) and HexCer(d18:1/24:1) as abundant lipid species in these extracts (Figure 10B *upper panel*). Product ion scan of the respective pacSph-labelled pacHexCer(d18:1/24:1) and pacHexCer(d18:1/16:0) species was performed. I identified a fragment at m/z 272 that's indicative of the modified sphingoid base after deacylation, and neutral loss of the glucose head group and water ($[M+H-Hex-FA-N_2]^+$) (Figure 10A). In this fragment the diazirine group is converted into a carben structure concomitant with the release of nitrogen. I observed minor amounts of a fragment with m/z 290 that retained the water ($[M+H-Hex-(FA-H_2O)-N_2]^+$) and of a fragment with m/z 300 with retaining the diazirine group ($[M+H-Hex-FA]^+$). A parent scan of m/z 272 reveals the respective pacSph-labelled lipid species with a mass difference of 36u (Figure 10B *lower panel*). For quantification of pacSph-labelled lipid species the transition of the molecular ion

(including the mass increase of 36u compared to non-labelled species) to the fragment ion with m/z 272 was used (Figure 11A). I validated this strategy by LC-MS/MS and found that it is applicable for ceramides, HexCer, LacCer and Gb3. A pronounced decrease in retention time was observed for the modified lipids. The observed labelled lipid species were reminiscent of the non-labelled analogues and reflected the species profile observed for the non-labelled lipids (Figure 11B).

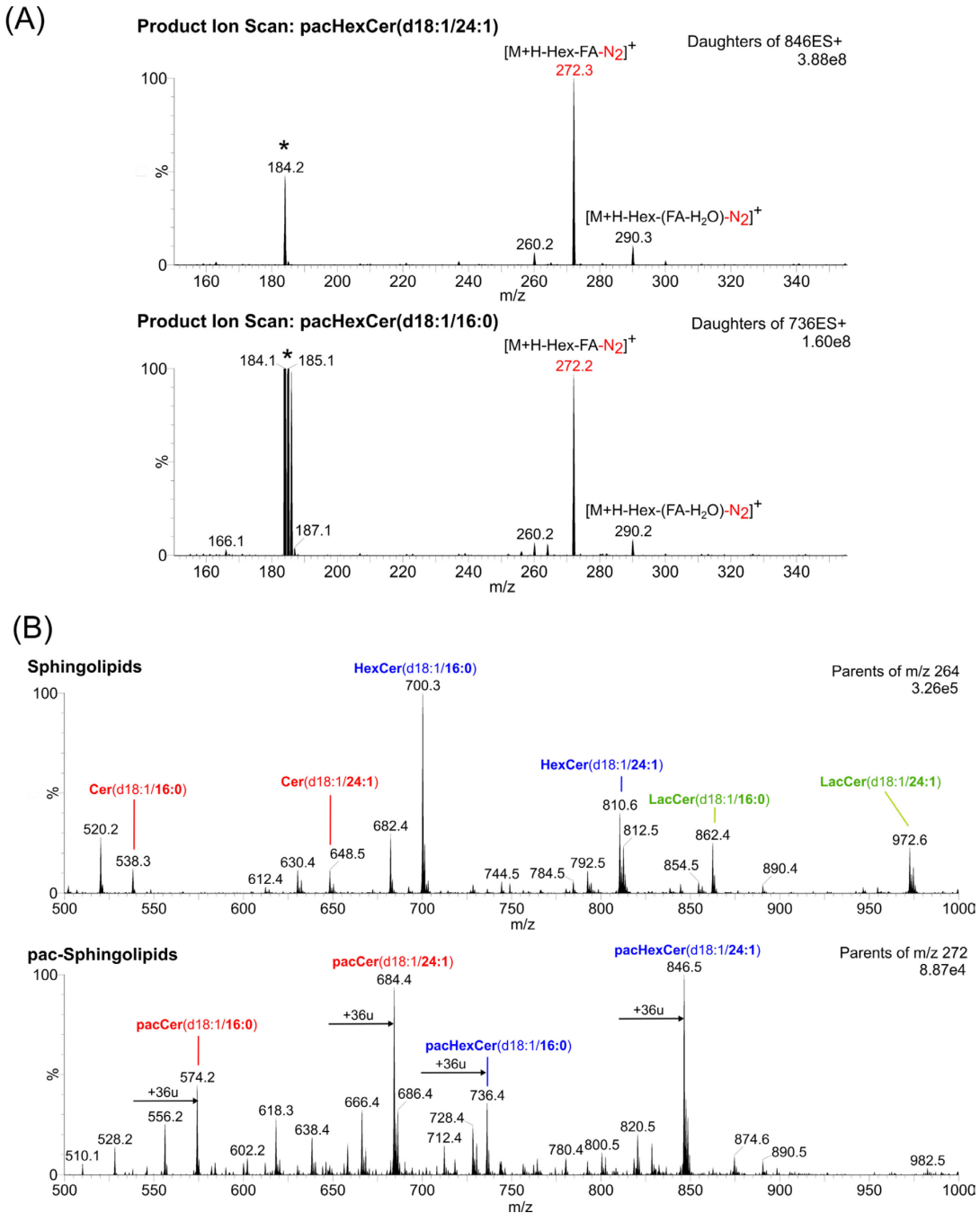

Figure 10 Mass spectrometric characterization of pac-sphingolipids.

Mass spectrometric characterization of pacSph-labelled lipids from pacSph-treated HK-2 cell culture extracts (6 µM, 4h). (A) Product ion scan of labelled pacHexCer(d18:1/16:0) (m/z 736.5) and

pacHexCer(d18:1/24:1) (m/z 846.5) from HK-2 extracts by direct injection mass spectrometry at 25 eV collision energy. Fragment ions observed include m/z 272.2 and m/z 290.2 and can be explained based on the chemical structure and modification introduced by pacSph. Since a lipid mixture was analysed, m/z 184 most likely is derived from phosphatidylcholine and/or sphingomyelin species (and isotopic peaks) with the same mass. Mass spectra were normalized to m/z 272.2 as 100%. (B) Parent ion scan of m/z 264.2 (for sphingolipids) and 272.2 (for pacSph-labelled sphingolipids) at 25 eV collision energy by direct injection mass spectrometry. Mass spectra are normalized to the base peak.

Degradation of pacSph via sphingosine-1-phosphate lyase (S1PL) produces phosphoethanolamine and hexadecenal. Hexadecenal (with a diazirine and terminal alkyne group) may be converted to a fatty acid and incorporated into glycerolipids. To monitor the extent of glycerolipid labelling, pac-modified phosphatidylcholine (PC) species were measured by LC-MS/MS. Incorporation of the functional groups leads to an increase in mass

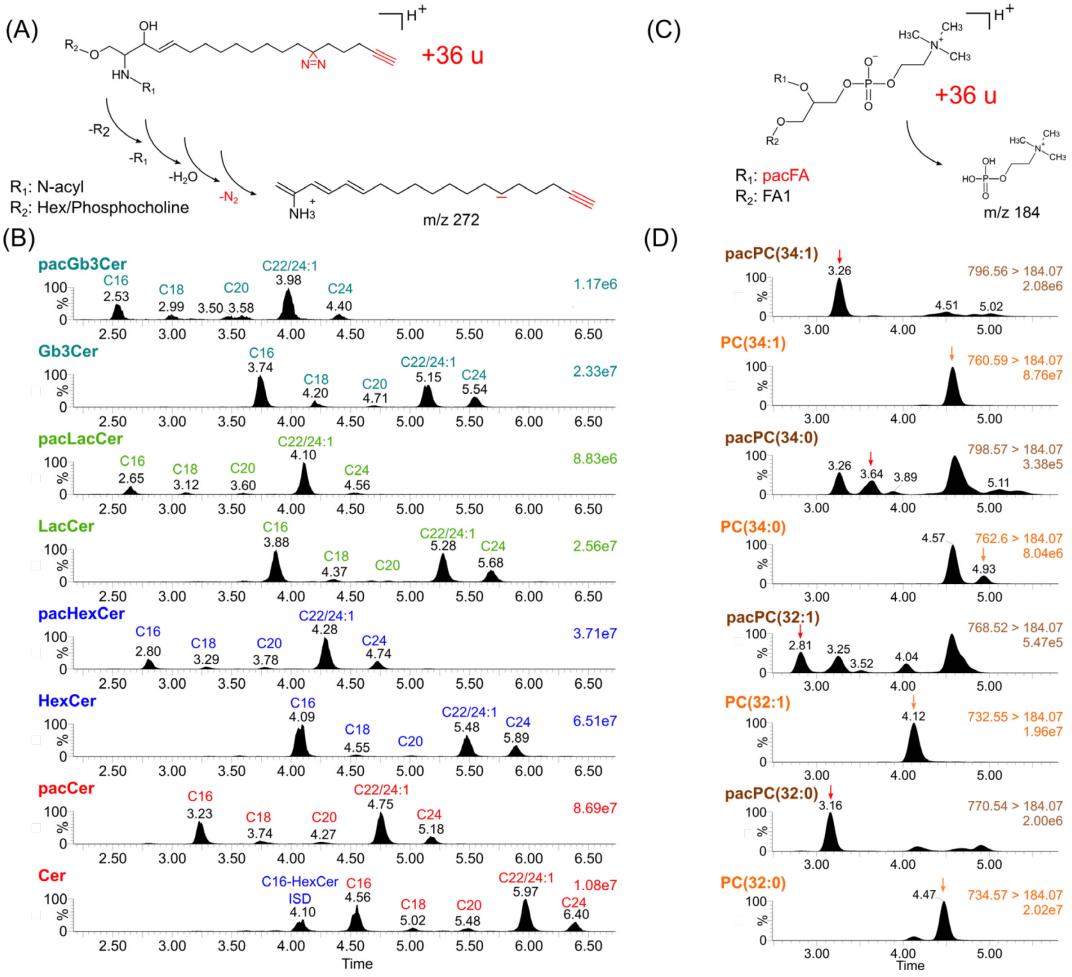

Figure 11 LC-MS/MS analysis of pac-Lipids.

Characterization of pacSphingolipids by LC-MS/MS. (A) Chemical structure of pacSphingolipids (+36u mass increase) and structure of the putative fragment m/z 272.2. (B) Analysis of HK-2 lipid extracts after pacSph labelling (6 µM, 4h) by multiple reaction monitoring (MRM) mode with the transition of

$[M+H]^+$ (+36u) to m/z 272.2 for a specified set of pacSph-labelled lipid species based on endogenous lipid abundance. Comparison reveals a reduction in retention time compared to non-labelled counterparts (analysed by $[M+H]^+$ > m/z 264.2). (C) Proposed fragmentation mechanism for modified pacPC species due to pacSph degradation by sphingosine-1-phosphate lyase (S1PL). Incorporation of one pacFA moiety yields pacPC with a mass increase of 36u compared to PC species. Generation of the energetically preferred phosphocholine fragment is still possible in pacPC and yields fragment m/z 184. (D) Analysis of labelled pacPC species and their non-labelled counterparts by MRM mode. Labelled species were measured with the transition of $[M+H]^+$ (+36u) > m/z 184.07. Arrows indicate peaks of the respective annotated compounds.

by 36 u compared to non-labelled PC species (Figure 11C). Analogous to PC, the energetically favoured phosphocholine fragment is produced during collision-induced dissociation (CID) in modified PC species as well. Using a limited set of marker species, this transition ($[M+H]^+$ (+36u) > m/z 184.07) can be used to monitor the extent of glycerolipid labelling in varying conditions (Figure 11D).

Genetic ablation of S1P lyase using CRISPR/Cas9

The major route for the degradation of sphingolipids is via the sphingosine-1-phosphate lyase pathway. Exogenous pacSph may be taken up by cells and incorporated in complex sphingolipids. Alternatively, pacSph may be converted to pac-sphingosine-1-phosphate (pacS1P) and degraded via the S1PL pathway to hexadecenal and ethanolamine. A hexadecenal derivative, which contains the introduced functional diazirine and terminal alkyne groups, may be recycled to pac-palmitate and then introduced into glycerolipids, reducing the sphingolipid-targeting specificity of labelling approach (Figure 12A).

Genetic ablation of S1PL was found to be a suitable mechanism to prevent labelling of glycerolipids (186). Alternative strategies would include, for example, indirect inhibition by depletion of pyridoxal-5-phosphate with FTY720 ((187)) or a direct inhibition strategy based on the use of a potent inhibitor for S1PL. The disadvantage of indirect inhibition is the relatively low specificity of the treatment, given that other enzymes, for example serine-palmitoyl-CoA transferase (SPT), a critical enzyme in de novo synthesis, are also dependent on pyridoxal-5-phosphate. Direct inhibition strategies rely on the availability of potent and specific inhibitors. One such inhibitor, which is directed to the active site of S1PL with an IC50 of 110 nM in cellular assays was published (188, 189) (Figure 12B).

I evaluated the applicability of this S1PL inhibitor (S1PL-I) (Figure 12B) for the prevention of glycerolipid labelling and found a reduction in glycerolipid labelling accompanied by an increase in sphingolipid labelling (Supplementary Figure 1).

Although first results with this inhibitor were promising, persistent glycerolipid labelling could be a problem for the identification of sphingolipid-interacting proteins and higher concentrations of the inhibitor appear to have an impact on GSL homeostasis (Supplementary Figure 1). To overcome these problems, I decided to genetically deplete S1PL to prevent glycerolipid labelling during pacSph labelling.

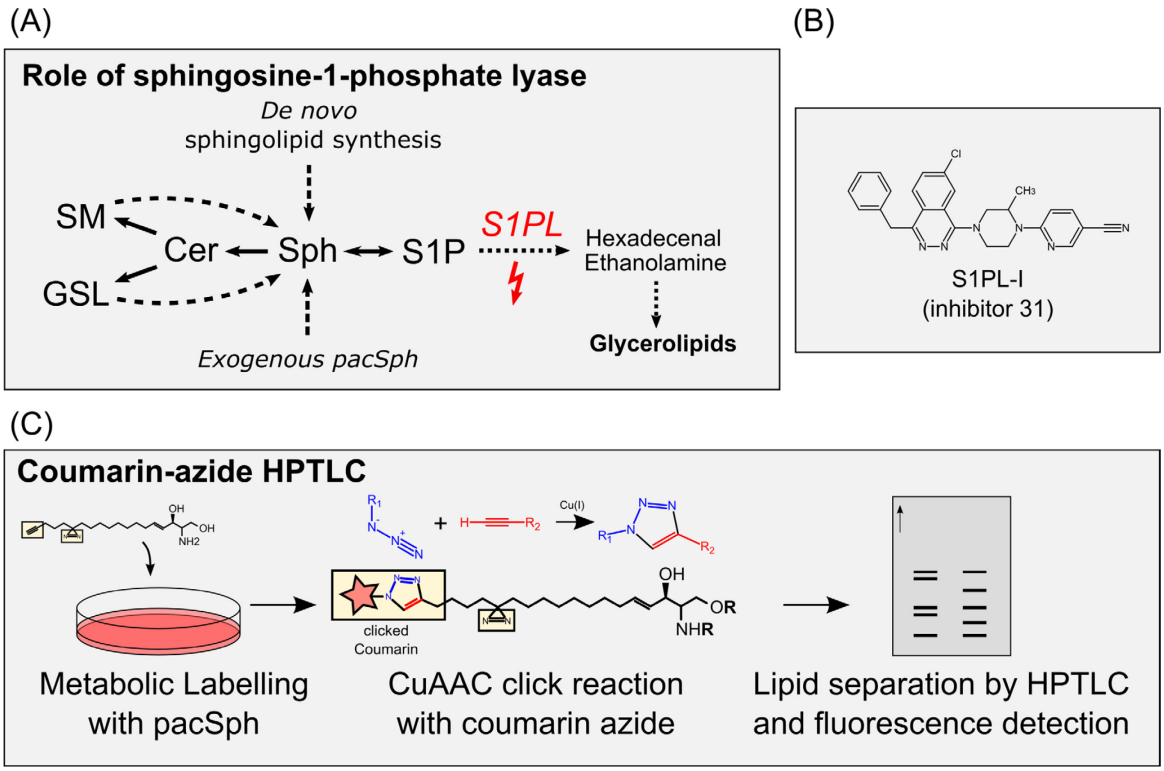

Figure 12 Role of S1PL and coumarin-azide assay.

(A) Role of S1PL metabolism for pacSph labelling. (B) Structure of S1PL-I (inhibitor 31). (C) Schematic of coumarin-azide based detection of pacSph labelled lipids by HPTLC. Cells are treated with pacSph probe, which is metabolically incorporated in other lipids. Lipid mixtures are extracted and labelled lipids are covalently linked to a fluorescent coumarin by CuAAC click chemistry. The derivatized lipid mixture can be separated by HPTLC and labelled lipids are visualized by UV fluorescence.

For the genetic knockout of sphingosine-1-phosphate lyase (S1PL) I employed the clustered regularly interspaced short palindromic repeats/Cas 9 (CRISPR/Cas9) genome editing system (190). CRISPR/Cas9 enables the introduction of double strand breaks at defined loci in the genome based on a guiding RNA molecule

(gRNA). General repair of these double strand breaks occurs via error-prone non-homologous end joining (NHEJ). NHEJ may introduce insertions or deletions at the cut site, that render the protein non-functional. The streptococcus pyogenes Cas9 (SpCas9) needs a protospacer adjacent motif (PAM) of 5'-NGG-3' upstream of the guiding sequence. I delivered the CRISPR/Cas9 gene editing system with the pSpCas9(BB)-2A-Puro (px459) plasmid, containing the coding sequence for the SpCas9, a *Bbs*I-accessible scaffold for the insertion of gRNA oligos and a puromycin resistance gene. Guide RNA candidates were designed using the CRISPOR tool (https://crispor.tefor.net/) (191, 192) and evaluated based on human genome (GRCh37/hg19) with the 100genomes SNP database. Candidate sequences were targeted to exon sequences of S1PL and selected based on efficiency and specificity as described by MIT and CFD score (Figure 13A, Table 2). *Bbs*I overhangs (5'-CACC-sense-gRNA and 5'-AAAC-antisense-gRNA) were added to the sequence. If necessary, an additional G was added between 5'-overlap and sense-gRNA for increased efficiency of the U6 promoter. Efficiency of gRNA1 and gRNA3 for S1PL knockout was demonstrated before (186).

Table 2 Guide RNA sequences selected to target the S1P lyase locus.

MIT score ranges from 0 – 100 and indicates uniqueness of the guide in the genome (193). CFD score ranges from 0 – 100 and correlates with the off-target cleavage fraction of a guide (194, 195). Bold letters indicate the targeted coding sequence on the S1PL locus, underlined G insertion of additional guanine for the U6 promoter.

Guide	Oligo-DNA Sequences (5'-3')	MIT score	CFD score
gRNA1	CACC<u>G</u>**AATCTCTAAGTAGGGCTCAA**	77	87
gRNA2	CACC<u>G</u>**CCTCTGGAACAGTGTACAGT**	82	94
gRNA3	CACC**GCCTCTATCTTGCGTAGTCC**	96	97

The selected gRNAs were ordered as complementary single stranded sequences and annealed. After restriction digest with *Bbs*I, DNA oligos were ligated into the gRNA scaffold of *Bbs*I. Correct insertion was confirmed by colony PCR and restriction digest with *Bbs*I and *EcoR*V. Transfection of HK-2 cells was done using the calcium phosphate transfection method. Selection with puromycin was started one day after transfection. Single cells were isolated, expanded and the resulting cell lines were screened based on their pacSph labelling profile by HPTLC and LC-MS/MS.

Glycerolipid labelling by pacSph was evaluated by LC-MS/MS analysis of selected pacPC species and in all out of seven tested cell lines no pacPC was detected (Figure 13B-C). This was further confirmed by HPTLC. Labelled lipids were visualized with copper-azide-alkyne cycloaddition-based (CuAAC) click chemistry by conjugation with 3-azido-7-hydroxycoumarin-azide (Jena Bioscience GmbH, Jena, Germany). Coumarin-azide is a fluorogenic compound and gains UV fluorescence (λ_{ex} 404 nm, λ_{em} 477 nm) after conjugation. Fluorescent lipids can be visualized using a fluorescence imaging system after separation on a HPTLC plate (Figure 12C). Not only was glycerolipid labelling completely abrogated, but I observed a strong increase in sphingolipid labelling in the tested clones (Figure 13D). Sphingolipid identity was confirmed by alkaline hydrolysis (AH). Clone 4 was selected for further experiments.

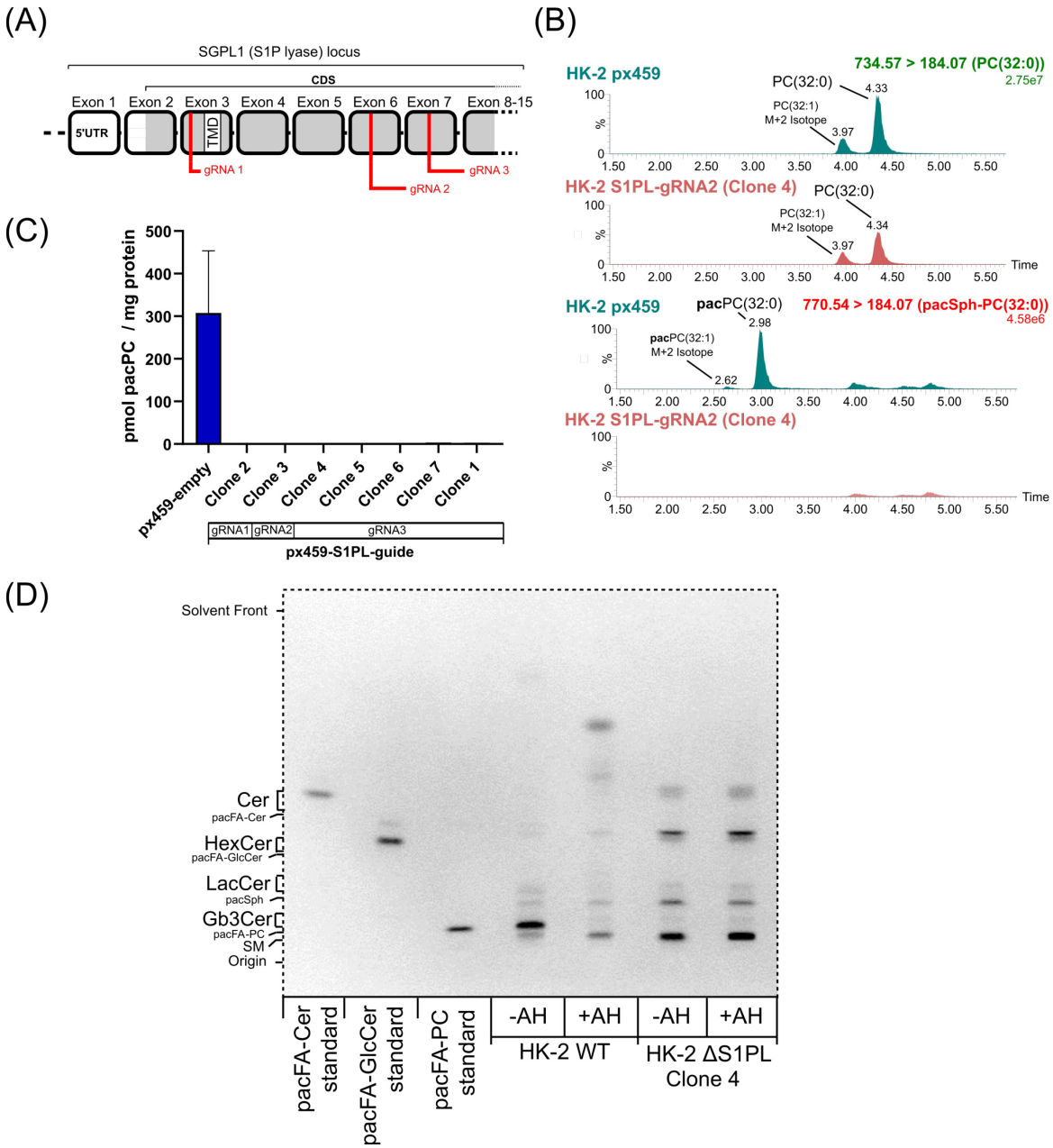

Figure 13 S1PL knockout in HK-2 cell line.

Glycerolipid labelling by pacSph was prevented by knockout of S1PL in HK-2 cells. (A) CRISPR/Cas9-based knockout strategy targeting exons 3, 6 and 7 to introduce indels by non-homologous end-joining (NHEJ). (B) Analysis of phosphatidylcholine species PC(32:0) (upper two chromatograms) and labelled pacPC(32:0) (lower two chromatograms) in control and S1PL-targeted HK-2 cells by LC-MS/MS in multiple reaction monitoring (MRM) mode. (C) Sum of analysed pacPC species in control and S1PL-targeted HK-2 cells. Graphs indicate mean+standard deviation. (D) HPTLC analysis of HK-2 wild type and S1PL-targeted clones after pacSph labelling and CuAAC-click with coumarin-azide with and without alkaline hydrolysis (AH) to degrade glycerolipids, but not sphingolipids. Clone 4 was obtained by transfection with px459-S1PL-guide3. Coumarin azide was visualized by UV fluorescence. The HPTLC plate was developed in CHCl3/MeOH/H2O/AcOH (65:25:4:1) to 50% and n-Hexane/ethyl acetate (1:1) to 100%.

Efficiency of globo-Series GSL labelling depends on labelling parameters

Labelling of specifically GSL with pacSph requires additional metabolic steps and an adjustment of labelling parameter can improve the yield of labelled GSL. I performed a time series experiment to determine optimal labelling parameters for a labelling of GSL and evaluated the impact of an additional chase time.

Confluent cultures of HK-2 ΔS1PL cells were treated with pacSph (6 µM) for defined time periods. Afterwards, the cells were harvested, lipids extracted and CuAAC-click reaction with coumarin-azide performed to visualize labelled lipids by HPTLC with UV fluorescence.

I found that a prolongation of labelling time up to 24h improves globo-series GSL labelling under these conditions (Figure 14A-B). The amount of labelled Gb3Cer was increased at 24h, while I observed a decrease in ceramide and HexCer labelling. Sphingomyelin labelling appears rather constant, its relatively fraction increases with increased labelling time. Labelling for more than 24h did not reveal a benefit, but rather a reduction in all labelled lipids. It is possible, that replenishing the labelling medium could further improve the labelling, but this was not experimentally validated. I found that a chase period after replacing the labelling medium with fresh normal growth medium could further improve the relative amount of labelled Gb3Cer. While a decrease in all labelled lipids is observable after 4h, the relative amount of labelled Gb3Cer is increasing due to the slower degradation compared to other sphingolipids (except sphingomyelin).

These adjusted conditions were validated by LC-MS/MS. HK-2 ΔS1PL cells were treated with pacSph (6 µM, 22h+4h (Pulse and Chase) or 4h (standard)) and lipids were extracted. LC-MS/MS analysis of pacSph-labelled lipids was performed and the relative $\log_2$-fold change between standard and modified labelling protocol for each lipid class was calculated. Compared to the 4h labelling protocol (standard), these changes combined yielded an overall improvement of 4.5-fold for the labelling of Gb3Cer and 2-fold for LacCer, while (hexosyl)ceramide labelling was reduced. No change was observed in sphingomyelin labelling.

I found that an increased labelling time results in a more pronounced labelling of VLC-FA sphingolipids, as seen by a proportionally higher increase in C22, C24:1, C24:0 species compared to C16-species (Figure 14E).

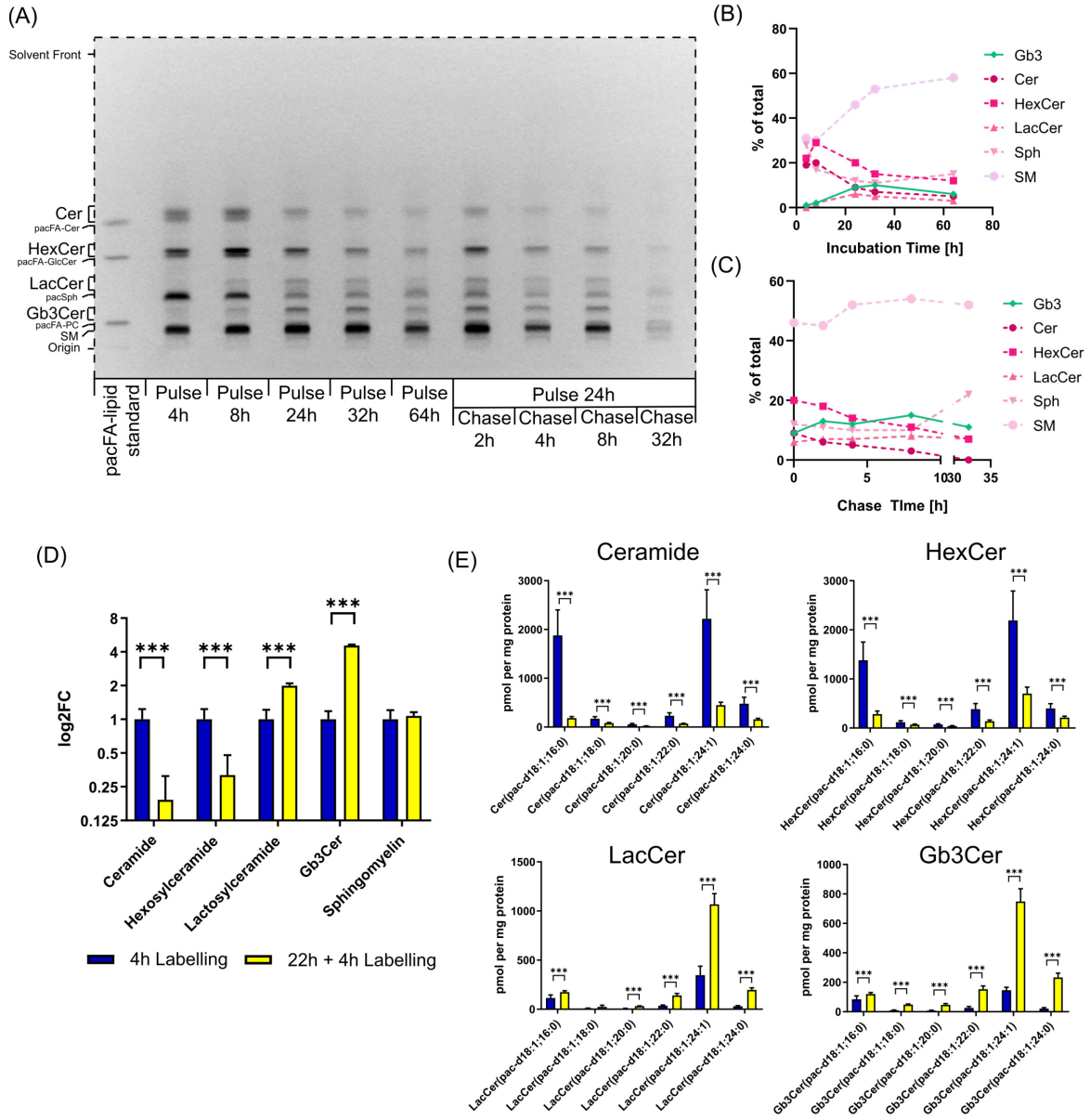

Figure 14 Evaluation of labelling parameters for Gb3Cer labelling.

HK-2 ΔS1PL cells were treated with pacSph (6 µM) in a time series experiment. (A) HPTLC plate of lipid extracts from cells treated for varying durations with pacSph. pacSph-labelled lipids were conjugated to coumarin-azide by CuAAC-click reaction and visualized by UV fluorescence. HPTLC plate was developed in CHCl3/MeOH/H2O/AcOH (65:25:4:1) to 50% and n-Hexane/ethyl acetate (1:1) to 100%. (B) Relative quantification of HPTLC bands for pulse time series. (C) Relative quantification of HPTLC bands for chase time series. (D) Evaluation of labelling conditions by LC-MS/MS. Standard labelling protocol (4h) was compared to a modified labelling protocol (22h + 4h; Pulse + Chase). The relative fold change in cumulated lipid species of each lipid class was calculated compared to the standard protocol. (E) Changes on pac-lipid species level with 4h labelling and 22h + 4h labelling (Pulse+Chase). Graph indicates mean + standard deviation (n = 4). Statistical testing was done by unpaired, two-tailed Student's t-test with Holm-Sidak correction for multiple comparisons (*** $p < 0.001$).

Density of the cell layer is associated with Gb3Cer expression

The expression of Gb3Cer in cell culture was linked to contact inhibition before. To test if the density of the culture has an impact on Gb3Cer expression and the incorporation of pacSph into globo-series GSL, I grew ΔS1PL cells to subconfluent (~70%) and confluent (100%) density, treated the cultures with pacSph (6 µM, 4h) and harvested the cells by scraping without further treatment. After lipid extraction, I analysed non-labelled and labelled Gb3Cer species by LC-MS/MS.

I found the major Gb3Cer species (including C16:0-, C18:0-, C24:1- and C24:0-N-acyl) were significantly increased in confluent cells, while other sphingolipids were not affected, indicating an upregulation of the Gb3Cer synthesizing metabolic pathway with increased cell density (Figure 15A-B). These changes were not limited to the non-labelled sphingolipid pool but also resulted in an increase in incorporation of the pacSph base into Gb3Cer across all abundant Gb3Cer species (Figure 15C-D). I also observed a slight increase in ceramide labelling.

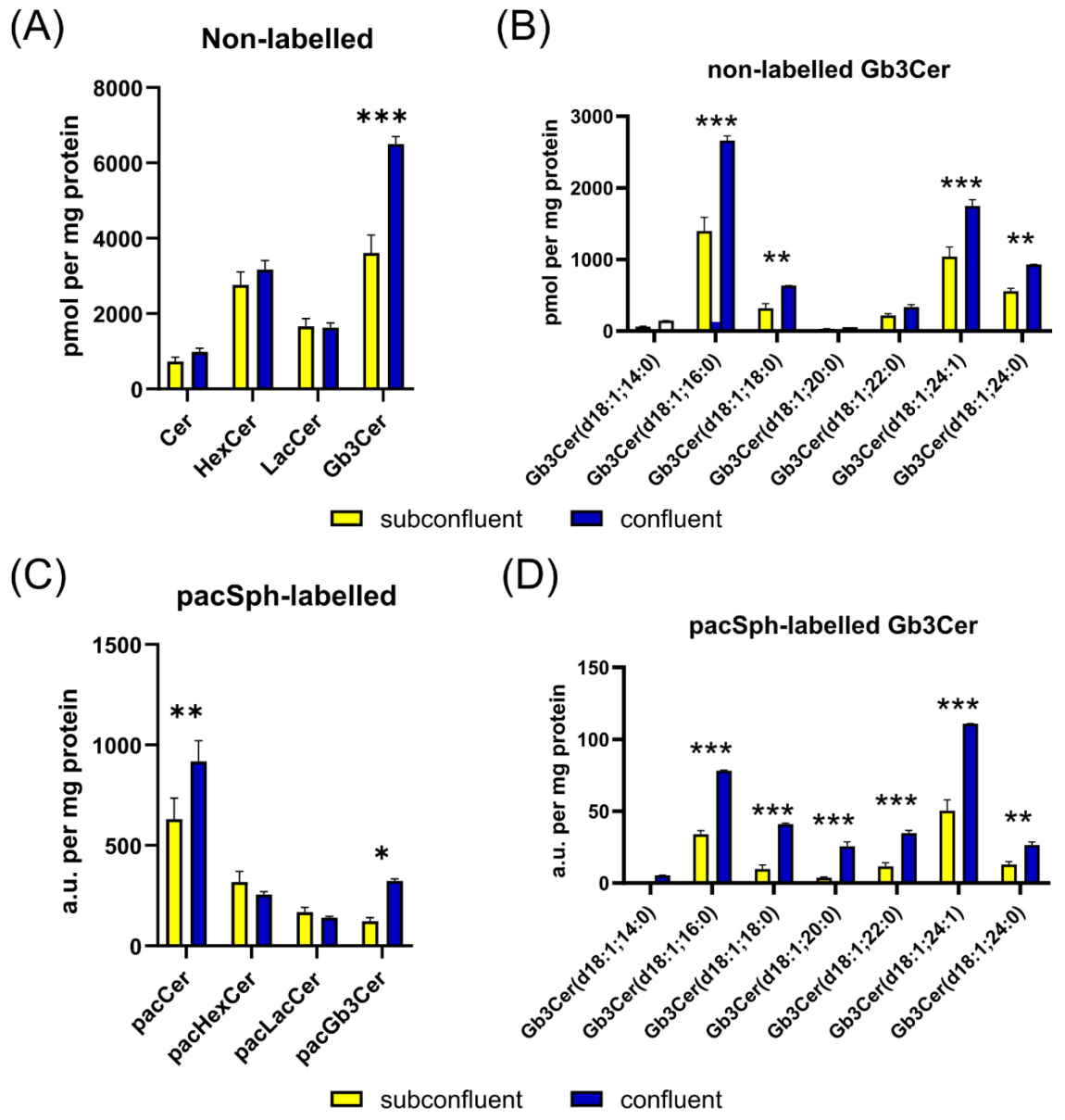

Figure 15 Cell density influences Gb3Cer expression.

Lipid extracts of HK-2 ΔS1PL cells (clone 4) obtained from pacSph-labelled cultures of different density were analysed by LC-MS/MS. (A) Sum of measured lipid species by lipid class of the non-labelled lipid pools. (B) Changes in non-labelled Gb3Cer species. (C) Sum of measured lipid species by lipid class of the pacSph-labelled lipid pools. (D) Changes in pacSph-labelled Gb3Cer species. Graphs indicate mean + standard deviation. Statistical testing was done by two-way analysis of variance with Sidak's multiple comparisons test (** $p < 0.01$; *** $p < 0.001$).

Oleic acid treatment

Lipid-rich western-type diet can induce Gb3 synthase activity in mice (97). Treatment of HK-2 cells with oleic acid may mimic these findings and could affect Gb3Cer levels.

To investigate this, I pre-treated HK-2 cells with albumin-bound oleic acid (64 µM) or albumin alone (64 µM) for one hour. Afterwards, HK-2 cells were treated with pacSph (3 µM, 22h) in presence of S1PL-I (200 nM). Lipids were extracted and pacSph-labelled and non-labelled lipids analysed by LC-MS/MS. In the non-labelled lipid pool a decrease in ceramide and HexCer and an increase in Gb3Cer could be observed (Figure 16A) that could be primarily attributed to an increase in C24:1-Gb3Cer (Figure 16B *left*). In line with these findings pacSph-labelled Gb3Cer species strongly shifted towards C24:1-pacGb3Cer, with a decrease in all other species (Figure 16 *right*).

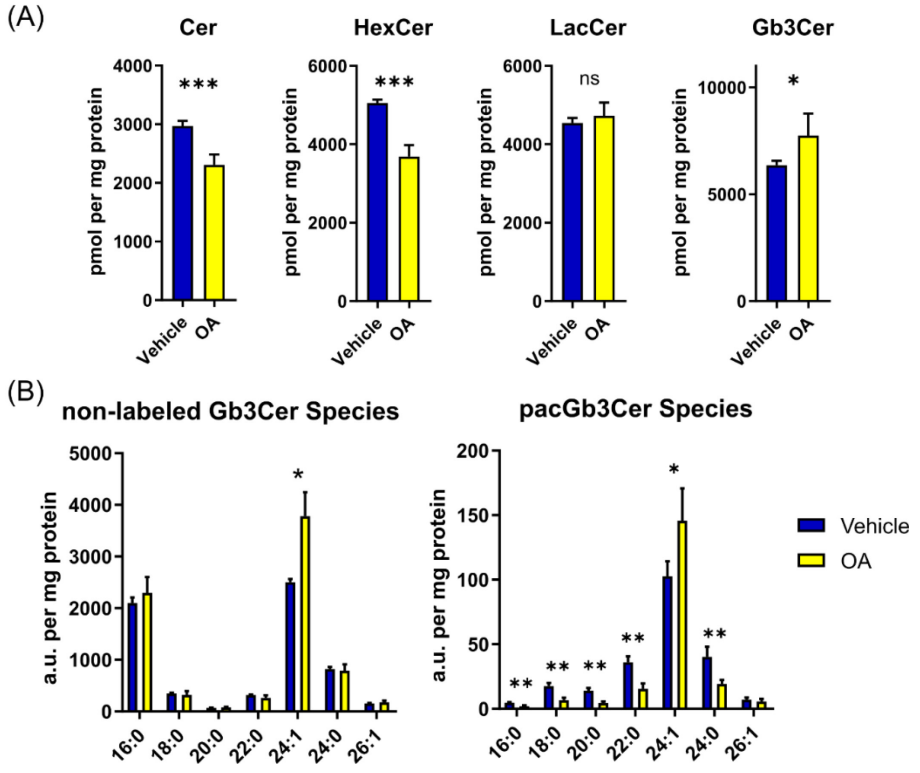

Figure 16 Oleic acid treatment induces change in Gb3Cer expression pattern.

HK-2 cells were treated with albumin-bound oleic acid (OA) and changes in sphingolipid levels and pacSph labelling were measured by LC-MS/MS. (A) Non-labelled lipid pools by lipid class. (B) Analysis of Gb3Cer species distribution in non-labelled (left) and labelled (right) lipids. Graphs indicate mean + standard deviation (n = 4). Statistical testing was done unpaired, two-tailed Student's t-test with Holm-Sidak correction for multiple testing (* $p < 0.05$, ** $p < 0.01$, *** $p < 0.001$).

4.1.3 Genetic ablation of Gb3 synthase using CRISPR/Cas9

The aim of the presented experiments is the identification of globo-series GSL interacting proteins by using pacSph in a pull-down assay. This procedure will reveal not only globo-series GSL-interacting proteins, but also other sphingolipid-interacting proteins. To achieve specificity towards globo-series GSL, I performed a knockout of Gb3 synthase in HK-2 cells. Gb3 synthase knockout will prevent the synthesis and labelling of globo-series GSL and by direct comparison of cells with or without Gb3 synthase globo-series GSL-interacting proteins may be identified.

To knockout Gb3 synthase I used the same CRISPR/Cas9 NHEJ strategy as presented for the knockout of S1PL. I knocked out Gb3 synthase in HK-2 wild type cells for performing phenotypic studies of the effect of Gb3 synthase knockout and in HK-2 ΔS1PL cells for a differential comparison in a pull-down proteomic study with Gb3 synthase expressing cells.

Two exons are described for Gb3 synthase, whereas the first exon covers solely the 5'UTR region (Figure 17A). Analysis of functional domains revealed a glycosyl-transfer domain with a *DXD* sugar-binding motif. To ensure a loss of catalytic activity, I selected guide RNA candidates upstream to this region. Efficacy of the used gRNA candidates in targeting the Gb3 synthase locus was confirmed by targeting proliferative and easy-to-transfect HEK293 cells. Transfection of HK-2 cells was done using the calcium phosphate method. After selection with puromycin single cells were isolated and expanded into new clonal cell lines.

Table 3 Guide RNA sequences for targeting the Gb3 synthase locus.

Guide	Oligo-DNA Sequences (5'-3')	MIT score	CFD score
gRNA1	CACCG**CTGCACGGCCGCGTACCAGT**	98	99
gRNA2	CACCG**CATGATCTACTGGCACGTTG**	94	96
gRNA3	CACC**GCCGCGTACCAGTCGGCCAG**	94	99
gRNA4	CACC**GGACCAGCACGTGGGATTCG**	90	96

MIT score ranges from 0 – 100 and indicates uniqueness of the guide in the genome (193) CFD score ranges from 0 – 100 and correlates with the off-target cleavage fraction of a guide (194, 195). Bold letters indicate the targeted coding sequence on the S1PL locus, underlined G insertion of additional guanine for the U6 promoter.

Gb3 synthase knockout in HK-2 wild type

In HK-2 wild type cells Gb3 synthase was targeted with gRNA2. I characterized Gb3 synthase targeted HK-2 (wild type) cells based on the expression of globo-series GSL by HPTLC and LC-MS/MS (Figure 17B-C). HPTLC of two clones revealed a loss of globo-series GSL and an accumulation of the Gb3 synthase substrate lactosylceramide (Figure 17B *left*). Bands on the running at the same height as Gb4Cer are not Gb4Cer, but rather glycosphingolipids of the asialoganglio- or lacto-series (Gg4Cer and Lc4Cer, respectively). Although ganglioside expression is weaker compared to neutral glycosphingolipids, small changes in the expression profile were detectable including possibly an increase in GD2 and a reduction in GM1 expression (Figure 17B *right*). I was able to confirm the loss of Gb3Cer by LC-MS/MS (Figure 17C). I analysed the lipid expression in 10 different Gb3S-targeted cell lines, 8 of these clones were devoid of Gb3Cer expression, indicating a high efficiency of the gene editing (Figure 17D). As expected, the Gb3S substrate LacCer was increased in most clones that lacked Gb3Cer. Further confirmation for a successful knockout of Gb3 synthase was obtained on genetic level by sanger sequencing in combination with TIDE deconvolution (not shown) (196).

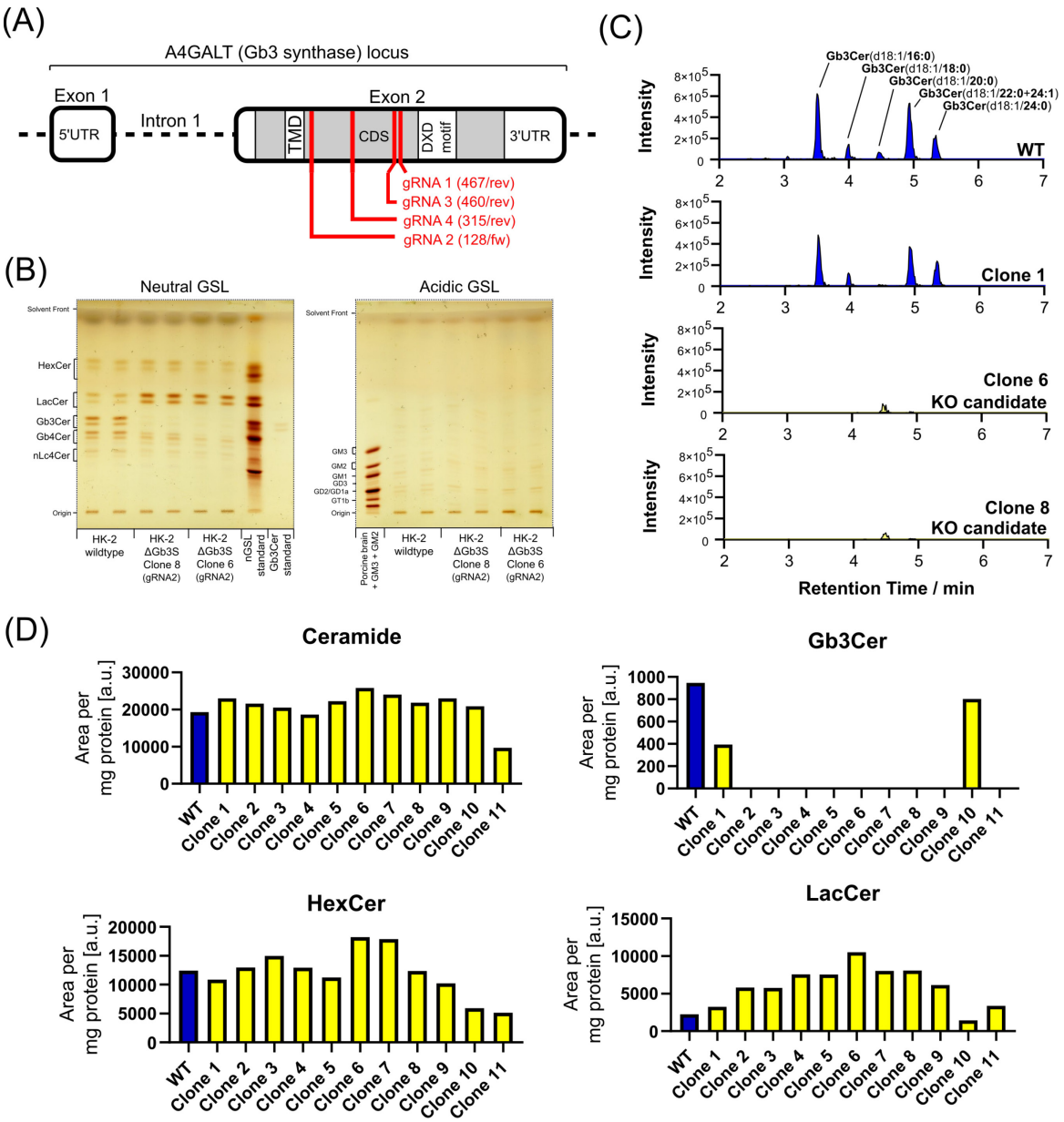

Figure 17 CRISPR/Cas9-mediated knockout of Gb3S in HK-2 wild type.

Gb3 synthase was targeted in HK-2 wild type cells using the CRISPR/Cas9 system. (A) Gb3 synthase locus with indication of transmembrane domain (TMD), coding sequence (CDS), DXD sugar binding motif and targeting sequences of gRNA candidates. (B) HPTLC analysis of neutral and acidic GSL in two Gb3S-targeted clones and wild type cells. GSL were stained using orcinol reagent. HPTLC plates were developed in chloroform/acetone (1:1) and chloroform/methanol/0.2% $CaCl_2$ (60:35:8) subsequently over the full length of the plate. (C) LC-MS/MS analysis of two Gb3S targeted clones. Chromatograms show Gb3Cer species measured in MRM mode. (D) Lipid analysis of 10 Gb3S-targeted clones. Bars indicate sum of the measured lipid species by lipid class.

Gb3 synthase knockout in HK-2 ΔS1PL

For the double knockout of Gb3 synthase and sphingosine-1-phosphate lyase I decided to use a consecutive knockout strategy. A consecutive strategy may have advantages over targeting both enzymes in parallel. By isolation of a ΔS1PL clone, I expect less clonal variation as compared to the wild type cell population. For a comparison of ΔS1PL against ΔS1PL/ΔGb3S as planned for the pull-down experiment this order ensures similar genetic backgrounds.

HK-2 ΔS1PL clone 4 was selected for an additional knockout of Gb3 synthase and targeting by CRISPR/Cas9 as described before. I isolated 78 clones and expanded these clones into new cell lines. Characterization of the clones was performed by LC-MS/MS measurement of Gb3Cer species. Although Gb3Cer expression is lower in most of the characterized clones, I identified only one clone without expression of Gb3Cer (Figure 18A). It is possible that HK-2 ΔS1PL cells acquired tolerance towards further editing, due to a change in cellular repair mechanisms or integration of the puromycin resistance gene after initial gene editing. I further characterized this clone and confirmed the loss of globo-series GSL expression in this cell line. I did not observe apparent changes in cell morphology after knockout of Gb3 synthase at low or high cell densities (Figure 18B). HPTLC analysis of the clone revealed a lack of globo-series GSL expression and an increase in LacCer (Figure 18D), which is in line with the previous observations (Figure 17B). I performed a sensitive immune overlay with anti-Gb3 antibody to ensure the diminished Gb3Cer expression even at low levels (Figure 18D), which further confirmed the absence of Gb3Cer. HPTLC analysis of acidic GSL revealed changes between HK-2 ΔS1PL and HK-2 ΔS1PL/ΔGb3S cells. In double knockout cells I observed an increase in gangliosides GM3 and GM2 compared to ΔS1PL cells (Figure 18E) and in-line with the observations from Gb3S knockout in HK-2 wild type cells (Figure 17B), a decrease in GM1 expression (Figure 18E). This change in ganglioside expression was further investigated by an immune overlay with anti-GD2 antibody indicating an increase in ganglioside GD2 expression due to knockout of the Gb3 synthase (Figure 18E). It was shown before that Gb3S expression is associated with a repression of ganglioside synthesis in neuronal cells (87), which may explain these findings. I treated HK-2 ΔS1PL and HK-2 ΔS1PL/ΔGb3S cells with pacSph (6 µM, 22h+4h) and conjugated the extracted

lipid to coumarin-azide for visualization on a HPTLC plate. Glycerolipid labelling is still abolished in both cell lines. In ΔS1PL/ΔGb3S cells a reduction in Gb3Cer labelling and an increase in LacCer labelling could be observed as was expected (Figure 18C). Sphingomyelin labelling also appears to be most prominent and enhanced in double knockout cells.

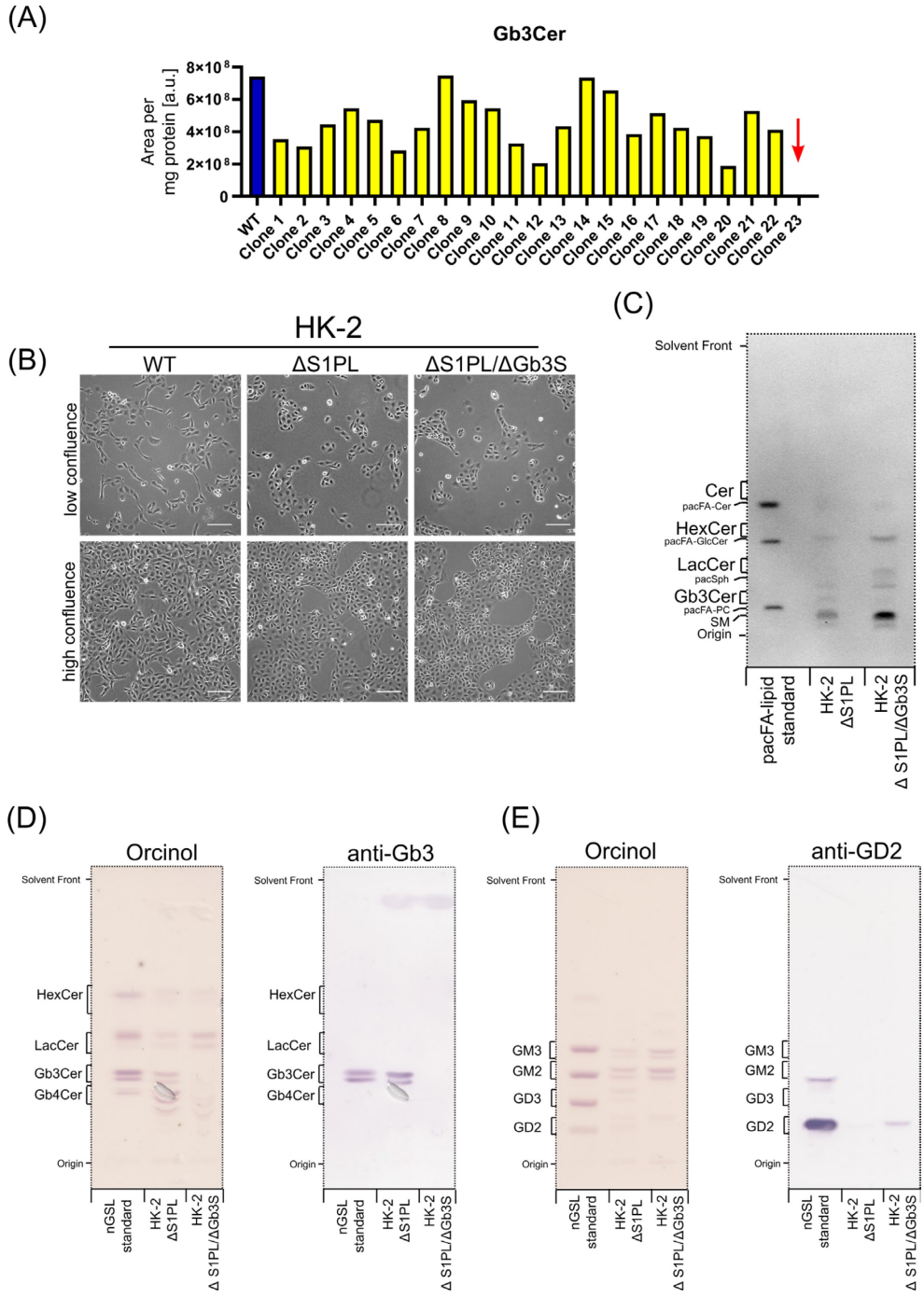

Figure 18 CRISPR/Cas9-mediated knockout of Gb3S in HK-2 ΔS1PL cells.

Gb3 synthase was targeted in HK-2 ΔS1PL cells using the CRISPR/Cas9 system. (A) Gb3S-targeted clones were characterized based on Gb3Cer expression by LC-MS/MS. Bar indicate sum of measured

Gb3Cer species. 23 clones out of 78 are shown. Red arrow indicates one clone without expression of Gb3Cer. (B) Brightfield images of wild type and engineered HK-2 cell lines at low and high cell density. (C) HPTLC analysis of pacSph-labelled lipids after conjugation to coumarin-azide by CuAAC-click reaction. Visualization by UV fluorescence. HPTLC plate was developed in CHCl3/MeOH/H2O/AcOH (65:25:4:1) to 50% and n-Hexane/ethyl acetate (1:1) to 100%. The lipid equivalent of 100 µg protein was loaded onto the plate. (D) HPTLC analysis of neutral glycosphingolipids after alkaline hydrolysis and fractionation by anion exchange (DEAE). Glycosphingolipids were stained by orcinol reagent (*left*). Gb3Cer was detected by immune overlay with chicken anti-Gb3Cer antibody (JM06/298, 1:50) and stained with alkaline phosphatase (*right*). The lipid equivalent of 200 µg protein was loaded onto the plate. The HPTLC plate was developed in chloroform/acetone (1:1) and chloroform/methanol/0.2% $CaCl_2$ (60:35:8) subsequently over the full length of the plate. (E) HPTLC analysis of acidic glycosphingolipids after alkaline hydrolysis and fractionation by anion exchange (DEAE). Glycosphingolipids were stained by orcinol reagent (*left*). Ganglioside GD2 was detected by immune overlay with anti-GD2 antibody and stained with alkaline phosphatase (*right*). The lipid equivalent of 200 µg protein was applied to the plate. The HPTLC plate was developed in chloroform/acetone (1:1) and chloroform/methanol/0.2% $CaCl_2$ (45:45:10) subsequently over the full length of the plate.

Pharmacological inhibition of glucosylceramide synthase

As a complementary strategy to a knockout of Gb3 synthase and due to the lack of inhibitors directly targeting Gb3S, I tested whether a pharmacological inhibition of glucosyl ceramide synthase (GCS), an enzyme upstream of Gb3 synthase, could successfully prevent globo-series GSL labelling. For this, I used the established GCS inhibitors Miglustat (at 100 µM) and Genz-123346 (at 5 µM).

I labelled HK-2 wild type, ΔS1PL, and ΔS1PL/ΔGb3S cells with pacSph (6 µM, 22h+4h) in presence of either 100 µM miglustat, 5 µM Genz-123346 or control treatment (dH2O) and harvested the cells without prior UV crosslinking. Subsequently, lipids were extracted, and pacSph-labelled lipids were coupled to coumarin-azide by CuAAC click reaction. Lipid extracts were separated by HPTLC and visualized by UV fluorescence (for pacSph-labelled lipids) or orcinol staining (for glycosphingolipids).

With both inhibitors a reduction in steady state levels of HexCer, LacCer and Gb3Cer could be observed, that was slightly more pronounced in Genz-123346 treated samples (Figure 19A). Labelling of GSL with pacSph was almost completely abolished with Genz-123346 treatment, while miglustat appears slightly less efficient at the indicated concentrations (Figure 19B). In addition, I found that GCS inhibition results in an increase in sphingomyelin labelling, which must be considered as an additional effect in pull-down experiments. I concluded, that both

treatments are sufficient to prevent Gb3Cer and globo-series GSL labelling by pacSph and GCS inhibition might provide an alternative strategy to validate globo-series GSL interacting proteins independent of a knockout of Gb3 synthase. For further experiments, I decided to use Genz-1233346 treatment.

In addition to pharmacological inhibition of Gb3Cer synthesis by inhibition of upstream enzymes, I used lentiviral transduction to stably re-express Gb3 synthase in Gb3 synthase-targeted knockout cells. Re-expression of Gb3 synthase did not result in restoring globo-series GSL expression (not shown).

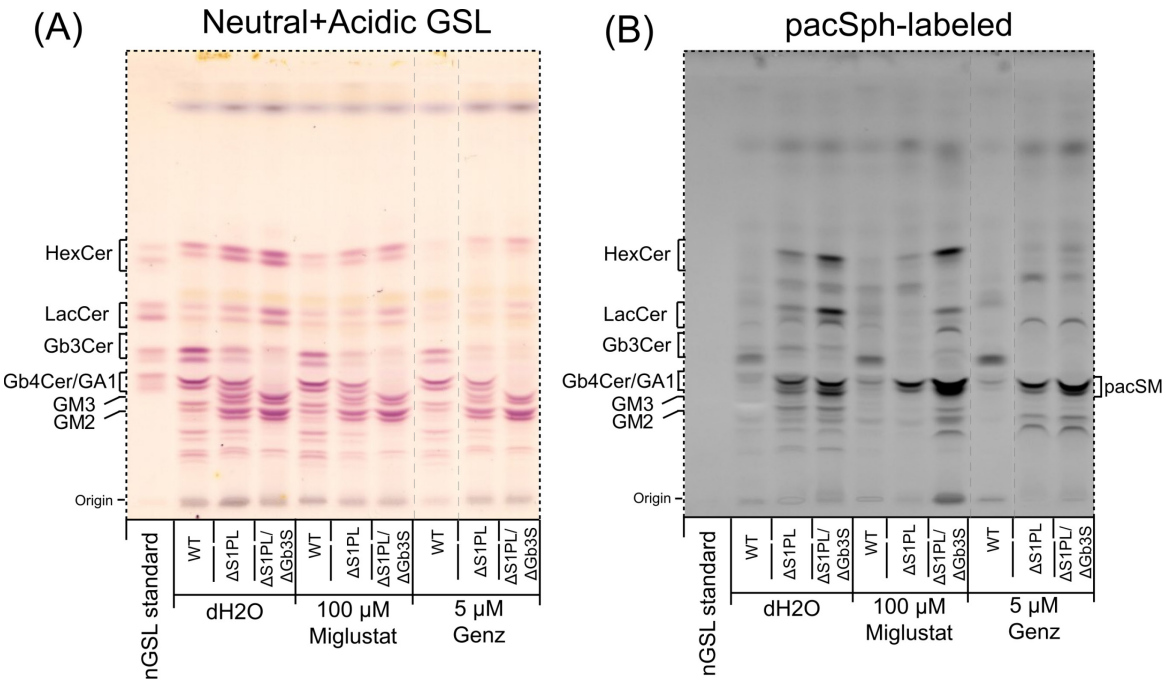

Figure 19 Pharmacological inhibition of GCS and pacSph labelling.

HPTLC analysis of HK-2 wild type, ΔS1PL and ΔS1PL/ΔGb3S cells after labelling with pacSph (6 µM, 22h+4h) and in presence of inhibitors for glucosylceramide synthase (GCS). Lipids were extracted and clicked to coumarin-azide. The lipid extract equivalent of 250 µg protein was applied to the plates. Plates were developed in chloroform/acetone (1:1) and chloroform/methanol/0.2% $CaCl_2$ (60:35:8) subsequently over the full length. (A) Glycosphingolipids were visualized by staining with orcinol reagent. Identity of gangliosides GM3 and GM2 was confirmed by mass spectrometry (not shown) (B) pacSph-labelled lipids were visualized by UV fluorescence. Dotted lines indicate reframing of the lanes to improved interpretation. Absence of Gb3Cer in ΔS1PL/ΔGb3S cells was further confirmed by direct injection mass spectrometry (data not shown).

4.1.4 Pull down proteomics analysis

To identify globo-series interacting protein, strategies for the purification of sphingolipid-protein conjugates had to be established. This includes the choice of purification strategy, selection of azide-conjugates, and conditions for UV crosslinking and click reaction.

Activation of the diazirine group by UV irradiation at 365 nm is a crucial step for proximity crosslinking of sphingolipids with interacting proteins and I tested several lamp setups (Supplementary Figure 2). I evaluated the use of streptavidin-dependent (in combination with cleavable and non-cleavable biotin-azide derivatives) and streptavidin-free strategies for the purification of protein-sphingolipid conjugates from cell extracts. CuAAC click efficiency may vary in solution and with a solid support agarose-azide requiring longer reaction times and resulting in lower yields. I decided to use a classical streptavidin-based strategy with a cleavable biotin-azide derivative (Dde-biotin-azide) (Supplementary Figure 2) due to the ability to monitor CuAAC-click biotinylation efficiency using SDS-PAGE and detection by horseradish peroxidase-coupled Neutravidin (Neutravidin-HRP) after membrane transfer. Using Dde-biotin-azide for purification proteins can be efficiently released by cleaving the Dde moiety under mild conditions (2% aqueous hydrazine). Mild elution conditions reduce contamination of the samples with denatured Neutravidin.

For CuAAC click chemistry catalytically active copper(I) is generated *in situ* during the reaction by reduction of a copper(II) source (197). Stabilization of copper(I) with a copper-chelating agent was shown to have beneficial effects for the CuAAC reaction. A commonly employed ligand is tris(triazolyl)amine (TBTA). TBTA use is limited by its low solubility in water, requires the use of dimethylsulfoxide (DMSO) for solubilization, which slows down CuAAC reaction kinetics. Novel ligands were designed with improved water solubility, improved reduction of copper toxicity in living cell systems and improved reaction kinetics (198–200). I decided to use tris(3-hydroxypropyltriazolylmethyl)amine (THPTA) as a copper-chelating ligand. The increase solubility in aqueous solution allows to use a ligand-to-copper ratio of 5:1. This was shown to protect histidine residues from oxidation, lower reaction oxygen species levels induced by copper(I) and avoid protein crosslinking (200).

To determine optimal parameters for a CuAAC click reaction between sphingolipid-protein conjugates (with a terminal alkyne group) and Dde-biotin-azide, I optimized the biotinylation efficiency using different concentrations of Dde-biotin-azide and sodium ascorbate as a reducing agent (Supplementary Figure 2).

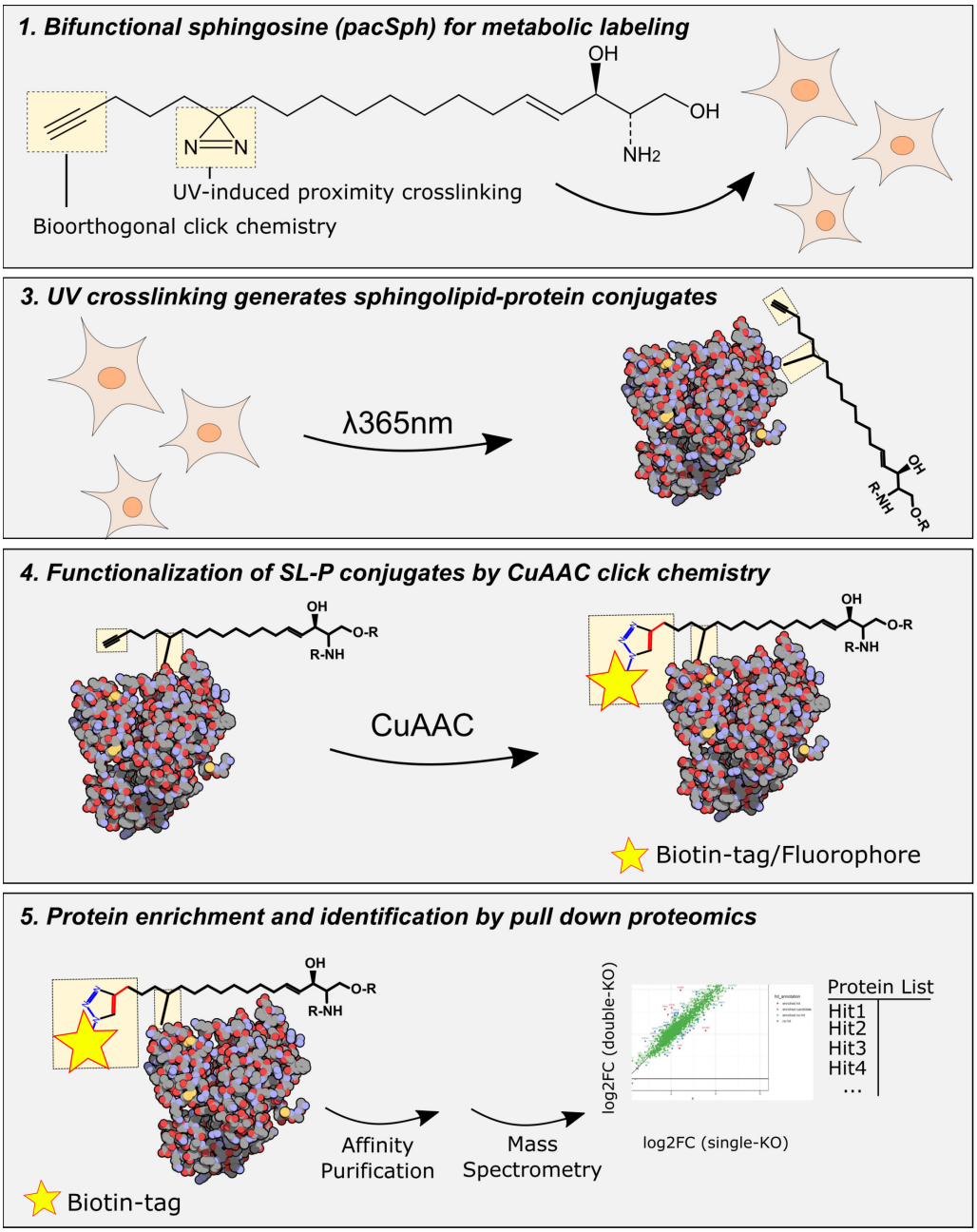

Figure 20 pacSph pull-down proteomics workflow.

For the identification of globo-series GSL-protein interactions HK-2 ΔS1PL and ΔS1PL/ΔGb3S cells were labelled with pacSph. Protein crosslinking was induced by UV irradiation at 365 nm. Protein-Lipid complexes were coupled to a cleavable biotin purification tag and enriched on neutravidin agarose. Released proteins were subjected to mass spectrometric analysis and protein identification. Differential comparison of ΔS1PL and ΔS1PL/ΔGb3S highlights proteins that are depleted after globo-series GSL depletion.

For the identification of globo-series GSL interacting proteins, I treated three replicates of HK-2 ΔS1PL and ΔS1PL/ΔGb3S cells with pacSph (6 µM, 22h + 4h (Pulse + Chase)). The cells were irradiated (365 nm, 5 min) on ice and proteins extracted. Non-protein-bound, pacSph-labelled lipids were removed by chloroform/methanol precipitation. Dde-biotin-azide was conjugated to sphingolipid-protein complexes by CuAAC click. Enrichment of sphingolipid-protein conjugates was performed on Neutravidin agarose resin. After extensive washing proteins were eluted by using buffered hydrazine solution and concentrated by chloroform/methanol precipitation. As a control one set of ΔS1PL samples was prepared without UV irradiation. I visually confirmed increased protein amounts in UV irradiated samples, indicating a successful pull-down.

Pull-down proteomics measurements and the necessary preparations were done by Dr Per Haberkant (Proteomics Core Facility, EMBL Heidelberg) and a bioinformatic analysis pipeline was provided by Dr Frank Stein (Proteomics Core Facility, EMBL Heidelberg).

Two screenings were performed with the same experimental conditions, but with a varying number of replicates (Exp1: n=1, Exp2: n=3). In both screenings I found a total of 1573 enriched proteins. 152 (10%) of these proteins were identified only in the first screening and 397 (25%) only in the second screening (Figure 22B). 1024 (65%) of the proteins were found in both screening experiments. Due to the higher statistical power, I will focus on the second screening experiment for the initial analysis and incorporate the data of the first experiment at a later stage.

I compared the proteins, that were found in samples with UV treatment (+UV) to a non-UV-treated control (-UV) and calculated a fold change for the relative enrichment of these proteins. In all +UV samples significantly higher protein amounts were detected (Supplementary Figure 3). Out of 1421 proteins, 1400 were found to be significantly enriched in the +UV treated ΔS1PL and ΔS1PL/ΔGb3S samples ($log_2FC \geq 1$ and $p \leq 0.05$) (Figure 21A-B).

Many of the observed high-quality hits ($log_2FC \geq 3$ and $p \leq 10^{-5}$) have been described in pacSph-based screenings before or are known interactors of sphingolipids and enzymes of sphingolipid metabolism (Table 4), demonstrating

the validity of the obtained data. The extended datasets are provided in the supplementary material.

Interestingly, also proteins of the de novo sphingolipid pathway (SPTLC1, KDSR) were found in the pulldown, though they are not metabolically engaged in the conversion of pacSph-labelled lipids, as well as proteins that are known as cargoes of clathrin-independent carriers and are dependent on glycosphingolipids for their endocytosis (CD44, ALCAM) (98, 201) have been observed in the dataset, and a systematic analysis of the provided data may reveal more cargoes of glycosphingolipid-dependent endocytic pathways.

Table 4 Examples for sphingolipid-interacting candidates in literature.

Non-exhaustive list of proteins that were previously described in pacSph-based screenings or are known as sphingolipid interactors and were found in the now presented data are described in the table. Experiments were performed in cooperation with Dr Per Haberkant and Dr Frank Stein (Proteomics Core Facility, EMBL Heidelberg).

Protein	Log_2FC	p-value	Reference
SSR1	5.11	9×10^{-11}	(202)
GPAA1	3.86	1×10^{-10}	(202, 203)
HS2ST1	3.98	3×10^{-10}	(202)
JAM3	3.86	3×10^{-10}	(202)
BSG	3.65	2×10^{-9}	(202, 204)
TGOLN2	4.72	1×10^{-9}	(204)
KCT2	5.97	6×10^{-9}	(205)
CD44	4.00	1×10^{-10}	(206)
CD47	5.28	3×10^{-9}	(206)
ITGA3	3.48	6×10^{-9}	(206)
SCCPDH	4.75	3×10^{-10}	(204)

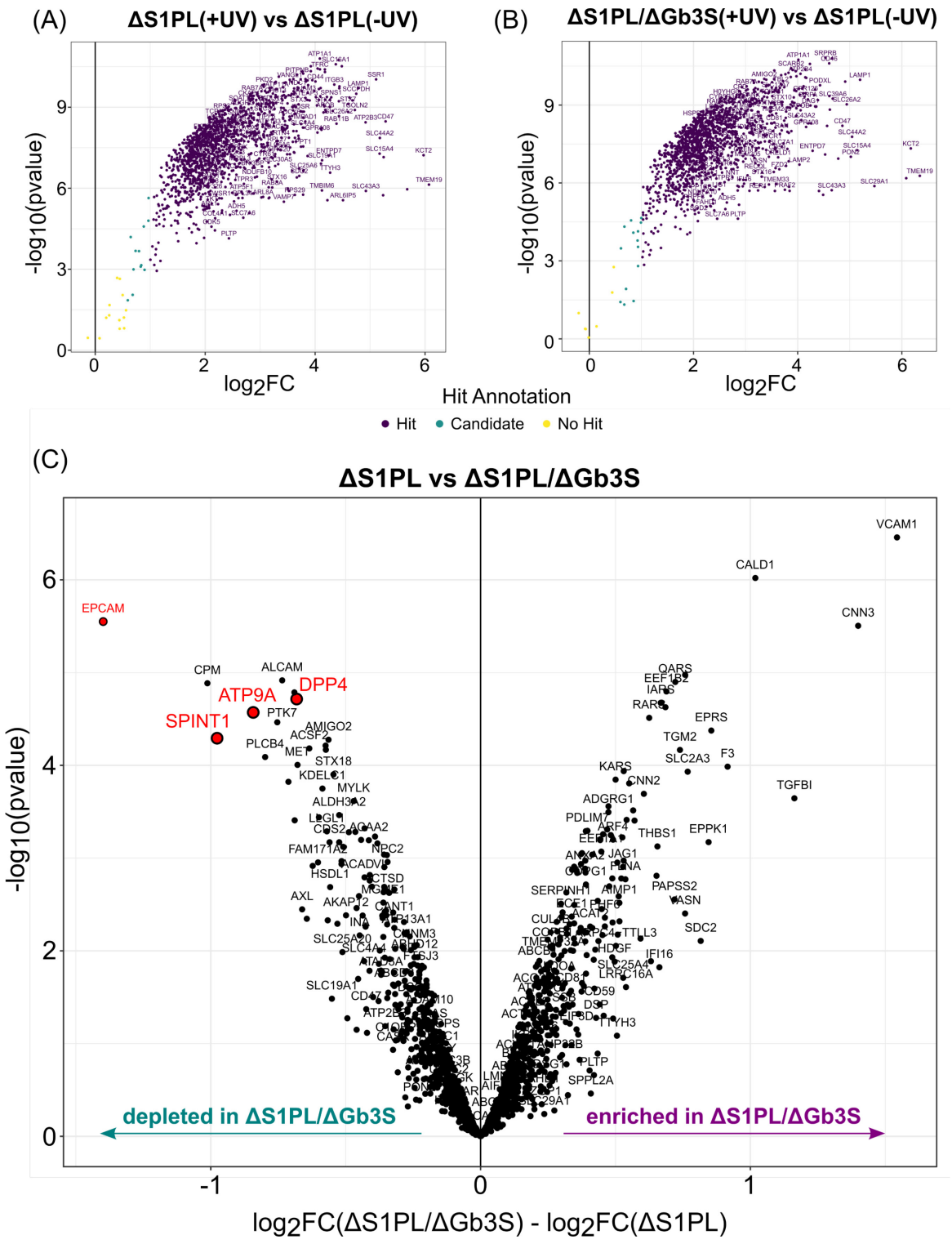

Figure 21 Pull-down proteomics comparison of ΔS1PL and ΔS1PL/ΔGb3S.

HK-2 ΔS1PL and ΔS1PL/ΔGb3S were labelled with pacSph (6 µM, 22h + 4h (Pulse + Chase)) and UV crosslinking was induced (365 nm, 5 min). Biotinylation with Dde-biotin-azide was performed by CuAAC-based click reaction. Protein-sphingolipid conjugates were enriched on Neutravidin agarose and eluted by 2% hydrazine treatment. Enriched proteins were identified and relative quantification was done by TMT10plex. (A) Volcano plot for the enrichment of proteins in UV-irradiated (+UV) HK-2 ΔS1PL cells compared to non-irradiated (-UV) ΔS1PL cells. Proteins with a fold change ≥ 2 and p ≤

0.05 were annotated as *hits*. (B) Volcano plot for the enrichment of proteins in UV-irradiated (+UV) HK-2 ΔS1PL/Gb3S cells compared to non-irradiated (-UV) ΔS1PL cells. Proteins with a fold change ≥ 2 and p ≤ 0.05 were annotated as *hits*. (C) Direct comparison of ΔS1PL and ΔS1PL/ΔGb3S cells. All candidate proteins are documented in the supplement (Table 35, Table 36). Proteomics sample preparation and measurement was done by Dr Per Haberkant (Proteomics Core Facility, EMBL Heidelberg). An analysis pipeline for the data was provided by Dr Frank Stein (Proteomics Core Facility, EMBL Heidelberg).

A direct comparison between ΔS1PL and ΔS1PL/ΔGb3S cells revealed several proteins that are significantly depleted in double knockout cells and that are candidates for a Gb3Cer interaction (Figure 21C). I observed not only depleted, but also enriched proteins. Given that knockout of Gb3S induces broader changes in lipid metabolism, protein enrichment may be related to enriched lipid species in ΔS1PL/ΔGb3S cells, as for example LacCer or ganglioside GM3 and GM2.

I correlated the results from Exp2 with the results from Exp1 and found a strong correlation between both datasets (Figure 22A). Gene set enrichment analysis of depleted and correlated candidates using the REACTOME database indicated a significant overrepresentation of MET signalling related proteins: REAC:R-HSA-6806942 (MET receptor activation) and REAC:R-HAS-6806834 (Signaling by MET). This overrepresentation was based on the presence of MET, SPINT1 and ITGA3 (Figure 22C-D). Other overrepresented terms indicated involvement in receptor tyrosine kinase activity and cell adhesion (Figure 22C).

I identified several proteins as candidates for further investigations (Table 5). A detailed analysis of the possible role of these proteins in the Gb3S phenotype is provided in the discussion.

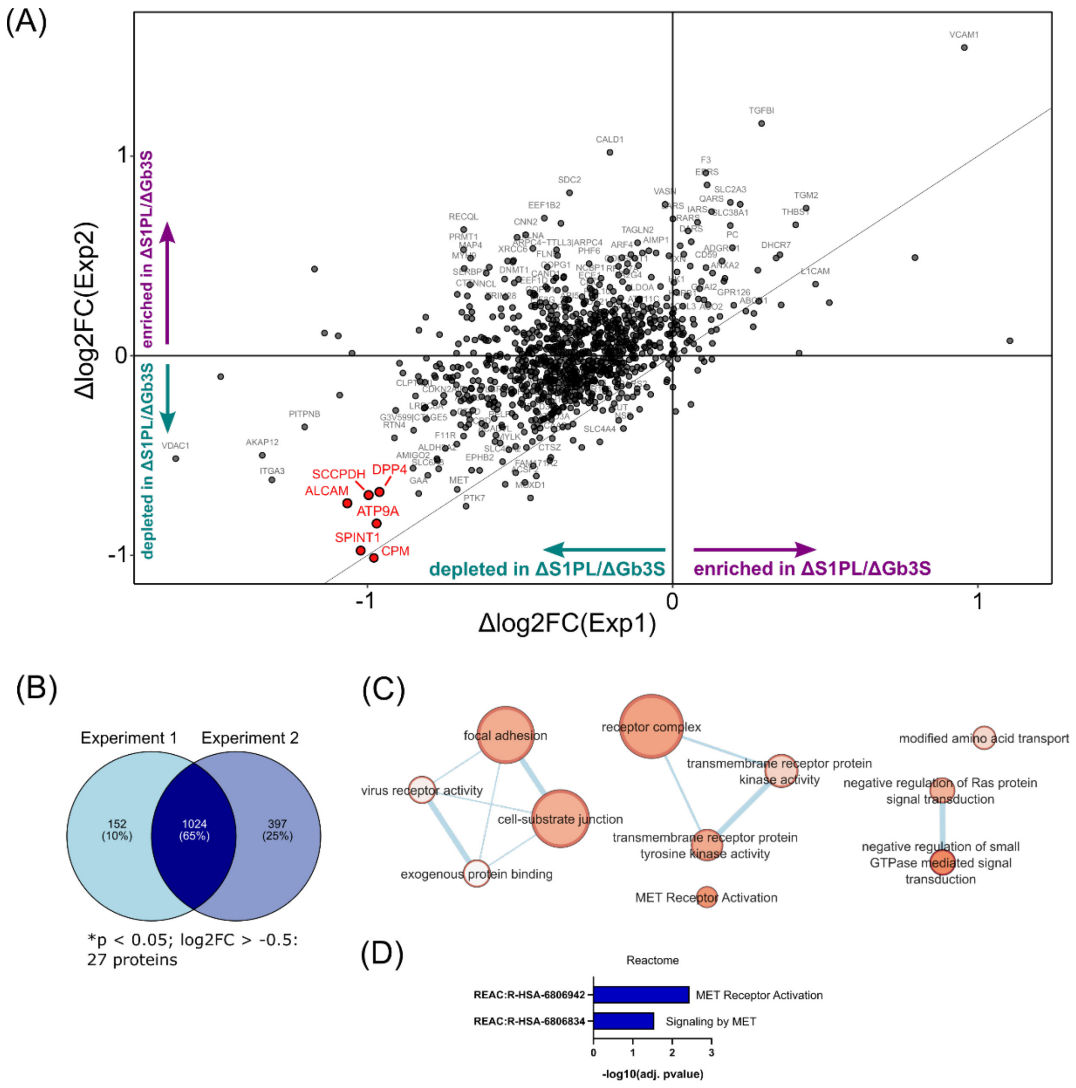

Figure 22 Comparison of pull-down experiments.

HK-2 ΔS1PL and ΔS1PL/ΔGb3S were labelled with pacSph (6 µM, 22h + 4h (Pulse + Chase)) and UV crosslinking was induced (365 nm, 5 min). Biotinylation with Dde-biotin-azide was performed by CuAAC-based click reaction. Protein-sphingolipid conjugates were enriched on Neutravidin agarose and eluted by 2% hydrazine treatment. Enriched proteins were identified and relative quantification was done by TMT10plex. (A) Correlation of $\Delta\log_2$FC between the two pacSph pull-down experiments performed (experiment 1: n=1; experiment 2: n=3). Candidates of interest are highlighted by colour. (B) Venn diagram indicates number of proteins that were identified in either of the two experiments. Proteins depleted higher than $\log_2$FC = -0.5 with a *p*-value < 0.05 were considered hit candidates for globo-series GSL interaction. (C) Gene set enrichment analysis of top 100 globo-series GSL-interaction hit candidates based on $\Delta\log_2$FC with p < 0.05 using gene ontology biological processes by gProfiler (D) Gene set enrichment analysis of globo-series GSL-interaction candidates compared to the reactome database. (E) Gene set enrichment analysis of globo-series GSL-interaction candidates compared to the gene ontology cellular compartments database. Proteomics sample preparation and measurement was done by Dr. Per Haberkant (Proteomics Core Facility, EMBL Heidelberg). An analysis pipeline for the data was provided by Dr. Frank Stein (Proteomics Core Facility, EMBL Heidelberg).

Table 5 Top protein candidates from pacSph pull-down Exp2.

The table highlights the most prominent candidate proteins for globo-series GSL-interaction and indicates if these proteins were considered hits ($log_2FC \leq 0.5$; $p \leq 0.05$) in both experiments (**+** hit; **-** no hit) and the respective relative enrichment. A comprehensive table of the screening results is provided in the supplementary material. Experiments were performed in cooperation with Dr Per Haberkant and Dr Frank Stein (Proteomics Core Facility, EMBL Heidelberg).

Gene	Description	Exp 2	Δlog_2FC	*p*-value	Exp 1	Δlog_2FC
EPCAM	Epithelial cell-adhesion molecule	+	-1.40	2.82E-06	-	-
CPM	Carboxypeptidase M	+	-1.01	1.30E-05	+	-0.98
SPINT1	Kunitz-type serine protease inhibitor	+	-0.97	5.23E-05	+	-1.02
ATP9A	Probable phospholipid-transporting ATPase IIa	+	-0.84	2.72E-05	+	-0.97
PLCB4	Phosphoinositide phospholipase C-β-4	+	-0.80	8.14E-05	-	-
PTK7	Inactive tyrosine-protein kinase 7	+	-0.75	3.43E-05	+	-0.68
ALCAM	Activated leukocyte cell adhesion molecule	+	-0.74	1.21E-05	+	-1.06
MOXD1	DBH-like monooxygenase protein 1	+	-0.71	1.51E-04	-	-0.47
GAA	Lysosomal alpha-glucosidase	+	-0.69	1.64E-05	+	-0.83
SCCPDH	Saccharopine dehydrogenase-like oxidoreductase	+	-0.69	3.92E-04	+	-0.99
DPP4	Dipeptidyl peptidase 4	+	-0.68	1.93E-05	+	-0.96

Table 6 Protein candidates that were considered for further analysis.

The table highlights properties and functions of protein candidates that were considered for further validation. (PM: plasma membrane; TGN: *trans*-Golgi network). Experiments were performed in cooperation with Dr Per Haberkant and Dr Frank Stein (Proteomics Core Facility, EMBL Heidelberg).

Gene	Function	Subcellular Localization	Tissue Expression	References
EPCAM	Homophilic interaction between cells; Role in embryonic stem cell proliferation and differentiation	PM	Many incl. Intestine, Kidney, Skin	(373)
CPM	Removes C-terminal residues from peptides and proteins; Extracellular protein/peptide degradation;	PM	Many incl. Intestine, Kidney	(374)
SPINT1	Inhibitor of HGF activator (HGFAC) and matriptase (ST14); Modulation of MET signalling	PM; Extracellular	Ubiquitous in epithelial cells	(211, 219, 375)
ATP9A	(Probable) lipid flippase; Sorting and vesicle biogenesis in endosomal trafficking; Regulation of exosome release	TGN; Endosome; PM	Ubiquitous, high in brain and pancreas	(248, 249, 251)
ALCAM	Interaction with CD6 in cell-cell contacts; Homophilic cell-cell contacts	PM	Ubiquitous	(376, 377)
SCCPDH	Lysine metabolism; Oxidoreductase activity	Mitochondrial (in rat liver)	Ubiquitous	(378)
DPP4	TCR-mediated T-cell activation; Cell adhesion, migration and tube formation; Extracellular matrix degradation	(apical) PM; Extracellular	Intestine and kidney	(379)

4.1.5 Proteome screening

In addition to the pull-down data, I performed a full proteome analysis of HK-2 wild type, ΔS1PL and ΔS1PL/ΔGb3S cells to correlate both datasets. Proteomics experiments were performed with the clones that were used for pull-down proteomics to enable the correlation of both datasets.

Sample preparation and proteomics measurement were done by Dr Per Haberkant (Proteomics Core Facility, EMBL Heidelberg), and an analysis pipeline was provided by Dr Frank Stein (Proteomics Core Facility, EMBL Heidelberg).

Analysis of the full proteome data hints at effects on cell respiration, SMAD protein regulation, BMP signalling and morphogenesis in response to knockout of S1PL (Figure 23A, Supplementary Figure 5).

The changes I observed after knockout of Gb3 synthase on the ΔS1PL background were comparatively smaller, compared to the changes induced by S1PL knockout (Figure 23B). Selection of a single clone after S1PL-targeting may have reduced clonal variation in the parental cell line used for Gb3 synthase-targeting. In direct comparison between HK-2 ΔS1PL and ΔS1PL/ΔGb3S cells, proteins associated with the morphogenesis, integrin binding and zymogen activation were found to be upregulated in ΔGb3S cells.

Interestingly, the target of SPINT1, hepatocyte growth factor activator (HGFAC) is upregulated after Gb3 synthase knockout (Figure 23C). Gene set enrichment of proteins enriched after Gb3 synthase knockout indicates changes in cell-matrix adhesion and integrin binding (Figure 23D). I did not observe significant gene set enrichment for proteins that were downregulated after Gb3 synthase knockout.

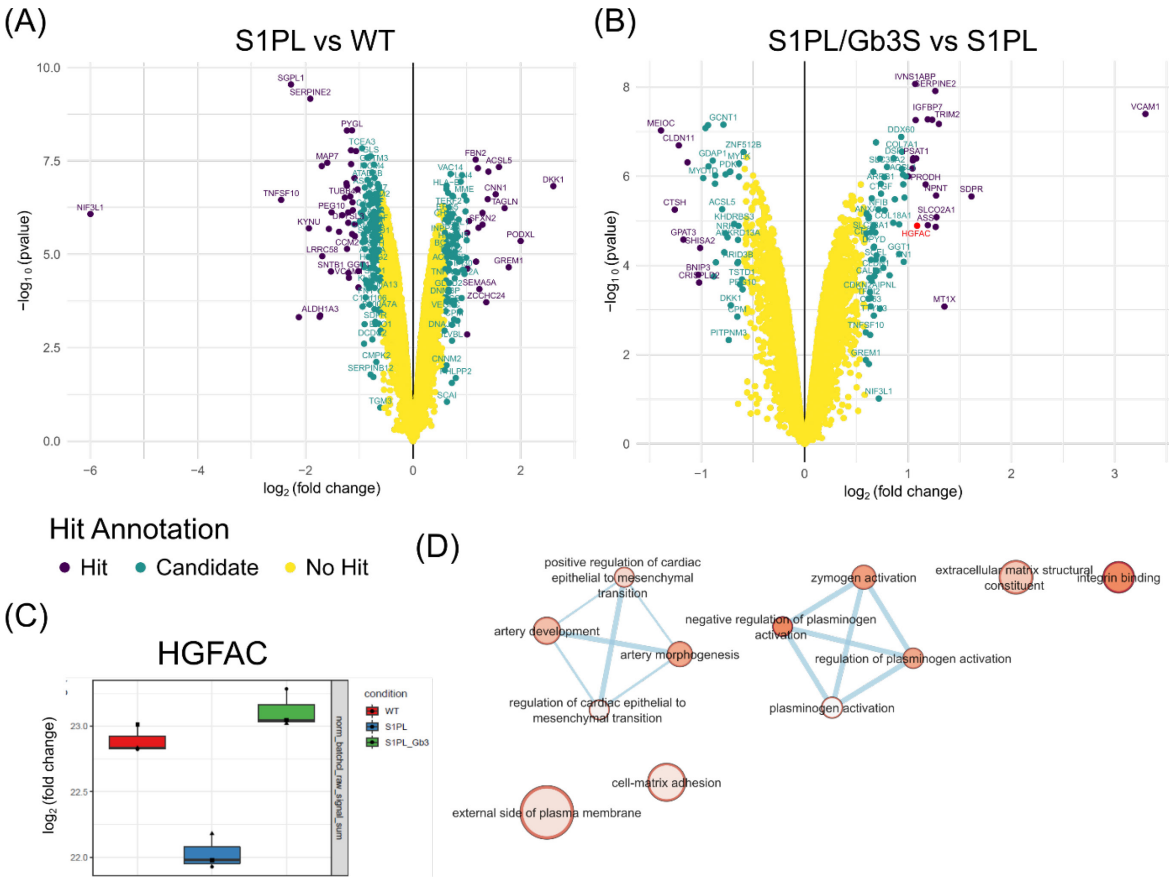

Figure 23 Full proteome analysis of HK-2.

HK-2 wild type, ΔS1PL and ΔS1PL/ΔGb3S were harvested for full proteome analysis. (A) Volcano plot of protein expression changes in HK-2 ΔS1PL compared to wild type cells. (B) Volcano plot of protein expression changes in HK-2 ΔS1PL/ ΔGb3S compared to ΔS1PL cells. (C) Relative protein counts observed for hepatocyte growth factor activator (HGFAC) in proteome analysis. (D) Gene set enrichment and network analysis of proteins significantly enriched in ΔS1PL/ΔGb3S cells compared to ΔS1PL cells using the gene ontology biological processes database and gProfiler. All candidate proteins are documented in the supplement (Table 37, Table 38). Proteomics sample preparation and measurement was done by Dr. Per Haberkant. An analysis pipeline for the data was provided by Dr. Frank Stein (Proteomics Core Facility, EMBL Heidelberg).

4.1.6 Correlation of pulldown and proteomics screening

I combined the data from pull-down experiment Exp2 with the proteomics screening and correlated the respective fold changes to evaluate the contribution of general changes in protein expression to a reduction or increase in the pull-down efficiency.

The data indicates a correlation between both data sets and proteins that were depleted in the pull-down experiments were also depleted in the full proteome (Figure 24A). For most globo-series GSL interaction candidates the depletion in pull-down experiments was higher compared to the depletion in the full proteome, which indicates that changes in the full proteome do not completely explain the depletion observed in pull-down experiments. Of note, SPINT1 was not detected in the full proteome, therefore no correlation could be made.

The Top3 score indicates the average area of the three peptides with the highest area that were measured for a protein across all samples. A correlation between Top3 scores of pull-down and full proteome experiments allows to evaluate the contribution of background proteins to the pull-down experiments. In this case a weak positive correlation (R^2 = 0.1159) was observed (Figure 24B), indicating a contribution of protein background to the pull-down screening experiment. Divergence from this correlation may hint at interesting protein candidates, as seen for example for ATP9A, ALCAM and SLC6A8.

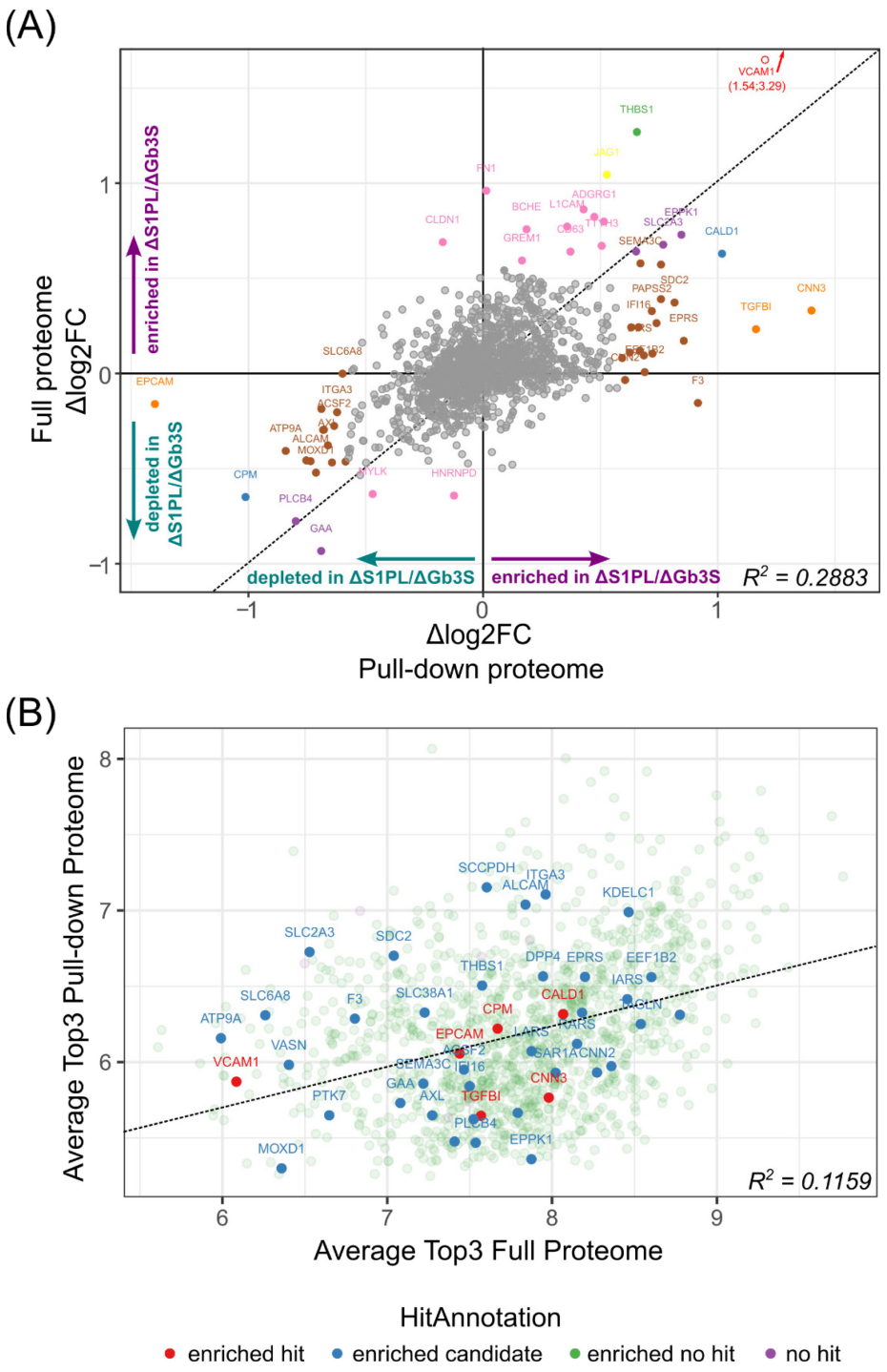

Figure 24 Correlation of pull-down experiments and full proteome.

Datasets of pull-down experiment 2 and full proteome analysis were correlated with respect to (A) Δlog_2FC of protein abundance between HK-2 ΔS1PL and ΔS1PL/ΔGb3S cells or (B) correlation between average top3 peptide abundances in full proteome and pull-down experiments across all samples indicates likelihood of enrichment of background proteins. Proteomics sample preparation and measurement was done by Dr. Per Haberkant. An analysis pipeline for the data was provided by Dr. Frank Stein (Proteomics Core Facility, EMBL Heidelberg).

4.1.7 In vitro validation of globo-series GSL interaction

pacSph pull down of endogenous proteins

To validate findings from pull-down experiments, I performed western blotting experiments after pacSph labelling and pull-down. In addition to genetic ablation of Gb3S, I used pharmacological inhibition of GCS by Genz-1233346 as control to check the dependence of protein labelling on globo-series GSLs and glycosphingolipids in general.

Cells were treated with pacSph (0.5 µM, 22h + 4h) with or without 5 µM Genz-123346. Proteins were extracted and subjected to CuAAC click reaction with biotin-PEG3-azide. Biotinylated protein-sphingolipid conjugates were enriched on solid support Neutravidin agarose and released by boiling in sample buffer. 5% of the input fraction was saved for comparison. SPINT1, EPCAM and ITGA3 were detected using antibodies against the endogenous proteins.

I found a reduction in SPINT1 and EPCAM pull-down in ΔS1PL/ΔGb3S cells and Genz-1233346-treated cells compared to ΔS1PL cells and relative to the input fraction (Figure 25A-B). The size of the effect appears smaller than the log_2FC of about -1 that I observed in pull-down proteomics experiments. Detection of SPINT1 in the input fraction was comparably weak and may need to be optimized. Pull-down of SPINT1 was dependent on crosslinking by UV irradiation. No such effect was observed for ITGA3 and the reduction in pull-down yield can be completely explained by the change in general protein abundance (Figure 25C). The changes in endogenous protein expression are in line with the findings from the proteome experiments (Figure 24A).

pacSph pull-down of overexpressed proteins

I performed further validation by stable overexpression of HA-tagged variants of saccharopine dehydrogenase (putative) (SCCPDH), carboxypeptidase M (CPM), and dipeptidyl peptidase (DPP4) in HK-2 ΔS1PL and ΔS1PL/ΔGb3S cells. An N-terminal HA-tag was introduced for detection on western blot using anti-HA antibody. pacSph labelling and pull-down was performed as described and analysis of protein-sphingolipid conjugates was done by western blotting.

I observed an enrichment of SCCPDH, CPM and DPP4 in the pull-down fractions. Gb3 synthase expression did not affect pull-down levels of SCCPDH or DPP4, but a reduced pull-down/input ratio was observed for CPM indicating a possible dependence on globo-series GSL expression (Figure 26A-C).

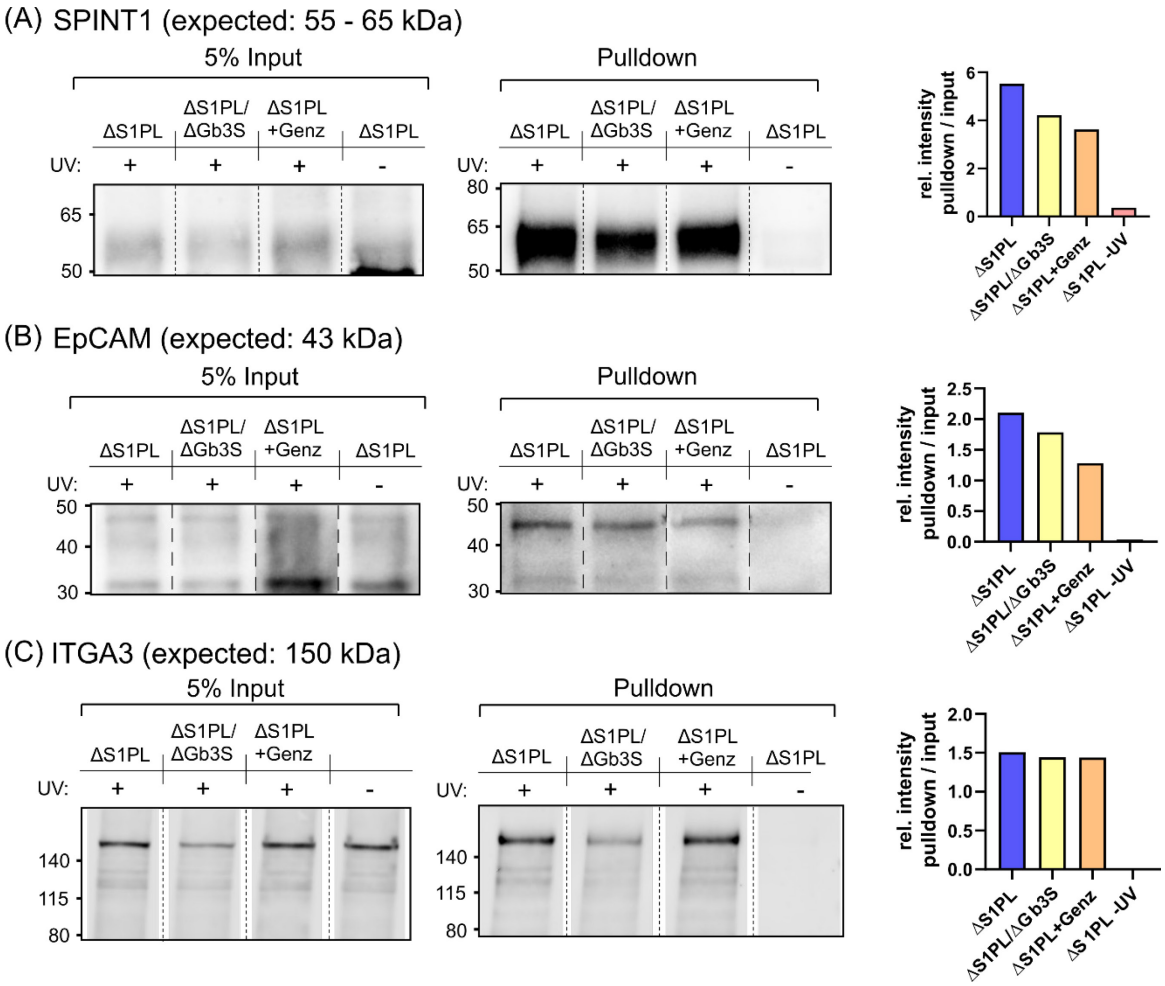

Figure 25 Pulldown of endogenous proteins after pacSph labelling.

HK-2 ΔS1PL, ΔS1PL/ΔGb3S and ΔS1PL cells treated with Genz-1233346 (5 µM) were labelled with pacSph (0.5 µM, 22h + 4h). Proximity crosslinking was induced by UV irradiation (365 nm, 5 min). Biotinlyation was performed with biotin-azide by CuAAC click reaction and protein-sphingolipid conjugates were enriched on Neutravidin agarose. Eluted proteins were separated by SDS-PAGE (10% bis-tris) and transferred onto nitrocellulose membrane. Proteins were identified with primary antibodies for (A) SPINT1, (B) EpCAM and (C) ITGA3 and detected with fluorophore-labelled secondary antibodies. *Left panel*s indicate 5% input fraction, *middle panels* pull-down fractions and *right panels* semiquantitative determination of the pull-down/input ratio.

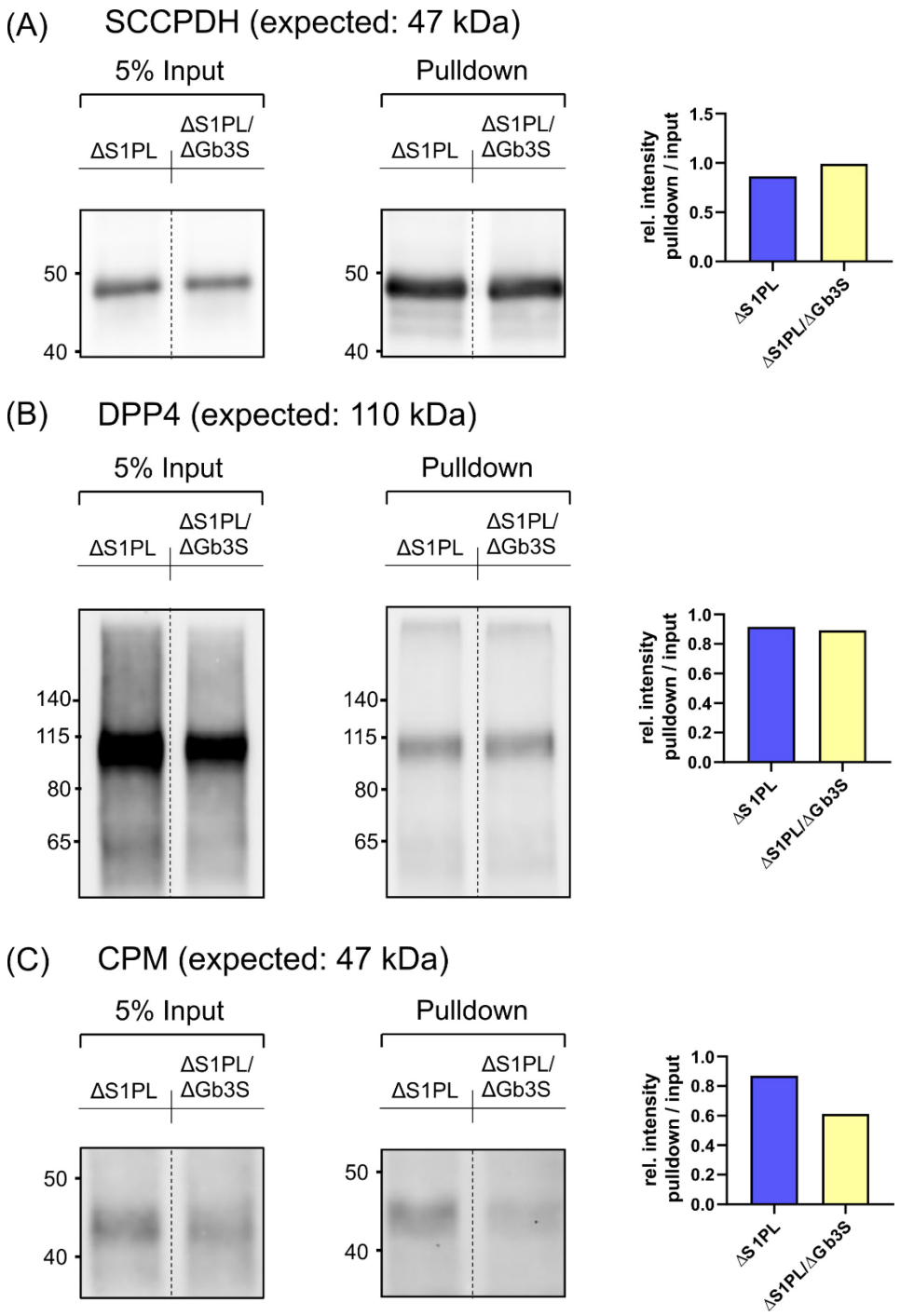

Figure 26 Pulldown of HA-tagged and overexpressed proteins.

HK-2 ΔS1PL and ΔS1PL/ΔGb3S were stably transfected with HA-tagged constructs of SCCPDH, DPP4 or CPM. The cells were labelled with pacSph (0.5 µM, 22h + 4h). Proximity crosslinking was induced by UV irradiation (365 nm, 5 min). Biotinylation was performed with biotin-azide by CuAAC click reaction and protein-sphingolipid conjugates were enriched on Neutravidin agarose. Eluted proteins were separated by SDS-PAGE (10% bis-tris) and transferred onto nitrocellulose membrane. Proteins were identified with a primary antibody against HA-tag and blots for (A) SCCPDH, (B) DPP4 and (C) CPM are shown. *Left panel*s indicate 5% input fraction, *middle panels* pull-down fractions and *right panels* semiquantitative determination of the pull-down/input ratio.

Proximity Ligation Assay

As a complementary validation approach, I used a proximity ligation assay (PLA)-based technique to detect an interaction between pacSph-labelled lipids and candidate proteins (PLA1) and between pacSph-labelled Gb3Cer and candidate proteins (PLA2) (Figure 27).

I seeded HK-2 ΔS1PL and ΔS1PL/ΔGb3S cells on non-coated glass coverslips and treated the cells with pacSph (0.5 µM, 22h + 4h). Proximity crosslinking was induced by UV irradiation (365 nm, 5 min) and cells were fixed on coverslips by paraformaldehyde treatment (4% PFA). Non-crosslinked lipids were removed and CuAAC click reaction was performed with Cy5-azide (PLA1) or not performed (PLA2). Immunolabelling of the epitopes was performed with the indicated antibodies (Figure 27, Table 12) and proximity of antibodies was detected using the DuoLink® assay kit according to the manufacturer instructions. Counterstaining with phalloidin-CF488A (Biotium Inc., Fremont, CA, USA) and DAPI was performed, and images were recorded as Z-stacks using a confocal microscope. PLA1 targets the interaction between pacSph-labelled lipids and candidate proteins (Figure 28A-C). I evaluated the assay by counting the number of PLA foci in a defined image area of 0.15 mm^2 and normalized it to the number of DAPI-positive nuclei. Several image areas were evaluated per PLA reaction. In addition, the mean Cy5 fluorescence was measured for each area to estimate efficiency of the CuAAC click reaction.

I observed a significant reduction in SPINT1-Cy5 PLA foci after Gb3 synthase knockout (Figure 28A), that I did not observe for ATP9A-Cy5 and cMET-Cy5 PLAs (Figure 28B-C), indicating that the interaction between SPINT1 and pacSph-labelled lipids is reduced. Although no significant difference was observed, Cy5 fluorescence was in average lower in ΔS1PL/ΔGb3S, and I cannot completely exclude an impact of CuAAC click efficiency on the number of PLA foci. Of note, phalloidin counterstaining was atypical and diffuse, not showing distinct actin fibres, after performing a CuAAC click reaction.

I used a PLA2 for confirmation of a Gb3Cer-SPINT1 interaction using an antibody targeted against Gb3Cer (Figure 27). I observed PLA foci in ΔS1PL cells that were

reduced after Gb3 synthase knockout, indicating a specific interaction between Gb3Cer and SPINT1.

A preliminary spatial analysis of localization did not reveal differences between both cell lines and needs to be repeated in a more targeted approach using organelle markers.

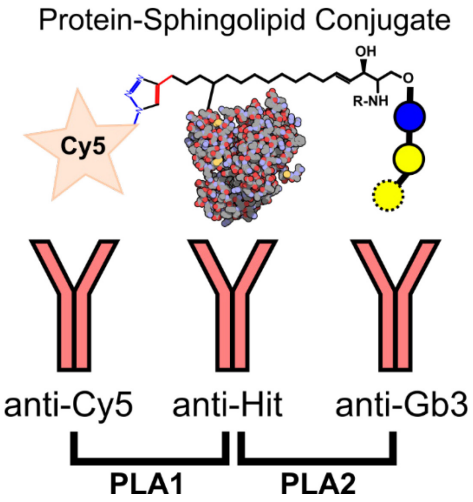

Figure 27 Proximity Ligation Assay scheme.

Proximity ligation assays can detect the proximity of between two antibodies. Two strategies were used for the evaluation of sphingolipid-protein interactions. PLA1 was used to confirm crosslinking between a pacSph-labelled lipid and a protein candidate. pacSph-labelled lipids were detected with an anti-Cy5 antibody after CuAAC click reaction with Cy5-azide. PLA2 confirms an interaction between the candidate protein and pacSph-labelled Gb3Cer. Protein-conjugated Gb3Cer was detected using an anti-Gb3Cer antibody that was directly labelled with a PLA probe.

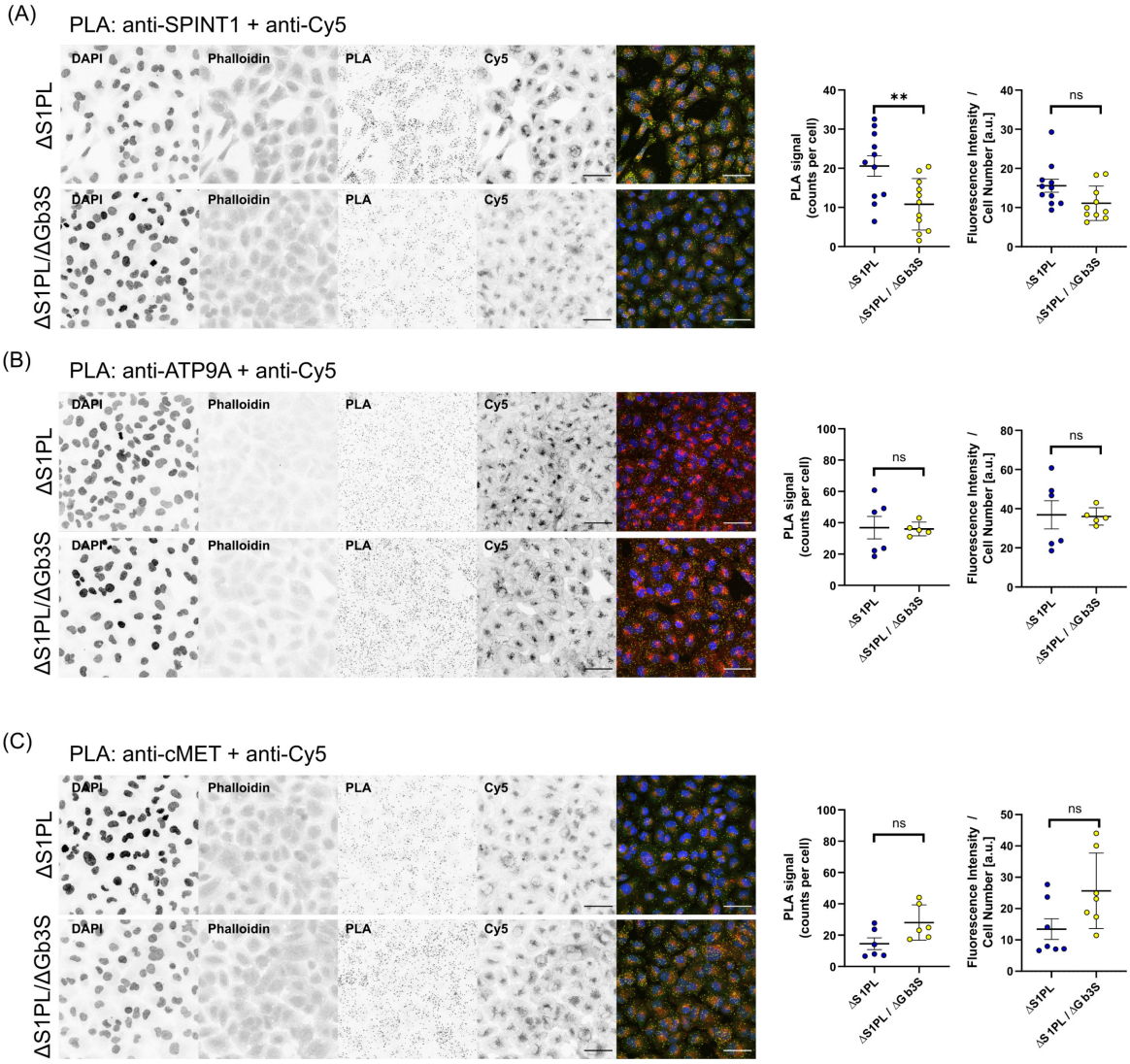

Figure 28 Proximity ligation assay for validation of candidates against Cy5.

HK-2 ΔS1PL and ΔS1PL/ΔGb3S cells seeded on coverslips, treated with pacSph (0.5 µM, 22h + 4h) and UV irradiated (365 nm, 5 min) afterwards. Cells were fixed with PFA (4%) and after removal of non-bound lipids, CuAAC click reaction was performed with Cy5-azide. PLA was performed with antibodies against Cy5 and candidate proteins (A) SPINT1, (B) ATP9A, and (C) cMET. PLA foci were counted and normalized by cell number. Cy5 fluorescence was averaged across the image frame and normalized by cell number. Graphs indicate mean ± standard deviation. Statistical testing was done by unpaired two-tailed Student's *t*-test (** $p < 0.01$).

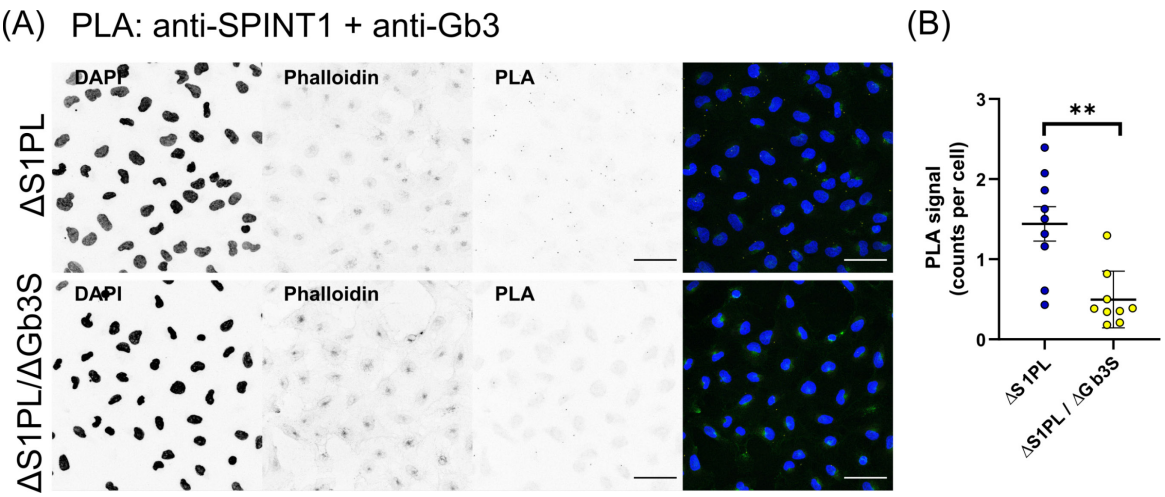

Figure 29 Proximity ligation assay for validation of protein hits against Gb3.

HK-2 ΔS1PL and ΔS1PL/ΔGb3S cells seeded on coverslips, treated with pacSph (0.5 µM, 22h + 4h) and UV irradiated (365 nm, 5 min) afterwards. Cells were fixed with PFA (4%) and non-bound lipids were removed. PLA was performed with antibodies against Gb3Cer (JM06/298, 1:200) and candidate protein SPINT1. PLA foci were counted and normalized by cell number. (B) Quantification of PLA signals in different field of views. Graphs indicate mean ± standard deviation (n = 9). Statistical testing was done by unpaired two-tailed Student's *t*-test (** $p < 0.01$).

4.1.8 Gb3S knockout and uptake effects

HK-2 cells were shown to exhibit a reduction in the uptake of fluorescein isothiocyanate (FITC)-labelled bovine serum albumin after Gb3 synthase knockout(97).

To evaluate a possible endocytosis phenotype in HK-2 cells, I tried to replicate these findings using FITC- and TexasRed (TR)-labelled bovine serum albumin (BSA). I treated HK-2 control and ΔGb3S cells with either 50 µg/mL (FITC-BSA$_{low}$) or 250 µg/mL (FITC-BSA$_{high}$) FITC-BSA for 10 min or 30 min. After vigorous washing, including an acidic wash step to remove surface-bound ligands, fluorescence was measured using a microplate reader.

The comparison between HK-2 controls and HK-2 ΔGb3S cells revealed a small, but significant, reduction with FITC-BSA$_{low}$ after 30 min and with FITC-BSA$_{high}$ after 10 min. A similar trend was observed after 30 min with high FITC-BSA$_{high}$, but not found to be significant (Figure 30A-B). These findings do not fully recapitulate the findings described in literature (97). An effect was also described for 10 min and 30 min at 100 µg/mL and 250 µg/mL.

As the uptake of xenobiotics, as for example gentamicin, is also thought to be affected by Gb3S deficiency in mice, I synthesized a gentamicin-TexasRed (Genta-TR) conjugate to follow gentamicin uptake *in vitro*. Treatment of HK-2 control and ΔGb3S with 50 µg/mL Genta-TR for 15 min or 30 min, followed by extensive washing, including an acidic wash step to remove surface-bound Genta-TR, did not reveal significant differences in uptake between both cell lines (Figure 30C). Effects of gentamicin toxicity may not be dependent on endocytosis, or *in vivo* effects were not replicated in the cell culture system with the tested conditions. Coupling of TexasRed to a small molecule like gentamicin may also affect uptake mechanisms.

As expected, the uptake StxB-Cy3 was profoundly inhibited in ΔGb3S cells in a pulsed experiment with 30 min preincubation at 4°C and shift to 37°C for 10 min (Figure 30D) due to the lack of the receptor Gb3Cer. Interestingly, in ΔS1PL cells StxB-Cy3 uptake was enhanced.

Furthermore, I investigated Genta-TR and TR-BSA uptake in HK-2 ΔS1PL and ΔS1PL/ΔGb3S to evaluate a possible uptake phenotype in S1PL-depleted cells. I compared uptake at 37°C. To control for unspecific binding, I performed a 4°C control. Uptake of Genta-TR or BSA-TR did not reveal significant differences between WT, ΔS1PL and ΔS1PL/ΔGb3S cells. This indicates that endocytosis is not affected in HK-2 ΔS1PL cells due to Gb3S deficiency.

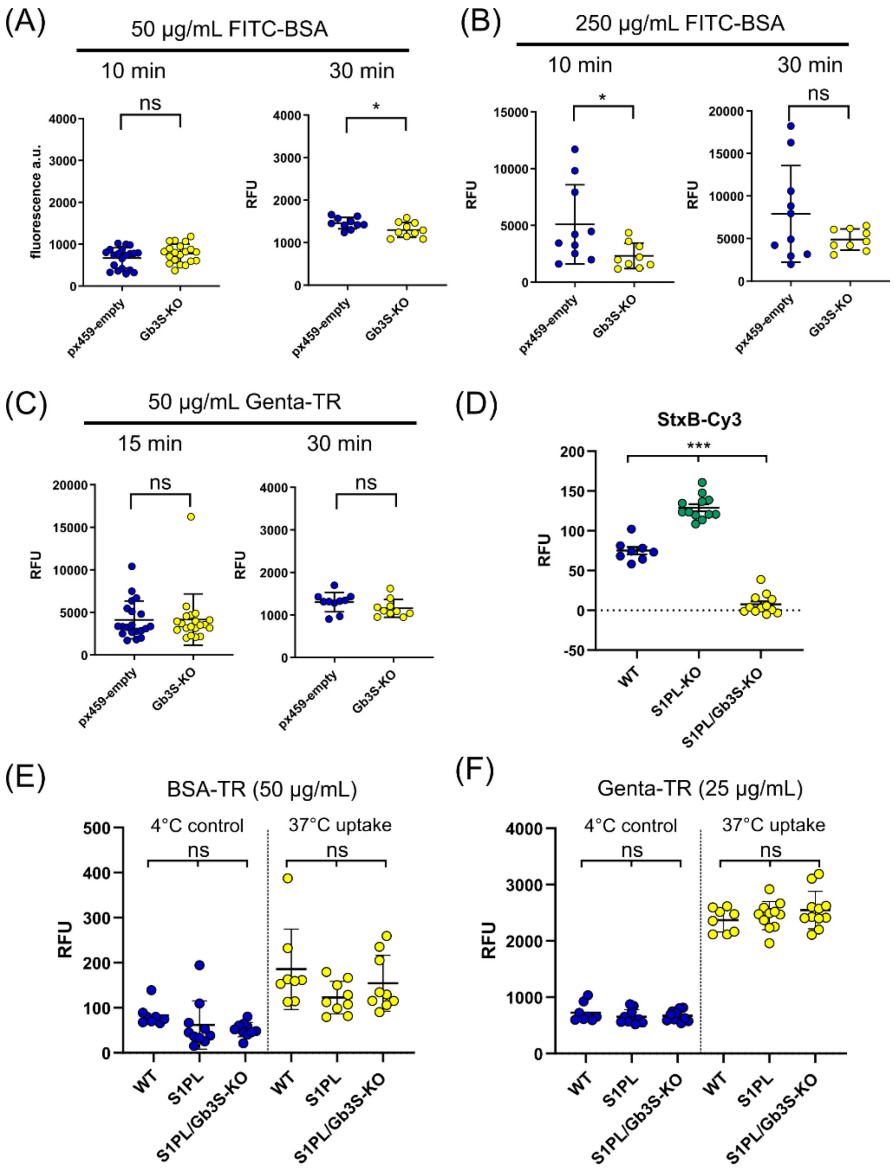

Figure 30 Endocytosis phenotype after Gb3 synthase knockout.

Endocytic uptake was evaluated in HK-2 and HK-2 ΔS1PL and compared to the respective Gb3S-deficient cells. Cells were treated with fluorophore-coupled compounds and fluorescence was determined after extensive washing and cell lysis. (A) HK-2 control (px459-empty) and ΔGb3S cells were treated with 50 µg/mL fluorescein isothiocyanate-coupled (FITC) BSA for 10 min or 30 min. (B) HK-2 control (px459-empty) and ΔGb3S cells were treated with 250 µg/mL fluorescein isothiocyanate-coupled (FITC) BSA for 10 min or 30 min. (C) HK-2 control (px459-empty) and ΔGb3S cells were treated with 50 µg/mL TexasRed-coupled gentamicin (Genta-TR) for 15 min or 30 min. Please note that time points are not directly comparable, due to different instrument settings. (D) HK-2 wild type, ΔS1PL and ΔS1PL/ΔGb3S were treated with StxB-Cy3 conjugate (1 µg/mL) in a pulsed uptake experiment. (E) HK-2 wild type, ΔS1PL and ΔS1PL/ΔGb3S cells were treated with 50 µg/mL BSA-TR for 20 min at 4°C or 37°C. (F) HK-2 wild type, ΔS1PL and ΔS1PL/ΔGb3S cells were treated with 25 µg/mL Genta-TR for 20 min at 4°C or 37°C. Treatment was performed at 4°C to monitor acid-wash resistant cell surface-binding or 37°C to monitor uptake of the compounds. Graph indicates mean + standard deviation. Statistical testing was done by Student's *t*-test (A-C) or one-way analysis of variance with Tukey's post-hoc correction for multiple testing (D) (* $p < 0.05$; *** $p < 0.001$).

4.1 Discussion

The presented results of this chapter are intended to provide a foundation for an in-depth analysis of the obtained datasets and hypothesis generation. I established the cell culture models and assay parameters to identify globo-series interacting proteins in immortalized proximal tubular epithelial cells. I identified several protein candidates and performed an initial validation of globo-series GSL interaction. Although HK-2 ΔS1PL/ΔGb3S cells did not exhibit the expected endocytosis phenotype under the conditions tested, the identification of protein interaction partners for globo-series GSL in PTEC may provide insights into the role of these lipids in the context of acute kidney injury and endocytosis.

4.1.1 Signalling phenotype and SPINT1 interaction

The results point to an interaction between globo-series GSLs, specifically Gb3Cer, and **SPINT1**, a Kunitz-type inhibitor of membrane-bound serine proteases. SPINT1 was significantly depleted in both pacSph pull-down experiments (section 4.1.4), western blot of pacSph pull-down fractions showed a decrease in SPINT1 binding after Gb3S knockout and GCS inhibition (Figure 25), and in proximity ligation assays a significant reduction of PLA foci was observed when targeting the SPINT1 interaction with pacSph-labelled lipids (via Cy5) (Figure 28) and with Gb3Cer (Figure 29). I did not observe a complete depletion of SPINT1-interaction signals in these assays, although the strongest effect was observed when targeting specifically the interaction with Gb3Cer by PLA. Residual signals may arise from background antibody binding of anti-Gb3Cer antibody (Supplementary Figure 4) and interaction by chance. PLA foci in SPINT1-Gb3Cer PLAs appear clustered and associated with specific cells. Given the heterogenous expression pattern of Gb3Cer on single cell level (88), this may correlate with Gb3Cer expression in the specific cells and could be part of future investigations.

SPINT1, also known as hepatocyte growth factor inhibitor HAI-1, is a 66 kDa type 1 transmembrane protein that is located on the cell surface and can be found in a membrane-bound and secreted, proteolytically truncated forms with 40/39 and 58 kDa that differ in inhibitory activity against various substrates (207). SPINT1 consists of a N-terminal and a C-terminal Kunitz domain (KD1 and KD2), a low-

density lipoprotein receptor (LDLR)-like domain, a transmembrane domain, and a cytoplasmic domain (207).

Lack of SPINT1 is linked to embryonic lethality in mice due to a lack of matriptase regulation and failure to form the placental labyrinth (208). Moreover, circulating SPINT1 was found to be a biomarker for pregnancies with poor placental function and fetal growth restriction (209). SPINT1 deficiency in skin was linked to ichthyosis (210). In colorectal mucosa of adenocarcinoma patients SPINT1 was found to be downregulated (211). It was shown, that SPINT1 is required for normal epithelial function through regulation of protease activation and suppression of excess degradation of epithelial junctional proteins (211, 212) and for the maintenance of epithelial integrity (213).

Expression of SPINT1 mRNA was observed in many tissues including kidney, intestine, and placenta and is linked mostly to epithelial cells (207). In kidney, SPINT1 is expressed in the tubular epithelium with a faint basolateral staining in the proximal tubules, a strong staining in distal tubules and collecting duct and no glomerular staining (212). This correlates with the previously reported localization of Gb3Cer in collecting duct and proximal tubules (97, 214, 215).

SPINT1 is an inhibitor of various membrane-bound and soluble serine proteases including hepatocyte growth factor activator (HGFAC), matriptase (ST14), hepsin and prostasin (216). HGFAC is a type II transmembrane serine protease (TTSP). HGFAC and ST14 are both capable of converting pro-HGF to HGF (217, 218). Interestingly, full proteome analysis indicated an increased abundance of HGFAC after Gb3S KO (Figure 23). The inhibitory activity of SPINT1 against HGFAC and matriptase/ST14 is mediated through KD1 (219, 220).

Interestingly, membrane bound SPINT1 has a high affinity for HGFAC and forms a reversible complex with it. This interaction is thought to retain HGFAC on the cell surface and to provide a pool of SPINT1-HGFAC from which HGFAC can easily be accessed under conditions like tissue injury and inflammation. These conditions are associated with an upregulation of SPINT1-HGFAC shedding (221). Truncation of SPINT1, to the low-affinity, 58 kDa isoform may induce a dissociation of the complex and a recovery of HGFAC activity. This mechanism may allow for a

controlled, localized, pericellular regulation of HGFAC activity in response to stimuli like tissue injury (221).

By inhibition and retention of HGFAC, SPINT1 can modulate the conversion of inactive pro-HGF to biologically active HGF, which triggers signalling through the MET receptor. MET is a receptor tyrosine kinase and expressed in epithelial cells of many organs including liver, pancreas, kidney (222). Signalling through MET is associated with many cellular signalling pathways that alter cellular processes including proliferation, motility, migration, and invasion. Moreover, MET signalling was linked to tissue repair responses, morphogenesis, and tumorigenesis (222). By control of the local availability of HGF, SPINT1 may be a modulator of MET signalling.

The Mesenchyme-derived hepatocyte growth factor (HGF) was found to be a potent mitogen and has been inflicted with the repair of injuries of a variety of tissues including renal tubular epithelial cells (223) by supporting epithelial cell growth (224–227). The induction of HGF activating enzyme is a specific feature of injured tissues and is proposed to be a mechanism for the spatial targeting of HGF signalling to injured tissues. In models of acute kidney injury, ectopic expression and exogenous administration of HGF were associated with renoprotective effects and a prevention of proximal tubular damage (228). Glycerol-induced kidney injury in rats was ameliorated by repeated injection of HGF, which was attributed to an activation of the MET receptor and mitogen-activated protein kinase (MAPK) pathway (229, 230) or an attenuation of the inflammatory response (231).

The conversion of pro-HGF to HGF regulates the biological effect of HGF in response to tissue injury. Targeting of HGF activity to injured tissues is achieved by the injury-induced expression of the enzymatic machinery (227). Active HGFAC is produced exclusively in injured tissue through proteolytic activation of pro-HGFAC by thrombin (227, 232, 233). Moreover, SPINT1 expression is strongly induced in injured proximal tubules (212). SPINT1 was found to be upregulated in regenerating epithelial cells of colon in a mouse colitis model and is thought to downregulate the proliferative response after initial activation of MET receptor signalling (221).

Matriptase (ST14), a serine protease with extracellular matrix degrading activity and the capability to convert pro-HGF to HGF, is an alternative target of SPINT1. SPINT1 is involved in the control of matriptase activity, which, if unchecked, promotes carcinogenesis (218). Maturation of matriptase requires an interaction with SPINT1 in the Golgi-complex, which is essential for the transport to the plasma membrane (211). Autocatalytic activation of matriptase is prevented by SPINT1 inhibition (217).

An investigation of the SPINT1 transport in polarized Madin-Darby canine kidney (MDCK) cells demonstrated that, after biosynthesis, SPINT1 is transported to the basolateral membrane, where approximately 15% is cleaved and shedded. The remaining SPINT1 is endocytosed and recycles between PM and endosome, before SPINT1 finally transcytoses to the apical membrane. SPINT1 is proteolytically digested and released or eventually degraded in the lysosome (234). The authors hypothesize that SPINT1 may have a function in transporting matriptase from the basolateral to the apical membrane.

The effects observed in Gb3S-deficient mice included protection against acute kidney injury in models of gentamicin-induced toxicity and rhabdomyolysis. These effects were attributed to a reduction in uptake of renotoxic compounds by tubular epithelial cells (97). It is tempting to speculate, that these effects are not only a consequence of changes in endocytic uptake but may also be attributed to changes in cellular signalling during inflammation and tissue repair. Although the mechanisms for renoprotection due to Gb3 synthase deficiency are unclear, it appears possible that the modulation of MET signalling, mediated by a SPINT1-Gb3Cer interaction may contribute to these biological effects. Loss of Gb3Cer and globo-series GSL may decrease the threshold for an activation of MET receptor signalling by increasing the availability of active HGFAC under homeostatic and/or pathological conditions. This corresponds with increased HGFAC levels as observed in the proteome analysis (Figure 23). A depletion of Gb3Cer may result in a reduction of inhibitory SPINT1 activity against HGFAC.

The regulation of growth factor receptor signalling by glycosphingolipids is an established concept (235). Ganglioside GD3 was found to activate epidermal growth factor receptor (EGFR) signalling in breast cancer cells (236). Ganglioside

GM1 regulates the localization of EGFR (237). Ganglioside GM3 has an inhibitory effect on EGF (Bremer 1986) and fibroblast growth factor (FGF) signalling, without a direct interaction with the receptor (238). EGFR activation was also reported for Gb4Cer (89). Recently. Gb3Cer and Gb4Cer were shown to activate FGF signalling in fibroblast (88). GM2 and GM3 were shown to be negative modulators of MET signalling (239). Interestingly, a heterodimer GM3/GM2 complex had a stronger inhibitory effect, compared to GM2 alone (240). This inhibitory effect was shown to be indirect through interaction with tetraspanin CD82 (239). This indicates that some effects cannot be attributed to a single lipid species, but rather require an interaction of lipids for their bioactive activity.

Further investigations are necessary to validate this hypothesis. The localization of a SPINT1-Gb3Cer interaction and a possible HGFAC accumulation could also hint at a biological function in transport, maturation, or complex formation of for example HGFAC.

4.1.2 Endocytosis phenotype and ATP9A interaction

Recent studies indicated that Gb3Cer modulates endocytic uptake processes in proximal tubular epithelial cells of mice (97). This is not in direct contradiction with a Gb3S-dependent signalling phenotype. I observed a significant reduction in FITC-albumin for low concentrations (50 µg/mL) at 30 min and for high concentrations (250 µg/mL) at 30 min in Gb3S depleted cells (section 4.1.8). Although significant, the observed effects are weaker compared to experiments in literature (97), which may be attributed to differences in assay execution and instrumentation. In addition, I evaluated uptake of a gentamicin-TexasRed (Genta-TR) conjugate but did not observe significant differences in uptake (Figure 30).

It may be argued that the lack of an effect for Genta-TR uptake can be attributed to the chemical modification of gentamicin (477 g/mol) with TexasRed (625 g/mol). Other studies indicate effective uptake of Genta-TR *in vivo* and *in vitro* (241–244). In general, the uptake of gentamicin in proximal tubular cells is thought to occur by receptor-mediated endocytosis associated with megalin/cubilin (245), but endosome-independent mechanisms were demonstrated in OK and MDCK cells (241). It is not clear if gentamicin(-TR) uptake as measured in this study is mediated by the same mechanism as the *in vivo* uptake in proximal tubular cells. With ΔS1PL

background I did not find differences in uptake with Genta-TR or BSA-TexasRed-conjugate.

I observed a change in glycosphingolipid expression due to S1PL KO with an increase in GM3 and GM2 expression (Figure 19). Although ganglioside GM3 has also been described in murine proximal tubular cells (246), this may have a compensatory effect on the depletion of globo-series glycosphingolipids and may abolish possible uptake effects. Assuming Gb3-dependent endocytosis is not functional in ΔS1PL, this may not exclude the possibility for an identification of globo-series GSL interacting proteins that are involved in the regulation of globo-series GSL-dependent endocytic processes.

The P4-type ATPase **ATP9A**, probable phospholipid-transporting ATPase IIA, is an interesting candidate in this regard and was highly ranked in both pull-down proteomics screenings (Figure 21). Due to the lack of a reliable antibody, validation by western blotting was not possible. The proximity ligation assay between ATP9A and Cy5 did not reveal a difference regarding Gb3S depletion (Figure 28). This may be improved by optimization in further investigations, as also PLA strongly depends on antibody quality and specificity. An overexpression of ATP9A may also facilitate the validation of a globo-series GSL-ATP9A interaction.

ATP9A is an integral membrane protein with 10 characteristic transmembrane domains (247). ATP9A expression was described in endosomes, TGN (248) and on the plasma membrane (249). ATP9A is expressed highly in the brain and testis but can also be found in the kidney associated with tubular structures (ATP9A Protein Expression Summary - The Human Protein Atlas, n.d.). Biallelic mutations in ATP9A have recently been linked to neurological disorders associated with postnatal microcephaly (POM) (251). The yeast ortholog Neo1p is associated with receptor-mediated endocytosis, vacuole biogenesis, vacuolar protein sorting (252).

Many members of the P-type ATPases family demonstrate lipid flippase activity and translocate specific lipids from exoplasmic/lumenal to cytoplasmic leaflets of the membrane (253–256). P4-type ATPases have been shown to modulate membrane bending and were implicated in vesicle biogenesis of the endocytic pathway which is associated with changes in lipid composition and distribution (257–260). Although P-type ATPases were assumed to translocate exclusively

glycerophospholipids (261–263), in a recent study ATP10D was shown to translocate GlcCer (264). The putative lipid flippase activity of ATP9A remains to be demonstrated (249).

An important function for ATP9A was demonstrated in the recycling pathway from endosomes to the plasma membrane, where it is localized to phosphatidylserine-positive and Rab11a/Rab11b-positive early and recycling endosomes (248). Moreover, ATP9A was implicated in sorting Wntless as part of a membrane modelling complex with protein MON2 homolog (MON2) and protein dopey-2 (DOPEY2) (265) and may be a regulator of exosome release (249)

Depletion of ATP9A was found to delay the recycling of the transferrin receptor, but not its internalization. Though the recycling rate was reduced it was not completely abrogated (248). Transport and degradation of EGF and Shiga toxin B fragment from early/recycling endosomes to the Golgi were not altered due to ATP9A depletion, indicating a crucial role in recycling to the plasma membrane.

Given the importance of endosomal recycling in proximal tubular epithelial cells for receptor-mediated endocytosis by megalin and cubilin and the need for an efficient sorting of receptor and cargoes for degradation or recycling (266), it is tempting to speculate that ATP9A plays a role in the endolysosomal system of proximal tubular cells. A direct link between a possible flippase activity, a lipid substrate and the recycling pathway was not established.

I can only speculate about possible role for globo-series glycosphingolipids in this process. Gb3Cer was associated with the induction of inward membrane curvature in response to lectin or Shiga toxin binding (267). In this sense, a translocation of Gb3Cer as lipid substrate of ATP9A to the cytoplasmic leaflet of endosomal vesicles may seem counterintuitive but could be relevant for vesicle remodelling and sorting. Interestingly, Morace et al. showed – without further commenting on it - an electron micrograph of a Gb3Cer-positive vesicle in which the staining indicates a localization of Gb3Cer on the cytoplasmic leaflet of the vesicle membrane (97). Furthermore, Gb3Cer may not be a lipid substrate of ATP9A, but interact directly with ATP9A or provide a membrane environment for the formation of protein complexes like the described MON2/DOPEY2/ATP9A complex.

Further validation of a Gb3Cer-ATP9A interaction and a possible functional role is necessary to investigate the presented hypothesis and a connection to endocytic trafficking.

4.1.3 Other protein candidates

Some hits from the pacSph pull-down proteomics experiments may also be candidates for further investigations. Epithelial cell adhesion molecule (EPCAM) and Integrin α3 (ITGA3) were high ranking hits in the screening (section 4.1.4). pacSph pull-down of both proteins was UV-dependent. Validation of an EPCAM-globo-series GSL interaction by western blotting indicated a reduction in pull-down efficiency due to Gb3S KO or GCS inhibition (section 4.1.7), thus indicating a possible globo-series GSL based interaction. The reduction observed for the pull-down of ITGA3 can be completely contributed to a reduction in ITGA3 levels, indicating a sphingolipid-, but not glycosphingolipid-dependent interaction.

Further candidates were evaluated after stable overexpression of HA-tagged constructs. Dipeptidyl peptidase 4 (DPP4) is ubiquitously expressed in the body and is an inhibitor of Glucagon-like peptide 1 (GLP-1). Inhibitors of DPP4 are used for the treatment of type 2 diabetes mellitus by improving insulin secretion of pancreatic β cells (268). DPP4 is a regulator of megalin expression in obese mice (269) and inhibition of DPP4 was found to protect renal tubular cells from free fatty acid-bound albumin-induced proximal tubular cell injury (270).

In proximal tubular epithelial cells DPP4 is trafficked to the brush border in a Galectin-dependent manner (271, 272). Galectins were proposed to play an important role in protein sorting to lipid microdomains for subsequent trafficking to their target compartments (273) and were shown to interact with glycosphingolipids in vesicle biogenesis (274). This could point out another possible role for globo-series GSL in apical trafficking of proteins, which may play an essential role for homeostasis of the proximal tubular endolysosomal network and the associated scavenging receptors.

In cisplatin-induced acute kidney injury, inhibitors of DPP4 accelerated kidney recovery due to anti-inflammatory effects and by promoting proliferation of proximal tubular epithelial cells (275), indicating a role during the tissue repair process.

Interestingly, pharmacological inhibition of GCS sensitized mice to cisplatin-induced acute kidney injury, which was attributed to an increase in ceramide levels (276). Glycerol-induced acute kidney injury associated changes in ceramide and hexosylceramide were comparable to cisplatin treatment (277). In contrast, tubule-specific knockout of GCS under the Pax8 promoter and GCS inhibition with Genz-1233346 resulted in reduced kidney damage in glycerol-induced acute kidney injury (97). It would be interesting to see if genetic ablation of Gb3S has renoprotective effects in cisplatin treatment.

An effect of DPP4 on these processes may be possible but needs further evaluation. Pull-down experiments in DPP4 overexpressing cells did not reveal a globo-series GSL-associated difference, but the correct subcellular expression of DPP4 is a factor that needs to be revised in future investigations.

4.1.4 Experimental discussion of pacSph experiments

The identification of sphingolipid-interacting proteins by pacSph pull-down depends on the metabolic distribution of the functional groups within the sphingolipid metabolic network. Distribution of the functional groups to globo-series GSL requires several metabolic conversion steps, thus an increase in incubation was associated with an improved labelling of glycosphingolipids (section 4.1.2). Labelling of sphingomyelin remained constantly high from early time points on, making up about 50% of the labelled lipid species, while Gb3Cer accounted for approximately 15% of the labelled species with optimized labelling conditions. I found that Gb3S knockout resulted in further increase of sphingomyelin labelling, which may induce a bias towards sphingomyelin-interacting proteins in pull-down experiments (section 4.1.3). In the comparison of ΔS1PL and ΔS1PL/ΔGb3S cells this bias may become visible as an increase in protein pull-down after Gb3S knockout, and therefore should be distinguishable from a depletion of globo-series glycosphingolipid-interactors. Moreover, gangliosides GM3, GM2, LacCer and GlcCer levels are increased in Gb3S knockout cells, which is also reflected in increased labelling of these metabolites. Similar to sphingomyelin, this change in abundance introduces a bias in pull-down experiments. Despite this increase in other species, only labelling of globo-series glycosphingolipids was reduced in ΔGb3S cells, indicating that depletion effects in pacSph pull-down proteomics experiments can be attributed to globo-series GSL expression.

I cannot exclude that other glycosphingolipids have compensatory effects and could replace globo-series glycosphingolipids in protein-sphingolipid interactions, which could result in an abolishment of globo-series GSL-based effects and may render these proteins unidentifiable in the current setting. A broad screening of ΔS1PL and ΔS1PL/ΔGb3S clones could help to identify clones with similar metabolic preferences and preferred features like strong globo-series expression. These reservations also apply to other validation strategies that depend on the pacSph labelling.

An increase in labelling time resulted in a bias towards very long chain-fatty acyl (VLCFA) sphingolipid species (Figure 14). This bias may benefit the identification of proteins with a preference for interaction with VLCFA-sphingolipids and may hinder the identification of proteins with a preference for LCFA-sphingolipids. Furthermore, subcellular distribution and microdomain-association can be based on acyl-chain composition. Preferences on protein-interaction with specific lipid species have been reported before (278, 279).

It is tempting to speculate about applications of the presented datasets in different contexts. Independent from globo-series glycosphingolipids, pull-down experiments in ΔS1PL cells could facilitate the investigation of sphingolipid-interacting proteins with an emphasis on proximal tubular epithelial cells. Proximal tubular epithelial cells are specialized for compound uptake, which is reflected in the expression of specialized PTEC-specific transport proteins and channels that may need sphingolipid-interactions for correct function and trafficking.

Fabry disease is the most common lysosomal storage disease and is characterized by α-Galactosidase A (GLA)-deficiency causing an accumulation of Gb3Cer in almost every cell type (280). Enzyme replacement therapy clears Gb3Cer storage but shows limited clinical efficacy (62). Disease onset in mostly adult patients does not directly correlate with already prenatal Gb3Cer storage (62). It is possible, that Gb3Cer has an impact on cellular functions that goes beyond lysosomal accumulation. Impaired autophagy (281), inflammation, and oxidative stress response due to GLA deficiency were demonstrated (62). Absence and accumulation of Gb3Cer may have an impact on interacting proteins and under my supervision, Andre Müller (Bachelor student, Lipid Pathobiochemistry Group,

DKFZ Heidelberg) generated ΔS1PL/ΔGLA cells that, in addition to the provided datasets, my provide further insights into possible interactors of Gb3Cer under conditions that mimic Fabry disease.

Gb3Cer expression was shown to be a regulator of cell identity (87, 88, 282) and changes in globo-series GSL are associated with the induction of epithelial-to-mesenchymal transition (EMT) (91). The exact mechanism of how globo-series GSL regulate broad changes in cellular programs remains unclear. Recently, a repressing effect of Gb3Cer levels on the transcription factor AUTS2 was described and found to retain neuronal cells in a stem-like state (87). It appears reasonable that a lipid-protein interaction acts as a sensor for changes in globo-series GSL levels. SPINT1 was shown to be a regulator of EMT in a pancreatic cancer cell line and may be one such candidate (283). Knockdown or knockout of both, SPINT1 and Gb3S, is associated with the expression of mesenchymal markers (91, 283) and both may share an EMT regulatory axis via HGF signalling (284, 285).

In summary, the obtained datasets may be a valuable tool for the generation of hypothesis and follow up studies on the presented proteins may strengthen a connection to the renal phenotypes observed in Gb3S knockout mice, but also provide insights into other phenotypes that are associated with dysregulated globo-series glycosphingolipid expression. Establishing dedicated kidney injury-based and endocytosis-based models for an evaluation of Gb3Cer-protein interaction effects may help to dissect a possible connection between effects on compound uptake and renoprotection and decipher a possible connection between Gb3-dependent uptake and signalling phenotypes.

4.1.5 Effect of Gb3S knockout

Knockout of Gb3 synthase affected not only the expression of globo-series glycosphingolipids, but was associated with an increase in HexCer, LacCer, GM3 and GM2. Furthermore, expression of low amounts of GD2 was induced after Gb3S knockout indicating a remodelling of the glycosphingolipid synthesis network (Figure 18E-F, Figure 19A). Interestingly, the MET receptor was also a candidate protein in the pacSph pull-down screening, but a change in interaction due to Gb3S KO could not be validated by PLA (Figure 28). Though not significant, PLA data rather points to an increase in interaction, which might be related to an increase in

abundance of ganglio-series GSL. For example, the ganglioside GD2 colocalizes with the MET receptor and constitutively activates MET receptor signalling in MDA-MB-231 breast cancer cells (286) and may be a candidate for such interaction.

It is of question whether the observed and possibly compensatory increase in ganglio-series glycosphingolipids can also be observed in mouse tissue. Under physiological conditions ganglioside GM3 is expressed in murine proximal tubular cells (246), but to the best of my knowledge in mouse tissue no reports of ganglio-series GSL changes in response to Gb3S knockout exist. If similar changes can be confirmed in mouse tissue, it may add another layer of complexity to untangling the Gb3S knockout phenotype.

Vascular cell adhesion protein 1 (VCAM1) was found to be upregulated in ΔS1PL/ΔGb3S cells and may be associated with the inflammatory response. Interestingly, treatment with Gb3Cer can enhance VCAM1 expression in human macrovascular endothelial cells under basal conditions (287). Furthermore, Gb3Cer treatment was reported to have a positive and negative immunomodulatory effect through toll-like receptor 4-mediated macrophage activation depending on the concentration (92, 93).

4.1.6 Limitations of the study

For this study, I decided to use a cell culture model system. Difficulties to evaluate tubular damage mechanisms on cellular level in *in vivo* animal models have been reported (288). The advantage of a use of primary renal proximal tubular epithelial cells are opposed to their limited availability and variability. A cell culture model system allows for a systematic analysis of tubular damage and repair mechanisms in the specific cell type of interest, proximal tubular epithelial cells. The reduced complexity and easy availability and applicability of genetic engineering tools compared to living organisms allow to use specific assays to interrogate protein-sphingolipid interactions.

In contrast to these advantages, current cell culture models cannot completely reflect the cellular environment and the interaction with other cell types *in vivo*. Proximal tubular epithelial cells inhabit a dynamic environment. Fluid shear stress was shown to be an important modulator of endocytic uptake (289). Cell polarization plays an important role in the formation of apical and basolateral

trafficking networks (290). A recent study demonstrated that polarity and renal proximal tubular epithelial cell characteristics can be improved in HK-2 by growing in 3D culture (288). This includes the formation of a tubule-like architecture, a restoration of Na^+ transport and an upregulation of kidney-development-related genes (288). These factors are not reflected in the model used for this study. Furthermore, all experiments were performed under homeostatic conditions. Challenging conditions by provoking the tissue repair response and specific triggering of endocytic pathways may provide further insights into the underlying mechanisms.

Further investigations are necessary to dissect and validate the observed effects. Proximity ligation experiments are highly dependent on the quality of the used antibodies and should be validated by knockdown.

Due to the lack of success in generating more double knockout clones, the experiments had to be conducted with a single combination of ΔS1PL and ΔS1PL/ΔGb3S cells. Although the analysis of multiple clones would be preferable to exclude clonal effects, the impact of these effects should be reduced in the ΔS1PL/ΔGb3S cell line due to the preceding selection process and limited cultivation time between the consecutive knockouts.

Knockout of S1PL could be considered a relatively harsh intervention with profound effects on various cellular processes and is in line with the changes I observed in glycosphingolipid and protein expression. Although this may render it more difficult to detect sphingolipid-protein interactions involved in these processes, it does not fully invalidate the approach to use these cells as a tool. Nevertheless, it highlights the need for a validation of identified interactions independent of the ΔS1PL background. In addition, ablation of Gb3 synthase may have more effects than depleting globo-series GSL levels and could glycosylate not only lipid but also protein substrates.

I found that Gb3Cer expression differs profoundly on single cell level. This indicates that the glycosphingolipid expression profile may not be hardwired and subject to culture conditions like the cellular environment and cell density. I observed an increase in Gb3Cer expression in response to increasing cell density (Figure 15). A recent study demonstrated that Gb3Cer depletion suppresses contact inhibition

in human mammary epithelial cells (291) and hints at an effect of Gb3Cer in growth regulation. The analysis of Gb3Cer effects on single cell level could provide additional insights compared to a stochastic whole culture-based approach.

4.1.7 Outlook

The presented results are not intended to provide final conclusions and a detailed mechanism for globo-series glycosphingolipid function in proximal tubular cells, but rather a foundation for further investigations of the presented hypothesis.

Further dissection and in-depth evaluation of signalling and endocytosis related phenotypes may help to improve the understanding of globo-series glycosphingolipid function in the kidney and could reveal novel targets for the prevention of acute kidney injury or aminoglycoside-induced renal damage.

5 Chapter 2 – Sphingolipids and KDSR mutations

5.1 Results

Since 2016 several patients with biallelic mutations in the *KDSR* have been identified (Table 7). These mutations were often associated with *erythrokeratodermia variabilis et progressiva* 4 (EKVP4; OMIM 617526) and palmoplantar keratoderma (thickening of palms and soles). The term **perio**rifical and **pt**chyotropic **er**ythrokeratoderma and the acronym PERIOPTER syndrome has recently been suggested for a description of the disease to highlight an affinity of the lesions for the body folds (292). A total of 14 patients with varying mutations in *KDSR* and a broad spectrum of skin involvement, ranging from severe ichthyosis-type Harlequin phenomenon to mild-to-none erythrokeratoderma have been identified to date (Table 7). The metabolic consequences of these mutations have been analysed before for two patients (183, 184) and did not find a strong reduction in sphingolipid synthesis, despite the essential role of KDSR in the de novo sphingolipid synthesis pathway. The aim of this project is to investigate metabolic consequences of biallelic KDSR mutations with an emphasis on sphingolipid *de novo* synthesis and alterations in sphingoid base metabolism, as well as the accumulation of intermediates, which could trigger unfaithful substrate utilization of other enzymes of the pathway and result in the formation of non-physiological sphingolipids.

Parts of the presented data have been published in Human Molecular Genetics (293). For the description of the experimental results the general letter-based nomenclature system for skin ceramides is used (Figure 7). Ceramide nomenclature in this chapter follows the guidelines for skin ceramides described by Motta et al. (1993) (141).

5.1.1 Identification of a patient with biallelic KDSR mutations

For this study I analysed tape-stripping material from stratum corneum, skin biopsies and whole blood samples of two patients with mutations in the *KDSR* gene. The clinical features and genotype of the first patient was described before by Bursztejn et al. (2019) (292). Biallelic mutations in the *KDSR* gene were reported for this patient. A c.178delA mutation was inherited from the father and introduces

(A)
KDSR Patient 1 (Bursztejn et al. 2019)

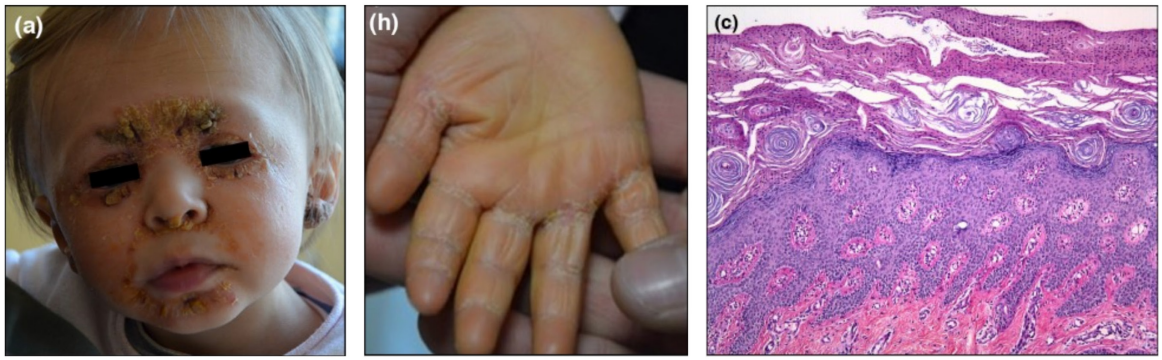

(B)
KDSR Patient 2 (Pilz et al. 2022)

(C)

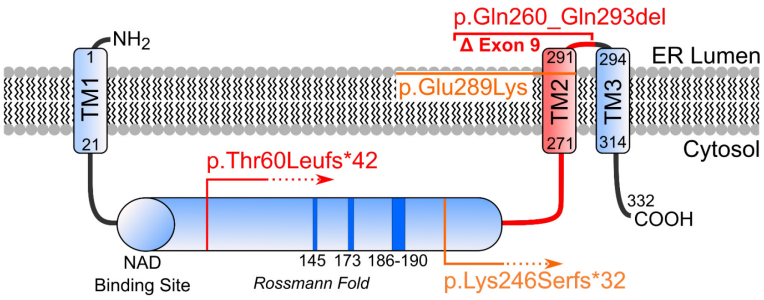

	Allele 1	Allele 2
Patient 1 *Female, 3y*	c.178delA p.Thr60Leufs*42	c.879G>A p.Gln260_Gln293del
Patient 2 *Female, 41y*	c.737_738delinsG p.Lys246Serfs*32	c.865G>A p.Glu289Lys

(D)

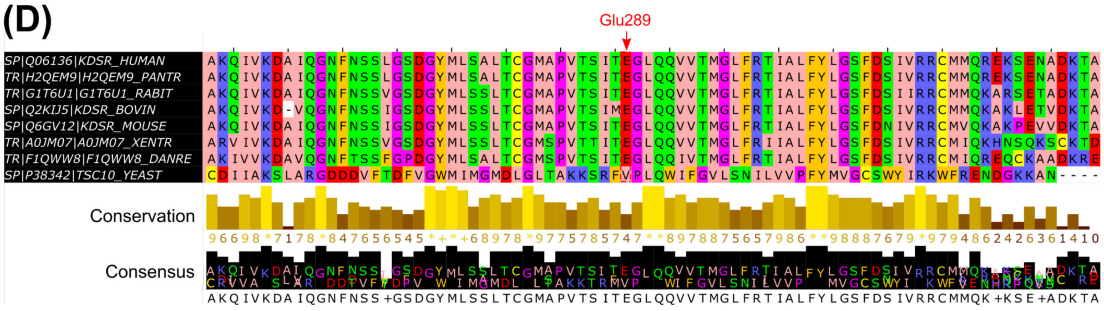

Figure 31 Patients with biallelic KDSR mutations.

(A) Photos of patient 1 taken at the age of 19 months. *(Left)* Keratotic lesions around the eyes and cheeks. The area around the lips is spared. *(Middle)* Palmoplantar keratoderma at the age of 19 months

(Right) H&E staining (x100) of buttock skin biopsy (showing a thickened and parakeratotic horny layer, rather broad stratum granulosum and acanthotic spinous cell layer. Photos were taken from (292). **(B)** Photos of patient 2 *(Left)* Harlequin-type ichthyosis phenomenon at birth. *(Middle)* Palmoplantar keratoderma at the age of 40 years and *(Right)* Keratotic involvement of nail folds. **(C)** Mutations observed for both patients and their localization in KDSR protein with respect to functional domains. For patient 1 a p.Thr60Leufs*42 frameshift mutation and a p.Gln260_Gln293del exon 9 skipping was described. Patient 2 exhibits a p.Lys246Serfs*32 frameshift mutation and a p.Glu289Lys amino acid exchange. Photos were taken from (293). **(D)** Glu289 is conserved across different species up to zebrafish *(Danio rerio*). Figure partially reproduced and modified from (292, 293). (License numbers for republication #5323550788932 and #5323550916865)

a premature stop codon, that leads to a loss of the catalytic domain (p.Thr60Leufs*42). The second allele carries a silent c.879G>A mutation that was inherited from the mother. This silent mutation leads to a synonymous p.Gln293= mutation. Earlier reports of this mutation found that the c.879G>A affects the exon splice site and causes a skipping of exon 9 (182). From one month on, the patient exhibits the typical symptoms of PERIOPTER syndrome with demarcated keratotic lesions in the face and the anogenital areas with an affinity for the body folds. At 19 months orange-coloured palmoplantar keratoderma and at the age of 2 years discrete hyperkeratosis on knees and elbows were noted. In a skin biopsy from the buttock, a thick stratum corneum layer and parakeratosis were noted (Figure 31A), while a biopsy from an axillary lesion revealed alternating orthohyperkeratotic and parakeratotic areas. Treatments with oral zinc and antimicrobial topical fusidic acid with oral josacine propionate had no beneficial effect. Tape stripping samples at the age of two years from palmar skin and at the age of four years from volar forearm skin, as well as a skin punch biopsy of palm skin and a whole blood sample were provided by Anne-Claire Bursztejn (Department of Dermatology, Nancy University Hospital, Vandoeuvre les Nancy, France). A more detailed description of the patient can be found in (292).

Samples of a second putative *KDSR* patient, identified by Judith Fischer (Faculty of Medicine, Institute of Human Genetics, Medical Center, University of Freiburg, Freiburg im Breisgau, Germany), were provided by Elise Brischoux-Boucher (University Hospital, Besançon, France). Photographs of the patient were provided by Francois Aubin (Service de Dermatologie et INSERM 1098 RIGHT, CHU et UFR Santé, Besançon, France). Next-generation amplicon-sequencing revealed compound heterozygous mutations in *KDSR*. The first allele carries a

c.737_738delinsG mutation that is predicted to induce a frameshift and protein truncation (p.Lys246Serfs*32). In the second allele a c.865G>A missense mutation was identified in exon 9 causing the exchange of an acidic with a basic amino acid (p.Glu289Lys) within a predicted transmembrane domain. I found that this amino acid is conserved across different organisms to *Danio rerio*, while there was no consensus with the yeast ortholog Tsc10 (Figure 31D). She was born with a congenital ichthyosis-type Harlequin phenomenon, which regressed spontaneously at one month age (Figure 31B). When one year old, she developed palmoplantar keratoderma that was associated with intermittent keratotic lesions in the vulvar area. Dry skin was noted around the eyelids, the nose, and the chin. Systemic treatment with retinoids at 10 years of age had no apparent benefit. Tape stripping samples from palmar and volar forearm skin at 41 years old, a skin biopsy from lesional sole and a whole blood sample at 43 years old were provided.

Table 7 displays the currently known KDSR patients and highlights the degree of skin involvement and thrombocytopenia that was described in some of the patients.

Table 7 Patients with KDSR mutations and observed pathologies.

Patient	Genetic mutation in *KDSR*	KDSR protein alteration	Pathological observations	Reference
#1	c.164_166delAAG (Exon 2); c.879G>A (Exon 9)	p.Gln55_Gly56delinsArg; p.Gln293= (Splice Site Mutation, Deletion of Exon 9)	erythrokeratodermia variabilis et progressiva 4 / PERIOPTER syndrome	Boyden et al. (2017); *Subject 429
#2	c.256-2A>C (Exon 4); c.879G>A (Exon 9)	p.Val86_Gln107del; p.Gln293= (Splice Site Mutation, Deletion of Exon 9)	erythrokeratodermia variabilis et progressiva 4 / PERIOPTER syndrome	Boyden et al. (2017); *Subject 101
#3	g.63,361,789_63,707,612inv (Exon 1+2); c.879G>A (Exon 9)	No expression; p.Gln293= (Splice Site Mutation, Deletion of Exon 9)	erythrokeratodermia variabilis et progressiva 4 / PERIOPTER syndrome	Boyden et al. (2017); *Subject 1107
#4	g.63,361,789_63,707,612inv (Exon 1+2); c.557A>T (Exon 6)	No expression; p.Tyr186Phe	erythrokeratodermia variabilis et progressiva 4 / PERIOPTER syndrome	Boyden et al. (2017); *Subject 438
#5	c.413T>G; c.417+3A>C	p.Phe138Cys; Deletion of Exon 5/5+6	Hyperkeratosis on palms, soles and anogenital areas; Thrombocytopenia	Takeichi et al. (2017); *Patient 1
#6	c.413T>G; c.417+3A>C	p.Phe138Cys; Deletion of Exon 5/5+6	Hyperkeratosis on palms, soles; Perianal erythema and hyperkeratosis; Thrombocytopenia	Takeichi et al. (2017); *Patient 2
#7	c.812G>A; c879G>A	p.Gly271Glu; p.Gln293= (Deletion of Exon 9)	Harlequin-ichthyosis like skin and death at age 37 days	Takeichi et al. (2017); Patient 3
#8	c.223_224delGA; c.544G>A	p.Glu75Asnfs*2; p.Gly182Ser	Harlequin-ichthyosis like skin developing into generalized erythroderma and fine scaling; Thrombocytopenia	Takeichi et al. (2017); *Patient 4
#9	***c.178delA (Exon 2); c.879G>A (Exon 9)***	***p. Thr60Leufs*42; p.Gln293= (Splice Site Mutation; Deletion of Exon 9)***	***erythrokeratodermia variabilis et progressiva 4 / PERIOPTER syndrome with palmoplantar keratoderma***	***Bursztejn et al. (2019); *Patient 1 in this study***
#10	c.460C>T; c.706C>T	p.Arg154Trp; p.Arg234*	Thrombocytopenia; Moderate anemia; Minor skin pathology	Bariana et al. (2019); *Propositus
#11	c.460C>T; c.706C>T	p.Arg154Trp; p.Arg234*	Thrombocytopenia; Moderate anemia; Minor skin pathology	Bariana et al. (2019); *Affected Sibling
#12	c.592G>A; c.865G>A	p.Glu198Lys; p.Glu289Lys	Generalized harlequin ichthyosis developing into palmoplantar keratoderma and leukokeratosis anogenitalis	Huber et al. (2020)
#13	***c.737_738delinsG; c.865G>A***	***p.Lys246Serfs*32; p.Glu289Lys***	***Generalized harlequin ichthyosis developing into palmoplantar keratoderma***	(293) ***Patient 2 in this study***
#14	*c.869G>A c.869G>A*	*p.Gly290Glu p.Gly290Glu*	Spontaneously resolving erythrokeratorderma, Thrombocytopenia	*Liu et al. (2020)*

The table highlights recently described patients with mutations in *KDSR* and the respective observed pathologies. Note patient #9 and patient #13 are the patients described in this study. Several patients with the exon 9 skipping c.879G>A mutation of patient 1 have been described. Patient #12 carries the c.865G>A mutation that was also observed in patient 2. Table modified from (293) License number for republication: #5323550916865.

5.1.2 3-ketodihydroceramide in epidermis of KDSR patients

To investigate whether the reduced activity of KDSR causes an accumulation of its substrate 3-ketodihydrosphingosine (KDS), which can subsequently be utilized by ceramide synthases (CerS) to form novel, non-physiological ceramides with a 3-keto-group in the sphingoid backbone structure, I needed to establish an LC-MS/MS based analytical method and synthesize the respective standards for these hypothetical compounds and their metabolic derivatives.

KDS may be acylated to form 3-ketodihydroceramide (NdK-Cer) (Figure 33), which may be a substrate for a desaturase to form 3-ketoceramide (NK-Cer). Further metabolization could occur by sphingomyelin synthases or glycosyltransferases to yield 3-keto(dihydro)sphingomyelin (NdK- and NK-SM) or 3-keto(dihydro)glucosylceramide (NdK-GlcCer and NK-GlcCer), respectively (Figure 32).

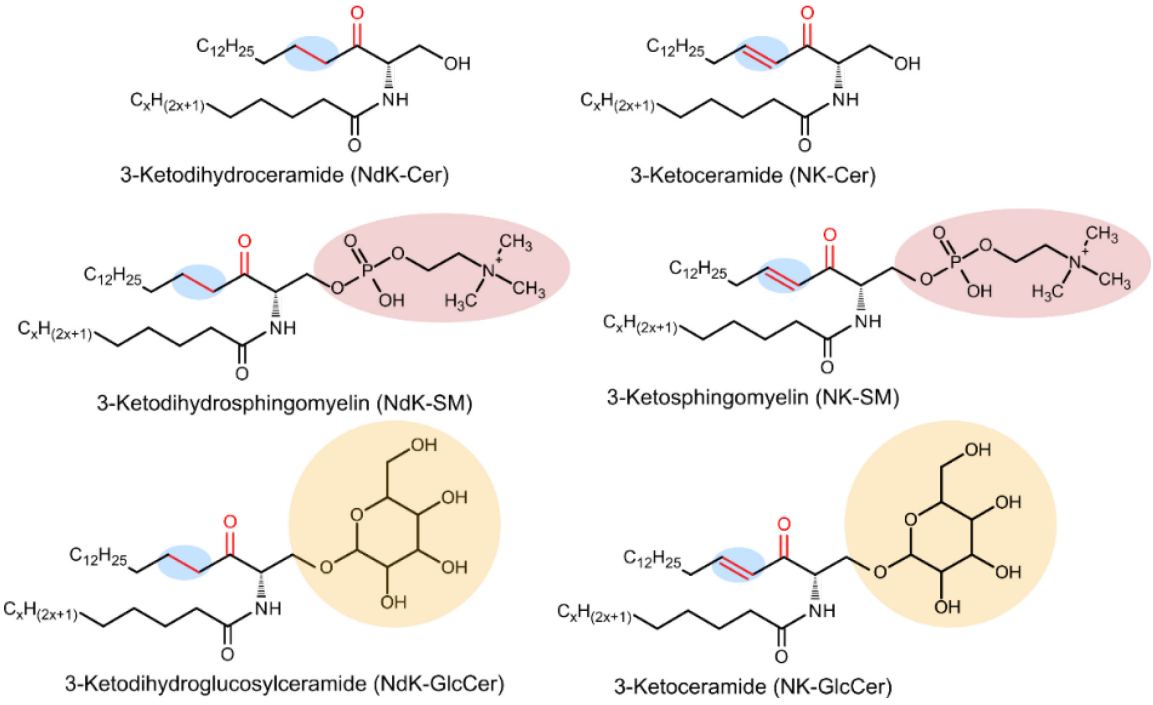

Figure 32 Keto-type ceramide derivatives.

Chemical structure of keto-type ceramides and derivatives including 3-ketodihydroceramide (NdK-Cer), 3-ketoceramide (NK-Cer), 3-ketodihydrosphingomyelin (NdK-SM), 3-ketosphingomyelin (NK-SM), 3-ketodihydroglucosylceramide (NdK-GlcCer) and 3-ketoglucosylceramide (NK-GlcCer). The 4-5 (double)bond (blue circle), 3-keto/hydroxyl group (red) and 1-OH modification (red/yellow circle) are highlighted as structural features that distinguish these compounds. Figure taken from (293). License number for republication: #5323550916865.

Synthesis and characterization of 3-ketodihydroceramides standards

3-ketodihydroceramide (NdK-ceramide) standards were synthesized by conjugation of activated fatty acids to KDS base of varying lengths. C12-, C18- and C24-KDS (*The term "C(number)" is used throughout this thesis to indicate the number of carbon atoms of the respective lipid species)* were coupled with non-hydroxylated C14-, C16- and C24-fatty acids to cover a broad spectrum of compounds in the skin (Figure 33B). Parts of these syntheses were performed in collaboration with Lukáš Opálka (Skin Barrier Research Group, Department of Organic and Bioorganic Chemistry, Faculty of Pharmacy in Hradec Králové, Charles University), who also provided the commercially non-available C24-KDS base. The synthesized compounds were quantified by weight.

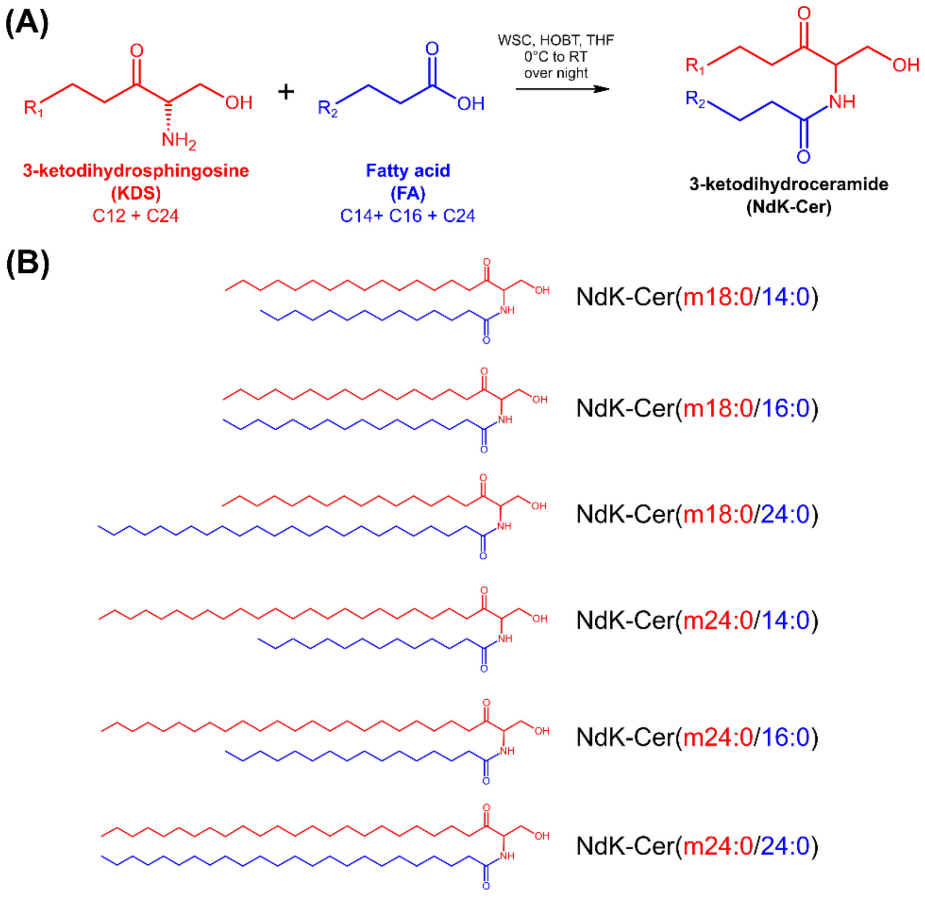

Figure 33 Synthesis of 3-ketodihydroceramide (NdK-Cer) standards.

NdK ceramides were synthesized by conjugation of the free sphingoid base with a fatty acid in a coupling reaction. (A) The reaction scheme for the synthesis of 3-ketodihydroceramides (NdK-Cer). (B) Several combinations of KDS base and fatty acid were prepared to cover the possible variability of NdK ceramides in the body: NdK-Cer(m18:0/14:0); NdK-Cer(m18:0/16:0); NdK-Cer(m18:0/24:0); NdK-Cer(m24:0/14:0); NdK-Cer(m24:0/16:0); NdK-Cer(m24:0/24:0).

The synthesized NdK-ceramide standards were characterized by LC-MS/MS analysis to determine fragmentation patterns and retention times of the compounds. Fragmentation of NdK-ceramides revealed a distinct fragment, specific for the 3-keto-sphingoid base at m/z 270 (for NdK-Cer(m18:0/X)) and m/z 354 (for NdK-Cer(m24:0/X)), that was not dependent on the N-acyl moiety (*X*). This fragment can be explained by a McLafferty-type rearrangement (McL) including the 3-keto group and the γ-Hydrogen of the 1-hydroxyl group and allows a distinction between NdK-ceramides and isobaric NS-ceramides (NS - with a sphingosine backbone) that only differ in the position of the double bond, as well as NdS-ceramides (NdS - with a sphinganine backbone) (Figure 34A, Supplementary Figure 6). Additional discrimination can be achieved by reversed phase liquid chromatography (Figure 34B-C). The exchange of a 3-hydroxyl group against the 3-keto group increases interaction with the stationary phase of the CSH C18 separation column used in this study. The retention times and collision energies for synthetical and hypothetical compounds are depicted in Figure 34B-C. Hypothetical compounds were estimated using a multiple linear regression model using sphingoid base length and fatty acyl length as determinants. The optimal collision energy for collision-induced dissociation (CID) of each standard for the most abundant fragments was empirically determined and hypothetical compounds were estimated using a multiple linear regression model. I observed a positive correlation between collision energy and sphingoid base and N-acyl length, whereas the dependence on N-acyl length was more pronounced.

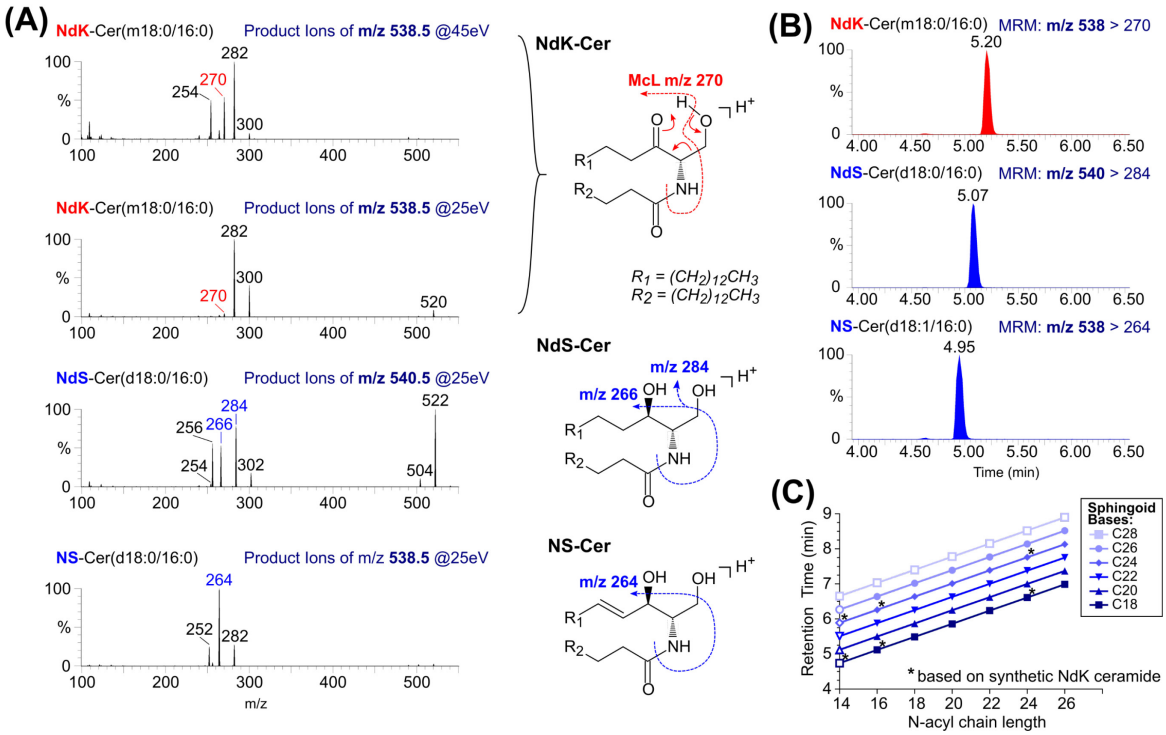

Figure 34 LC-MS/MS characterization of 3-ketodihydroceramides.

3-ketodihydroceramides (NdK-ceramides) were characterized to establish LC-MS/MS analysis conditions. (A) Product ion spectra of NdK-Cer(m18:0/16:0), NdS-Cer(d18:0/16:0) and NS-Cer(m18:0/16:0) were recorded at a collision energy of 25 eV (and 45 eV). Isobaric NdK-Cer and NS-Cer can be distinguished by the characteristic fragment m/z 270 that is generated due to neutral loss of formaldehyde in an McLafferty rearrangement (McL) that is dependent on the presence of the 3-keto group. (B) Retention time of NdK-Cer, NdS-Cer and NS-Cer in reversed phase chromatography. (C) Retention times as determined and estimated for different NdK-Cer standards. * indicates retention times that were empirically determined based on synthetic standards. Filled symbols indicates presence of these species in biological samples. Figure taken from (293). License number for republication: #5323550916865.

Accumulation of free KDS

New sphingoid bases are generated via the *de novo* sphingolipid biosynthesis pathway. *De novo* sphingolipid synthesis via the serine-palmitoyl-CoA transferase complex (SPT) leads to the formation of the first sphingoid base and intermediate metabolite 3-ketodihydrosphingosine (KDS) from its precursors *L*-serine and palmitoyl-CoA. Complex variants of SPT are promiscuous regarding their choice of substrate and an incorporation of longer acyl-CoAs results in the formation of sphingoid bases with increased length and sphingoid bases up to a length of 28 carbons have been described specifically in the skin (20, 131). KDS is rapidly converted by KDSR into sphinganine (Sa), which is not considered a rate limiting

factor in *de novo* sphingolipid synthesis. Sphingosine (So) is not a direct intermediate of *de novo* sphingolipid biosynthesis. Sphingosine bases are usually generated by desaturation of the N-acylated sphinganine (dihydroceramide) and free sphingosine is then obtained by release from ceramide due to the action of ceramidases (Figure 35C).

Stratum corneum of both KDSR patients and age-matched controls was collected by tape stripping of palmar and volar forearm (VA) skin with D-Squame® tapes. Palmar stratum corneum samples were taken from skin areas with palmoplantar keratoderma (lesional) and volar forearm samples from visually non-affected skin areas (non-lesional). Additional samples of palmar stratum corneum from the mother of patient 1 were provided. During tape stripping the outer layer of the stratum corneum is separated from the remaining skin in a reproducible manner by application of an adhesive disc with a defined pressure. Relative protein quantification on tapes was done by infrared densitometry at 850 nm using a SquameScan 850A device (Heiland electronic GmbH, Wetzlar, Germany). The resulting absorbance value correlates linearly with the amount of protein on the disc.

I analysed the impact of KDSR mutations on free sphingoid bases and especially on the levels of the substrate KDS and product sphinganine. KDS was not described in stratum corneum before, and I observed minor amounts of very long chain-KDS bases (VLC-KDS; *in accordance with fatty acid nomenclature, I will use the term "very long chain" or "VLC" to describe sphingoid bases with a length between 22 and 28 carbon atoms as opposed to "long chain" or "LC" sphingoid bases with a length of 13 to 21 carbon atoms*) ranging from C22-C26 in healthy controls. In patients with KDSR mutations I observed increased levels of free KDS (calculated as the sum of all measured KDS species) in palmar and volar forearm stratum corneum of both patients, though not significant in palmar stratum corneum of patient 2 (Figure 35A).

This accumulation of KDS indicates an insufficient capacity of KDSR to accomplish the scope of KDS influx, either due to a reduced conversion of KDS to sphinganine by KDSR or an increased flux into KDS by the preceding KDS reaction the is independent of the patients' skin state (lesional or non-lesional). No increase of

KDS was observed for the mother of patient 1, carrying the c.879G>A exon 9 splice site mutation, indicating that one healthy allele is sufficient to compensate the loss or reduced enzymatic function of the other allele in terms of substrate accumulation. The lipid-to-protein ratio was generally higher in volar forearm skin, which indicates differences between skin areas and explains the comparatively higher values for sphingoid bases, which I observed in volar forearm of patients.

As sphinganine is the product of the reduction of KDS by KDSR, I expected to find a decrease in sphinganine levels. This was observed in palmar skin of patient 2 (as compared to age-matched control group 2), but not in volar forearm of both patients. In contrary, palmar skin of patient 1 even unveiled increased levels of sphinganine. This indicates a compensation mechanism in outer layers of epidermis of patient 1. This compensation may be due to sufficient residual KDSR activity or a reduction of sphinganine flux into other metabolites.

A pathway for sphinganine production from sphingosine is not known but could explain the increase observed in patient 1 via the salvage pathway. Interestingly, in a leukemia cell model with a knockout of KDSR also an increase of sphinganine was observed (294), which could hint at an underlying biological compensation mechanism.

Free sphingosine levels of patient 1 appear to be generally increased, while no difference was observed for patient 2. These differences observed between the patients hint at a heterogeneity in the disease characteristics of both patients. Although sphinganine levels were not changed, I observed an increase in free sphingosine in volar forearm of patient 1.

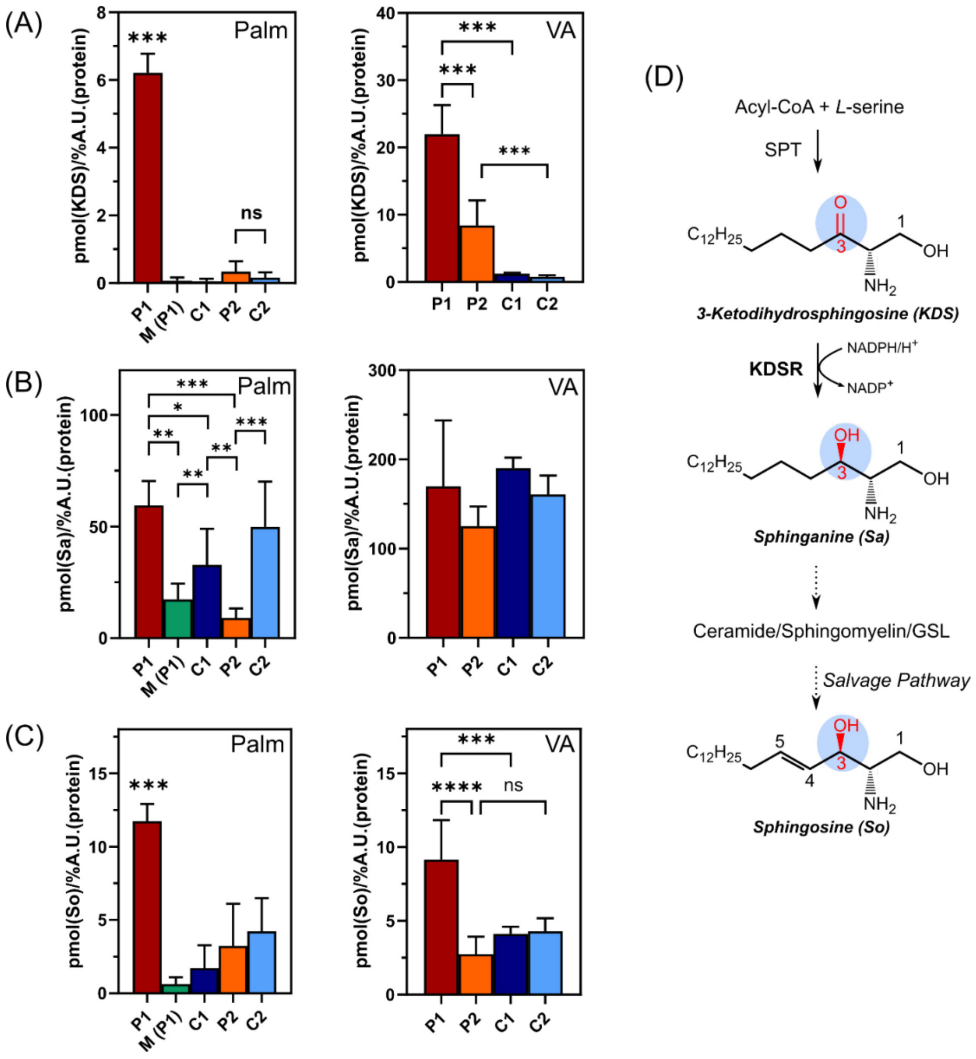

Figure 35 Analysis of free sphingoid bases in stratum corneum.

The free sphingoid bases **(A)** 3-ketodihydrosphingosine (KDS), **(B)** sphinganine (Sa) and **(C)** sphingosine (So) were measured in tape stripping stratum corneum samples of patients. The graph depicts the sum of the measured lipid species in each sphingoid base class. The *left* panel shows palmar stratum corneum (P1: n=4; P2 n=9) and for the mother of patient 1 (M(P1), 31y, n=4, homoallelic c.879G>A) and the *right* panel volar forearm (VA) stratum corneum (P1: n=4; P2: n=9). The age-matched control group 1 was comprised of a boy (3y, n=4) and a girl (3y, n=4) and control group 2 of a female (37y, n=3) and a male subject (51y, n=3). Statistical testing was done by ordinary one-way ANOVA with Tukey correction for multiple comparisons (*** p<0.001; ** p<0.01; * p<0.05). Graphs show mean + standard deviation. **(D)** Free sphingoid bases as products of sphingolipid metabolism. Figure partially taken from (293). License number for republication: #5323550916865.

Total sphingolipid hydrolysis reveals metabolized KDS

To chemically release all sphingoid bases in stratum corneum lipid extracts (free and bound in other sphingolipids) total hydrolysis with hydrochloric acid of palmar stratum corneum extracts was performed. Total hydrolysis cleaves the amide bond between fatty acyl and sphingoid backbone and removes possible modifications of

the 1-hydroxyl group. This reaction releases the free sphingoid base from complex sphingolipids (295). By quantitation of free and bound sphingoid bases, this procedure can address whether and to which extent KDS is present as building block in higher sphingolipids, for example ceramides, sphingomyelins, or glucosylceramides.

In proportion, KDS bases amounted for 25.3% and 35.2%, respectively, of the measured sphingoid bases (KDS, sphinganine and sphingosine species) in patient 1 and patient 2, while I only discovered low amounts of KDS base in control samples (Figure 36A) after total hydrolysis. Subtracting the amount of free KDS, almost all KDS bases found after total hydrolysis could be attributed to complex sphingolipids of unknown composition (Figure 36B). Interestingly, after hydrolysis a relative increase in long-chain KDS (LC-KDS) bases and a decrease in VLC-KDS was observed compared to the free base (Figure 36C-D), indicating a majority of C18- and C20-KDS species was released due to total hydrolysis, and hinting at a higher affinity of metabolizing enzymes towards these species or differences in substrate availability. An increase in KDS levels in control samples was also observed, but at a generally low level.

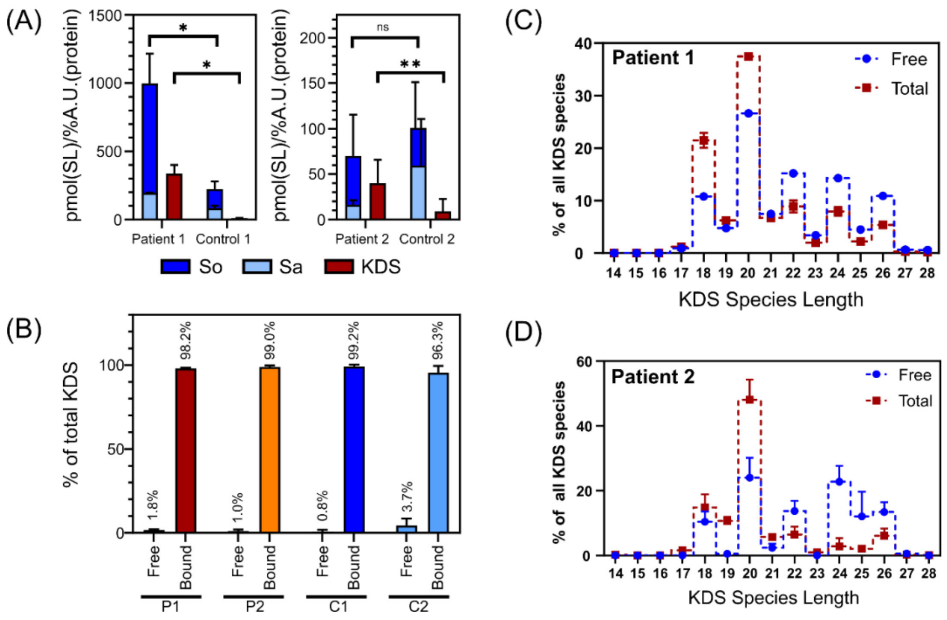

Figure 36 Increased KDS after total hydrolysis of sphingolipids.

Analysis of free and bound sphingoid bases in palmar stratum corneum. (A) Amount of total 3-hydroxyl bases (stacked, blue) and 3-keto bases (red) in patients and control groups after acid hydrolysis. Student's t-test (* $p<0.05$; **$p<0.01$) (Graph shows mean+SD, n=2 (P1 and C1) and n=7 (P2 and C2). (B) Ratio of free and bound KDS base. Bound KDS was determined as the difference between the

amount of free and total KDS (Graph shows mean+SD). (C+D) Profile of KDS species in patient 1 and patient 2, respectively, before and after total hydrolysis indicating an increase in LC-KDS species C18 and C20 (Graph shows mean+SD). Figure modified from (293) License number for republication: #5323550916865.

Identification of 3-ketodihydroceramide in patient stratum corneum

Reports in literature suggest that ceramide synthases could be able to utilize KDS as a substrate in *in vitro* experiments (296). Though not described under physiological conditions *in vivo*, the formation of these products may be possible under pathological conditions. I used the previously described method and the specific McLafferty fragment (Figure 34A) to investigate the presence of possible 3-ketodihydroceramides (NdK-ceramides) in the patients' stratum corneum.

To cover a broad range of NdK-ceramide species, I decided to focus on combinations with an even-numbered KDS backbone (ranging from C18 to C28) and even-numbered N-linked fatty acyl residue (ranging from C16 to C26). I found several prominent signals in patient samples, that were not present in control samples and that matched the retention time of the synthetic standards indicating the presence of 3-ketodihydroceramide primarily in patient samples (Figure 37A-C). Exemplarily, chromatograms for NdK-ceramides with C18-KDS sphingoid base and varying N-linked fatty acyl length (C16 – C26) (Figure 37A), and chromatograms with C24-N-fatty acyl and varying KDS base length (C18 – C28) (Figure 37B) are displayed for the analysis of palmar stratum corneum samples. The fragment ratios of the observed compounds fitted the ratios observed with synthetic standards confirming these compounds are 3-ketodihydroceramides (Figure 38A-B). In all cases the specific McLafferty fragment was present and used for the quantification of 3-ketodihydroceramides.

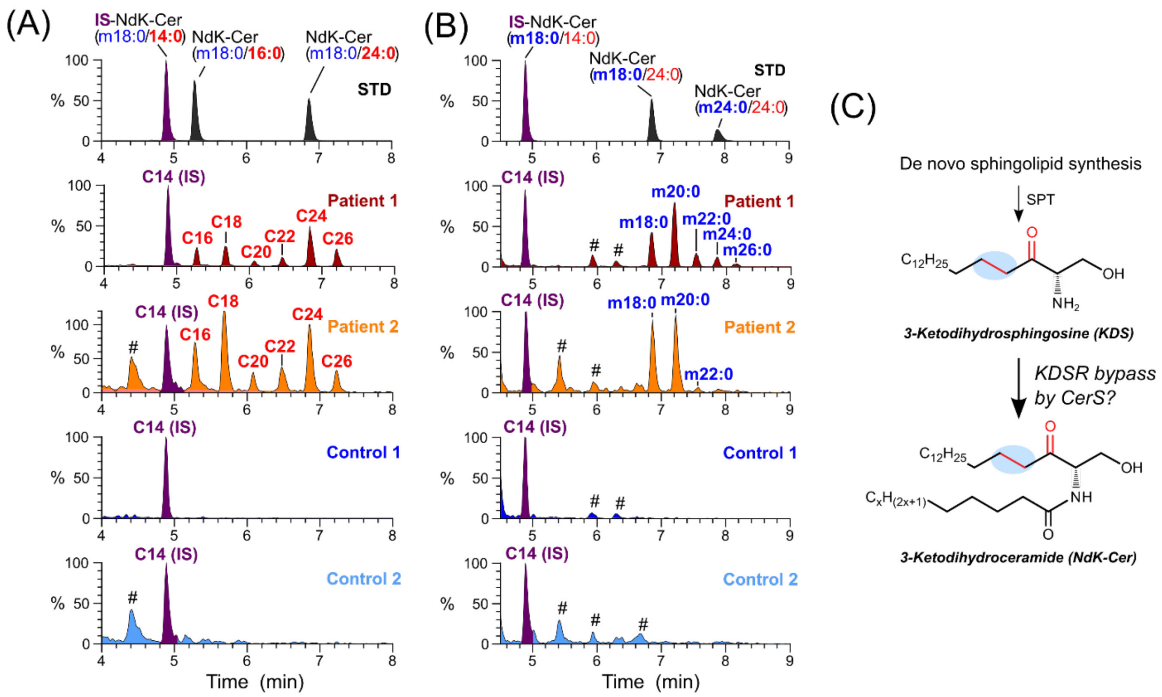

Figure 37 3-ketodihydroceramides in stratum corneum of KDSR patients.

LC-MS/MS analysis of NdK-ceramides reveals multiple distinct signals with the characteristic McLafferty fragment. Lipids from tape stripped stratum corneum discs were extracted and NdK-ceramides were analysed by LC-MS/MS using reversed phase chromatography and the characteristic transition of $[M+H]^+$ > McL (McLafferty fragment) (Figure 34A). (A) Chromatograms show NdK-ceramides with C18-KDS base **(blue)** and varying lengths of N-acyl residue **(red)** for synthesized standards of KSDR patients and samples from healthy controls. (B) Chromatograms show NdK-ceramide analysis with varying KDS base length (blue) and constant N-lignoceryl residue of synthesized standards of KDSR patients and healthy controls. Signal intensities are normalized to the base peak. NdK-Cer(m18:0/14:0) (C14 (IS)) was added as an internal standard (purple). # indicates non-specific signals. (C) Structure of NdK-ceramide and hypothetical pathway for the generation of NdK-ceramides by N-acylation of KDS. Figure modified from (293) License number for republication: #5323550916865.

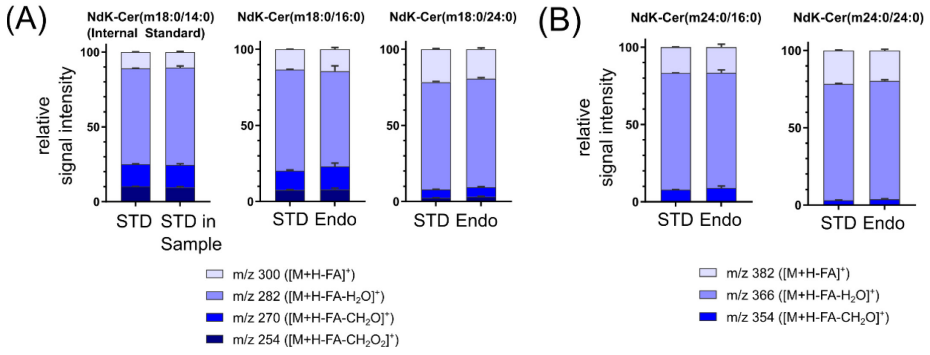

Figure 38 Fragmentation pattern of endogenous NdK-ceramides.

NdK-ceramides produce a specific fragmentation pattern. The transition of the molecular ion $[M+H]^+$ to the fragment ions $[M+H-FA]^+/[M+H-FA-H_2O]^+/[M+H+FA-CH_2O]^+/[M+H-FA-CH_2O_2]^+$ was used in multiple

reaction monitoring mode (MRM) to determine a fragmentation profile at a constant collision energy of 35 eV of each the observed peaks in biological samples (Endo) and compare it to synthetic standards (STD). The graph indicates the relative signal intensities for each transition of the respective peak or compound for NdK-ceramides with a **(A)** C18-KDS base or a **(B)** C24-KDS base. The transition to $[M+H\text{-}FA\text{-}CH_2O_2]^+$is not depicted for C24-KDS-containing NdK-ceramides due to the overlap with the transition to $[M+H\text{-}FA\text{-}H_2O]^+$ in C22-KDS-containing NdK-ceramides (Δ28u). Figure modified from (293). License number for republication: #5323550916865.

Absolute and relative quantification in stratum corneum

To get a quantitative estimate of the relative NdK ceramide content of selected marker species (lignoceric (C24:0) and cerotic acid (C26:0)-containing ceramides covering the even-chained sphingoid base length range from C18 to C28) was evaluated in comparison to non-hydroxylated ceramides with variable sphingoid base structures (NX-type ceramides) of the same species composition. The investigated NX-type ceramides included NS-ceramides (sphingosine backbone), NdS-ceramides (sphinganine backbone), NP-ceramides (phytosphingosine backbone) and NH-ceramide (6-hydroxysphingosine backbone).

With 6.9% and 9.1% respectively, NdK-ceramides were found to make up a considerable fraction of the measured NX-type ceramide species in lesional palmar stratum corneum of both patients (Figure 39A *left*). Interestingly, NdK-ceramides were not only identified in lesional palmar stratum corneum, but also in non-lesional volar forearm stratum corneum. In non-lesional volar forearm stratum corneum the relative amount of NdK-ceramide species was similar for patient 1 (11.7%), but lower for patient 2 (1.6%) (Figure 39B *left*). These differences may be related to the state of the skin at this time. The absence of visible lesions may not exclude underlying pathological changes. In lesional palmar stratum corneum of both patients, as well as (apparently) non-lesional volar forearm of patient 1, I observed a relative reduction of NP-ceramides and an increase in NS-ceramides, indicative of pathological changes in skin properties. Similar effects were observed in lesional stratum corneum of atopic dermatitis and psoriasis vulgaris patients ((297) and this study section 5.1.4). The [NP]/[NS] ratio (298) was found to be a marker for transepidermal water loss (TEWL) and was correlated with keratinocyte differentiation (298). A binary distinction between lesional and non-lesional areas may not suffice to cover a continuous spectrum of pathological changes in the patients.

In addition to relative changes in NX-ceramide ratios, I observed a marked reduction in total NX-ceramides of patient 2 in palmar stratum corneum, that was not observed to the same degree in volar forearm or in patient 1 (Figure 39A-B *right*).

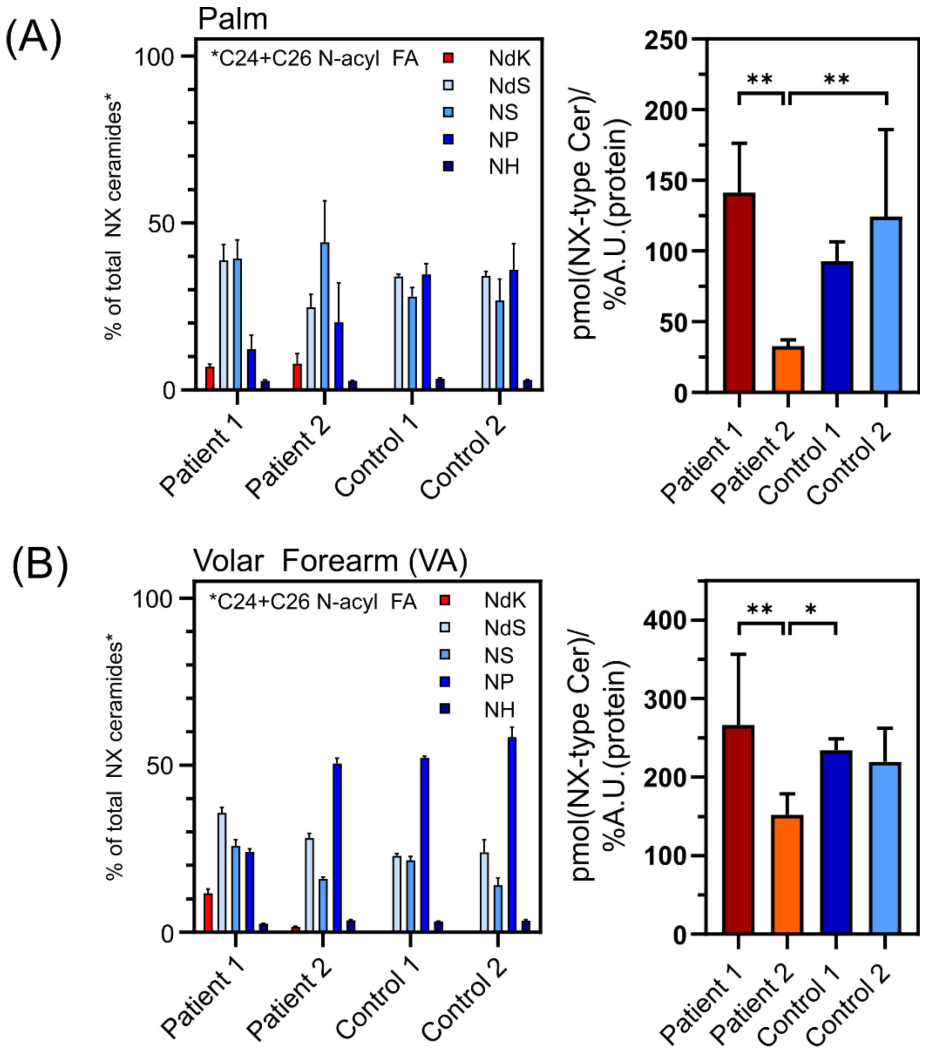

Figure 39 NX-type ceramides in stratum corneum of KDSR patients.

NdK- and NX-type ceramides (including NS (sphingosine base), NdS (sphinganine base), NH (6OH-sphingosine base), NP (phytosphingosine base) ceramides) were quantified and the sum of all measured species was determined in (A) palm and (B) volar forearm of KDSR patients and healthy controls. For quantification a set of marker species with varying even-chained sphingoid bases (C18 – C28) and N-lignoceric acid (C24) or N-cerotic acid (C26) residues. *Left* panels depict the relative amount of respective ceramide classes and *right* panels the absolute level of all measured NX-type ceramides. Statistical testing was done by ordinary one-way ANOVA with Tukey correction for multiple comparisons (** $p<0.01$; * $p<0.05$). Graphs show mean + standard deviation. Figure partially taken from (293). License number for republication: #5323550916865.

The total NdK-ceramide amount in stratum corneum was estimated by summing up NdK-ceramide species with even-chained sphingoid bases (C18 – C28) and even-chained N-acyl residues (C16 – C26). Due to the limited availability of sample material, the complete indicated range of NdK-ceramide species could not be investigated for patient 2 and few species (with expected minor amounts) are missing in the evaluation, possibly underestimating the amount of NdK-ceramide *(for comparison check Figure 54)*. Significant amounts of NdK-ceramide were observed in palmar stratum corneum of KDSR patients (Figure 40 *left*) and even higher amounts in volar forearm of patient 1 (Figure 40 *right*). The reason for this could be an underlying and unknown pathology or differences in the biological effects due to lipid species composition *(for comparison check Figure 54)*. It is also possible that differences in the total amount of lipids between volar forearm and palmar stratum corneum contribute to a higher tolerance towards the presence of NdK-ceramides, although compared to NX-type ceramides the relative levels appear to be higher in volar forearm. The low amounts of 3-ketodihydroceramides found in control samples can be attributed to the presence of minor amounts of the NdK-Cer(m24:0/24:0) species.

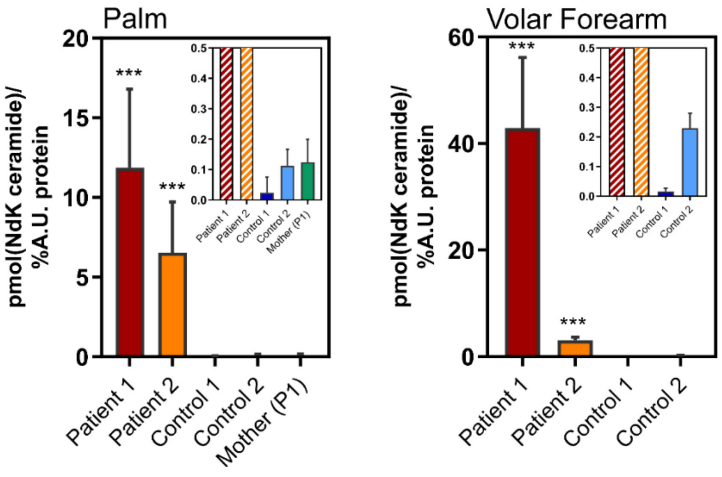

Figure 40 Quantification of NdK-ceramide in KDSR patient stratum corneum.

The level of NdK-ceramides in palmar (P1: n=2; P2: n=6; control group C1: n=6; control group C2: n=6) and volar forearm (P1: n=4; P2: n=6, control group C1: n=4; control group C2: n=6) stratum corneum of KDSR patients was determined as sum of all even-chained NdK-ceramide species with C18-C28 KDS base and C16-C18 N-acyl residue. Due to limited sample amount not all species of NdK-ceramides could be measured for P2 and C2 and (expected) minor species (Figure 54) are missing, possibly underestimating NdK-ceramide amount in these samples. Statistical testing comparing KDSR patients and the respective controls was done using a two-tailed Student's t-test (*** $p<0.001$). Graphs show mean + standard deviation.

KDS and NdK ceramides in epidermis and dermis

For the further assessment of NdK-ceramide occurrence in different tissues and body fluids I obtained skin punch biopsies and blood samples of the palm (patient 1) or sole (patient 2). Due to the invasive nature of the procedure and to minimize the impact on the patients, only one sample per patient was obtained. The skin punch biopsies were enzymatically digested using dispase, which allows a separation of dermis and epidermis. Skin biopsies of KDSR patients were characterized by a thickened epidermal layer compared to control samples. Separated tissue sample fractions were lyophilized and subjected to lipid extraction for a quantification of NdK-ceramide content. While stratum corneum sample indicate changes in the upper layer of the skin and could be considered an indirect measurement of changes in sphingolipid metabolism in stratum basale and stratum granulosum, epidermal and dermal biopsies provide insights into sphingolipid metabolism at the place of biosynthesis.

Quite strikingly, no NdK-ceramides were observed in the dermis fraction of the skin of both patients, while I observed a high abundance in epidermis samples (Figure 41A). This indicates a close association of NdK-ceramides with the pathological changes in the patients' epidermis and a possible connection of NdK-ceramide formation to the skin- and keratinocyte-specific sphingolipid metabolism.

Similar to stratum corneum samples, free KDS was higher in epidermis, but also dermis, of KDSR patients (Figure 41C-D). In contrast, I observed high levels of free sphinganine in control epidermis samples that appear to be completely diminished in both KDSR patients, while only minor changes in free sphingosine were observed (Figure 41C). This effect was not observed in dermis samples (Figure 41D). The reduction of free sphinganine in epidermis could indicate a lack of KDSR activity especially under high demand conditions as observed during production of skin barrier lipids, while the presence of low levels of KDS does not contribute to apparent pathological changes. This is in line with the observation of increased free KDS in whole blood samples of both patients compared to a control sample (Figure 41). I was not able to identify NdK-ceramides in whole blood samples of the patients.

In comparison to other NX-type ceramides in epidermis, NdK-ceramides made up approximately 20% and 28% of these lipids in patient 1 and patient 2, respectively (Figure 42A). I was able to confirm the decrease in NP-ceramides and increase in NS-ceramides that I observed in stratum corneum also in total epidermis, pointing to a possible defect in keratinocyte differentiation (298). The level of NX-type ceramides (including NdK-ceramide) in relation to dry weight was strongly reduced for both patients in epidermis (Figure 42A *right*) and slightly reduced in dermis (Figure 42B *right*). Given the high increment in NX-type ceramide levels between epidermis and dermis (appr. 15000 pmol NX-Cer/mg dry weight in epidermis versus 225 pmol NX-Cer/mg dry weight dermis) an incomplete separation of both skin layers and minor contamination of dermis samples with epidermis could have an impact on lipid levels in dermis, and cannot be fully excluded, especially in control sample with a comparatively thin epidermal layer. This may contribute to the difference observed in dermal lipid levels.

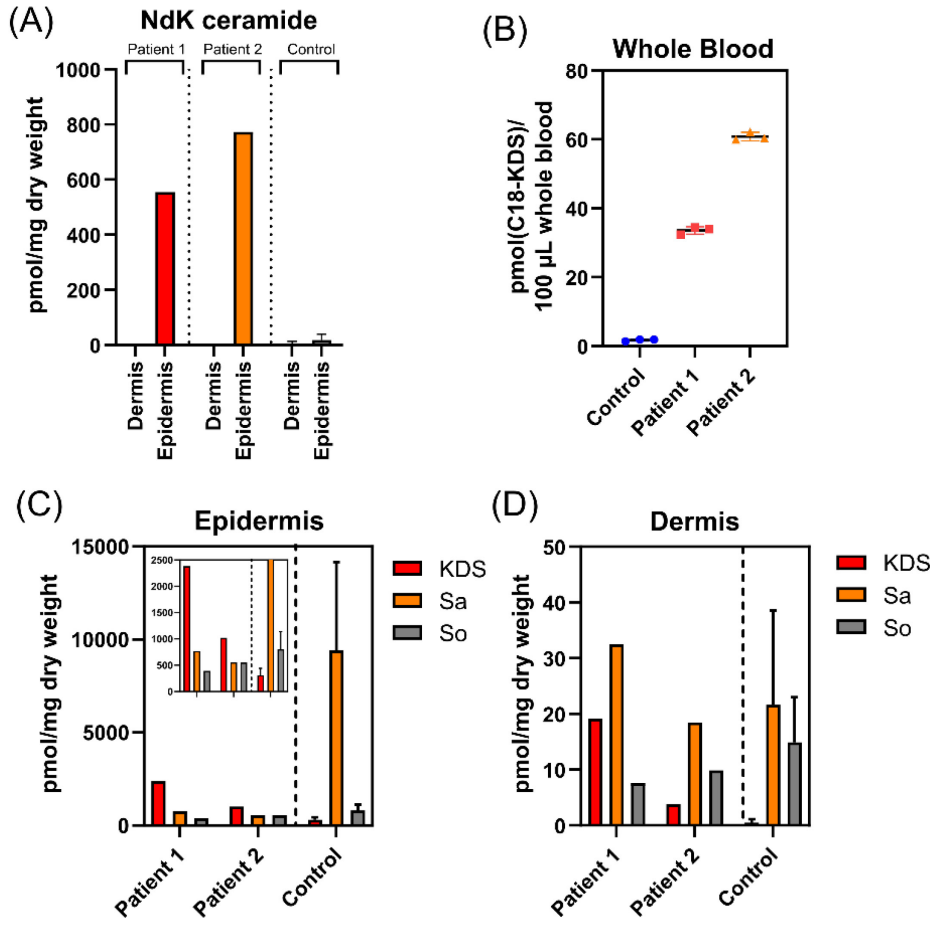

Figure 41 Sphingoid base and NdK-ceramide analysis of biopsy samples.

Skin punch biopsies and whole blood samples of KDSR patients were obtained. Skin punch biopsies from the palm (patient 1, n=1) or the sole (patient 2, n=1) were enzymatically digested with dispase and separated into an epidermal and dermal fraction. The tissue samples were lyophilized, the dry weight was determined, and lipids were extracted. (A) NdK-ceramides were measured and quantified by LC-MS/MS and compared to lipid extracts from healthy control samples (male, 84y, right ventral thigh; female, 70y, forehead; female, 62y, shank; n=1 respectively). (B) Free sphingoid bases from whole blood samples were extracted, the amount of free KDS analysed by LC-MS/MS and compared to a control sample (male, 51y) (n=3, technical replicates). (C) Free sphingoid bases in complete epidermis of KDSR patients were analysed by LC-MS/MS and compared to control samples. Lipid species of one class were summed to estimate the total amount per class. (D) Free sphingoid bases in dermis of KDSR patients were analysed and compared to control samples. Graphs show mean + standard deviation. Figure partially taken from (293). License number for republication: #5323550916865.

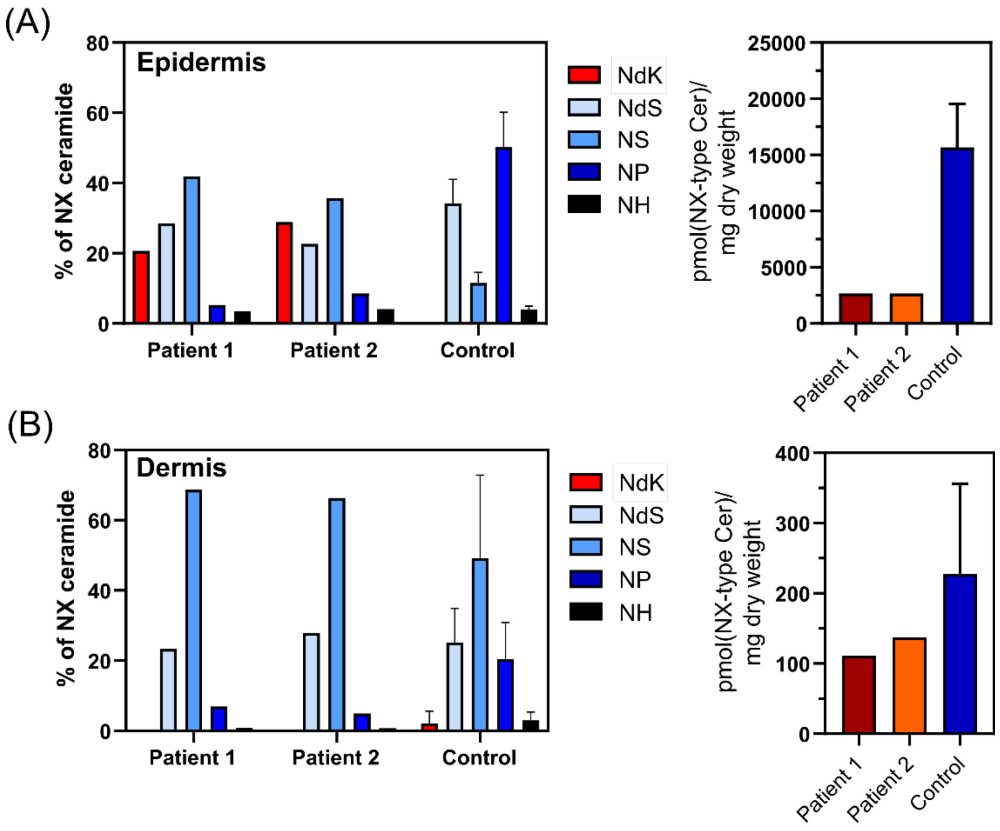

Figure 42 Analysis of NdK- and NX-type ceramides in dermis and epidermis.

NX-type ceramides (including NS (sphingosine), NdS (sphinganine), NH (6OH-sphingosine), NP (phytosphingosine)) were quantified and the relative amount of each NX-ceramide class is depicted in the left panel for (A) epidermis or (B) dermis samples from KDSR patients (n=1) or controls (male, 84y, right ventral thigh; female, 70y, forehead; female, 62y, shank; n=1 respectively). Right panels show the sum of NX-type ceramides measured in the respective fractions. Graphs show mean + standard deviation.

5.1.3 No derivatives of NdK-ceramide in patient skin

3-ketoceramides

The discovered 3-ketodihydroceramides (NdK-ceramides) may be substrates for further enzymatic metabolization. A dihydroceramide desaturase like DES1 or DES2 may be able to introduce a 4,5-*trans*-double bond into the molecule to yield 3-ketoceramides (NK-ceramides).

To check this hypothesis a nervonic acid containing synthetic ceramide standard (Cer(d18:1/24:1)) was oxidized with 2,3-dichlor-5,6-dicyano-1,4-benzoquinone (DDQ) to convert the 3-hydroxyl group into a 3-keto group (299). Furthermore, a non-enzymatic rearrangement for 3-ketoceramides by Michael addition under mild alkaline conditions was reported (300). To be able to evaluate the presence of rearranged NK-ceramides in patient samples, cyclization of NK-ceramide standard was induced by treating the oxidized compounds with 0.1M sodium hydroxide (NaOH). The respective 3-keto-derivatives were prepared by Adam Majcher (ERASMUS student) under my supervision.

NK-ceramides eluted later than NS-ceramides (+0.07 min). Too peaks with m/z 646.5 were observed in single reaction monitoring (SRM) mode (Figure 43A). While the first peak fits to the expected mass of C24:1-NK-ceramide, the second peak seems to be derived from in-source decay of a compound with a molecular ion at m/z 716.5 (+70 u) (Figure 43B). The in-source decay to m/z 646.5 and identical product ion spectra indicate the formation of an unknown side product (likely a C24:1-NK-ceramide conjugate). For the product of the cyclization reaction (cNK-ceramide) I observed an increased retention time compared to NS-ceramides (+0.34 min) (Figure 43A *top*).

Although, minuscule amounts of the fragment m/z 268.2 were observed, 3-ketoceramides do not perform an abundant McLafferty type rearrangement, possibly due to the conjugation of the π-electrons between the 3-keto group and the 4,5-trans-double bond. I expected increased in-source elimination of the 1-hydroxyl group as water driven by the possible extension of the π-electron system, but the observed in-source water loss was weaker compared to NS-ceramides (Figure 43B). NK-ceramides produce an intense fragment at m/z 280.1 ($[M+H-FA]^+$) and a less intense fragment at m/z 298.2 ($[M+H-(FA-H_2O)]^+$). These

fragments were used for a screening of NK-ceramides in epidermis of patient 1, but no NK-ceramide could be detected in stratum corneum or biopsy samples (Figure 44A). In addition, cyclized NK-ceramide generated a characteristic fragment involving the N-acyl residue at m/z 434.2. I did not observe signals for cyclic NK-ceramides that were distinguishable from noise in stratum corneum of patient 1 (Figure 44B).

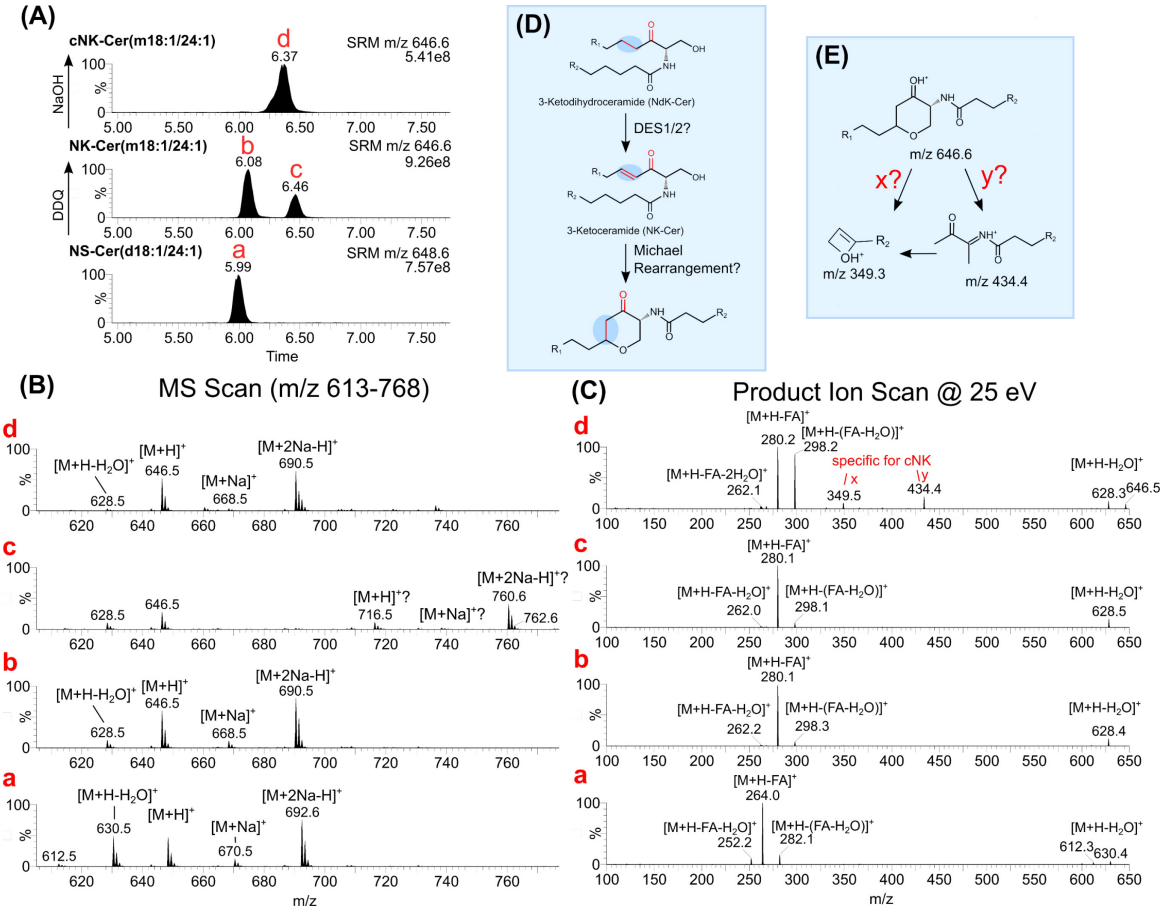

Figure 43 Characterization of (cyclic) 3-ketoceramide.

NS-ceramide(d18:1/24:1) was oxidized and treated with sodium hydroxide (NaOH) to yield 3-ketoceramide(m18:1/24:1) and a possible cyclic Michael-type rearrangement product (cNK-Cer(m18:1/24:1)). (A) Chromatograms show single reaction monitoring for NS-, NK- and cNK-ceramide at m/z 648.6 (NS-Cer) and m/z 646.6 (NK- and cNK-Cer). (B) Full MS scan (m/z 613 – 768) of eluting compounds. Predicted molecular ions are annotated for the observed peaks. Letter codes refer to chromatograms from (A). (C) Product ion scan of compounds a – d performed at 25 eV collision energy. (D) Chemical structure and hypothetical route for biosynthesis of NK- and cNK-ceramides. (E) Hypothetical fragmentation mechanism for the generation of fragments x and y (see product ion spectra) in cNK-ceramides. Data produced jointly with Adam Majcher.

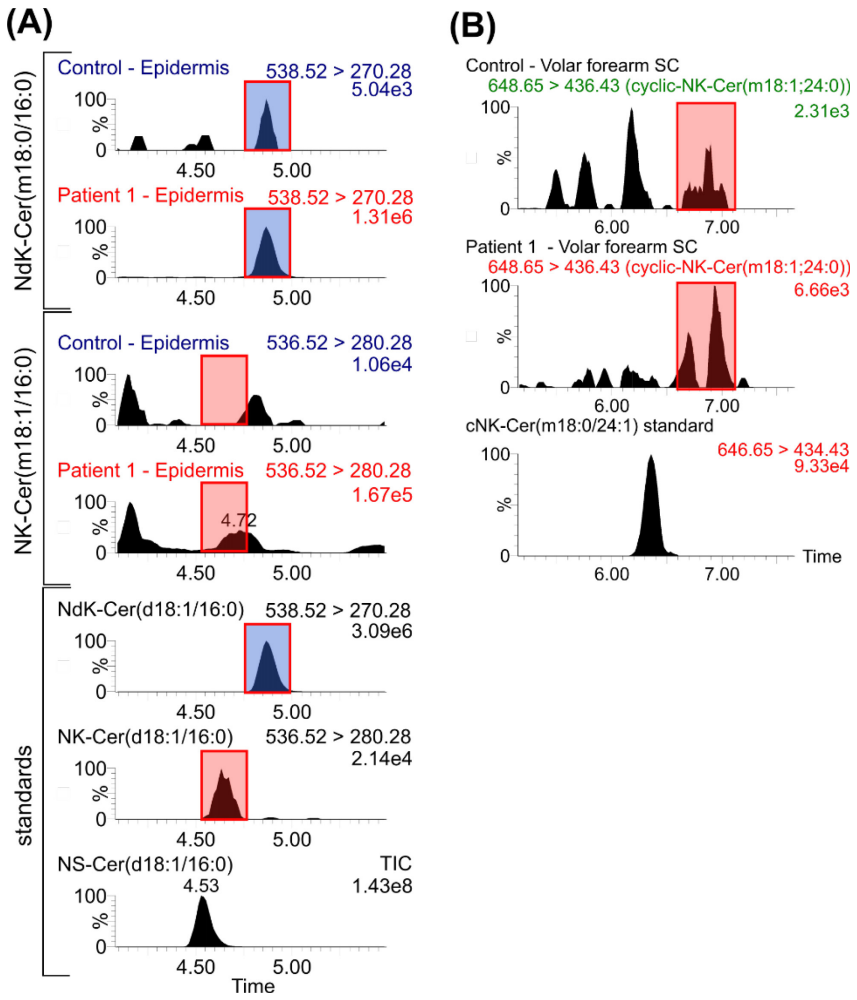

Figure 44 Analysis of 3-ketoceramide and cyclic 3-ketoceramide.

NdK-ceramide, NK-ceramide and cyclic NK ceramide were determined in epidermal biopsies and stratum corneum samples of KDSR patients. (A) Chromatograms show transitions for C16-NS-, NK- and NdK-ceramide species in synthetic standards and epidermal lipid extracts from patient 1 and control. Coloured boxes indicate the expected retention time of the respective lipid species (red – NK-Cer; blue – NdK-Cer). (B) Chromatograms show transitions for C24-cNK-ceramide in volar forearm stratum corneum lipid extracts of patient 1 and control. Red boxes indicate expected retention time in biological samples.

Analysis method for 3-keto-sphingomyelin derivatives

For the transfer into lamellar bodies and the incorporation into lipid lamellae of the skin barrier, the derivatization of ceramides to glucosylceramide or sphingomyelin is considered a requirement (301). To investigate the formation of 3-keto-sphingomyelin and 3-keto-glucosylceramide derivatives the respective standards were prepared by oxidation of the 3-hydroxyl group to a 3-keto group with DDQ (302) and subsequent reduction of the 4,5-trans-double bond with hydrogen and palladium on charcoal (Pd/C) as a catalyst.

An isolated mixture of sphingomyelins from porcine brain with varying N-acyl chains and a d18:1-sphingosine was used to generate either keto-dihydrosphingomyelin or keto-sphingomyelin as shown in Figure 32. This mixture resembles the sphingomyelin profile of brain extracts with a C18-sphingosine backbone conjugated to stearic acid (C18:0), but also other fatty acyl residues in lower concentrations (Figure 45A). The consecutive oxidation/reduction procedure allows the generation of a broad spectrum of 3-ketodihydrosphingomyelin and 3-ketosphingomyelin species.

I characterized these standards to establish an LC-MS/MS method for an analysis of KDSR patient samples. An evaluation of the retention time using the previously established reversed phase-chromatography method demonstrated a small difference (0.05 min) between isobaric NS- and NdK-sphingomyelin species. The 4,5-unsaturated 3-ketosphingomyelin eluted appr. 0.14 min earlier than the NS-sphingomyelin equivalent (Figure 45A-B). In addition, the fragmentation of sphingomyelin results in an energetically highly preferred, charged phosphocholine ion (m/z 184) that is insufficient for a distinction between NS- and NdK sphingomyelin. Fragmentation of the $[M+H]^+$ molecular ion of NdK-Cer(m36:1) and NK(m36:0) using standard conditions did not reveal further fragments suitable for a differentiation from NS-Cer(d36:1) (Figure 45C).

It was demonstrated before that the formation of the phosphocholine fragment (m/z 184) can be suppressed by promoting the formation of the lithium adduct $[M+Li]^+$, which provides structural information about the lipid moiety of sphingomyelin (303). In this mechanism the 3-hydroxyl group is required to stabilize the resulting fragments. I found, that in presence of a 3-keto group an intense fragment with m/z

190 is generated for 3-keto-containing sphingomyelins, but not for 3-hydroxy-sphingomyelins (Figure 45D). These fragments allow to distinguish isobaric NS- and NdK-sphingomyelin species. The fragment likely resembles the lithiated phosphocholine fragment, which is formed in absence of a 3-hydroxyl group. For analytical purposes this behaviour was exploited by post-column injection of lithium acetate into the chromatographic flow and subsequent fragmentation of lithium adducts.

Interestingly, the effect on retention time of the 3-keto group appears to be reversed for sphingomyelin compared to ceramides. While 3-ketodihydroceramides (NdK-Cer) elute after the equivalent dihydroceramide (NdS-Cer), 3-ketodihydrosphingomyelin (NdK-SM) elute slightly earlier than equivalent dihydrosphingomyelin (NdS-SM). With the 1-OH modification being the only difference between the molecules, this points to a difference in interaction between the phosphocholine group and the 3-keto group compared to the 3-hydroxy group that could affect hydrophobic interactions in reversed phase chromatography. It could be speculated that the 3-hydroxy group forms a intramolecular H-bond with the phosphate moiety, which is not possible with the 3-keto group.

I used palmar stratum corneum of patient 1 to screen for keto-type sphingomyelin (NdK-SM and NK-SM) with the described method. The applicability of this method for biological samples was tested by spiking control extracts with synthetic NdK-sphingomyelin. These analyses did not reveal signals that were indicative of the presence of these compounds in stratum corneum (Figure 46A). For the formation of lipid lamellae most sphingomyelin in the stratum corneum is hydrolysed to yield ceramides. The lack of an apparent accumulation of NdK- or NK-sphingomyelin could also indicate a possible degradation of these compounds in stratum corneum.

To further elucidate this, I analysed epidermal and dermal biopsies of both patients. I did not observe marked signals for the presence of NdK-sphingomyelin of NK-sphingomyelin in epidermis (Figure 46B) or dermis (Figure 46C). This indicates, that 3-ketodihydroceramides are not converted to 3-ketodihydrosphingomyelin or 3-ketosphingomyelin in a significant manner.

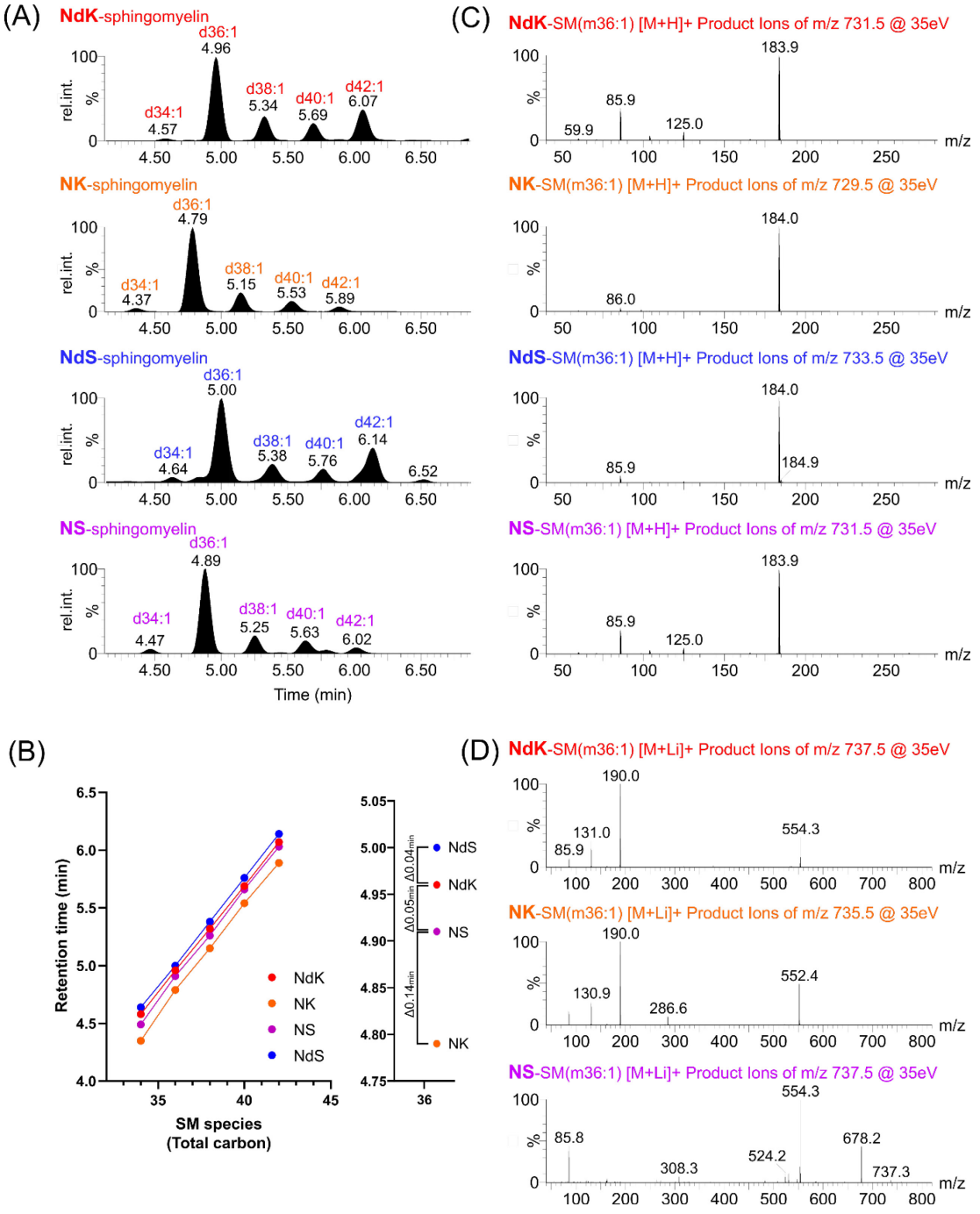

Figure 45 LC-MS/MS characterization of keto-type sphingomyelin.

Oxidation (DDQ) and reduction (H_2 on Pd/C) of a porcine brain sphingomyelin mix yielded NdK- and NK-sphingomyelin, which were characterized using LC-MS/MS. (A) Retention time of NS-, NdS-, NK-, and NdK-sphingomyelins on a reversed phase C18 CSH column. Sum chromatograms are generated by combination of multiple MRM transitions for each lipid class (B) Correlation of the retention time with number of carbon atoms of the respective species (*left* panel) and indication of the retention time differences for species with 36 carbon atoms (*right* panel). (C) Product ion spectra for the $[M+H]^+$ molecular ion of SM-derivatives with 36 carbons recorded at 35 eV collision energy. (D) Product ion spectra recorded for $[M+Li]^+$ molecular ions of SM-derivatives at 35 eV collision energy and with infusion of lithium acetate into the LC flow. Data produced jointly with Adam Majcher.

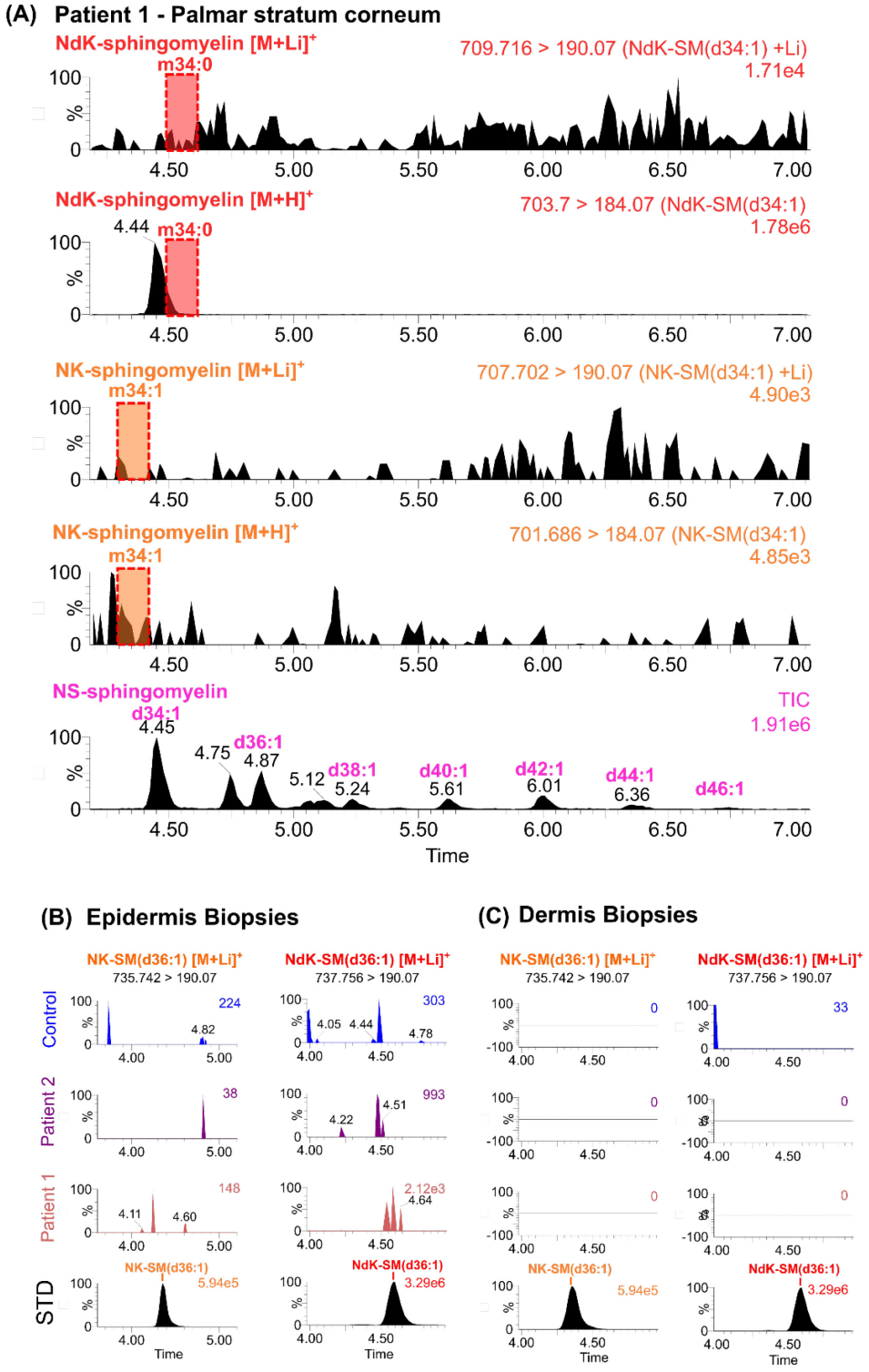

Figure 46 Analysis of keto-type sphingomyelin in patient samples.

Lipid extracts from palmar stratum corneum of patient 1 and skin biopsy material from patient 1 and patient 2 were subjected to keto-type sphingomyelin analysis. (A) Chromatograms show total ion current (TIC) for NS-sphingomyelin and analytical transitions for $[M+H]^+$ and $[M+Li]^+$ of NK- and NdK-sphingomyelin(d34:x) in the patient sample. The expected elution time is highlighted for NK-SM(d34:1) *(orange)* and NdK-SM(d34:0) *(red)*. (B) Epidermal and (C) dermal lipid extracts were analysed regarding the presence of NK- and NdK-SM. Exemplarily the transitions for $[M+Li]^+$ to m/z 190.07 of N(d)K-SM(d36:x) are shown. Chromatograms of synthetic standards indicate the expected elution time.

Analysis of 3-keto-glucosylceramides

Alternatively, to keto-type sphingomyelin, NdK-ceramide could be metabolized to the respective glucosylated form (Figure 32). 3-ketodihydroglucosylceramide (NdK-GlcCer) and 3-ketoglucosylceramide (NK-GlcCer) were prepared from synthetic GlcCer(d18:1/24:1) by oxidation with DDQ and reduction with H_2 and Pd/C.

The observed retention times of the synthesized standards are documented in Figure 47 (*left*). NdK-GlcCer produced analogous to NdK-ceramides a characteristic McLafferty fragment (m/z 270), which I used for screening of these compounds in patient samples. I did not observe the formation of a McLafferty-type fragment in NK-GlcCer (m/z 268). The main fragment observed in NK-GlcCer for the C18-sphingoid base was at m/z 280 ($[M+H-FA-(Glc-H_2O)]^+$) (Figure 47) analogous to what I observed for NK-ceramides (Figure 43).

Screening of palmar stratum corneum of patient 1 and epidermal biopsies of both KDSR patients did not reveal significant signals indicative for NdK-GlcCer or NK-GlcCer (Figure 48A-D). From these data I conclude that neither N(d)K-GlcCer nor N(d)K-SM do accumulate in the patients' skin in detectable amounts.

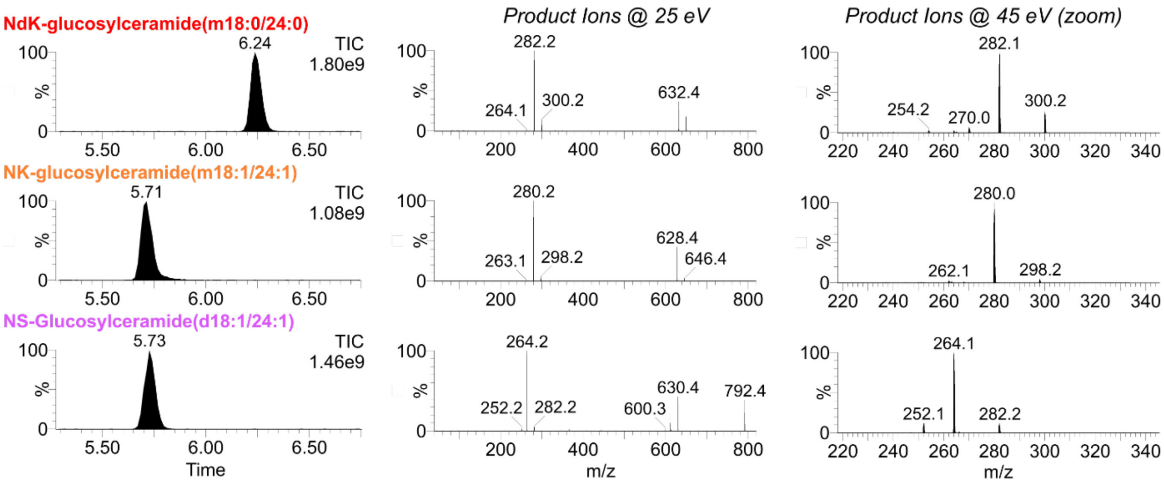

Figure 47 Characterization of keto-type glucosylceramides.

Characterization of 3-ketodihydroglucosylceramide (NdK-GlcCer) and 3-ketoglucosylceramide (NK-GlcCer) by LC-MS/MS. (A) Retention time of synthetic NS-GlcCer(d18:1/24:1), NK-GlcCer(m18:1/24:1) and NdK-GlcCer(m18:0/24:0). (B+C) Product ion scan of the respective $[M+H]^+$ molecular ions at (B) 25 eV and (C) 45 eV collision energy. Data produced jointly with Adam Majcher.

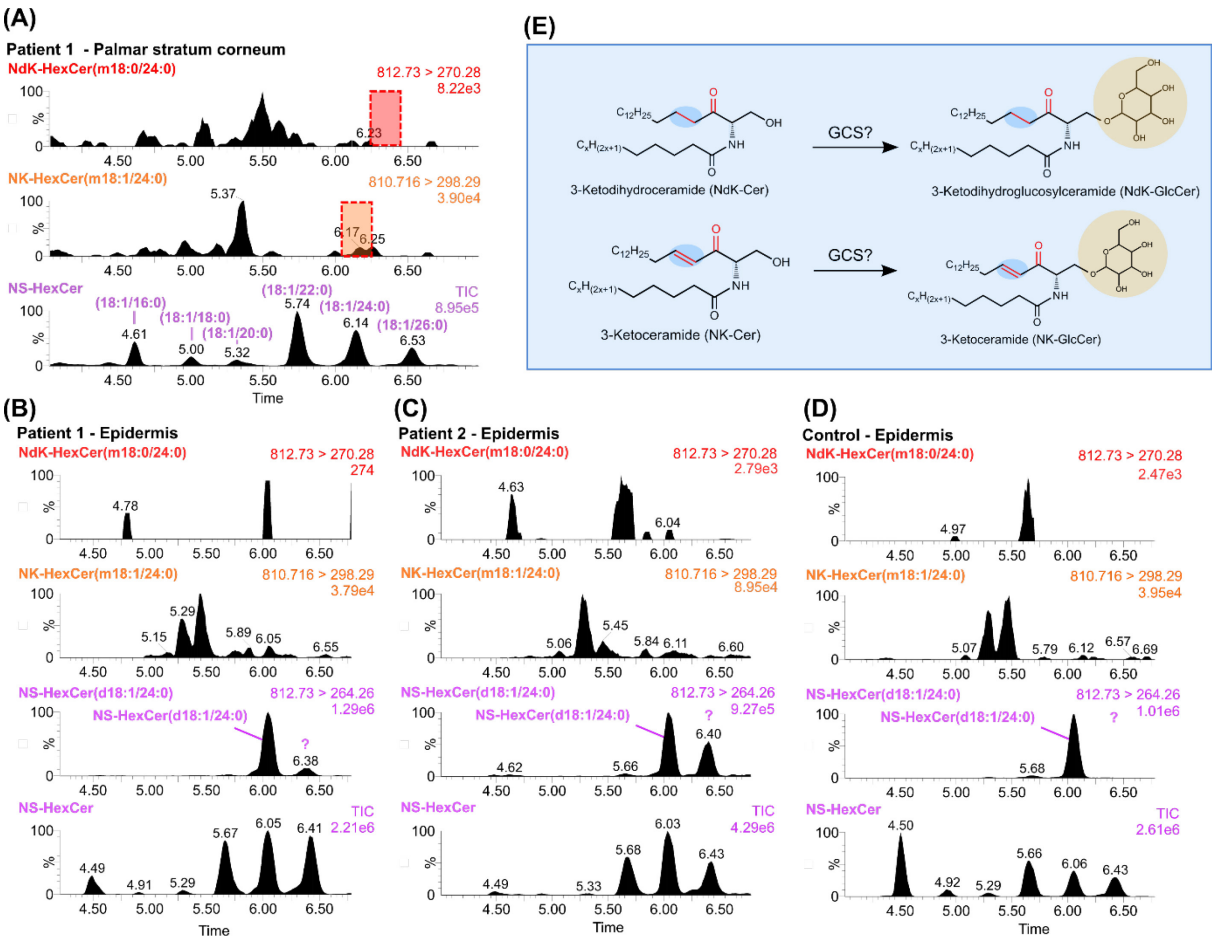

Figure 48 Keto-type GlcCer in stratum corneum and skin biopsies.

Stratum corneum of patient 1 and epidermis biopsies of both KDSR patients and a control were analysed for the presence of 3-ketodihydroglucosylceramide (NdK-GlcCer) and 3-ketoglucosylceramide (NK-GlcCer). (A) Lipid extracts from palmar stratum corneum of patient 1. Chromatograms show the respective transitions for the detection of NS- (total ion current), NK- and NdK-GlcCer(m18:0/24:0). Intensities are normalized to the base peak and intensity values are indicated in the upper right corner. Red and orange box indicate expected retention time for NdK- and NK-GlcCer species, respectively (B-D) Chromatograms for transitions of NS- (total ion current), NK-, and NdK-GlcCer(m18:0/24:0) in epidermal lipid extracts of (B) patient 1 (C) patient 2 and (D) control. (E) Chemical structure and hypothetical enzymatic reaction for the generation of NK- and NdK-GlcCer species.

5.1.4 Reduced sphingolipid length in KDSR, AD and Pso

Shorter sphingoid bases in KDSR patients

Lipid length is an important factor for the function of lipid lamellae (304). As mentioned before (section 5.1.2), I observed species of varying length of free sphingoid bases.

Strikingly, in patient samples from palm, apart from the general increase in free KDS, a relative increase in free LC-KDS (C18 and C20) compared to free VLC-KDS (C22 - C28) was noticed. In both patients the average chain length was significantly reduced not only for KDS (by up to 2.5 carbon atoms), but also for sphinganine (by up to 3 carbon atoms) and sphingosine (by up to 1.8 carbon atoms) (Figure 49A-B). In volar forearm samples these differences are smaller. Free KDS length was significantly reduced only in patient 1 (0.3 carbon atoms) (Figure 50A-B).

For sphinganine and sphingosine the reduction in length I observed in patient 1 was bigger compared to patient 2 (1 carbon atom vs 0.2 carbon atoms (Sa) and 3 carbon atoms vs 1 carbon atom (So)) (Figure 49C-F, Figure 50C-F). These stronger effects in patient 1 could further point to an unnoticed underlying pathology or a differentiation defect and are in line with the observed higher amount of NdK-ceramides in volar forearm of patient 1 (Figure 40).

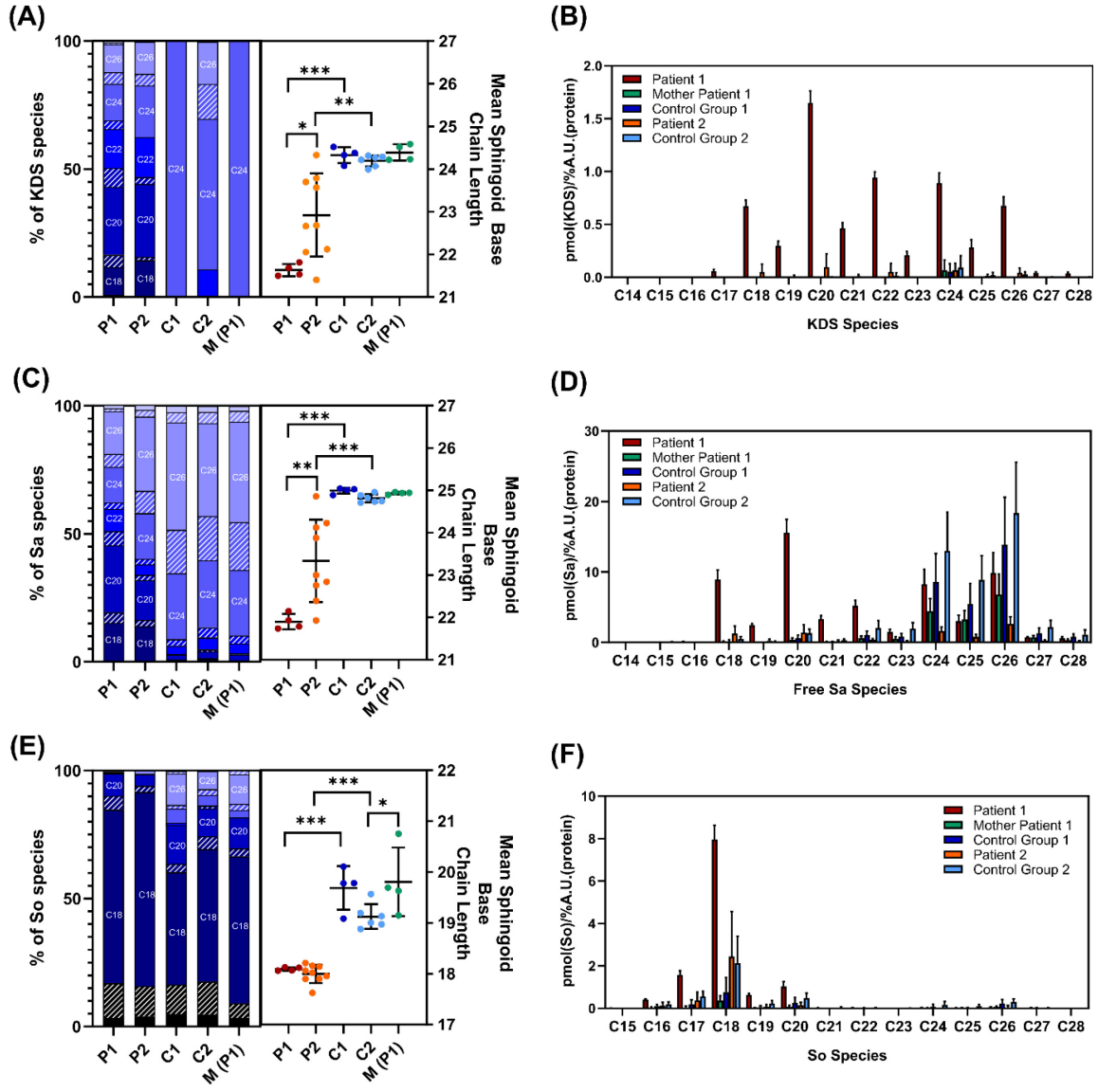

Figure 49 Sphingoid base length analysis in palmar stratum corneum.

Overview of measured KDS species as determined in palmar stratum corneum tape stripping lipid extracts. The relative amount of each species and the average length for (A) KDS, (C) sphinganine and (E) sphingosine are depicted in the left or right panel, respectively, for patient 1 (n=4), patient 2 (n=9), control group 1 (male, 3y, n=4; female, 3y, n=4), control group 2 (male, 51y, n=3; female, 37y, n=3) and the mother of patient 1 (31y, n=4, monoallelic c.879G>A). The absolute levels of single lipid species are plotted for (B) KDS, (D) sphinganine and (F) sphingosine. Statistical testing was done by ordinary one-way ANOVA with Tukey correction for multiple comparisons (*** p<0.001; ** p<0.01; * p<0.05). Graphs show mean + standard deviation. License number for republication: #5323550916865.

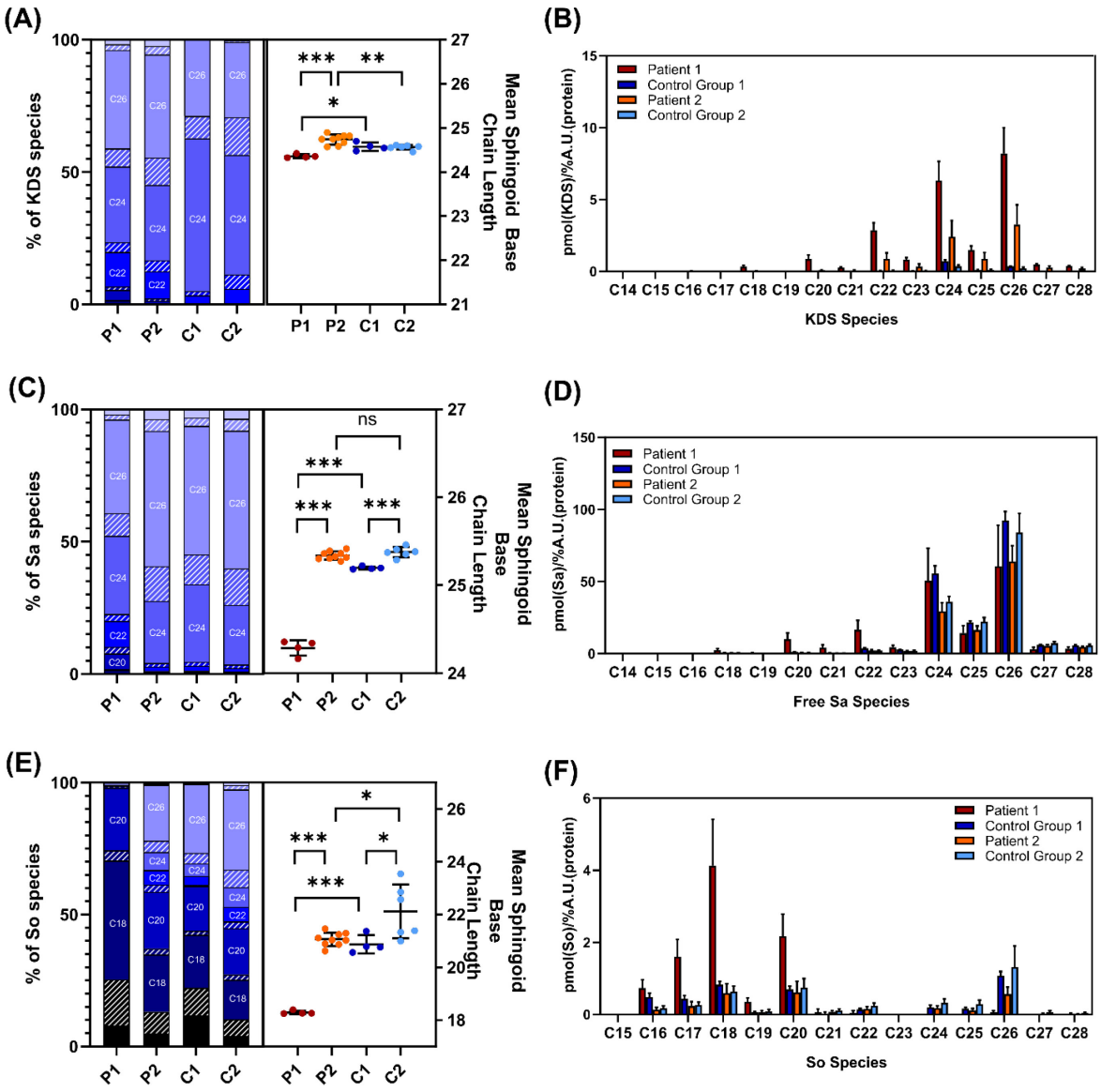

Figure 50 Sphingoid base length analysis in volar forearm stratum corneum.

Overview of measured KDS species as determined in palmar stratum corneum tape stripping lipid extracts. The relative amount of each species and the average length for (A) KDS, (C) sphinganine and (E) sphingosine are depicted in the left or right panel, respectively, for patient 1 (n=4), patient 2 (n=9), control group 1 (male, 3y, n=4; female, 3y, n=4), control group 2 (male, 51y, n=3; female, 37y, n=3) and the mother of patient 1 (31y, n=4, monoallelic c.879G>A). The absolute levels of single lipid species are plotted for (B) KDS, (D) sphinganine and (F) sphingosine. Statistical testing was done by ordinary one-way ANOVA with Tukey correction for multiple comparisons (*** p<0.001; ** p<0.01; * p<0.05). Graphs show mean + standard deviation.

This length reduction effect for free sphingoid bases could be confirmed in epidermal biopsies of both KDSR patients (Figure 51A), while, as expected, dermis contained only minor amounts of free C18-sphingoid bases (Figure 51B). The relatively low amount of free sphingoid bases in dermis and the presence of VLC-sphinganine (0.5% of epidermal level) could hint at an incomplete separation from the epidermal fraction.

In epidermal biopsies a strong increase in free LC-KDS was observed and a loss of VLC-sphinganine. In comparison to stratum corneum samples, less free VLC-KDS species were observed in patient epidermis, and almost no free VLC-sphinganine or VLC-sphingosine (Figure 51A). These findings could be related to the thickening of the epidermal layer that I observed in patient biopsies and a failure of keratinocytes to differentiate and initiate the production of VLC-species. Although only one biopsy sample per patient could be analysed, the similar effects observed in both patients indicate biological significance of these findings.

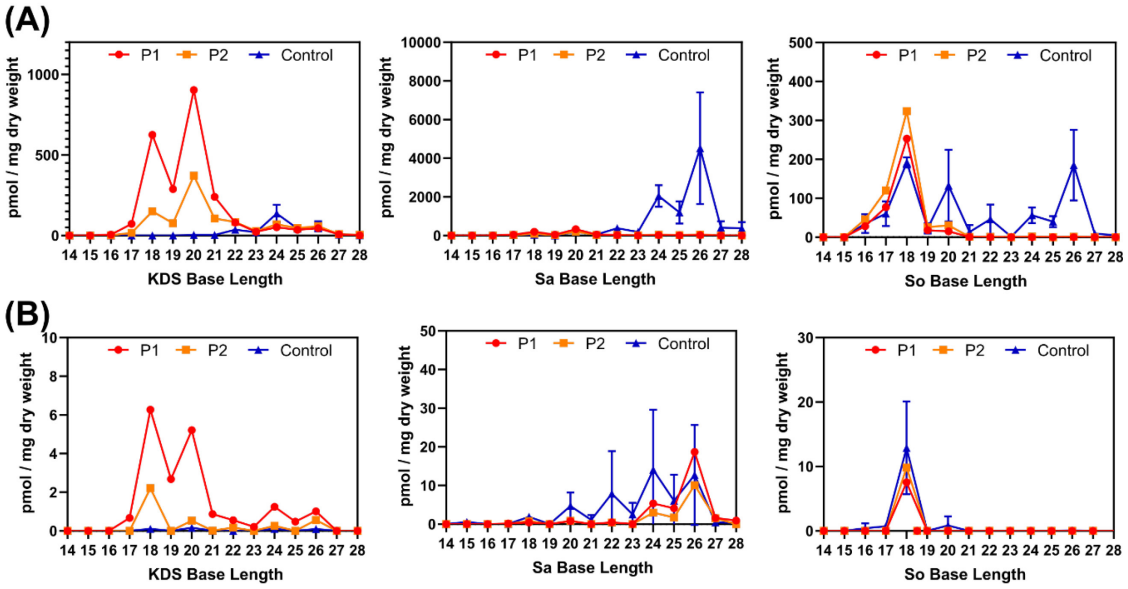

Figure 51 Sphingoid base analysis in epidermis and dermis biopsies.

Skin punch biopsies were enzymatically digested and separated into dermal and epidermal fractions. Levels of free sphingoid bases in (A) epidermis and (B) dermis of KDSR patients and control (male, 84y, right ventral thigh; female, 70y, forehead; female, 62y, shank; n=1 respectively). KDS (left), sphinganine (middle) and sphingosine (right). Graphs show mean + standard deviation.

Sphingoid bases in atopic dermatitis and psoriasis vulgaris

To investigate, if this length reduction effect generalizes across other skin pathologies like *atopic dermatitis* (AD) and *psoriasis vulgaris* (Pso), I obtained tape stripping stratum corneum samples of lesional and non-lesional skin areas of three AD and two Pso patients (Table 8) in cooperation with Dr Silvia Mihalceanu, Prof Dr Knut Schäkel, Prof Dr Alexander Enk (Hautklinik Heidelberg). I extracted lipids from the tape stripping discs and performed LC-MS/MS analysis analogous to KDSR patients.

Table 8 Overview of atopic dermatitis and psoriasis vulgaris patients.

Patient	Age	Sex	PASI / EASI	BSA	Location
Pso-1	57	Female	13.1	10.5%	Lateral abdominal (left)
Pso-2	25	Male	10.1	11%	Lateral abdominal (right)
AD-1	28	Female	11.7	12%	Forearm (left)
AD-2	57	Female	16.9	35%	Forearm (right)
AD-3	26	Female	10.5	14%	Armpit (left)

PASI: Psoriasis Activity Index; EASI: Eczema Area and Severity Index; BSA: Body Surface Area

An analysis of free sphingoid bases revealed a reduced length in both Pso patients in lesional skin areas, but not in non-lesional areas (Figure 52A, C, E). The effect was weaker compared to KDSR patients for KDS (up to 1 carbon atom), sphinganine (up to 0.6 carbon atoms) and stronger for sphingosine (up to 3 carbon atoms). For an interpretation of these findings, it should be considered that I osberved generally less VLC-sphingosine in palmar stratum corneum, which could explain the bigger difference observed in samples from lateral abdominal skin. No marked difference was observed in KDS and sphinganine length between palmar and non-palmar skin areas. In AD patients the observed effects were more differentiated and varied between the patients, which may be explained by differences in diseases severity, disease state and other factors like age. Especially for patient AD-2 with a comparatively higher eczema area and severity index (EASI = 16.9) and involved body surface area (BSA = 35%), KDS and sphinganine length was affected not only in lesional, but also non-lesional skin (Figure 52B, D). For patient AD-1 (EASI 11.7; BSA 12%) only KDS length was affected in lesional skin, while in patient AD-3 (EASI 10.5; BSA 14%) KDS,

sphinganine and sphingosine length were affected in lesional skin areas (Figure 52B, D, E). Overall, it appears that sphingoid base length reduction is a common feature in different skin pathologies und may be attributed to a common underlying mechanism, possibly a loss of keratinocyte differentiation and hyperproliferation.

In addition to changes in average free sphingoid base length, I found that the levels of free sphingoid bases are affected in Pso and AD patients. In both diseases, I observed increased KDS levels in lesional skin areas (Figure 52A, B *middle and right panel*). In lesional skin of Pso patients the amount of LC-sphingosine, but not VLC-sphingosine is significantly increased (Figure 52E *middle and right panel*).

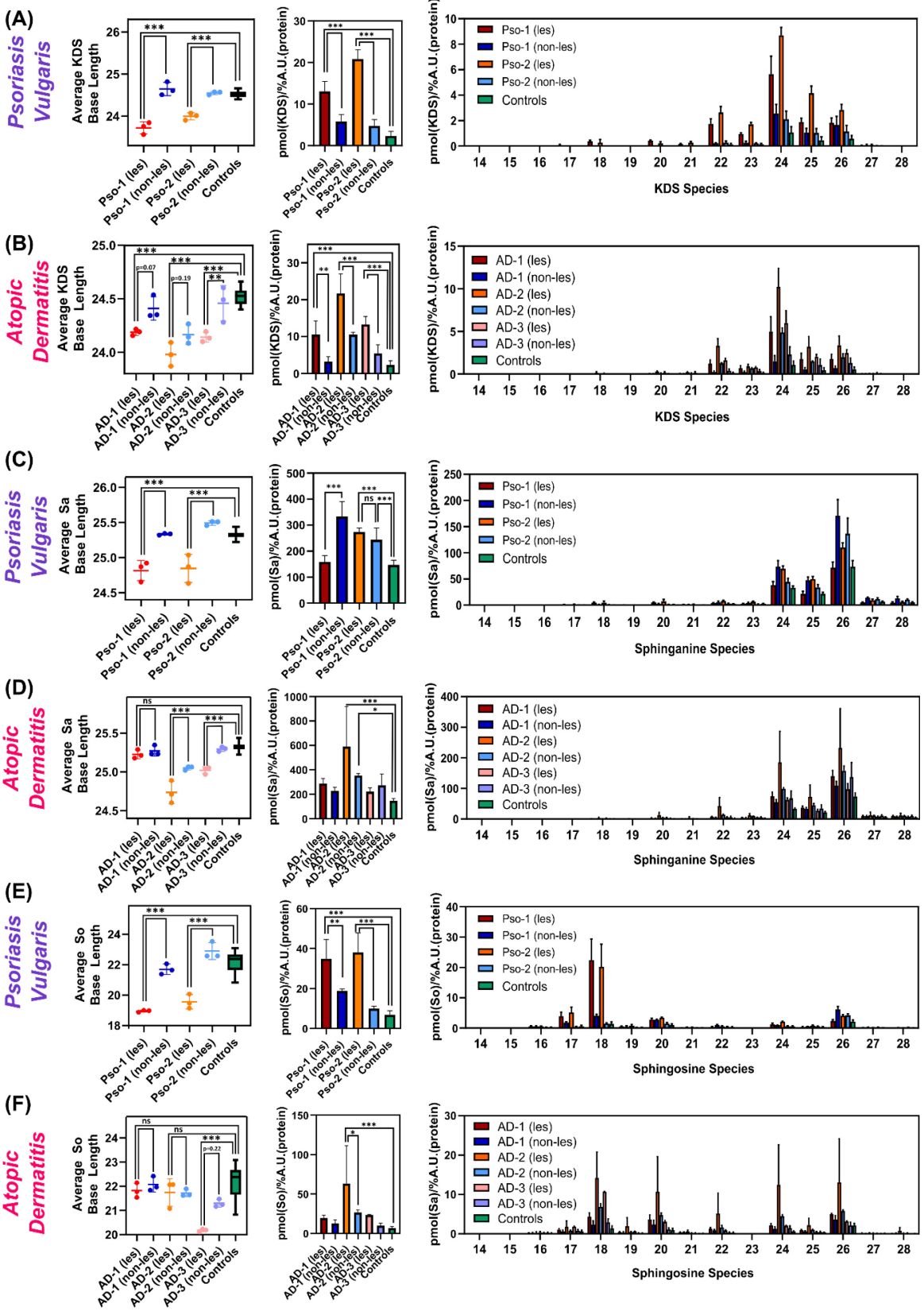

Figure 52 Sphingoid base length in AD and Pso patients.

Free sphingoid bases were extracted from stratum corneum tape stripping disc material three patients diagnosed with atopic dermatitis (AD) and two patients diagnosed with psoriasis vulgaris (Pso). Samples were acquired from lesional and non-lesional skin of forearm (AD-1, AD-2), armpit (AD-3) or

the lateral abdominal region (Pso-1, Pso-2). A detailed description of the patients is provided in Table 8. The average length, sum and amount of single lipid species of (A, B) free KDS, (C,D) free sphinganine and (E, F) free sphingosine was determined in lesional and non-lesional skin for each patient (n=3) and a control group (n=15). Statistical testing by ordinary one-way ANOVA with Tukey correction for multiple comparisons (*** - $p<0.001$; ** - $p<0.01$; * - $p<0.05$) (Graph shows mean + standard deviation).

VLC-sphinganine is incorporated into NdS-ceramide

It is unclear to what extent VLC-sphingoid bases are incorporated into other sphingolipids like ceramides. I investigated the abundance of different NdS-ceramide species to evaluate differences between skin areas and the effect of lesions as seen in KDSR patient 1 and map the abundance of each species.

I observed the N-acylation products of VLC-sphinganine (NdS-ceramides) up to a sphingoid base length of C26 with C22 and C24 as the major sphingoid bases in volar forearm of control samples and a slightly reduced length in palmar stratum corneum samples of controls (Figure 53 *bottom*). A very similar pattern emerged in volar forearm stratum corneum samples of KDSR patient 1, with a slight reduced sphingoid base length compared to control samples. In contrast, a very strong reduction of sphingoid base length was found in lesional palmar stratum corneum with almost all species being comprised of C18 and C20 sphingoid bases. In addition, N-acyl length is reduced in lesional palmar stratum corneum. While the majority of NdS-ceramide was found to contain C24 and C26 N-acyl residues, a major amount of C16- and C18 N-acyl NdS-ceramides was found in lesional palmar stratum corneum (Figure 53 *top*). Although reduced sphingoid base length seems to correlate with local variances due to different skin areas, a more pronounced association with a lesional skin state was observed.

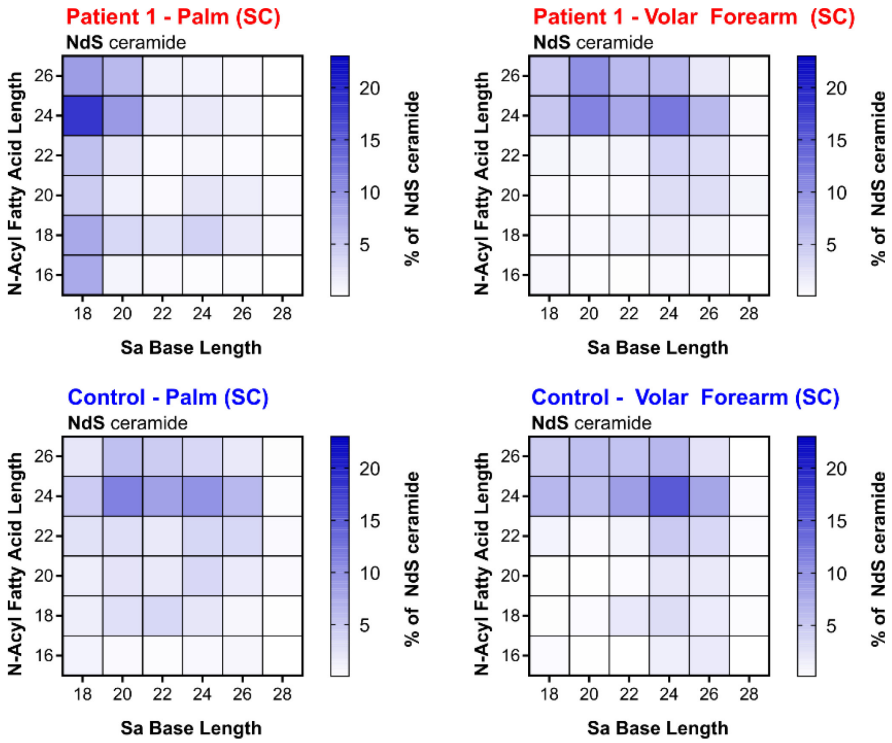

Figure 53 Relative abundance of NdS-ceramide species in stratum corneum.

NdS-ceramides with even-chained KDS base length ranging from C18 to C28 and N-acyl length ranging from C16 to C26 in stratum corneum of patient 1 and a control (female, 3y) were quantified. Relative levels of each species are shown in the heatmap. License number for republication: #5323550916865.

Skin state also affects NdK-ceramide species or vice versa?

I analysed the abundance of NdK-ceramide species in both patients' stratum corneum and complete epidermis samples. Similar to NdS-ceramide, I observed primarily VLC-KDS containing species (C22 and C24) in volar forearm samples and a very pronounced reduction to LC-KDS containing species (C18 and C20) in lesional palmar stratum corneum together with a reduction of N-acyl length. These effects were even more pronounced in epidermal biopsy samples. Despite the availability of free VLC-KDS, solely LC-KDS appears to be N-acylated into NdK-ceramides in lesional palmar stratum corneum, possibly due to a higher ceramide synthase affinity for LC-sphingoid bases. Nevertheless, conversion of VLC-KDS to NdK-ceramide is possible and can be observed in non-lesional volar forearm stratum corneum. The biological effects of sphingolipids are not only dependent on their core structural motifs, but also on the length of N-acyl residue and sphingoid base. It seems possible, that NdK-ceramide species of different length composition have altered biological effects, with a possibly higher contribution of LC-KDS-based species to pathogenesis.

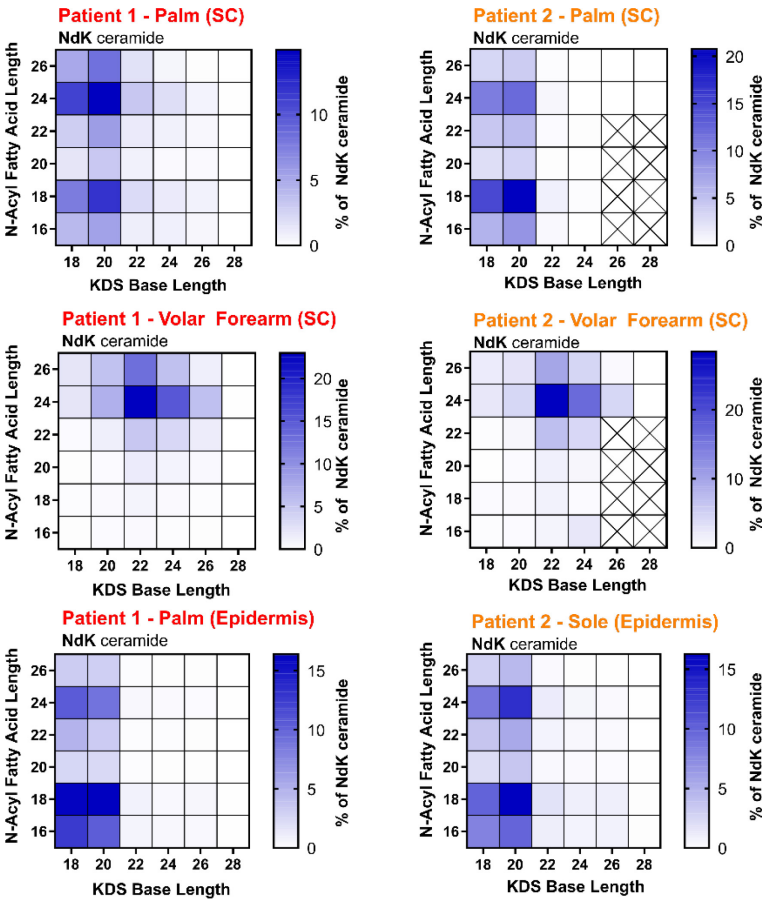

Figure 54 Relative abundance of NdK-ceramide species in SC and epidermis.

NdK-ceramide species with even-chained KDS base length ranging from C18 to C28 and N-acyl length ranging from C16 to C26 were quantified in stratum corneum (SC) and epidermis of both KDSR patients. Relative levels of the respective species are shown in the heatmap. License number for republication: #5323550916865.

Length of N-acyl and sphingoid base affected in ceramide

For an evaluation of changes in sphingoid base and N-acyl length across multiple samples, I decided to use the average length of sphingoid bases or N-acyl residues of all lipid species in a lipid class as a characteristic value and established the range of these values in volar forearm stratum corneum of a control group. For the analysis, I considered combinations of even-chained sphingoid bases (C18 – C28) and N-acyl residues (C16 – C26). Control samples were collected from five different subjects in triplicates and, interestingly, exhibited a very narrow range of observed ceramide lengths (Figure 55), indicating a tight regulation and control of mechanisms contributing to their synthesis.

For KDSR patients I observed a significant reduction of sphingoid base length and N-acylation length in all NX-type ceramides, except for NP ceramides in all samples

of palmoplantar keratoderma-affected skin areas (Figure 55 *red*). In non-lesional volar forearm stratum corneum of patient 1 NS- and NH-ceramide lengths were significantly reduced, though with a smaller effect size compared to palmar samples. Interestingly, similar effects were observed in both *psoriasis vulgaris* patients. While lesional skin areas demonstrated a strong reduction in sphingolipid length, non-lesional areas were not affected and NP-ceramide contained even longer N-acyl species. A more differentiated response was observed in atopic dermatitis patients. While a reduction of sphingoid base length was observed in patients AD-2 and AD-3 in NS- and NdS-ceramides, an increase was observed in patient AD-1. Non-lesional skin may also show differences in sphingolipid length in atopic dermatitis, which may be related to alterations on a molecular level in a pre-acute skin state. A change in average sphingolipid length may be of use as a marker for pathological changes of the skin in the future and could correlate with other parameter of skin state like permeability.

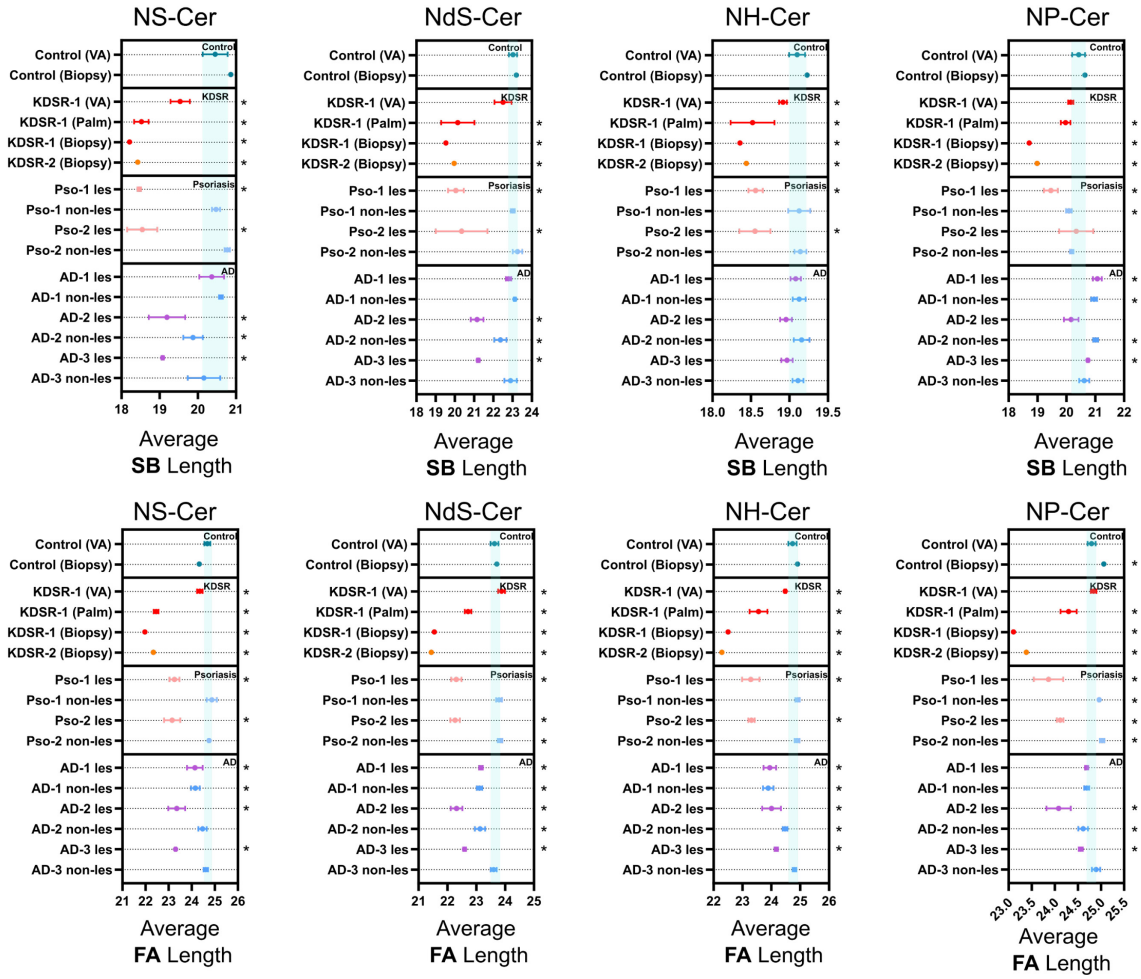

Figure 55 NX-type ceramide sphingoid base and N-acyl length in KDSR, AD and Pso patients.

NX-ceramides (including NS- (sphingosine), NdS- (sphinganine), NH- (6OH-sphingosine) and NP- (phytosphingosine) containing ceramides) with even-chained KDS base length ranging from C18 to C28 and N-acyl length ranging from C16 to C26 were quantified in stratum corneum of KDSR, atopic dermatitis and psoriasis vulgaris patients (n=3), volar forearm (VA) stratum corneum of controls (n=5) and in epidermal biopsies of KDSR patients (n=1). The average length of the sphingoid base backbone and N-acyl residue was calculated and plotted in (A) for NS-ceramides, (B) for NdS-ceramides, (C) for NH-ceramides and (D) NP-ceramides. Statistical testing was done by one-way ANOVA with Dunnett correction for multiple comparison. (* indicates significant difference ($p < 0.01$) to control (VA)). Graph shows mean + 95% confidence interval.

5.2 Discussion

5.2.1 3-ketodihydroceramides in epidermis of KDSR patients

The presented work demonstrates that mutations in the *KDSR* gene can result in the formation of novel, non-canonical and structurally distinguished dihydroceramides with a sp^2-hybridized 3-keto group instead of a sp^3-hybridized *erythro*-3-hydroxy group. I established a LC-MS/MS-based method to quantify these unknown sphingolipids in human stratum corneum and tissue samples and found that these 3-ketodihydroceramides are present in lesional and non-lesional stratum corneum and lesional epidermal biopsies of patients with biallelic mutations in the *KDSR* gene and they could not be observed to the same extend in control samples. This observation further supports the assumption that the novel mutations of *KDSR* in patient 2 indeed have metabolic consequences, which was previously unknown.

Although earlier studies of KDSR patients investigated changes in the general sphingolipid profile of skin (183) or KDS in plasma (184), no specific analysis of 3-ketodihydroceramides was performed, and it appears likely that these compounds will also be found in other patients suffering from mutations in KDSR, if the respective analysis is done.

5.2.2 Reports of 3-keto-sphingolipids in literature

Reports of 3-ketodihydroceramides in literature are scarce. By increasing the flow through the initial rate limiting step of the SPT due to overexpression of SPTLC1 and SPTLC2 and by feeding additionally the substrates *L*-serine and palmitate, expression of NdK-Cer was achieved in a cell culture of HEK293 cells pointing out that a saturation of cells with KDS will shuttle it into acylation rather than accumulation (305). Later, HeLa cells were shown to express low amounts of long chain (C16- and C18-N-acyl) 3-ketodihydroceramides (306). This was attributed to the fact, that HeLa cells lack regulation by the transcription factor FOXC1 (307). FOXC1 was found to be regulating KDSR expression (308) and lack of FOXC1 could result in lower KDSR activity and cause the formation of detectable 3-ketodihydroceramides in these cells (306).

Another study investigated the sphingoid base composition of rat liver mitochondria and submitochondrial fractions (309). The study reported glucosylceramide and lactosylceramide in inner membranes of mitochondria, that contained exclusively the 3-ketodihydrosphingosine backbone structure. Additionally, 41% of inner mitochondrial membrane ceramides were found to have a keto-sphinganine backbone. 3-keto-glucosylceramide and 3-ketodihydroceramide were found in outer mitochondrial membranes at 26% and 15.6%, respectively. The presence of a rather implausible t21:1 phytosphingosine base was reported in this study as well. I analysed rat liver homogenate for 3-ketoglucosylceramides and was not able to observe signals indicative of the presence of these compounds (data not shown). This may still be a matter of analyte enrichment, since no (sub)mitochondrial enrichment was performed.

Besides these reports, 3-ketodihydroceramides have not been reported in human tissues or other organisms.

5.2.3 The role of KDSR in de novo sphingolipid biosynthesis metabolism of 3-keto-sphingolipids

The canonical sphingolipid *de novo* biosynthesis pathways describes the synthesis of ceramides from *L*-serine and palmitoyl-CoA via the intermediates 3-ketodihydrosphingosine, sphinganine and dihydroceramide in the presented order. It is commonly accepted, that the 3-keto-group in 3-ketodihydrosphingosine is reduced to a 3-hydroxy group in sphinganine by KDSR in a NADPH-dependent manner (25). In early investigations of the sequence of these enzymatic steps it was hypothesized that there is an isomerization mechanism that may yield sphingosine from 3-ketodihydrosphingosine. Fujino and Nakano demonstrated in vitro an enzymatic conversion of 3-ketodihydrosphingosine to sphingosine in an NADPH-independent manner with enzymes obtained from rat liver particulate (310, 311) indicating the possibility for an alternative pathway for the reduction of the 3-keto-group by isomerization. They also demonstrated *in vitro* an enzymatic conversion of 3-ketodihydrosphingosine to 3-ketosphingosine (312). Though this isomerization mechanism may explain the increased amounts of sphingosine bases in KDSR patients' epidermis, it provides no explanation for the presence of sphinganine and dihydroceramides without an additional - yet unknown – reaction,

to convert the sphingosine bases to sphinganine bases. Even though these findings did not contribute to the canonical model of *de novo* sphingolipid biosynthesis, it appears possible that some of these mechanisms increase in importance under conditions of a dysfunctional *de novo* sphingolipid metabolism caused by mutations in *KDSR* and a metabolic bypass for dysfunctional KDSR may exist.

Studies of the *de novo* sphingolipid biosynthesis pathway by Kishimoto et al. investigated the metabolism of 4,5-unsaturated 3-ketoceramides to address the question whether the reduction of the 3-keto-group occurs at the level of the sphingoid base or the level of an N-acylated ceramide derivative (313). Ventricular injection of exogenous 3-ketoceramide([1-^{14}C]m18:1/[1-$^{3}H_2$]24:0) into the heart of rats and analysis of the liver one hour after injection revealed an equal ^{14}C/^{3}H labelling ratio in ceramides indicating the possibility for a conversion of 3-keto-ceramide to ceramides without hydrolysis of the N-linked lignoceryl group (314). Similar findings were reported for *in vivo* metabolism of exogenous 3-ketoceramide([1-^{14}C]m18:1/[1-$^{3}H_2$]24:0) after injection into rat brain. A conversion of the injected material into ceramide (without hydroxylated N-acyl residue), cerebroside and sphingomyelin and for some sphingolipid species considerable fatty acid remodelling was observed (315).

Although Shoyama and Kishimoto did not observe changes in labelling ratio this does not necessarily prove that radioactivity of sphingoid base and N-linked acyl derives from the same molecule. N-acyl hydrolysis before conversion of 3-ketoceramide to ceramide cannot be completely excluded. If there is a direct reduction of the 3-keto group in 3-ketoceramide, it could be speculated that there is a yet unknown KDSR-independent pathway for the reduction the 3-keto-group in 3-ketodihydroceramides or that KDSR could also accept 3-ketoceramide and possibly 3-ketodihydroceramide as a substrate opening the possibility for an alternative pathway for ceramide synthesis. It is possible that an inefficient conversion of 3-ketodihydroceramide as a competitive substrate for 3-ketodihydrosphingosine may further reduce KDSR activity towards 3-ketodihydrosphingosine.

Using mouse brain microsomes, Morell and Radin demonstrated that ceramide synthases may be able to use 3-ketodihydrosphingosine *in vitro* as an alternative acceptor for the stearoyl-CoA moiety. No direct data was shown, and it is unclear if other substrates were tested together with 3-ketodihydrosphingosine (296). Brain tissue contains primarily ceramide synthase 1 (CerS1) that is known to synthesize neuronal C18:0-FA containing ceramides (316) which might explain why only the stearoyl-CoA moiety was reported to be accepted by 3-ketodihydrosphingosine. The different ceramide synthases (CerS1-6) vary in the specificity for the acyl-CoA substrate (317) but little is known about the sphingoid base specificity and differences regarding the sphingoid base substrate. A variability in the utilization of 3-ketodihydrosphingosine by certain ceramide synthases may be possible. Especially murine CerS3 was shown to have a broad substrate specificity towards acyl-CoAs (42, 43). This could be important given the extraordinary role of CerS3 for skin sphingolipid metabolism (43, 149, 318–320) and could explain why 3-ketodihydroceramides were only found in the epidermal layer, which is characterized by increasing expression of CerS3 with keratinocyte differentiation (149).

Interestingly, Sphingolipid Δ(4)-desaturase DES1 (DEGS1), the enzyme that desaturates dihydroceramide at the 4,5-position (32) (and candidate for a possible desaturation of 3-ketodihydroceramides), was shown to be promiscuous regarding the utilization of retinol as a substrate (321). Treatments with retinoids were shown to alleviate KDSR patients' symptoms in some cases (182). It is tempting to speculate, that retinoids are competitive substrates for dihydroceramides, and treatment with retinoids might lower the amount of produced desaturated 3-ketoceramide, a possibly highly reactive allylic ketone, but further investigations are needed to support this hypothesis. Since systemic retinoid treatment as transcription regulator acts on many cellular mechanisms, often associated with a lot of side effects, it would be interesting to see if a more specific inhibition of DES1 mimics the symptom relief observed with retinoids.

The skin is one of the few organs that expresses sphingolipids with a 4-hydroxy-sphinganine (or phytosphingosine) base. They are generated via enzymatic conversion of sphinganine by Sphingolipid Δ(4)-desaturase/C4-monooxygenase DES2 (DEGS2). DEGS2 is highly expressed in the skin and upregulated during

keratinocyte differentiation (322), which may provide a link to the skin pathology observed with KDSR mutations. In addition to its 4-monooxygenase activity to produce phytosphingosine, DEGS2 is also a 4,5-desaturase for sphinganine and may be another interesting candidate for a conversion of 3-ketodihydroceramide to 3-ketoceramide that could explain the strong skin association of the disease.

Interestingly, sphingolipid synthesizing bacteria do not reduce KDS to sphinganine, but bacterial ceramide synthases integrate KDS directly to produce NdK-ceramides (323). NdK-ceramides then are reduced to dihydroceramides by a bacterial ceramide reductase (CerR), which phylogenetically appears to be most closely related to NADH dehydrogenase 1A subcomplex subunit 9 (NDUF9A), which is a component of Complex I in the mitochondrial oxidative phosphorylation pathway (323).

A relatively low specificity of sphingolipid metabolizing enzymes was shown for other enzymes of the pathway. Lysosomal glucosylceramide β-glucosidase (GBA) from human placenta was shown to be able to also degrade β-*D*-glucosyl-3-ketoceramide with similar v_{max}, but higher K_m value, compared to glucosylceramide in a liposomal assay system (324, 325). Similarly, a survey for inhibitors of mitochondrial ceramidase (mtCDase) revealed that 3-ketoceramide behaves as a competitive substrate when compared to ceramide (326).

Given the low specificity of anabolic and catabolic enzymes of sphingolipid metabolism regarding the stereoisomeric *threo*- or *erythro*- conformation of the 3-hydroxy group (327–329), the oxidation state of this group may not be an essential structural determinant for the affinity of many enzymes of sphingolipid metabolism. This indicates that in general a metabolization of epidermal 3-ketodihydroceramides towards glucosylceramide and sphingomyelin 3-ketoderivatives may be possible. I did neither detect the respective glucosylceramide or sphingomyelin derivatives, nor a 4,5-unsaturated (rearranged) 3-ketoceramide in stratum corneum, epidermis or dermis of the patients. Stratum corneum may not be the ideal sample type to investigate the presence of glucosylceramide or sphingomyelin derivatives as most epidermal glucosylceramide should be hydrolysed to ceramide(330). Also, an analysis of epidermal biopsies of KDSR patients did not reveal any 3-keto-

(dihydro)glycosphingolipids or 3-keto-(dihydro)sphingomyelins, indicating, that there may be a mechanism, that prevents their formation. This might be a failure of enzymatic conversion. Localization of 3-ketodihydroceramide in the cell may also be an important factor for an interaction with other metabolizing enzymes. Sphingomyelin synthesis may require a transport by ceramide transfer protein (CERT) to the *trans*-Golgi network. Glucosylceramide synthesis is localized to the *cis*-Golgi. Also, a fast degradation and reactivity of 3-keto-precursors and 3-keto-products or an abundance below the limit of detection of the method I used, may render it difficult to detect these compounds in patient samples.

Several non-enzymatic reactions of 3-keto-sphingolipids have been reported. Alkaline conditions above pH 11.5 in aqueous solution and only 0.0005M Na2CO3 in chloroform/methanol (2:1 (v/v)) can induce a β-eliminative cleavage of 3-ketocerebroside and 3-ketosphingomyelin yielding a C1-dehydroxylated sphingoid base with a 1,2-double bond that forms a π-conjugated system with the 3-keto-group and the 4,5-double bond (331). The 4,5-unsaturated 3-ketoceramide was shown to undergo cyclization under mild alkaline conditions by a Michael-type addition (300). Interestingly, Iwamori and Nagai state that application of 3-ketocerebroside and 3-ketosphingomyelin to a TLC plate and leaving it overnight at room temperature results in a β-eliminative cleavage of at least 60% of the 3-ketosphingolipid, highlighting the importance of careful and controlled sample preparation for the detection of these compounds. The reactive nature of these compounds could explain difficulties in detecting them.

Given the pH requirement for the β-eliminative cleavage a similar reaction in the aqueous milieu of the body appears unlikely, although the reactivity may be affected by incorporation of 3-ketosphingolipids into cellular membranes or extracellular lipid lamellae. The pH in intracellular and extracellular compartments differs and especially stratum corneum provides a rather acidic environment (ranging from pH 4.1 – 5.8 (332)). Pathological changes have been reported to increase the pH of the skin (332) and topical lotions or cleanser often have a high pH (333), which potentially interferes with the analysis of 3-ketodihydroceramide derivatives.

5.2.4 Functional consequences of 3-ketosphingolipids

To explain to differences between sphingosine backbone and sphinganine-backbone containing ceramides in apoptosis-induction, Norman Radin hypothesized, that 3-ketoceramides may have an important function in the mitochondrial regulation of apoptosis as reactive allylic ketones (334, 335). He argues that the only difference between ceramide and dihydroceramide, the 4,5-trans-double bond has a major impact on their respective biological functions. This could be explained due to the structure of ceramide and the unusual reactivity of the C-3 hydroxy group as part of an allylic alcohol. The 3-hydroxy group of sphingolipids can be chemically oxidized to a 3-keto group using 2,3-dichloro-5,6-dicyanobenzoquinone (302), which is structurally related to ubiquinone of complex III of the mitochondrial respiratory chain. As part of a physiological apoptosis-inducing pathway ubiquinone may be able to oxidize ceramide to 3-ketoceramide, that may react by *(A)* elimination of water and formation of a 1,2-double bond in a conjugated π-electron system together with the 3-keto group and the 4,5-double bond, *(B)* Michael addition of glutathione (GSH), amines or thiols to the 4,5-double bond or *(C)* elimination of formaldehyde in a reverse Mannich reaction yielding again an allylic ketone that can undergo addition of GSH (334). These hypotheses are supported by the observation that (short-chain) 3-ketoceramides are more potent inducers of mitochondrial apoptosis compared to (short-chain) ceramides in HL-60 and HeLa cells, while pre-treatment with GSH protected from the pro-apoptotic effect of 3-ketoceramide (336, 337). Furthermore, it was confirmed that 3-ketoceramide can undergo Michael addition with GSH (337).

Taking this into account, the generated 3-ketodihydroceramides in patients with *KDSR* mutations may be converted to 4,5-desaturated 3-ketoceramide via an enzymatic or a non-enzymatic reaction. I did not observe 3-ketoceramide nor a possible cyclic rearrangement product (300) in stratum corneum samples of KDSR patients, but it appears possible that these reactive allylic ketones undergo conjugation with GSH, thiol- or amine-containing proteins and are rapidly depleted after their formation. An analysis by LC-MS/MS could reveal potential 3-ketoceramide-GSH conjugates in epidermal or stratum corneum samples of the patients. Furthermore, this may result in a depletion of GSH levels in cells with a high burden of 3-ketosphingolipids and lower their tolerance towards oxidative

stress and the generation of reactive oxygen species (ROS). The relatively low reactivity of the 3-ketodihydroceramide backbone may allow its accumulation and renders its detection possible compared to 4,5-unsaturated allylic ketones. A possible future *in vitro* experiment to check this could involve treatment with exogenous 3-ketodihydroceramides and a measurement of GSH and ROS levels and 3-ketoceramide-GSH adducts. This mechanism may explain the biological need for a fast and efficient reduction of the 3-keto group by KDSR in the first place.

Interestingly, the study of a loss-of-function kdsr^{I105R} mutation in zebrafish described a hepatic injury phenotype that was associated with depletion of GSH levels (despite GSH synthesis and reduction enzymes are highly upregulated) and swollen mitochondria with cristae damage in the mutant animals. This was attributed to sphingosine-1-phosphate (S1P) accumulation and (hyper)activation of the salvage pathway. Deletion of sphingosine kinase 2 (sphk2) suppressed liver defects in the mutants (338). Park and colleagues found increased levels of sphingolipids but did not study 3-ketosphingolipids. It is possible that the production of reactive 3-ketoceramides may contribute to the observed depletion of GSH and oxidative stress in kdsr mutant zebrafish and the observed liver phenotype.

KDSR was also found to be an essential gene in a CRISPR/Cas9 library screening of leukaemia cells (294). The authors presented a link between free KDS in the endoplasmic reticulum and an inhibition of the unfolded protein response, but non-canonical 3-keto-sphingolipids were not considered in this study. Given the intrinsically increased oxidative stress of leukaemia cells (339), a loss of KDSR function, concomitant with an increase in 3-ketoceramide and a depletion of the ROS scavenger GSH may also explain the strong dependency on KDSR in leukaemia cells and it may provide a promising target for exploiting this vulnerability.

In summary, given the high non-enzymatic reactivity of allylic ketones by Michael addition and cyclization, as well as the demonstrated conjugation to GSH and the depleted GSH levels in kdsr mutant zebrafish, the lack of detection of 4,5-unsaturated 3-ketoceramides does not exclude the biosynthesis and biological effects of these metabolites and further experimental validation should be considered to investigate the transient generation of these compounds.

5.2.5 Pathological role for keto-dihydroceramides in skin metabolism

KDSR mutations may have other biological consequences considering the characteristics of sphingolipid metabolism in the skin. The most frequently reported pathological response to KDSR mutations is erythrokeratodermic skin with scaly lesions and palmoplantar keratoderma. Skin sphingolipid metabolism differs greatly from other tissues. Concordant with the differentiation of keratinocytes, sphingolipid *de novo* synthesis is thought to be upregulated in suprabasal cell layers during the generation of barrier lipids (142). Generated ceramide is immediately converted to glucosylceramide and sphingomyelin and transferred into lamellar bodies. The high rate of ceramide synthesis and its increasing abundance is thought to necessitate these protective measures against ceramide induced apoptosis (340).

KDSR was shown to have a ten times higher specific activity compared to serine palmitoyl-CoA transferase (25, 341) and is not considered the rate-limiting step in *de novo* sphingolipid synthesis. The residual capacity of mutant forms of KDSR to turnover of 3-ketodihydrosphingosine to sphinganine may still meet the demand of most tissues and may not lead to an accumulation of 3-ketosphingolipids. This may not be the case with an increase in *de novo* synthesis as seen in differentiating skin.

Thrombocytopenia is another pathology observed in some KDSR patients (183, 184). Thrombopoiesis is characterized by a marked increase in mass of megakaryocytes (and possible activation of *de novo* sphingolipid synthesis) before the shedding of pro-platelets (342–344), that are devoid of *de novo* sphingolipid synthesis (345). Though there is no direct data on SPT activity, an upregulation of sphingolipid *de novo* synthesis during differentiation could explain the sporadically observed thrombocytopenia in KDSR patients.

The fate of 3-ketodihydroceramides in differentiating keratinocytes is unclear. Consistent with the presented hypothesis, they may form adducts with glutathione or other antioxidants and deplete the ROS scavenging system in maturing keratinocytes. As an external organ the skin is considered the organ with the highest ROS exposure (346) and exposed to various other stressors like environmental pollutants, UV irradiation and mechanical stress. This highlights the

need for a working system to prevent oxidative damage (340, 347) and the cornified envelope is considered the first line of defence against ROS (348). This combination of a depleted scavenging system and increased oxidative stress may explain the often-observed localization of skin lesions to body folds that are prone to mechanical stress. Defects of the skin barrier have been linked to compensatory hyperproliferation of keratinocytes (349). Similarly, mechanical stress can induce hyperproliferation of keratinocytes (350, 351), that may in turn lead to the production of additional 3-ketosphingolipids and a depletion of the ROS scavenging system.

The major role for sphingolipid metabolism in the skin is the formation of skin barrier lipids. Structural differences as seen in 3-ketosphingolipids may have an impact on the formation of lipid lamellae. In model skin lipid membranes, it was demonstrated that (dihydro)ceramides with unusual stereochemistry at the 3-hydroxy group (*threo* instead of *erythro*) can increase permeability of the barrier (352), while the lack of a 4,5-trans-double bond does not significantly alter permeability (353), although other studies have shown an impact on lipid barrier phases (354). 3-ketodihydroceramides may transition into lipid lamellae and the different stereochemistry of the 3-keto group and altered ability to form intermolecular bonds could disturb the packaging of the lipid sheets and reduce barrier function. Oxidative damage and barrier dysfunction in turn is associated with an increase in SPT activity and ceramide production (340, 355), which may further enhance the formation of 3-ketodihydroceramides causing positive feedback loop. It is unclear whether 3-ketodihydroceramides are packed into lamellar bodies. For ceramides this necessitates the enzymatic formation of a glucosyl- or phosphocholine-derivative and active transfer by ABCA12 (301). The fact that these derivatives were not observed in epidermal biopsies may argue against this mechanism. The proposed model for the biogenesis of lamellar bodies suggests that they are derived from the trans-Golgi network (TGN) (356), which may contain 3-ketodihydroceramide that could be integrated into lamellar bodies.

The localization and fate of 3-ketodihydroceramides in keratinocytes and in the macrostructure of the epidermis as well as their possible mode of action remains an important question for future investigations.

Furthermore, it remains an important question why some skin areas are affected while other, despite the presence of 3-ketodihydroceramides, do not exhibit pathological signs. It has been shown that the skin of different areas of the body varies in lipid and protein composition (357). In addition, environmental and physiological factors like UV irradiation, temperature, the presence of hair follicles and sweat glands, physical strains and exposure to chemicals may vary across different skin areas. Differences in protein or lipid composition and lipid-to-protein ratio in palmar epidermis may render bioactive effects of 3-ketodihydroceramides more relevant. The lipid content of palmar tape stripping discs was generally lower compared to volar forearm tape stripping discs.

5.2.6 Sphingoid bases and ceramides are shorter in KDSR patients

In addition to the described 3-ketodihydroceramides, I observed a reduction in the length of free sphingoid bases and ceramides in lesional, palmar stratum corneum of both KDSR patients. The length of sphingoid bases in non-lesional, volar forearm stratum corneum was not reduced or only slightly reduced.

Free sphingoid bases including sphingosine, sphinganine and phytosphingosine are implicated in the protection of the inner cutaneous layer against pathogenic microbial infection (34, 43, 358–360). Furthermore, free sphingoid bases, and especially sphinganine, were shown to promote the formation of VLC- ceramides and keratinocyte differentiation in a confluence-induced in vitro keratinocyte differentiation model (361).

Several factors determine the length of sphingoid bases. The body produces C18-, and in some cases C20-sphingoid bases (19), in most tissues. In the human skin “unusually” long free sphinganines (20), total (free and bound) VLC-sphingoid bases (131), and covalently bound omega-hydroxy-ceramides up to C22-sphingoid bases have been described in human epidermis (21). Though VLC-sphingoid bases make up a major portion of sphingoid bases, their presence is often unacknowledged in comparative studies. Although the presence of VLC-sphingoid bases in total hydrolysates of skin lipids was shown (131), the specific N-acylation of VLC-sphinganine as a main contributor to the dihydroceramide population was not demonstrated before. The fact that in healthy human stratum corneum N-acylated VLC-sphinganine (NdS-ceramide) makes up a high proportion of all NdS-

ceramide species (Figure 53) should be considered when reviewing lipid class changes in earlier studies. Though in NS-, NP- and NH-ceramides a higher proportion of C18- and C20-sphingoid bases was observed, considerable amounts of VLC sphingoid bases could still be observed in stratum corneum. These findings indicate that DEGS1, DEGS2 and a putative 6-hydroxylase can utilize VLC-sphingoid base substrates. Considering the strong effect on sphingoid base length observed in KDSR patients, but also *psoriasis vulgaris* and in part *atopic dermatitis* patients it may not be sufficient to examine changes in only C18-sphingoid base containing ceramides.

Given the sparse literature about VLC-sphingoid bases a specific biological role has not been established and remains a subject for speculation. It appears possible, that the incorporation and intermolecular arrangement in the lipid lamellae of the human skin barrier requires VLC-sphingoid bases. The antimicrobial effect of sphingoid bases may also be increased though investigations demonstrating this are lacking. Short acyl-chains of NS-ceramides were shown to transition into the gel phase, which could be related to an increased transepidermal water loss as seen in atopic dermatitis patients (354)and a reduction of sphingoid base length in ceramides may have similar effects on the skin barrier.

The length of sphingoid bases is determined by the availability of substrates, specifically acyl-CoA and VLC-acyl-CoA, the SPT complex subunit composition (SPTLC3 has been shown to have less stringent substrate requirements (14) and ssSPTb is important for longer C20-sphingoid base production (19)) and the specificity of the metabolizing enzymes. Though KDSR has a high substrate turnover (362), it was shown to have a slower reaction velocity and a higher Michaelis constant for C20-3-ketodihydrosphingosine compared to the C18-variant (363). This effect could be even more pronounced with longer bases. A reduction of KDSR activity due to mutation could favour the conversion of shorter 3-ketodihydrosphingosines, resulting in the severe reduction of sphinganine length that I observed in lesional palmar skin of the patients, but does not explain a reduction in KDS base length.

Elongation of acyl-CoAs (via ELOVL1 and ELOVL4) for the generation of ultra-long-chain ceramides (ULC-Cer) is important for the biosynthesis of the barrier lipids and is associated with keratinocyte differentiation. Defective keratinocyte differentiation as seen in skin pathologies could influence substrate availability. It could be argued that VLC-sphingoid bases are a by-product of increased synthesis of VLC-and ULC-acyl-CoAs for ULC-ceramide production. The observation that mice do not express VLC-sphingoid bases, but ULC-ceramides argues against this hypothesis.

The reduction in sphingoid base length does not only affect physiological sphingolipids. 3-ketodihydroceramide from lesional palm stratum corneum was significantly shorter than from non-lesional volar forearm stratum corneum. This may influence the biological effects of these compounds, for example with respect to enzyme affinity or biological effects. C16-ceramides are specifically associated with apoptosis induction (364). A desaturation of LC-3-ketodihydroceramides (especially C16-N-acylated) to (possible) bioactive 3-ketoceramides may be favoured under these conditions.

Similar effects on sphingolipid length were observed in *atopic dermatitis* and *psoriasis vulgaris* patients. Especially for *atopic dermatitis* the heterogeneity of the disease may need to be considered given the small sample size of three different patients. Including more patients into the study may help to explain the changes observed in *atopic dermatitis*. A reduction in sphingoid base length may be a more general effect of erroneous keratinocyte differentiation and an interesting subject for future studies of not only *psoriasis vulgaris* and *atopic dermatitis* but also other skin pathologies. The similar effect in *psoriasis vulgaris* and KDSR patients indicates that a reduction of sphingoid base length may be a general feature especially of hyperkeratotic skin disorders.

5.2.7 Genetic aspects of the specific mutations for protein function

Due to the low number of patients identified, it is difficult to draw genotype-phenotype correlations. A broad phenotypic variability has been observed for the skin involvement, ranging from mild and spontaneously resolving erythrokeratoderma to severe Harlequin-like ichthyosis (Table 7). This variability may be explained by the different mutations of the patients that could affect KDSR

activity to different degrees, but also age, gender, environmental factors, skin care routine and genetic predispositions may contribute to disease pathogenesis. Despite the severe Harlequin phenomenon at birth, the lack of the typical PERIOPTER symptoms in patient 2 could be explained by residual catalytical activity of the proteins coded by both *KDSR* alleles.

The c.879G>A mutation of the functional KDSR variant of patient 1 was observed in four other patients (out of 12 described patients) from two different pedigrees (182, 183) and causes a skipping of exon 9 that includes the sequence for the second transmembrane domain. The mother of patient 1 carries the same mutation without apparent pathologies or detectable amounts of 3-ketodihydroceramides. It can be concluded that a healthy second allele compensates potential effects of the mutation.

Although there was no exon skipping observed in patient 2, the c.865G>A (p.Glu289Lys) mutation (reported in one other patient (365)) seems to affect a critical amino acid of the second transmembrane domain. Residual activity from the second allele with a c.737_738delinsG mutation (inducing a frameshift and premature stop codon), affecting the Rossmann fold of the protein, cannot be excluded. The energetically unfavourable position of glutamate within the plasma membrane may hint at a specific function in protein-protein or protein-lipid interactions and the exchange of an acidic glutamate against a basic lysine (p.Glu289Lys) likely disturbs possible interactions. Other mutations involving the second transmembrane domain have been reported (182, 183, 365, 366) and include c.879G>A (exon 9 skipping) and a c.869G>A (p.Gly290Glu) mutation. The prevalence of mutations involving exon 9 indicates a role of the C-terminus for not only enzymatic function, but possibly also regulation and interaction with other proteins, as for example SPT or CerS.

The presence of sphingolipids indicates that the mutant KDSR variants investigated still have residual activity. An activation of the salvage pathway was hypothesized (182, 184) to compensate a lack of ceramides and mismatches in metabolic balance by hydrolysis of sphingomyelin and glycosphingolipids. In the skin this mechanism seems unlikely to be able to supply the necessary amount of additional sphingoid bases for the formation of the skin barrier. Although it was

shown that a dietary intake of sphingolipids can affect the state of the skin barrier(367), salvage of dietary sphingolipids from the blood stream seems unlikely, given the presence of skin-specific VLC-sphingoid bases that are likely derived from *de novo* synthesis and never had been reported in serum or plasma.

5.2.8 Future investigations and outlook for patients

Future investigations may focus on the contribution of 3-ketodihydroceramide to pathogenesis. Since primary keratinocytes of the patients are not available, modelling of these mutations in established cell lines seems to be a feasible approach. If the level of *de novo* synthesis is not sufficient to trigger 3-keto-ceramide production stimulation of the cells with KDS may be an option to simulate high SPT activity. Alternatives include overexpression of the respective large SPT subunits or reduction of ORMDL inhibition. Other approaches could include modelling the overload of KDSR to enhance 3-ketodihydroceramide production or external treatment with these compounds. Readouts may include the analysis of KDSR activity towards different KDS substrates, analysis of ceramide-GSH adducts, which could be produced *in vitro* as analytical standards, effects on the redox balance of cells or tissue and possible treatments to reduce oxidative burden could be evaluated. The preference of different ceramide synthases for KDS substrates could also be tested *in vitro* as well as desaturase activity towards 3-ketodihydroceramides. Additionally, mutant forms of KDSR can be expressed in production organisms like yeast or insect hosts and substrate affinity may be assayed *in vitro*.

Furthermore, synthetic NdK-Ceramides with stable isotope labelling in both, the KDS base and the N-acyl chain could be used to revisit the possibility of mammalian cells to reduce NdK-Ceramides to NdS-Ceramides, paralleling the bacterial ceramide reductase pathway. Mass spectrometric detection will prove if the double labelled compounds stay intact prior to reduction. Possibly, such pathway exists in most, but not all, cell types of the mammalian body, giving rise to NdK-Ceramides in epidermis but not dermis or blood.

If a mechanistic link between keto-type sphingolipids and pathogenesis can be established several therapeutic strategies may be feasible. The production of 3-ketodihydroceramides could be blocked by reduction of SPT activity using topical

application of inhibitors like myriocin (368) to reduce 3-ketodihydrosphingosine reduction to a level that does not exceed the enzymatic capacity of mutant KDSR. This reduction needs to be balanced against *de novo* synthesis, which is necessary for skin barrier lipid production. Other strategies may prevent the formation of bioactive metabolites like the hypothesized 3-ketoceramides by blocking the respective enzyme. If 3-ketoceramides turn out to deplete the oxidative stress scavenging system several strategies may be feasible to counteract this including an application of GSH and enhancement of GSH production (for example via Vitamin D3) or the use of antioxidants to reduce oxidative burden.

6 Material and Methods

6.1 Materials and Devices

6.1.1 Devices and Instruments

Table 9 Instruments and devices.

Equipment	Manufacturer
20 port Vacuum Extraction Manifold	Agilent Technologies Inc., California, USA
ABT 120-4M scale	Kern & Sohn GmbH, Balingen-Frommern, Germany
BioLinker UV crosslinker	Vilber Lourmat Deutschland GmbH, Eberhardzell, Germany
Camag TLC Sprayer	Camag Chemie-Erzeugnisse & Adsorptionstechnik AG & Co. GmbH, Muttenz, Switzerland
Casy cell counter and analyzer	Roche Life Science, Basel, Switzerland
Cell culture incubator C200	Labotect, Goettingen, Germany
Centrifuge 5415C	Eppendorf AG, Hamburg, Germany
Centrifuge 5417R	Eppendorf AG, Hamburg, Germany
Centrifuge 5804R	Eppendorf AG, Hamburg, Germany
Centrifuge 5810R	Eppendorf AG, Hamburg, Germany
ChemiDoc™ MP Imaging System	Bio-Rad Laboratories, Hercules, CA, USA
D100-D-Squame Sampling Discs	Clinical and Derm LLC., Dallas, Texas, USA
D500-D-Squame Pressure Intrument	Clinical and Derm LLC., Dallas, Texas, USA
Evaporator	Gebr. Liebisch GmbH & Co. KG, Bielefeld, Germany
Incubator B6030	Heraeus Holding GmbH, Hanau, Germany
Incubator B6060	Heraeus Holding GmbH, Hanau, Germany
Incubator BD115	BINDER GmbH, Tuttlingen, Germany
Julabo SW20 water bath	JULABO GmbH, Seelbach, Germany
Keyence BZ-9000 fluorescence microscope	Keyence Deutschland GmbH, Neu-Isenburg, Germany
Leica SP5 confocal microscope	Leica Microsystems, Wetzlar, Germany
Linomat IV	Camag Chemie-Erzeugnisse & Adsorptionstechnik AG & Co. GmbH, Muttenz, Switzerland
Magnetic Stirrer MR3002	Heidolph Instruments GmbH, Schwabach, Germany
MiniAmpPlus Thermal Cycler	Thermo Fisher Scientific, Waltham, MA, USA
Mini-PROTEAN® tetra cell	Bio-Rad Laboratories, Hercules, CA, USA
Mr Frosty	Thermo Fisher Scientific, Waltham, MA, USA
Nikon Eclipse Ts2-FL inverted microscope	Nikon Corporation, Tokyo, Japan
Safety cabinet MAXISAFE 2030i	Thermo Fisher Scientific, Waltham, MA, USA

Sartorius MC1 laboratory LC4800P	Sartorius AG, Goettingen, Germany
SpectraFluor Plus	Tecan Group AG, Männedorf, Switzerland
Synergy H1 microplate reader	BioTek Instruments GmbH, Bad Friedrichshall, Germany
Thermomixer comfort	Eppendorf AG, Hamburg, Germany
Tissue Lyser II	Qiagen N.V., Venlo, Netherlands
Ultrasonic water bath Sonorex Super	Bandelin electronic GmbH & Co. KG, Berlin, Germany
Vacupack plus	KRUPS, Solingen, Germany
Vilber Lourmat 365nm 8W Tubes	Vilber Lourmat Deutschland GmbH, Eberhardzell, Germany
Vortex mixer K 7-2020	neoLab Migge GmbH, Heidelberg, Germany
Waters I-class UPLC system	Waters GmbH, Eschborn, Germany
WTW pocket pH meter pH 3110	Xylem Analytics Germany Sales GmbH & Co.KG, Weilheim, Germany
Xevo TQS mass spectrometer	Waters GmbH, Eschborn, Germany

6.1.2 Reagents and Media

All chemicals were obtained from Sigma Aldrich (St. Louis, MO, USA), Avanti Polar Lipid (Alabaster, AL, USA), Carl Roth GmbH & Co.KG (Karlsruhe, Germany), AppliChem GmbH (Darmstadt, Germany), Thermo Fisher Scientific (Waltham, MA, USA), Cayman Chemicals (Ann Arbour, MI, USA), Merck Millipore (Darmstadt, Germany) and Honeywell International Inc. (Morristown, NJ, USA) in analytical grade, if not stated otherwise. Materials used for tissue culture were of cell culture grade, if available.

Table 10 Reagents and media.

Reagent	Supplier
2,3-Dichloro-5,6-dicyano-1,4-benzoquinone	Sigma Aldrich Inc., St. Louis, MI, USA
2-Propanol LC-MS CHROMASOLV®	Thermo Fisher Scientific, Waltham, MA, USA
3-azido-7-hydroxycoumarin	Jena Bioscience GmbH, Jena, Germany
Acetic acid	Thermo Fisher Scientific, Waltham, MA, USA
Agarose	Carl Roth GmbH & Co. KG, Karlsruhe, Germany
Ampicillin	Sigma Aldrich Inc., St. Louis, MI, USA
Ammonium formate	Sigma Aldrich Inc., St. Louis, MI, USA
Biotin-PEG3-azide	Jena Bioscience GmbH, Jena, Germany
CaCl2	Sigma Aldrich Inc., St. Louis, MI, USA

Chloroform HPLC-grade	Honeywell International Inc., Morristown, NJ, USA
Citric acid monohydrate	Thermo Fisher Scientific, Waltham, MA, USA
CuSO4	Jena Bioscience GmbH, Jena, Germany
Cy5-azide	Jena Bioscience GmbH, Jena, Germany
Dde Biotin-PEG4-Azide (284BP-22678)	Tebu-bio GmbH, Offenbach am Main, Germany
DDQ	Sigma Aldrich Inc., St. Louis, MI, USA
Dimethylsulfoxide (DMSO)	Sigma Aldrich Inc., St. Louis, MI, USA
Dulbecco's PBS (#D8537)	Sigma Aldrich Inc., St. Louis, MI, USA
Ethanol	Sigma Aldrich Inc., St. Louis, MI, USA
Ethylenediaminetetraacetic acid (EDTA)	Sigma Aldrich Inc., St. Louis, MI, USA
FBS, charcoal stripped (F6765)	Sigma Aldrich Inc., St. Louis, MI, USA
Fetal Calf Serum (FCS)	Thermo Fisher Scientific, Waltham, MA, USA
FITC-albumin	Thermo Fisher Scientific, Waltham, MA, USA
Formic acid	VWR International, Radnor, PA, USA
Gentamicin sulfate	Serva Electrophoresis GmbH, Heidelberg, Germany
Gibco™ DMEM/F-12 (#11320074)	Thermo Fisher Scientific, Waltham, MA, USA
Gibco™ IMDM (#12440053)	Thermo Fisher Scientific, Waltham, MA, USA
Hank's buffered saline solution (HBSS)	Thermo Fisher Scientific, Waltham, MA, USA
HEPES	Thermo Fisher Scientific, Waltham, MA, USA
HOBT	Sigma Aldrich Inc., St. Louis, MI, USA
HPTLC silica gel 60 F_{254}	Merck KGaA, Darmstadt, Germany
Hydrazine Monohydrate	Thermo Fisher Scientific, Waltham, MA, USA
Isobutyl methacrylate	Sigma Aldrich Inc., St. Louis, MI, USA
Lithium acetate	Sigma Aldrich Inc., St. Louis, MI, USA
Methanol	Thermo Fisher Scientific, Waltham, MA, USA
Methanol LC-MS CHROMASOLV®	Thermo Fisher Scientific, Waltham, MA, USA
Midori Green Advance (617004)	Nippon Genetics Europe GmbH, Dueren, Germany
Miglustat	Cayman Chemical, Ann Arbor, MI, USA

N-(3-dimethylaminopropyl)-N′-ethylcarbodiimide	Sigma Aldrich Inc., St. Louis, MI, USA
N, N-Dimethylformamide	Sigma Aldrich Inc., St. Louis, MI, USA
NaOH	Thermo Fisher Scientific, Waltham, MA, USA
Orcinol monohydrate	Sigma Aldrich Inc., St. Louis, MI, USA
Palladium on charcoal	Sigma Aldrich Inc., St. Louis, MI, USA
PenStrep (2.5%)	Thermo Fisher Scientific, Waltham, MA, USA
Phalloidin-CF488A	Cell Signaling Technology, Denver, MA, USA
Phosphate-buffered saline (PBS)	Sigma Aldrich Inc., St. Louis, MI, USA
Puromycin	Carl Roth GmbH & Co. KG, Karlsruhe, Germany
Q5 polymerase	New England Biolabs GmbH, Frankfurt, Germany
Ringer solution	VWR International, Radnor, PA, USA
RP18 material	Waters GmbH, Eschborn, Germany
SOC Medium	Thermo Fisher Scientific, Waltham, MA, USA
Sodium ascorbate	Jena Bioscience GmbH, Jena, Germany
StxB-Cy3	Kindly provided by Ludger Johannes
T4 DNA Ligase	New England Biolabs GmbH, Frankfurt, Germany
T7 Endonuclease I (M0302S)	New England Biolabs GmbH, Frankfurt, Germany
TAQ Polymerase (#733-1301)	VWR International, Radnor, PA, USA
Tris[(1-benzyl-1H-1,2,3-triazol-4-yl)methyl]amin (TBTA)	Sigma Aldrich Inc., St. Louis, MI, USA
TCEP (0.5M) (#646547)	Sigma Aldrich Inc., St. Louis, MI, USA
TEMED	Carl Roth GmbH & Co. KG, Karlsruhe, Germany
Tetrakis(acetonitrile)copper(I)tetrafluoroborate	Sigma Aldrich Inc., St. Louis, MI, USA
TexasRed-albumin	Thermo Fisher Scientific, Waltham, MA, USA
TexasRed-X succinimidyl ester	GeneCopoeia Inc., Rockwell, MD, USA
THF	Sigma Aldrich Inc., St. Louis, MI, USA
Tris(3-hydroxypropyltriazolylmethyl)amine (THPTA)	Sigma Aldrich Inc., St. Louis, MI, USA
Trypsin	Thermo Fisher Scientific, Waltham, MA, USA
Tween-20	Sigma Aldrich Inc., St. Louis, MI, USA

Water LC-MS CHROMASOLV	Thermo Fisher Scientific, Waltham, MA, USA
Wheat Germ Agglutinin-CF488A	Biotium, Fremont, CA, USA
NeutrAvidin-HRP	Thermo Fisher Scientific, Waltham, MA, USA
NeutrAvidin agarose (#29200)	Thermo Fisher Scientific, Waltham, MA, USA

6.1.3 Buffers and Solutions

Table 11 Buffers and solutions.

Solution	Composition
10x PBS, pH 7.4	1.5M NaCl, 30mM KCl, 80mM Na2HPO4, 20mM KH2PO4
1X PBS, pH 7.4	150 mM NaCl, 3 mM KCl, 8 mM Na2HPO4, 2 mM KH2PO4
10x TBS, pH 7.5	0.2M Tris-Base, 1.5M NaCl
1x TBS-T, pH 7.5	20 mM Tris-Base, 150 mM NaCl, 0.1% Tween-20
2X HBS	50 mM HEPES, 280 mM NaCl, 1.5 mM Na2HPO4, pH 7.0 with HCl + filter sterilized
DNA purification buffer	500mM Tris-HCl, 100mM EDTA, 100mM NaCl, 1%SDS, (add freshly) 0.85mg/mL Proteinase K
Transformation Buffer 1 (TFB1), pH 5.8	30 mM Kac, 10 mM CaCl2, 50 mM MnCl2, 100 mM KCl, 15% glycerol (w/v), pH adjusted with 0.2M acetic acid
Transformation Buffer 2 (TFB2), pH 7.0	10 mM MOPS, 10 mM KCl, 75 mM CaCl2 15% glycerol (w/v), pH adjusted with 1M NaOH
50X TAE buffer, pH 8.0	50 mM EDTA, 2M Tris-base, pH adjusted with glacial acetic acid
Agarose gel loading buffer	0.25% xylene cyanol FF in 1:1 glycerol/Tris-HCl
Lysis Buffer (Pull-down)	50 mM HEPES, 150 mM NaCl, 1% SDS, 2x Protease Inhibitor, Benzonase
Solubilization Buffer (Pull-down)	50 mM HEPES, 150 mM NaCl, 1% SDS, 2x Protease Inhibitor
Elution Buffer (Pull-down)	50 mM HEPES, 150 mM NaCl, 1% SDS, 2% hydrazine (v/v)
3X Sample Buffer	40% glycerol (w/v), 250 mM Tris-HCl, 8% SDS, 5% β-mercaptoethanol, 0.01% Bromophenol Blue
PBS++	PBS with 0.5 mM $CaCl_2$ and 1 mM $MgCl_2$

6.1.4 Antibodies

Table 12 Antibodies.

Abbreviations: rb – rabbit, ck – chicken, ms – mouse, sw - swine, WB – western blotting, PLA – proximity ligation assay, I-TLC – immune thin layer chromatography, IF - immunofluorescence

Antibody Target	Species	Application	Supplier
SPINT1 (hHAI-1 Ecto)	rb (poly)	WB: 1:1000	Bio-techne, Minneapolis, USA
SPINT1 (#15036-1-AP)	rb (poly)	PLA: 1:100	Proteintech, Manchester, UK
c-MET	rb (poly)	WB: 1:1000 PLA: 1:100	Proteintech, Manchester, UK
ATP9A (#PA5-97489)	rb (poly)	PLA: 1:100	Thermo Fisher Scientific, Waltham, MA, USA
EPCAM	ms (mono)	Undil.	Kindly provided by Claudia Tessmer (GPCF, DKFZ Heidelberg)
Gb3Cer	ck (poly)	IF: 1:100 I-TLC: 1:50	Kindly provided by J. Müthing (JM06/298-1)
GD2 (#554272)	ms (mono)	I-TLC: 1:50	BD Biosciences, Franklin Lakes, NJ, USA
Cy5 (B-2) sc-166896	ms (mono)	PLA: 1:100	Santa Cruz Biotechnology, Dallas, TX, USA
ITGA3 (A-3) sc-374242	ms (mono)	WB: 1:1000	Santa Cruz Biotechnology, Dallas, TX, USA
HA-tag	rb	WB: 1:1000	Cell Signaling Technology, Danvers, MA, USA
Gb3Cer-PLA-MINUS	ck (poly)	PLA: 1:100	DuoLink ProbeMaker
Secondary antibodies			
Anti-mouse-IgG-AP	gt	I-TLC: 1:187.5	Thermo Fisher Scientific, Waltham, MA, USA
Anti-chicken-IgG-AP	gt	I-TLC: 1:187:5	Thermo Fisher Scientific, Waltham, MA, USA
Anti-mouse-HRP	rb	WB: 1:1000	Agilent, Santa Clara, CA, USA
Anti-rabbit-HRP	sw	WB: 1:1000	Agilent, Santa Clara, CA, USA
Anti-chicken-AlexaFluor594	gt	IF: 1:200	Invitrogen, Waltham, MA, USA
Anti-mouse-AlexaFluor488	gt	IF: 1:200	Invitrogen, Waltham, MA, USA

6.1.5 Kits

Table 13 Kits.

Kit	Supplier
DuoLink® In Situ Probemaker MINUS	Sigma Aldrich Inc., St. Louis, MI, USA
DuoLink® In Situ Detection Reagent Orange	Sigma Aldrich Inc., St. Louis, MI, USA
QIAquick PCR Purification Kit	Qiagen N.V., Venlo, Netherlands
QIAGEN®Plasmid Mini Kit	Qiagen N.V., Venlo, Netherlands
QIAGEN®Plasmid Maxi Kit	Qiagen N.V., Venlo, Netherlands
QIAquick Gel Extraction Kit	Qiagen N.V., Venlo, Netherlands
Pierca BCA assay	Thermo Fisher Scientific, Waltham, MA, USA

6.1.6 Lipids

Table 14 Lipids for synthesis or as analytical standards.

Lipid	Supplier
C18-KDS	Matreya LLC., State College, PA, USA
C24-KDS	Kindly provided by Lukas Opalka
Palmitic acid	Sigma Aldrich Inc., St. Louis, MI, USA
Stearic acid	Sigma Aldrich Inc., St. Louis, MI, USA
Lignoceric acid	Sigma Aldrich Inc., St. Louis, MI, USA
Myristic acid	Sigma Aldrich Inc., St. Louis, MI, USA
pacSph	Kindly gifted by Per Haberkant / Avanti Polar Lipids Inc., Alabaster, AL, USA
Total ganglioside porcine brain	Avanti Polar Lipids Inc., Alabaster, AL, USA
GM2 (Tay-Sachs)	Kindly gifted by the Herbert Wiegandt lab, Marburg
GM3 (bovine milk)	Avanti Polar Lipids Inc., Alabaster, AL, USA
LacCer	Matreya LLC., State College, PA, USA
Neutral GSL mix	Kindly gifted by the Herbert Wiegandt lab, Marburg
Sphingomyelin (isolated porcine brain)	Matreya LLC., State College, PA, USA
pacFA-Cer	Avanti Polar Lipids Inc., Alabaster, AL, USA
pacFA-GlcCer	Avanti Polar Lipids Inc., Alabaster, AL, USA
pacFA-PC	Avanti Polar Lipids Inc., Alabaster, AL, USA
C16-Dihydroceramide	Avanti Polar Lipids Inc., Alabaster, AL, USA

C24-Dihydroceramide	Avanti Polar Lipids Inc., Alabaster, AL, USA
C16-Phytoceramide	Avanti Polar Lipids Inc., Alabaster, AL, USA
C18-Phytoceramide	Avanti Polar Lipids Inc., Alabaster, AL, USA
C24-Phytoceramide	Avanti Polar Lipids Inc., Alabaster, AL, USA
NdK-Cer(m18:0/16:0)	This study and Pilz et al. 2022 Synthesized by me
NdK-Cer(m18:0/24:0)	This study and Pilz et al. 2022 Synthesized by Lukáš Opálka
NdK-Cer(m24:0/14:0)	This study and Pilz et al. 2022 Synthesized by Lukáš Opálka
NdK-Cer(m24:0/16:0)	This study and Pilz et al. 2022 Synthesized by Lukáš Opálka
NdK-Cer(m24:0/24:0)	This study and Pilz et al. 2022 Synthesized by Lukáš Opálka
NdK/NK sphingomyelin mix	This study and Pilz et al. 2022 Synthesized by Adam Majcher
NdS sphingomyelin mix	This study and Pilz et al. 2022 Synthesized by Adam Majcher
NdK-GlcCer(d18:1/24:0)	This study and Pilz et al. 2022 Synthesized by Adam Majcher
NdK-GlcCer(d18:1/24:1)	This study and Pilz et al. 2022 Synthesized by Adam Majcher
(Cyclic) NK-Cer(d18:1/24:1)	This study and Pilz et al. 2022 Synthesized by Adam Majcher

Lipid standards

Table 15 Internal standard mix used for pacLipid LC-MS/MS analysis.

Internal standard	pmol per sample	
Cer(d18:1/14:0)	10	Synthesized by Roger Sandhoff
Cer(d18:1/19:0)	10	Synthesized by Roger Sandhoff
Cer(d18:1/25:0)	10	Synthesized by Roger Sandhoff
Cer(d18:1/31:0)	10	Synthesized by Roger Sandhoff
GlcCer(d18:1/14:0)	10	Synthesized by Roger Sandhoff
GlcCer(d18:1/19:0)	10	Synthesized by Roger Sandhoff
GlcCer(d18:1/25:0)	10	Synthesized by Roger Sandhoff

GlcCer(d18:1/31:0)	10	Synthesized by Roger Sandhoff
SM(d18:1/12:0)	100	Avanti Polar Lipids Inc., Alabaster, AL, USA
SM(d18:1/17:0)	100	Avanti Polar Lipids Inc., Alabaster, AL, USA
SM(d18:1/31:0)	100	Synthesized by Roger Sandhoff
D31-PC(34:1)	100	Avanti Polar Lipids Inc., Alabaster, AL, USA
Gb3Cer(d18:1/19:0)*	10	Synthesized by Roger Sandhoff
LacCer(d18:1/14:0)*	5	Synthesized by Roger Sandhoff
LacCer(d18:1/19:0)*	5	Synthesized by Roger Sandhoff
LacCer(d18:1/27:0)*	5	Synthesized by Roger Sandhoff

* not used in all measurements as internal standard and quantification by external standards

Table 16 Internal standard mix used for skin ceramide LC-MS/MS analysis

Internal standard	pmol per sample	
GlcCer(d18:1/14:0)	12.5	Synthesized by Roger Sandhoff
GlcCer(d18:1/19:0)	12.5	Synthesized by Roger Sandhoff
GlcCer(d18:1/25:0)	12.5	Synthesized by Roger Sandhoff
GlcCer(d18:1/31:0)	12.5	Synthesized by Roger Sandhoff
Cer(d18:1/14:0)	20	Synthesized by Roger Sandhoff
Cer(d18:1/19:0)	20	Synthesized by Roger Sandhoff
Cer(d18:1/25:0)	20	Synthesized by Roger Sandhoff
Cer(d18:1/31:0)	20	Synthesized by Roger Sandhoff
SM(d18:1/12:0)	10	Avanti Polar Lipids Inc., Alabaster, AL, USA
SM(d18:1/17:0)	10	Avanti Polar Lipids Inc., Alabaster, AL, USA
SM(d18:1/31:0)	10	Synthesized by Roger Sandhoff
C12-KDS	125	Matreya LLC., State College, PA, USA
C17-Sphinganine	87	Avanti Polar Lipids Inc., Alabaster, AL, USA
C14-Sphingosine	51.5	Avanti Polar Lipids Inc., Alabaster, AL, USA
NdK-Cer(m18:0/14:0)	20.5	This study and Pilz et al. 2022 Synthesized by Lukáš Opálka
PC(24:0)	40	Avanti Polar Lipids Inc., Alabaster, AL, USA
PC(28:0)	37	Avanti Polar Lipids Inc., Alabaster, AL, USA
PC(44:0)	28	Avanti Polar Lipids Inc., Alabaster, AL, USA
PC(48:0)	26	Avanti Polar Lipids Inc., Alabaster, AL, USA

6.2 Methods – Chapter 1

6.2.1 Cell culture and Cloning

Cell Lines

Cell Line	Origin	Source	Genetic Modifications
HEK293	Human embryonic kidney	In house	WT
HEK293 ΔGb3S	Human embryonic kidney	This study	ΔGb3S
HK-2	Immortalized human proximal tubular epithelial cell line	(185) ATCC #CRL-2190	WT
HK-2 ΔGb3S	Immortalized human proximal tubular epithelial cell line	This study	ΔGb3S
HK-2 ΔS1PL	Immortalized human proximal tubular epithelial cell line	This study; Generation assisted by Emily Steffke	ΔS1PL
HK-2 ΔS1PL/ΔGb3S	Immortalized human proximal tubular epithelial cell line	This study	ΔS1PL/ΔGb3S

Cultivation of the HEK293T cell lines

HEK293T cells were cultured at 37°C and 5% CO2 in a humidified incubator. Iscove's modified Dulbecco media (IMDM) with 10% fetal calf serum (FCS) and 1% penicillin/streptomycin (P/S) was used as culture medium. HEK293 cells were cultured as adherent cells and in monolayers. At 80% confluence the cells were subcultured and split at a 1:10 ratio in new cell culture flasks. In brief, cell layers were washed once with prewarmed 1X phosphate-buffered saline (PBS) and trypsinated with Trypsin-EDTA solution (0.05% Trypsin, 0.5mM EDTA) for 5 min at 37°C. The detached cells were suspended in IMDM (10% FCS, 1% P/S) to quench the enzymatic reaction and pelleted by centrifugation at 160 x g for 5 min at room temperature. The cell pellet was resuspended in fresh IMDM (10% FCS, 1% P/S) and seeded at a 1:10 split ratio into new cell culture flasks.

Cultivation of the HK-2 cell lines

HK-2 cells were cultured at 37°C and 5% CO2 in a humidified incubator. Dulbecco's modified Eagle medium/F-12 (DMEM/F-12) with 10% FCS and 100 U/mL penicillin and 100 µg/mL streptomycin was used as culture medium. HK-2 cells were cultured as adherent cells and in monolayers. Cells were subcultured at 80% confluence and split twice a week at a 1:10 or 1:4 ratio in new cell culture flasks. In

brief, cell layers were washed once with prewarmed 1X phosphate-buffered saline (PBS) and trypsinated with Trypsin-EDTA solution (0.05% Trypsin, 0.5mM EDTA) for 5 min at 37°C. The detached cells were suspended in DMEM/F-12 (10% FCS, 1% P/S) to quench the enzymatic reaction and pelleted by centrifugation at 160 xg for 5 min at room temperature. The cell pellet was resuspended in fresh DMEM/F-12 (10% FCS, 1% P/S) and seeded at a 1:10 or 1:4 split ratio into new plates.

Cell counting

Counting of cells was performed using a CASY cell counter and analyzer. Trypsinated cells were resuspended by pipetting and diluted 1:200 in isotonic CASYton buffer in CASYcups. Before measurement, CASYcups were inverted three times. Samples were measured according to the manufacturer's instructions and the instrument was cleaned three times with CASYton after the measurement.

Cryopreservation and Thawing

Cells were seeded in culture dishes of an appropriate size to yield a sufficient number of cells at 90% confluence. Cell detachment was performed as described for the respective cell lines. After centrifugation cells were resuspended in freeze medium (FCS, 10% DMSO) and frozen at -80°C with a rate of approximately 1°C/min using a precooled (4°C), 2-propanol-filled *Mr. Frosty* device. For long-term storage cryopreserved vials were transferred to and stored in the vapor phase of a liquid nitrogen tank.

For thawing cell vials were obtained from the storage location. The cells were thawed rapidly in a 37°C water bath and immediately diluted in prewarmed (37°C), full medium. The thawed cells were centrifugated at 160 x g for 5 min at room temperature. The pellet was resuspended in full medium and seeded into appropriate cell culture flasks. The next day, medium was exchanged to remove cell debris.

Mycoplasma testing

Mycoplasma testing was performed by PCR using the Venor™ GeM mycoplasma detection kit (MP-0025) according to the manufacturer's instructions using cell culture supernatant.

Transfection of HK-2 cells

For overexpression and delivery of CRISPR/Cas9 targeting constructs HK-2 cells were transfected using the calcium phosphate method (369, 370). Target cells were seeded into 6-well plates to reach 50% - 70% confluence after one day of cultivation. One hour before transfection, media was replenished with full standard growth medium (DMEM/F-12, 10% FCS, 1% P/S). Transfection solutions were prepared as described (Table 17). Slowly and dropwise transfection solution B was added to transfection solution A, while gently snapping the tube to facilitate mixing of the solutions. The final transfection mix was incubated for 25 min at room temperature. After incubation, slowly and dropwise the transfection mix was added to the cells, while gently agitating the plate. Transfection was performed for 24h and afterwards the transfection medium was removed, cells were stringently washed with 1X PBS and standard growth medium was added for further cultivation. If required, selection was started the next day.

Table 17 Calcium phosphate precipitation solutions

Transfection Solution A	
2x HBS	100 µL

Transfection Solution B	
2M $CaCl_2$	12.2 µL
Plasmid DNA	2.5 µg
ddH_2O	To 100 µL

Transfected plasmids

Cells were transfected using the calcium phosphate method with the indicated plasmids (Table 18). Selection was performed using puromycin (4 µg/mL) for 14 days for stable overexpression. Cell lines were expanded, and aliquots were frozen.

Table 18 Plasmids and transfected target cells

Plasmid	Target	Characteristic/Use
px459-empty	HK-2	Cas9, no gRNA, control, Puro
px459-SGPL1-gR1	HK-2	Cas9, gRNA targeting S1PL, Puro
px459-SGPL1-gR2	HK-2	Cas9, gRNA targeting S1PL, Puro
px459-SGPL1-gR3	HK-2	Cas9, gRNA targeting S1PL, Puro

px459-A4GALT-gR1	HK-2	Cas9, gRNA targeting Gb3S, Puro
px459-A4GALT-gR2	HK-2	Cas9, gRNA targeting Gb3S, Puro
px459-A4GALT-gR3	HK-2	Cas9, gRNA targeting Gb3S, Puro
px459-A4GALT-gR1	HK-2 ΔS1PL	Cas9, gRNA targeting Gb3S, Puro
px459-A4GALT-gR2	HK-2 ΔS1PL	Cas9, gRNA targeting Gb3S, Puro
px459-A4GALT-gR3	HK-2 ΔS1PL	Cas9, gRNA targeting Gb3S, Puro
pLVX-puro-empty	HK-2 ΔS1PL	Control, Puro
pLVX-puro-CPM-HA	HK-2 ΔS1PL	Overexpression of CPM-HA, Puro
pLVX-puro-DPP4-HA	HK-2 ΔS1PL	Overexpression of DPP4-HA, Puro
pLVX-puro-SCCPDH-HA	HK-2 ΔS1PL	Overexpression of SCCPDH-HA, Puro
pLVX-puro-empty	HK-2 ΔS1PL/ΔGb3S	Control, Puro
pLVX-puro-CPM-HA	HK-2 ΔS1PL/ΔGb3S	Overexpression of CPM-HA, Puro
pLVX-puro-DPP4-HA	HK-2 ΔS1PL/ΔGb3S	Overexpression of DPP4-HA, Puro
pLVX-puro-SCCPDH-HA	HK-2 ΔS1PL/ΔGb3S	Overexpression of SCCPDH-HA, Puro

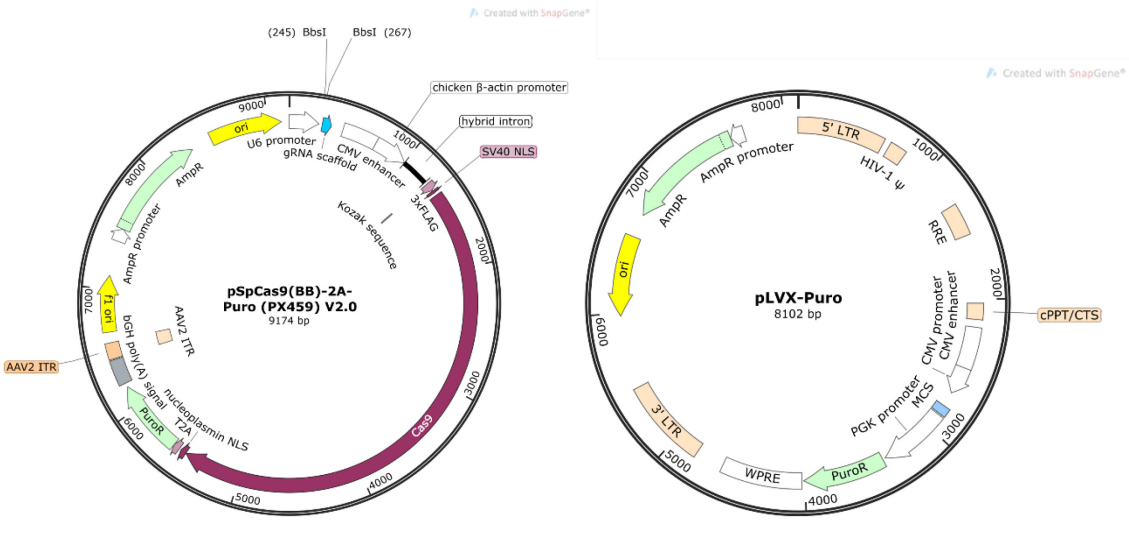

Figure 56 Vector maps of pSpCas9(BB)-2A-Puro (px459) and pLVX-Puro

Generation of CRISPR/Cas9 edited cell lines

Targeting guides were established using the CRISPOR tool (192). For S1PL transcript ID ENST00000373202.8 and for Gb3S transcript ID ENST00000401850.5 from the Ensembl database (371) were obtained and used for guide RNA design as described in section 4.1.2 and 4.1.3. Guide sequence oligos were cloned into the pSpCas9(BB)-2A-Puro (addgene, #PX459) vector backbone (Figure 56), which co-expresses the sgRNA, SpCas9 and a puromycin resistance gene. Target cells were transfected as described. Selection was performed using puromycin (4 µg/mL) in full growth medium for 4 days. Single clones were isolated from the transfected cell population after selection with puromycin (4 days, 4 µg/mL) and expanded in a 96-well plate containing full growth medium. Individual clones were characterized by either glycosphingolipid expression (for Gb3S targeting) or pacSph labelling (for S1PL targeting) by HPTLC and UPLC-MS^2. Genomic loci were analysed by Sanger sequencing and raw sequencing data was evaluated by tracking of indels by decomposition (TIDE) (196).

Isolation of genomic DNA for PCR and sequencing

For DNA isolation from cultured cells 700 µL DNA purification buffer (incl. 10 µL of 10 mg/mL proteinase K) was added to a cell pellet and incubated overnight at 58°C. 300 µL saturated NaCl was added to the cells and mixed. The suspension was centrifuge at 12,000 rpm for 15 min at 4°C. 700 µL of the supernatant were transferred into a fresh reaction tube. RNA was digested by addition of 2 µL RNAse A (2 mg/mL) and incubation at 37°C for 20 min. DNA was precipitated by addition of 700 µL 2-propanol (analysis grade). After mixing and repeated centrifugation, the supernatant was discarded, and the resulting DNA pellet washed with ice-cold ethanol (70%). DNA was dried at room temperature and dissolved in an appropriate amount of dH2O.

Cultivation of bacteria

E. coli DH5α were cultured in lysogenic broth medium (LB medium) or on lysogenic broth agar (LB agar) at 37°C (200 rpm for liquid cultures). If required, ampicillin (Sigma Aldrich, St. Louis, MO, USA) was added as an antibiotic selection marker at 50 - 100 µg/mL.

Table 19 Composition of lysogenic broth medium and agar.

LB Medium (or agar), pH 7.0	%w/v
Tryptone	1
NaCl	0.5
Yeast Extract	0.5
Optional: Agar	1.5

Table 20 Bacterial strain used for cloning.

Bacterial Strain	Characterization	Supplier
E. coli DH5α	F$^-$Φ80*lac*ZΔM15 Δ(*lac*ZYA-*arg*F) U169 *rec*A1 *end*A1 *hsd*R17(r_k^-, m_k^+) *pho*A *sup*E44 *thi*-1 *gyr*A96 *rel*A1 λ$^-$	Thermo Fisher Scientific, Waltham, MA, USA

Generation of chemically competent bacteria

Equipment for the generation of chemically competent bacteria was kept sterile and precooled. *E. coli* DH5α were plated on LB agar and incubated overnight at 37°C. One colony was used to inoculate a 5 mL overnight culture (37°C, 200 rpm) in LB medium. 1 mL of this culture was used to inoculate four times 200 mL LB medium and growth was monitored until an optical density (OD_{550nm}) of 0.3 to 0.4 was reached. Bacterial cultures were spun down (5 min, 2500 rpm, 4°C) and resuspended in precooled transformation buffer (TFB1). Cultures were incubated 10 min on ice and centrifuged again (5 min, 2500 rpm, 4°C). After resuspension of the bacterial pellet in precooled transformation buffer (TFB2), the suspension was incubated on ice for 45 min. Aliquots were prepared and stored at -80°C.

Transformation of chemically competent bacteria

Chemically competent bacteria (*E. coli* DH5α) were thawed on ice. 4 µL of plasmid or ligation mix were added to the bacteria on ice. Bacteria are incubated for 30 min on ice. Heat shock was performed at 42°C for exactly 90 sec. Afterwards, bacteria were incubated on ice for 2 min and 450 µL SOC medium was added before incubation at 37°C and 800 rpm in a thermoshaker for 30 min. An aliquot of the transformation mix was plated onto an agar plate containing a selection marker and incubated over night at 37°C.

Freezing of glycerol stocks

Liquid overnight culture of the desired plasmid producing bacteria were prepared (37°C, 200 rpm). 500 µL of the bacterial culture was added to 500 µL of 50% glycerol in a 2 mL screw-capped tube and gently mixed. Glycerol stocks were frozen at -80°C.

Agarose Gel Electrophoresis

For gel casting, agarose was dissolved in 1X TAE buffer at 1% or 2% (w/v) depending on the size of the DNA by heating in a microwave oven. DNA samples were applied in 1X loading buffer and DNA was visualized using Ethidium bromide or Midori Green Advance DNA stain. Gels were developed for 30 – 40 min at 120V.

Restriction Digest

Restriction digests were performed using the recommended parameters (Table 21). The standard reaction volume was 20 µL with 1 – 2 µg DNA and 2U restriction enzyme. Complete digest was controlled by agarose gel electrophoresis (1% gel) and digested plasmids were purified using QIAGEN gel extraction kit according to the manufacturer instructions.

Table 21 Parameters used for restriction digests.

Restriction enzyme	Digest conditions
*Bbs*I (Thermo Fisher Scientific, Waltham, MA, USA)	2h, 37°C
*EcoR*V conc. (Roche Diagnostics, Basel, Switzerland)	2h, 37°C
*EcoR*I (Invitrogen, Waltham, MA, USA)	2h, 37°C
*BamH*I (Invitrogen, Waltham, MA, USA)	2h, 37°C

Ligation

Ligation was performed using a molar vector-to-insert ratio of 1:4. Ligation was performed with 50 - 100 ng of digested plasmid using T4 DNA Ligase in T4 DNA Ligase buffer for 1h at room temperature followed by transformation of chemically competent *E.coli* DH5α.

Cloning and vector construction for CRISPR-KO

Guide RNA sequences were ordered as single stranded and complementary DNA oligos with overlaps for *Bbs*I restriction-ligation cloning and an additional guanine base for the U6 promoter, if necessary (section 4.1.2 and 4.1.3). Complementary oligos were annealed at a concentration of 100 µM by incubation in a water-filled 2.5 L beaker at 98°C and continuous cooling to 35°C. Correct annealing was controlled by agarose gel electrophoresis (2% gel) and products were purified using the QIAGEN gel extraction kit according to the manufacturer instructions. Restriction digest of pSpCas9(BB)-2A-Puro (addgene, #PX459) plasmid was done with *Bbs*I as described before. Linearization was controlled by agarose gel electrophoresis. Ligation of linearized pSpCas9(BB)-2A-Puro with guide oligo DNA was done using T4 DNA ligase as described. Competent *E.coli* DH5α were transformed as described. Per guide sequence 8 colonies were picked and correct insertion was controlled by colony PCR. One colony per guide sequence was selected for inoculation of an overnight culture (5 mL). Plasmid DNA was extracted using QIAGEN Plasmid Mini kit according to the manufacturer's instructions and a control digest was performed with *Bbs*I and *Eco*RV to ensure insertion of the guide sequence. Increased amount of plasmid DNA were generated in bacterial maxi cultures (200 mL) and extracted using QIAGEN Maxi kit according to the manufacturer instructions.

Cloning of genes for overexpression

Coding DNA sequences of target genes were amplified from pre-isolated cDNA of human kidney by PCR using proofreading Q5 polymerase. Primers were designed to include an HA-tag, a Kozak sequence and *Eco*RI or *Bam*HI restriction cut site for cloning. PCR was performed with 2 µL cDNA, in 50 µL reaction volume (1 µL 10 mM dNTPs, 5 µL 5 µM F/W primer mix, 0.2 µL Q5 polymerase, 10 µL 5X Q5 reaction buffer). PCR products were purified by agarose gel electrophoresis and extracted using a QIAGEN gel extraction kit according to the manufacturer's instructions. Restriction digest and ligation of purified PCR products and pLVX vector was done as described before. Competent *E.coli* DH5α were transformed, and correct insertion was checked by colony PCR as described. Positive colonies were used to inoculate mini cultures and plasmid DNA was extracted using QIAGEN Plasmid mini kit according to the instructions. A control restriction digest

was performed, and correct sequence was confirmed by Sanger sequencing (Eurofins).

Colony PCR

Correct ligation of inserts and vector was checked by colony PCR. Colonies were picked with a sterile pipet tip and briefly dipped into a PCR tube. Parameters for PCR reactions were optimized for each reaction (Table 22). For CRISPR/Cas9 plasmid colony PCRs were performed using hU6-rev and guide-sense as primer pairs.

Table 22 Colony PCR.

Reagent	Volume
Reaction buffer 10x	1.5 µL
dNTPs (10 mM)	0.5 µL
F/R Primer Mix (5 µM)	1.5 µL
Taq polymerase	0.25 µL
filled to 15 µL with nuclease-free water	

Primers and Oligos

Table 23 Primer and oligo sequences.

For guide RNA the targeting sequence highlighted by bold letters.

	Sequence (5'-3')	Application
hU6-rev	CTGCAGACAAATGGCTCTA	Annealing control
A4GALT-gR1-sense	CACCG**CTGCACGGCCGCGTACCAGT**	CRISPR/Cas9 Colony PCR
A4GALT-gR1-antisense	AAAC**ACTGGTACGCGGCCGTGCAG**C	CRISPR/Cas9
A4GALT-gR1+3-fwd	CCGTTGTAGTGGTCCACGAA	gDNA PCR
A4GALT-gR1+3-rev	CTTCTGAGCTGCTTCCCGAA	gDNA PCR
A4GALT-gR2-sense	CACCG**CATGATCTACTGGCACGTTG**	CRISPR/Cas9 Colony PCR
A4GALT-gR2-antisense	AAAC**CAACGTGCCAGTAGATCATG**C	CRISPR/Cas9
A4GALT-gR2-fwd	GACTCCACCGAGCACATGAA	gDNA PCR
A4GALT-gR2-rev	CTCCTGGTCTGATCTGGGGA	gDNA PCR
A4GALT-gR3-sense	CACC**GCCGCGTACCAGTCGGCCAG**	CRISPR/Cas9 Colony PCR
A4GALT-gR3-antisense	AAAC**CTGGCCGACTGGTACGCGGC**	CRISPR/Cas9
A4GALT-gR4-sense	CACC**GGACCAGCACGTGGGATTCG**	CRISPR/Cas9 Colony PCR
A4GALT-gR4-antisense	AAAC**CGAATCCCACGTGCTGGTCC**	CRISPR/Cas9
A4GALT-gR4-fwd	TTCGGGAAGCAGCTCAGAAG	gDNA PCR
A4GALT-gR4-rev	ATCTACTGGCACGTTGTGGG	gDNA PCR
SGPL1-gR1-sense	CACCG**AATCTCTAAGTAGGGCTCAA**	CRISPR/Cas9

		Colony PCR
SGPL1-gR1-antisense	AAAC**TTGAGCCCTACTTAGAGATT**C	CRISPR/Cas9
SGPL1-gR2-sense	CACCG**CCTCTGGAACAGTGTACAGT**	CRISPR/Cas9 Colony PCR
SGPL1-gR2-antisense	AAAC**ACTGTACACTGTTCCAGAGG**C	CRISPR/Cas9
SGPL1-gR3-sense	CACC**GCCTCTATCTTGCGTAGTCC**	CRISPR/Cas9 Colony PCR
SGPL1-gR3-antisense	AAAC**GGACTACGCAAGATAGAGGC**	CRISPR/Cas9
SGPL1-gR3-Exon7-Fwd	GTTGTTCCCTCTTCAGGGTCC	gDNA PCR
SGPL1-gR3-Exon7-Rev	ATCTGGTCCCCCATTGAACAG	gDNA PCR
SGPL1-gR1-Exon3-Fwd	AGAAATGACATTGATATTGGGGGT	gDNA PCR
SGPL1-gR1-Exon3-Rev	TCCTATCTCTCAGCAATTAGTTTGA	gDNA PCR
SGPL1-gR2-Exon6-Fwd	GGCAAGTGAGGTGGAAGACA	gDNA PCR
SGPL1-gR2-Exon6-Rev	AAGTCAGCCAGCTGCATGTT	gDNA PCR
A4GALT_gDNA_F	CCGACGAATTCACCATGTACCCCTACGAC GTCCCCGACTACGCCTCCAAGCCCCCCG	cDNA amplification for subcloning
A4GALT_gDNA_R	TGTGGATCCTCACAAGTACATTTTCATGG CCTCG	cDNA amplification for subcloning
SCCPDH_gDNA_F	CCGACGAATTCACCATGTACCCCTACGAC GTCCCCGACTACGCCGCGACCGAGCAGA GG	cDNA amplification for subcloning
SCCPDH_gDNA_R	TGTGGATCCTCAGACTTCAGAGCTGCTAA TAACACTAAACTCAA	cDNA amplification for subcloning
DPP4_gDNA_F	CCGACGAATTCACCATGTACCCCTACGAC GTCCCCGACTACGCCAAGACACCGTGGA AGGTTCTTC	cDNA amplification for subcloning
DPP4_gDNA_R	TGTGGATCCTCAAGGTAAAGAGAAACATT GTTTTATGAAGTGGC	cDNA amplification for subcloning
CPM_gDNA_F	CCGACGAATTCACCATGTACCCCTACGAC GTCCCCGACTACGCCGACTTCCCGTGCC TCTG	cDNA amplification for subcloning
CPM_gDNA_R	TGTGGATCCTCATTTGAAGAATATGTGCA AAAGACTCACTAAAA	cDNA amplification for subcloning

6.2.2 Protein assays

Metabolic labelling of cultured cells with pacSph

For metabolic labelling pacSph (25 mM ethanoic stock) was diluted to 6 µM (pull-down proteomics) or 0.5 µM (pull-down western blotting and PLA) in DMEM/F-12 (1:1) with 10% charcoal-treated FCS and 1% P/S. Cells were washed once with 1X PBS and labelling medium was added. After 22h the labelling medium was removed, and full growth medium was added for 4h. If inhibitors were used, they were added during the labelling and chase period (5 µM Genz-1233346 or 100 µM Miglustat in dH_2O). For the formation of protein-sphingolipid conjugates the cells

were washed and overlayed with cold 1X PBS and irradiated by UV light (365 nm, 5x 8W, 5 min, BioLinker) on an ice-cooled metal block. After irradiation, cells were washed with 1X PBS and harvested by scraping in 1.4 mL cold 1X PBS. Cells were pelleted at 4000 rpm and 4°C for 4 min and the pellet was either snap-frozen and stored at -80°C or directly used for subsequent analysis.

Pull-down of protein-sphingolipid conjugates for proteomics identification

For each replicate and condition one 10 cm dish of the respective cell line was prepared and grown to confluence. Cells were metabolically labelled with pacSph as described before. Cell pellets were resuspended in 200 µL lysis buffer, vortexed and kept on ice for 30 min. To facilitate lysis, the suspension was ultrasonicated two times for one minute in an ice bath before rotating for 10 min at 25 rpm. Non-bound lipids were removed by 2x methanol/chloroform precipitation as described. The resulting protein pellet was resuspended in 200 µL resolubilization buffer (RB) by vigorous shaking at 37°C till the pellet was dissolved. Insoluble particulates were removed by centrifugation at 14,000 x g at room temperature for 5 min and the protein solution was transferred into a new reaction tube. A 6 µL aliquot was saved for protein determination by Pierce BCA protein assay according to the instructions.

Aliquots of 1 mg total protein were prepared, and volumes adjusted to 200 µL with RB. CuAAC click reactions were prepared as described (Table 24) and incubated at 38°C and 600 rpm for 2h. After the reaction, proteins were precipitated by 2x methanol/chloroform precipitation as described and resolubilized in 200 µL RB.

After click reaction insoluble material was removed by centrifugation with 0.22 µm spin filters (Corning) (14,000 rpm, 10 min, RT). Samples were diluted to 0.2% SDS with SDS-free RB. For enrichment of biotinylated proteins, 200 µL Neutravidin agarose slurry (equivalent to 100 µL beads) per sample were prepared in a reaction tube. Neutravidin agarose was equilibrated with 2x with 1X PBS and 2x with RB (0.2% SDS). Protein solutions were added to the preequilibrated Neutravidin agarose and were incubated at room temperature and 25 rpm for 2h. Neutravidin beads were washed 15x with 1 mL RB and 2x with 1 mL SDS-free RB. Bound proteins were eluted with 300 µL RB supplemented with 2% hydrazine and 0.05% SDS and samples were incubated at room temperature and rotating at 25 rpm for 30 min. Supernatants were collected in fresh reaction tubes, proteins were re-

eluted with 200 µL RB and combined with the first elution. Proteins were precipitated by chloroform/methanol and resolubilized in 40 µL RB for proteomics analysis.

Table 24 CuAAC click reaction for pull-down proteomics.

Compound	Stock	Volume
THPTA	50 mM	100 µL
CuSO4	25 mM	40 µL
Protein	5 mg/mL	200 µL
Dde-PEG4-biotin-azide	50 mM (in DMSO)	20 µL
Sodium ascorbate	1M	1.5 µL
RB	1X	687.5 µL

Pull-down of protein-sphingolipid conjugates for western blotting

For each replicate and condition one 10 cm dish of the respective cell line was prepared and grown to confluence. Cells were metabolically labelled with pacSph as described before. Cell lysis and protein extraction were done as described before.

Aliquots of 200 µg total protein were prepared, and volumes adjusted to 100 µL with resolubilization buffer (RB). CuAAC click reactions were prepared as described (Table 25) and incubated at 38°C and 350 rpm for 3h. After the reaction, proteins were precipitated by 2x chloroform/methanol precipitation as described and resolubilized in 200 µL RB.

Table 25 CuAAC click reaction for western blot analysis.

Compound	Stock	Volume
TBTA	2.5 mM	5 µL
CuSO4	25 mM	5 µL
Protein	5 mg/mL	100 µL
Biotin-PEG3-azide	25 mM (in DMSO)	5 µL
Sodium ascorbate	25 mM	5 µL
RB	1X	5 µL

Insoluble material was removed by centrifugation with 0.22 µm spin filters (Corning) (14,000 rpm, 10 min, RT). An aliquot of 10 µL (5%) was saved as input fraction. Samples were diluted to 0.2% SDS with SDS-free RB. For enrichment of biotinylated proteins, 50 µL Neutravidin agarose per sample were prepared in a reaction tube. Neutravidin agarose was equilibrated with 2x with 1X PBS and 2x

with RB (0.2% SDS). Protein solutions were added to the preequilibrated Neutravidin agarose and were incubated at room temperature and 25 rpm for 2h. Neutravidin beads were washed 15x with 1 mL RB and 2x with 1 mL RB (without SDS). Bound proteins were eluted with 20 µL elution buffer and 10 µL 3x sample buffer by boiling at 95°C for 15 min each. Supernatants were collected in fresh reaction tubes.

SDS-PAGE and Western Blotting

Proteins were separated by one-dimensional and discontinuous SDS-polyacrylamide gel electrophoresis (SDS-PAGE) based on bis-tris gels. Gels for separation (10%) and stacking (5%) were prepared as described (Table 26). Samples were diluted in 3X sample buffer and heated at 95°C for 5 min before loading the gels. Bis-tris gels were run in 1X MOPS running buffer incl. 1X reducing agent at 50 mA const. per gel for approximately one hour.

Table 26 Buffers for casting of SDS-PAGE gels.

Buffer	Composition
3X gel buffer	1M bis-tris, pH 6.5
Resolving gel (10%)	1/3 3X gel buffer, 1/3 acrylamide (30%; 37:5:1), 1/3 ddH2O
Stacking gel (5%)	1/3 3X gel buffer, 1/6 acrylamide (30%; 37:5:1), 3/6 ddH2O

Table 27 Buffers for gel running and western blotting.

Buffer	Composition
5X MOPS running buffer	250 mM MOPS, 250 mM Tris, 5 mM EDTA, 0.5% SDS, no pH adjustment
200X Reducing agent	1M sodium bisulfite
10X Towbin transfer buffer	0.25M Tris-base, 1.92M glycine
1X Transfer buffer	1X Towbin buffer, 20% methanol
Stripping Buffer, pH 7.0	52.5 mM Tris-HCl, 2.1% SDS, 50 mM DTT (fresh)

For protein transfer onto nitrocellulose membranes, the gels were pre-equilibrated in Towbin buffer (20% methanol) for 20 min. Proteins were transferred by wet tank transfer in Towbin buffer (20% methanol) at 350 mA const. for 90 min or 90 mA at 4°C overnight. Membranes were rinsed in 1X TBS-T and blocked with 5% BSA/TBS-T for 1h while gently agitating. Primary antibodies were applied at the indicated dilutions (Table 12) in blocking buffer at 4°C overnight. Membranes were washed 3x 5 min in 1X TBS-T and secondary antibody solutions were applied at the indicated dilutions in blocking buffer and at room temperature for 1h.

Membranes were washed 3x 5 min with TBS-T and 1x 5 min with TBS before detection by either chemiluminescence (Bio-Rad ECL) or fluorescence.

Detection of biotinylated proteins by Neutravidin-HRP

Biotinylation of proteins by CuAAC click reaction was checked by staining with Neutravidin-HRP conjugate. Proteins were separated by SDS-PAGE and transferred onto nitrocellulose as described before. Blocking was done with 5% BSA/TBS-T and membranes were incubated with 1:20,000 Neutravidin-HRP in blocking buffer at 4°C overnight. Biotinylated proteins were detected by chemiluminescence (Bio-Rad ECL).

Proximity ligation assay with pacSph labelled cells

Cells were seeded on untreated glass coverslips in 24 well plates at 35,000 cells per well one day prior to pacSph treatment. After treatment with pacSph (0.5 µM, 22h + 4h) cells were UV irradiated (365nm, 5 min) on an ice-cooled metal block. Cells were fixed with 4% paraformaldehyde (PFA) for 15 min at room temperature. If anti-Gb3Cer antibody was used, fixation was repeated once. After fixation coverslips were washed with 1X PBS and 2x with methanol to remove non-bound lipids. CuAAC click reaction was performed on coverslips with 55 µL of click mix as described (Table 28). The reaction was incubated for 1h at room temperature. Afterwards coverslips were rinsed with 3x with 1X PBS, 2x with methanol and once with ddH_2O. Cells were permeabilized with 0.2% Triton X-100 in PBS for 5 min at room temperature and blocked with DuoLink® Blocking Solution for 1h at 37°C in a humidity chamber.

Table 28 CuAAC click reaction for proximity ligation assay.

Click mix	Final concentration
Sodium ascorbate	1 mM
TBTA	0.1 mM
CuSO4	1 mM
Cy5-azide	0.08 mM

Primary antibodies were applied as indicated (Table 12) diluted in DuoLink® Antibody Diluent. Chicken anti-Gb3Cer antibody was directly labelled with the DuoLink® PLA-MINUS probe with a DuoLink® ProbeMaker kit according to the manufacturer's instructions (DuoLink®, Sigma Aldrich). If anti-Gb3Cer-MINUS

antibody was used, all antibodies were diluted in DuoLink® ProbeMaker Diluent. 40 µL of diluted primary antibodies were applied per coverslip and incubated at 4°C overnight in a humidity chamber. DuoLink® PLA assay was performed according to the instructions. In brief, antibodies with conjugated PLA Probes (PLUS-anti-rabbit and MINUS-anti-mouse) were diluted 1:5 in DuoLink® Antibody Diluent. If anti-Gb3Cer-MINUS antibody was used as a primary antibody, only PLUS-anti-rabbit was added at this step. Coverslips were washed 2x 5 min in 1X DuoLink® Wash Buffer A at room temperature before applying the PLA probe solutions and incubated for 1h at 37°C. PLA probes were ligated at 37°C for 30 min with DuoLink® Ligase. After washing 2x 5min with 1X DuoLink® Wash Buffer A, amplification was performed with DuoLink® In-situ Orange (DUO92007) at 37°C for 100 min. Coverslips were washed in 1X DuoLink® Wash Buffer B and counterstained with phalloidin-CF488A (1:200) and DAPI. Z-stacks were acquired by confocal microscopy with a 40X objective. PLA foci were counted and normalized to the number of DAPI-positive nuclei.

Immunofluorescence studies

Cells were seeded on uncoated glass coverslips at the desired density in a 24 well plate. For fixation, cells were covered with 4% PFA for 15 min at room temperature. Coverslips were washed 3x with 1X PBS for 5 min and blocked with 5% BSA/PBS for 60 min at room temperature. Primary antibodies (Table 12) were prepared in antibody dilution buffer (1% BSA/PBS supplemented with or without 0.1% Triton-X100) and applied to the coverslips overnight at 4°C. Coverslips were washed 3x with 1X PBS for 5 min and fluorophore-conjugated secondary antibodies were applied for 2h at room temperature in the dark. DAPI stock solution was diluted 1:20,000 in PBS. After 3x 5 min 1X PBS wash, DAPI staining solution was applied for 5 min at room temperature in the dark. Coverslips were mounted onto glass slides and left for drying at least 1h at room temperature in the dark. If not imaged immediately, samples were stored at 4°C.

Albumin and gentamicin uptake assays

For uptake assays cells were seeded into 96 well plates at 25,000 cells per well and grown until confluence was reached. The cells were kept serum-free for 24h before the assay. Cells were washed 2x with pre-warmed 1X PBS. FITC-albumin, BSA-TexasRed or gentamicin-TexasRed were diluted in Ringer solution (pH 7.4)

to the indicated concentrations (25 µg/mL, 50 µg/mL or 250 µg/mL) and 200 µL were added to the cells for the indicated time (10 min, 15 min or 30 min). Cells were incubated either at 37°C or 4°C as control. Afterwards cells were washed 4x with cold Ringer solution and 2x with ice-cold 50 mM MES/150 mM NaCl (pH 5.0) buffer. Wash buffers were removed, and the cells were lysed in 100 µL ice-cold 0.1% Triton X-100/20 mM MOPS buffer by incubation on ice for 1h. Fluorescence was measured using a Synergy H1 microplate reader.

StxB-Cy3 uptake assay

Cells were seeded into 96 well plates at 25,000 cells per well and grown until confluence was reached. The cells were kept serum-free 24h before the assay. StxB-Cy3 was diluted to 1 µg/mL in ice-cold complete DMEM/F-12. The cells were washed 2x with pre-warmed 1X PBS and incubated with StxB-Cy3 solution for 30 min at 4°C in the dark. Unbound StxB-Cy3 was removed by washing 3x with ice-cold PBS^{++}. Pre-warmed complete DMEM/F-12 was added and the cells were shifted to 37°C for 10 min. Afterwards, the medium was aspirated and 50 µL ice-cold lysis buffer (0.1% Triton X-100/20 mM MOPS) was added. Cells were shaken on ice for 10 min and fluorescence was measured at λ_{ex} 545 nm and λ_{em} 570 nm using a Synergy H1 microplate reader.

Synthesis of gentamicin-TexasRed

Gentamicin-TexasRed was synthesized as described in (97, 372). In brief, 300 µmol from a 50 mg/mL solution of gentamicin sulphate in 100 mM K_2CO_3/$KHCO_3$ buffer (pH 10) was gently mixed with 3 µmol from 3.9 mM Texas Red-X succinimidyl ester in *N, N*-Dimethylformamide at RT for 8 days. Reversed Phase C-18 cartridges (Waters) were used to separate the conjugated product from unconjugated gentamicin and dye. The fractions were analysed on a silica gel plate and product identity was confirmed by mass spectrometry. The product was lyophilized and quantified by fluorescence. Aliquots were stored at -20°C in the dark.

Chloroform/methanol precipitation

To 200 µL cell suspension, 480 µL methanol, 160 µL chloroform and 640 µL ddH_2O were added and the suspension was vortexed after each addition. After centrifugation at 16,000 x g at room temperature for 5 min, the upper phase was

removed. To the lower phase 300 µL methanol were added and the suspension vortexed. Centrifugation was repeated with the same parameters and the upper phase was removed.

Full proteomics sample preparation

Cells were seeded at 2 x 10^6 cells in a 10 cm dish and grown to 80% to 90% confluence. Cell layers were washed 2x with pre-warmed PBS and harvested by trypsin/EDTA (0.05%/0.5mM). Cells were pelleted by centrifugation (1000 x g, 5 min, 4°C) and washed 3x with 5 mL cold PBS. After the last wash cells were resuspended in 2.5 mL cold PBS and counted using a Casy cell analyzer. An aliquot of 2 x 10^6 cells was transferred into a fresh, precooled 1.5 mL reaction tube and pelleted by centrifugation (4,000 rpm, 4 min, 4°C). Pellets were snap-frozen in liquid nitrogen and stored at -80°C before further analysis.

Proteomics analysis of pull-down fractions and full proteome

Sample preparation and proteomics measurements were done by Dr Per Haberkant (Proteomics Core Facility, EMBL Heidelberg). A description of the methods was provided by Per Haberkant and is indicated by quotation marks. In general, paragraphs that are not written by me, will be phrased by quotation marks.

“LC-MS/MS analysis. Cell pellets were lysed in 200 µl of 50 mM HEPES/NaOH, pH 8.5 supplemented with 1% SDS and protease cocktail inhibitor EDTA-free (Roche, #11873580001). Protein concentration of lysates were determined by BCA protein determination (Pierce, #23225). 10 µg of each lysate were subjected to an in-solution tryptic digest using a modified version of the Single-Pot Solid-Phase-enhanced Sample Preparation (SP3) protocol (PMID: 25358341, PMID: 29565595). Lysates were added to Sera-Mag Beads (Thermo Scientific, #4515-2105-050250, 6515-2105-050250) in 10 µl 15% formic acid and 30 µl of ethanol. Binding of proteins was achieved by shaking for 15 min at room temperature. SDS was removed by 4 subsequent washes with 200 µl of 70% ethanol. Proteins were digested overnight at room temperature with 0.4 µg of sequencing grade modified trypsin (Promega, #V5111) in 40 µl HEPES/NaOH, pH 8.4 in the presence of 1.25 mM TCEP and 5 mM chloroacetamide (Sigma-Aldrich, #C0267). Beads were separated, washed with 10 µl of an aqueous solution of 2% DMSO and the combined eluates were dried down. Peptides were reconstituted in 10 µl of H2O

and reacted for 1 h at room temperature with 80 µg of TMT10plex (Thermo Scientific, #90111) (PMID: 24579773) label reagent dissolved in 4 µl of acetonitrile. Excess TMT reagent was quenched by the addition of 4 µl of an aqueous 5% hydroxylamine solution (Sigma, 438227). Peptides were reconstituted in 0.1 % formic acid, mixed to achieve a 1:1 ratio across all TMT-channels and purified by a reverse phase clean-up step (OASIS HLB 96-well µElution Plate, Waters #186001828BA). Peptides were subjected to an off-line fractionation under high pH conditions (PMID: 25358341). The resulting 12 fractions were then analysed by LC-MS/MS on an Orbitrap Fusion Lumos mass spectrometer (Thermo Scentific) as previously described (PMID:30858367). To this end, peptides were separated using an Ultimate 3000 nano RSLC system (Dionex) equipped with a trapping cartridge (Precolumn C18 PepMap100, 5 mm, 300 µm i.d., 5 µm, 100 Å) and an analytical column (Acclaim PepMap 100. 75 × 50 cm C18, 3 mm, 100 Å) connected to a nanospray-Flex ion source. The peptides were loaded onto the trap column at 30 µl per min using solvent A (0.1% formic acid) and eluted using a gradient from 2 to 40% Solvent B (0.1% formic acid in acetonitrile) over 2 h at 0.3 µl per min (all solvents were of LC-MS grade). The Orbitrap Fusion Lumos was operated in positive ion mode with a spray voltage of 2.4 kV and capillary temperature of 275 °C. Full scan MS spectra with a mass range of 375–1500 m/z were acquired in profile mode using a resolution of 120,000 (maximum fill time of 50 ms or a maximum of 4e5 ions (AGC) and a RF lens setting of 30%. Fragmentation was triggered for 3 s cycle time for peptide like features with charge states of 2–7 on the MS scan (data-dependent acquisition). Precursors were isolated using the quadrupole with a window of 0.7 m/z and fragmented with a normalized collision energy of 38. Fragment mass spectra were acquired in profile mode and a resolution of 30,000 in profile mode. Maximum fill time was set to 64 ms or an AGC target of 1e5 ions). The dynamic exclusion was set to 45 s.

Acquired data were analysed using IsobarQuant (PMID: 26379230) and Mascot V2.4 (Matrix Science) using a reverse UniProt FASTA Homo sapiens database (UP000005640) including common contaminants. The following modifications were taken into account: Carbamidomethyl (C, fixed), TMT10plex (K, fixed), Acetyl (N-term, variable), Oxidation (M, variable) and TMT10plex (N-term, variable). The mass error tolerance for full scan MS spectra was set to 10 ppm and for MS/MS

spectra to 0.02 Da. A maximum of 2 missed cleavages were allowed. A minimum of 2 unique peptides with a peptide length of at least seven amino acids and a false discovery rate below 0.01 were required on the peptide and protein level (PMID: 25987413)."

Bioinformatic analysis of proteomics data

Bioinformatic analysis of proteomics data were provided by Dr Frank Stein (Proteomics Core Facility, EMBL Heidelberg). A description of the methods was provided by Frank Stein and is indicated by quotation marks.

"The raw output files of IsobarQuant (protein.txt – files) were processed using the R programming language (ISBN 3-900051-07-0). Only proteins that were quantified with at least two unique peptides were considered for the analysis. Raw signal-sums (signal_sum columns) were first cleaned for batch effects using limma (PMID: 25605792) and further normalized using vsn (variance stabilization normalization - PMID: 12169536). During the normalization of IP conditions, separate coefficients were estimated for cross-link and non-cross-link conditions in order to maintain abundance differences. Proteins were tested for differential expression using the limma package. The replicate information was added as a factor in the design matrix given as an argument to the 'lmFit' function of limma. A protein was annotated as a hit with a false discovery rate (fdr) smaller 5 % and a fold-change of at least 100 % and as a candidate with a fdr below 20 % and a fold-change of at least 50 %."

6.2.3 Lipid assays

Lipid extraction from cultured cells for pacLipid analysis

Cells were seeded in 6 cm dishes to the desired density and treatments were performed as indicated. Cell layers were washed 2x with PBS and harvest by scraping in 1 mL cold PBS. Suspended cells were collected in 1.5 mL reaction tubes and pelleted by centrifugation (4,000 rpm, 4 min, 4°C). If necessary, cell pellets were stored at this step by freezing to -80°C. Cell pellets were resuspended in 300 µL cold PBS. 600 µL methanol and 150 µL chloroform were added and samples were vortexed after each addition. Precipitating proteins and cell debris were removed by centrifugation (14,000 rpm, 5 min, RT) and used for protein determination by Pierce BCA assay after hydrolysis in 100 µL 1M NaOH. Organic

supernatant was transferred into a fresh 2 mL reaction tube and phase separation was induced by addition of 300 µL chloroform and 600 µL 0.1% acetic acid in H_2O. Samples were vortexed after each addition and centrifuged (14,000 rpm, 5 min, RT). The lower layer was collected and transferred into a new 1.5 mL reaction tube and solvents were evaporated under nitrogen stream at 39°C.

For CuAAC click reaction with coumarin azide and subsequent visualization of pacLipids on a HPTLC plate, the lipid extracts were resuspended in 8 µL chloroform. A CuAAC click mix was prepared (Table 29) and 30 µL of CuAAC click mix were added to the lipid extracts. Dissolving of lipids in chloroform was facilitated by repeated vortexing and spinning with a tabletop centrifuge. CuAAC click reactions were performed at 42°C for 1h. Lipid/CuAAC mixes were directly applied to TLC plates for analysis.

Table 29 CuAAC click reaction for coumarin-TLC.

Compound	Volume
3-azido-7-hydroxycoumarin (44.5 mM)	2.5 µL
Tetrakis(acetonitrile)copper(I)tetrafluoroborate in acetonitrile (10 mM)	250 µL
Ethanol	1 mL

Lipid extraction from cultured cells for glycosphingolipid analysis

For the analysis of their glycosphingolipids by HPTLC or LC-MS/MS cells were seeded into 10 cm dishes and treatments were performed as indicated. Cells were harvested by scraping in 1 mL cold PBS and collect in pre-rinsed screw-capped glass vials on ice. After addition of 3 mL 2-propanol the cell suspension was dried under nitrogen stream at 39°C. All subsequent steps were performed at room temperature. Lipid extraction was carried out by addition of 3 mL chloroform/methanol/water (10:10:1, v/v/v), careful vortexing and sonication for 3 x 3 minutes. After centrifugation at 2,700 x g for 10 minutes the supernatant was transferred into a new pre-rinsed glass vial and dried under nitrogen stream. The pellet was reextracted with chloroform/methanol/water (30:60:8, v/v/v), combined with the first extract and dried under nitrogen stream. The remaining pellet was used for protein determination by Pierce BCA assay after hydrolysis in 0.5 mL 1M NaOH. Alkaline hydrolysis of the lipid extracts was performed with 1 mL 0.1M

potassium hydroxide (KOH) in methanol at 50°C for 3 hours and samples were neutralized by addition of 6 µL glacial acetic acid. The hydrolysed extract was dried under nitrogen stream and reconstituted in 5 mL 0.1M potassium acetate (KAc) by vortexing and 3 x 3 minutes sonication. Lipid extracts were desalted using 200 mg preconditioned RP18 SPE columns (Waters). Samples were loaded onto the columns and tubes washed with 5 mL 0.1M KAc which was added onto the column. Bound lipids were washed with 3 column volumes (cv) ddH_2O and eluted into pre-rinsed glass tubes with 2 cv methanol and 2 cv chloroform/methanol (1:1, v/v). Neutral and acidic glycosphingolipids were then separated using diethylaminoethyl (DEAE) sepharose columns. Desalted extracts were applied onto preconditioned (2 cv methanolic KAc (1M), 2 cv methanol, 2 cv C/M/W (30:60:8)) 200 mg DEAE columns. Neutral lipids in the flow through and from 3 cv methanol washes were collected in pre-rinsed glass tubes. Acidic lipids were eluted with 3 cv 500 mM methanolic KAc (2x) into the dH_2O-rinsed previously used samples tubes. Both extracts were dried under nitrogen stream and acidic lipids were subject to an additional desalting step by RP18 SPE before further analysis.

High-performance thin layer chromatography (HPTLC)

Equivalents of 75 µg or 200 µg protein (as indicated) were spotted on high-performance TLC plates (HPTLC, Silica gel 60 F254, Merck) using an automated TLC loader (Linomat IV, Camag) and plates were developed as indicated. In brief, pacLipid analysis was done by a first run in $CHCl_3$/MeOH/H_2O/AcOH (65:25:4:1) to 50% and a second run in *n*-Hexane/ethyl acetate (1:1) to 100%. Glycosphingolipid analysis was done by a pre-run with chloroform/acetone (1:1) and a run in chloroform/methanol/water (60:35:8) both over the full length of the plate. Glycosphingolipids were visualized by spraying the plate with orcinol reagent and developing at 120°C for 10 minutes. pacLipids were visualized by coumarin fluorescence using a BioRad ChemiDoc MP.

HPTLC Immune Overlay

Samples preparation, lipid extraction and HPTLC separation were done as described. Neutral lipids were separated by chloroform/acetone (1:1) and chloroform/methanol/0.2% $CaCl_2$ (60:35:8) over the full length of the plate. Acidic glycosphingolipids were separated by chloroform/acetone (1:1) and chloroform/methanol/0.2% $CaCl_2$ (45:45:10) over the full length of the plate. Dried

HPTLC plates were fixed in Plexigum solution (0.5% (w/v) isobutyl methacrylate in *n*-Hexane/chloroform) for 2 min. HPTLC plates were air dried under a fume hood for 5 min. Blocking was done with 1% BSA in PBS for 30 min at room temperature. Primary antibodies were diluted in blocking buffer as indicated (Table 12) and 250 µL were applied to the HPTLC plates. Plates were covered with a plastic wrap to ensure even distribution of the antibody solution and incubated in a humidity chamber at 4°C over night. The plates were washed 4x with 0.05% Tween-20/PBS and 1x with 1% BSA/PBS for 5 min each. Secondary antibodies were diluted in blocking buffer and 300 µL were applied to the plates. Plates were covered with plastic wraps and incubated for 2h at room temperature in a humidity chamber. Afterwards, HPTLC plates were washed 5x with 0.05% Tween-20/PBS for 5 min by agitation on a swivel table. For development a SigmaFast™ BCIP®/NBT tablet was dissolved in 10 mL ddH_2O by vortexing and ultrasonication. HPTLC plates were dipped in BCIP/NBT solution and developed until bands appear. Development was stopped by washing in ddH_2O and subsequent drying under air. Visualized bands were recorded and HPTLC plates were destained and defixed with acetone for 5 min. The plate was left to dry under air and glycosphingolipids were visualized by staining with orcinol reagent and development at 120°C for 10 min.

Protein determination

Total protein content was determined from hydrolysed protein pellets (1M NaOH, 37°C, 4h). Protein solutions were diluted 1:10 with ddH_2O and protein content was determined using the Pierce BCA assay in microplate format according to the manufacturer's instructions.

LC-MS/MS analysis

Lipid extracts were dissolved in methanol/H_2O (95:5) for LC-MS/MS analysis and in methanol/H_2O (95:5) + 5 mM ammonium formate for direct injection mass spectrometry (DI-MS).

Equivalents of 100 µg or 250 µg protein were aliquoted into screw-capped GC vials in a total volume of 1 mL and 5 pmol ceramide standards (Cer(d18:1/14:0); Cer(d18:1/19:0); Cer(d18:1/25:0); Cer(d18:1/31:0)), 50 pmol sphingomyelin standard (SM(d18:1/12:0); SM(d18:1/17:0); SM(d18:1/31:0)) and 2.5 pmol

hexosylceramide standards (HexCer(d18:1/14:0); HexCer(d18:1/19:0); HexCer(d18:1/25:0); HexCer(d18:1/31:0)) were added as internal standards.

UPLC-ESI-(QqQ)MS^2 analysis was performed on a Xevo TQ-S tandem mass spectrometer coupled to an automated Acquity I-class UPLC system using an ACQUITY UPLC® CSH C18 100 mm x 2.1 mm (pore size 1.7 µm) column from Waters Corporation. The column was equilibrated in 57% buffer A (50% methanol, 0.1% formic acid, 10 mM ammonium formate) and 43% buffer B (99% 2-propanol, 1% methanol, 0.1% formic acid, 10 mM ammonium formate) and lipids were eluted with increasing amount of buffer B at a flow rate of 0.35 mL/min with the indicated gradient (Table 30). Total method run time was 14 minutes. The column was kept at 60°C.

Table 30: UPLC gradient for pacLipids.

UPLC-MS^2 gradient used for pacLipid analysis. Solvent A (50% methanol, 50% water, 10 mM ammonium formate, 0.1% formic acid, 5 µM citrate) and solvent B (1% methanol, 99% isopropanol, 10 mM ammonium formate, 0.1% formic acid, 5 µM citrate). Additives and solvents were of HPLC-grade.

Time [min]	Flow rate	% A	% B	Type of curve
Initial	0.35	57	43	Initial
0.20	0.35	57	43	Linear (6)
0.40	0.35	50	50	Linear (6)
4.00	0.35	30	70	Linear (6)
10.00	0.35	5	95	Linear (6)
11.00	0.35	5	95	Linear (6)
11.50	0.35	1	99	Linear (6)
12.00	0.35	57	43	Linear (6)
14.00	0.35	57	43	Linear (6)

Detection by MS/MS was done by electron spray ionization in positive mode (ESI+) with multiple reaction monitoring (MRM) mode. The respective transitions for the investigated compounds are described (Table 31). Source temperature was kept at 100°C. Capillary voltage was set to 3.0 kV and cone voltage to 50V.

Direct infusion mass spectrometry was performed with a flow rate of 5 µL/min in parent ion scan, product ion scan, neutral loss, or full scan mode as indicated.

Table 31 Multiple reaction monitoring (MRM) transitions for pacLipid analysis

Compound		Transition		Collision energy [eV]
		Precursor Ion	Product Ion	
Cer	Quantifier	$[M+H]^+$	$[M+H-(H_2O+FA)]^+$ (m/z 264)	25-36
	Quantifier2	$[M+H-H_2O]^+$	$[M+H-(H_2O+FA)]^+$ (m/z 264)	25-36
HexCer	Quantifier	$[M+H]^+$	$[M+H-Hex-(H_2O+FA)]^+$ (m/z 264)	44
LacCer	Quantifier	$[M+H]^+$	$[M+H-2Hex-(H_2O+FA)]^+$ (m/z 264)	44
Gb3Cer	Quantifier	$[M+H]^+$	$[M+H-3Hex-(H_2O+FA)]^+$ (m/z 264)	50
Gb4Cer	Quantifier	$[M+H]^+$	$[M+H-3Hex-HexNAc-(H_2O+FA)]^+$ (m/z 264)	60
SM	Quantifier	[M+H]+	[Phosphocholine+H]+ (m/z 184)	34
PC	Quantifier	[M+H]+	[Phosphocholine+H]+ (m/z 184)	35
pacCer	Quantifier	[M+H]+ (+36u)	$[M+H-(FA+H_2O)-N_2]^+$ (m/z 272.2)	26 - 31
	Quantifier2	$[M+H-H_2O]^+$ (+36u)	$[M+H-(FA+H_2O)-N_2]^+$ (m/z 272.2)	26 - 31
pacHexCer	Quantifier	[M+H]+ (+36u)	$[M+H-Hex-(FA+H_2O)-N_2]^+$ (m/z 272.2)	44
pacLacCer	Quantifier	[M+H]+ (+36u)	$[M+H-2Hex-(FA+H_2O)-N_2]^+$ (m/z 272.2)	44
pacGb3Cer	Quantifier	[M+H]+ (+36u)	$[M+H-3Hex-(FA+H_2O)-N_2]^+$ (m/z 272.2)	44
pacPC	Quantifier	[M+H]+ (+36u)	[Phosphocholine+H]+ (m/z 184)	34
pacSM	Quantifier	[M+H]+ (+36u)	[Phosphocholine+H]+ (m/z 184)	35

6.3 Methods – Chapter 2

6.3.1 Synthesis of lipid standards

Synthesis of 3-ketodihydroceramides

Synthesis was performed as described before (293). “1 mg of C18- or C24-3-ketodihydrosphingosine were mixed with 1.2 equivalents of myristic acid, palmitic acid or lignoceric acid, 3 equivalents HOBT and dried. 0.5 mL of dry THF was added and the reaction mixture was cooled to 0°C in an ice bath. 2 equivalents *N*-(3-dimethylaminopropyl)-*N'*-ethylcarbodiimide were added, the temperature was slowly increased to room temperature and stirred overnight under nitrogen atmosphere. The reaction was quenched with water (0.25 mL) and evaporated to dryness. The crude product was purified by column chromatography on silica with CHCl3/MeOH (50:1).”

Synthesis of (cyclic) 3-ketoceramide, 3-keto(dihydro)sphingomyelin, and 3-keto(dihydro)glucosylceramide

Synthesis was performed as described before (293). Cer(d18:1/16:0) for the synthesis of (cyclic) NK-ceramide, GlcCer(d18:1/16:0) for the synthesis of NK/NdK-glucosylceramides and an isolated (non-hydroxylated) porcine brain sphingomyelin mixture for the synthesis of NK/NdK-sphingomyelin were purchased from Matreya, LLC. The α,β-unsaturated 3-hydroxy group of NS-ceramide, NS sphingomyelin or NS glucosylceramide was oxidized using DDQ. In brief, 500 µg of NS-sphingomyelin was dried in a PTFE-screw capped glass tube and 100 µL of DDQ in anhydrous THF (3% for NS-Cer, 6% NS-GlcCer, 10% for NS-SM (w/v)) was added. The mixture was vortexed and incubated at 37°C for 48 hours. After given time the reaction was diluted with 1 mL chloroform and solid-phase extraction on normal phase silica was performed. Fractions were eluted with 100% chloroform, chloroform/methanol (80:20) and 100% methanol and analysed by TLC.

The NK sphingolipid products were dried under N_2 stream and used for analysis or reduction by Pd/C catalysed hydrogen gas. Cyclization of NK-ceramides by Michael rearrangement was induced by treatment with 0.1M NaOH in methanol/chloroform. For reduction, lipids were dissolved in 1 mL dry methanol and a catalytic amount of 10% (w/w) palladium on charcoal was added. Under

hydrogen atmosphere the reaction was stirred in a Schlenk tube at RT overnight. For solid-phase extraction the reaction mixture was diluted with 2 mL chloroform and elution performed as described before. The NdK sphingolipid reaction product was dried under N_2 stream and used for analysis. Furthermore, NS sphingomyelin was reduced to NdS sphingomyelin as described above.

6.3.2 Sample preparation and lipid extraction

Tape stripping

Tape stripping was done as described before (293). Tape stripping procedures and genetic analysis took place in a diagnostic setting and are in accordance with federal laws / Declaration of Helsinki – Ethical Principles for Medical Research Involving Human Subjects. Patients consent for publication of their images was obtained.

A D-Squame disc (Clinical and Derm LLC., diameter 22 mm) was placed on the skin. The area was marked with four dots to secure consecutive tape stripping. The D-Squame Disc Applicator (Clinical and Derm LLC.) was pressed onto the disc until the pressure of the upcoming screw can be recognized by the thumb and was kept like this for five seconds. The disc was peeled off carefully. In total, 8 (Patient 1) or 6 (Patient 2) consecutive D-Squame discs were collected this way from the same skin location.

Lipid extraction from tape stripping material

A SquameScan 850A (Heiland electronic GmbH, Wetzlar, Germany) was used to determine the relative protein content of the D-Squame discs according to the instructions of the manufacturer.

Two consecutive discs were extracted together with an internal standard mix (Table 16) with 5 mL chloroform/methanol/water (30:60:8) at 37°C in an ultrasonication bath for 15 min. After centrifugation at 3500 g and room temperature for 10 min, 4.5 mL supernatant was transferred into a fresh glass tube and the discs were reextracted. Combined extracts were dried under a gentle nitrogen stream at 45 °C and dissolved in 1 mL chloroform/methanol/water (10:95:5) for ceramide analysis or methanol/water (95:5) for sphingoid base analysis.

For acid methanolysis, 500 µL of HCl_{conc}/water/methanol (8.6:9.4:82 (v/v/v)) were added to dried lipids samples and incubated at 80 °C for 20 h. Afterwards, the solvent was removed under a gentle nitrogen stream at 45°C.

Lipid extraction from skin biopsies

Skin punch biopsies were collected and frozen fresh at -80°C. Skin biopsies were thawed on ice. To separate dermis and epidermis the tissue was submerged in 4 mL dispase solution (2.5 mg/mL in PBS) in the well of a 6-well plate with the epidermal side facing down. The tissue was digested for 16h at 4°C and briefly rinsed in 1X PBS. Epidermis and dermis were mechanically separated using fine forceps and collected in 2 mL tubes for further analysis. Samples were lyophilized, minced with a scalpel and the dry weight was determined.

For the extraction of epidermal and dermal lipids the samples were spiked with 250 µL internal standard mix and 1 mL chloroform/methanol/water mixture (30:60:8) was added together with a stainless-steel bead. Sample disruption was done using a Tissue Lyser II bead mill (Qiagen, LLC.) with 2 x 2 min pulses at 30 Hz. Subsequently, the samples were vortex and ultrasonicated for 5 min at 37°C. After centrifugation at 13000 rpm for 5 min, the supernatant was collected in fresh tubes. The remaining pellet was reextracted with a mixture of chloroform/methanol/water (10:10:1) and combined with the first extract. Samples were dried under a gentle stream of nitrogen at 45°C. For LC-MS/MS analysis dried lipid extracts were redissolved in 1 mL chloroform/methanol/water (10:95:5) and transferred to GC vials.

Lipid extraction from whole blood samples

Whole blood of KDSR patients and a control was collected in ETDA-coated blood collection tubes. 100 µL aliquots were prepared in 2 mL tubes in three technical replicates. To the samples 950 µL of a mixture of 1-butanol/methanol (1:1, 10 mM ammonium formate) and 100 µL of internal standard mixture was added. Samples were ultrasonicated for 5 min at room temperature and centrifuged at 13000 rpm for 10 min. Supernatants were collected and dried under a gentle stream of nitrogen at 45°C. For KDS analysis by LC-MS/MS the samples were reconstituted in 200 µL chloroform/methanol/water/formic acid (10:95:5:1) and transferred to GC vial with inserts.

6.3.3 Lipid analysis

Liquid chromatography-coupled mass spectrometry

Sphingolipids were analysed by UPLC-ESI-MS^2 according to (29, 48) with slight modifications. In brief, sphingolipids were measured in reversed-phase-LC mode. For the analysis of NdK-sphingomyelin 10 mM lithium acetate was added to the flow at a rate of 20 µL/mL. In general, 10 µl aliquots were injected. For quantification, lipids were detected in MRM mode (Table 34).

UPLC-ESI-(QqQ)MS^2 analysis was performed on a Xevo TQ-S tandem mass spectrometer coupled to an automated ACQUITY I class UPLC system using an ACQUITY UPLC® CSH C18 100 mm x 2.1 mm (pore size 1.7 µm) from Waters Corporation. The gradient was run as described (Table 32-Table 33) and total run time was 14 minutes. The column was kept at 60°C. Samples were dissolved in chloroform/methanol/water (10:95:5) for membrane sphingolipid analysis and methanol/water (95:5) for sphingoid base analysis and in general 10 µL of sample (100% injection needle capacity) were injected. Data was recorded in multiple reaction monitoring (MRM) mode with the indicated transitions (Table 34).

Table 32: UPLC gradient for membrane sphingolipids.

LC-MS^2 gradient used for membrane sphingolipid analysis. Solvent A (50% methanol, 50% water, 10 mM ammonium formate, 0.1% formic acid, 5 µM citrate) and solvent B (1% methanol, 99% isopropanol, 10 mM ammonium formate, 0.1% formic acid, 5 µM citrate). Additives and solvents were of HPLC-grade.

Time [min]	Flow rate [mL/min]	% A	% B	Type of curve
Initial	0.35	57	43	Linear (6)
0.20	0.35	57	43	Linear (6)
0.40	0.35	50	50	Linear (6)
4.00	0.35	30	70	Non-linear (7, starting slow)
10.00	0.35	5	95	Linear (6)
11.00	0.35	5	95	Linear (6)
11.50	0.35	1	99	Linear (6)
12.00	0.35	57	43	Linear (6)
14.00	0.35	57	43	Linear (6)

Table 33 UPLC gradient for sphingoid bases.

LC-MS^2 gradient used for free sphingoid base analysis. Solvent A (50% methanol, 50% water, 10 mM ammonium formate, 0.1% formic acid, 5 µM citrate) and solvent B (1% methanol, 99% isopropanol, 10 mM ammonium formate, 0.1% formic acid, 5 µM citrate). Additives and solvents were of HPLC-grade.

Time [min]	Flow rate [mL/min]	% A	% B	Type of curve
Initial	0.35	65	35	Linear (6)
0.2	0.35	65	35	Linear (6)
0.4	0.35	58	42	Linear (6)
4.0	0.35	30	70	Non-linear (7, starting slow)
10	0.35	5	95	Linear (6)
11	0.35	5	95	Linear (6)
11.5	0.35	1	99	Linear (6)
12	0.35	65	35	Linear (6)
14	0.35	65	35	Linear (6)

Table 34 Multiple reaction monitoring (MRM) transitions for skin ceramides

Compound	Transition	Precursor Ion	Product Ion	Collision energy [eV]
KDS	Quantifier	$[M+H]^+$	$[M+H - H_2CO]^+$	15
Sphinganine	Quantifier	$[M+H]^+$	$[M+H - (H_2O+H_2CO)]^+$	12
Sphingosine	Quantifier	$[M+H]^+$	$[M+H - (H_2O+H_2CO)]^+$	8
	+ Quantifier	$[M+H - H_2O]^+$	$[M+H - (H_2O+H_2CO)]^+$	8
NdK-Ceramides	Quantifier	$[M+H]^+$	$[M+H - (FA+H_2CO)]^+$	35-50
	Qualifier	$[M+H]^+$	$[M+H - (FA+H_2O+CO)]^+$	39-57
NK-Ceramides	Quantifier	$[M+H]^+$	$[M+H - (H_2O+FA)]^+$	37-45
	Qualifier	$[M+H]^+$	$[M+H - FA]^+$	37-45
NdS-Ceramides	Quantifier	$[M+H]^+$	$[M+H - FA]^+$	21-31
	Qualifier	$[M+H]^+$	$[M+H - (H_2O+FA)]^+$	25-35
NS-Ceramides	Quantifier	$[M+H]^+$	$[M+H - (H_2O+FA)]^+$	19-29
	+ Quantifier	$[M+H - H_2O]^+$	$[M+H - (H_2O+FA)]^+$	19-29
	Qualifier	$[M+H]^+$	$[M+H - (H_2O+FA)]^+$	19-29
NP-Ceramides	Quantifier	$[M+H]^+$	$[M+H - (H_2O+FA)^+$	25-35
	Qualifier	$[M+H]^+$	$[M+H - FA]^+$	23-32
NH-Ceramides	Quantifier	$[M+H]^+$	$[M+H - (H_2O+FA)]^+$	24-34
	+ Quantifier	$[M+H - H_2O]^+$	$[M+H - (H_2O+FA)]^+$	24-34
	Qualifier	$[M+H]^+$	$[M+H - (H_2O+FA)]^+$	24-34
NS-Sphingomyelin	Quantifier	$[M+H]^+$	$[Phosphocholine+H]^+$ (m/z 184)	35
NdK-Sphingomyelin	Quantifier	$[M+H]^+$	$[Phosphocholine+H]^+$ (m/z 184)	35
	Qualifier	$[M+Li]^+$	$[Phosphocholine+Li]^+$ (m/z 190)	28
NK-Sphingomyelin	Quantifier	$[M+H]^+$	$[Phosphocholine+H]^+$ (m/z 184)	35
	Qualifier	$[M+Li]^+$	$[Phosphocholine+Li]^+$ (m/z 190)	28
NS-HexCer	Quantifier	$[M+H]^+$	$[M+H - (H_2O+FA+Hex)]^+$	44
NdK-HexCer	Quantifier	[M+H]+	$[M+H - (FA+H_2CO+Hex)]^+$	47-57
	Qualifier	[M+H]+	$[M+H - (FA+H_2O+Hex)]^+$	30-36
NK-HexCer	Quantifier	[M+H]+	$[M+H - (FA+H_2O+Hex)]^+$	30-36
	Qualifier	[M+H]+	$[M+H - (FA+Hex)]^+$	30-36

6.3.4 Sequencing analysis of KDSR patients

KDSR patient 2 was identified and sequenced by Prof Dr Judith Fischer (University Hospital Freiburg).

Sequencing and mutation analysis of patient 1 was described by (21). “Patient 2 mutation analysis was performed using next generation amplicon-sequencing (HaloPlex Custom Kit, Agilent Technologies, Inc. Santa Clara, CA, USA) on the MiSeq system (paired-end 2x150bp, Illumina, San Diego, CA, USA). The mutations found in *KDSR* (NM_0002035) and *KRT17* (NM_000422) were validated by Sanger sequencing. Bioinformatics analysis was done using the commercial software SeqNext (JSI medical systems) and an in-house bioinformatics pipeline (analysis of coding sequences +/- 20 bp at intron/exon boundaries). Exons, which did not fulfill the minimal quality criteria (coverage <20x) have not been resequenced by Sanger sequencing. Classification of detected sequence variants was performed according to the standards and guidelines of the ACMG (American College of Medical Genetics and Genomics, (46)) and nomenclature of detected sequence variants according to HGVS Nomenclature v15.11(47).” (293)

7 References

1. Harayama,T. and Riezman,H. (2018) Understanding the diversity of membrane lipid composition. *Nature Reviews Molecular Cell Biology 2018 19:5*, **19**, 281–296.
2. van Meer,G., Voelker,D.R. and Feigenson,G.W. (2008) Membrane lipids: where they are and how they behave. *Nat Rev Mol Cell Biol*, **9**, 112–124.
3. Quehenberger,O., Armando,A.M., Brown,A.H., Milne,S.B., Myers,D.S., Merrill,A.H., Bandyopadhyay,S., Jones,K.N., Kelly,S., Shaner,R.L., *et al.* (2010) Lipidomics reveals a remarkable diversity of lipids in human plasma. *Journal of Lipid Research*, **51**, 3299–3305.
4. Hannun,Y.A. and Obeid,L.M. (2002) The Ceramide-centric Universe of Lipid-mediated Cell Regulation: Stress Encounters of the Lipid Kind *. *Journal of Biological Chemistry*, **277**, 25847–25850.
5. MacEyka,M. and Spiegel,S. (2014) Sphingolipid metabolites in inflammatory disease. *Nature 2014 510:7503*, **510**, 58–67.
6. Muralidharan,S., Shimobayashi,M., Ji,S., Burla,B., Hall,M.N., Wenk,M.R. and Torta,F. (2021) A reference map of sphingolipids in murine tissues. *Cell Reports*, **35**, 109250.
7. Merrill,A.H. (2002) De Novo Sphingolipid Biosynthesis: A Necessary, but Dangerous, Pathway *. *Journal of Biological Chemistry*, **277**, 25843–25846.
8. Stoffel,W., Sticht,G. and LeKim,D. (1968) Degradation in vitro of Dihydrosphingosine and Dihydrosphingosine phosphate to Palmitaldehyde and Ethanolamine phosphate. *Hoppe-Seyler's Zeitschrift fur Physiologische Chemie*, **349**, 1745–1748.
9. Hanada,K. (2003) Serine palmitoyltransferase, a key enzyme of sphingolipid metabolism. *Biochimica et Biophysica Acta (BBA) - Molecular and Cell Biology of Lipids*, **1632**, 16–30.
10. Tidhar,R. and Futerman,A.H. (2013) The complexity of sphingolipid biosynthesis in the endoplasmic reticulum. *Biochimica et Biophysica Acta (BBA) - Molecular Cell Research*, **1833**, 2511–2518.
11. Kitatani,K., Idkowiak-Baldys,J. and Hannun,Y.A. (2008) The sphingolipid salvage pathway in ceramide metabolism and signaling. *Cellular Signalling*, **20**, 1010–1018.
12. Braun,P.E., Morell,P. and Radin,N.S. (1970) Synthesis of C18- and C20-Dihydrosphingosines, Ketodihydrosphingosines, and Ceramides by Microsomal Preparations from Mouse Brain. *Journal of Biological Chemistry*, **245**, 335–341.
13. Braun,P.E. and Snell,E.E. (1967) The biosynthesis of dihydrosphingosine in cell-free preparations of Hansenula ciferri. *Proc Natl Acad Sci U S A*, **58**, 298–303.
14. Lone,M.A., Hülsmeier,A.J., Saied,E.M., Karsai,G., Arenz,C., von Eckardstein,A. and Hornemann,T. (2020) Subunit composition of the mammalian serine-palmitoyltransferase defines the spectrum of straight and methyl-branched long-chain bases. *Proc Natl Acad Sci U S A*, **117**, 15591–15598.
15. Hornemann,T., Richard,S., Rütti,M.F., Wei,Y. and von Eckardstein,A. (2006) Cloning and initial characterization of a new subunit for mammalian serine-palmitoyltransferase. *J Biol Chem*, **281**, 37275–37281.

16. Hanada,K., Hara,T., Nishijima,M., Kuge,O., Dickson,R.C. and Nagiec,M.M. (1997) A Mammalian Homolog of the Yeast LCB1 Encodes a Component of Serine Palmitoyltransferase, the Enzyme Catalyzing the First Step in Sphingolipid Synthesis *. *Journal of Biological Chemistry*, **272**, 32108–32114.
17. Han,G., Gupta,S.D., Gable,K., Niranjanakumari,S., Moitra,P., Eichler,F., Brown,R.H., Harmon,J.M. and Dunn,T.M. (2009) Identification of small subunits of mammalian serine palmitoyltransferase that confer distinct acyl-CoA substrate specificities. *Proc Natl Acad Sci U S A*, **106**, 8186–8191.
18. Nagiec,M., Baltisberger,J.A., Wells,G.B., Lester,R.L. and Dickson,R.C. (1994) The LCB2 gene of Saccharomyces and the related LCB1 gene encode subunits of serine palmitoyltransferase, the initial enzyme in sphingolipid synthesis. *National Acad Sciences*, **91**, 7899–7902.
19. Zhao,L., Spassieva,S., Gable,K., Gupta,S.D., Shi,L.Y., Wang,J., Bielawski,J., Hicks,W.L., Krebs,M.P., Naggert,J., *et al.* (2015) Elevation of 20-carbon long chain bases due to a mutation in serine palmitoyltransferase small subunit b results in neurodegeneration. *Proc Natl Acad Sci U S A*, **112**, 12962–12967.
20. Stewart,M.E. and Downing,D.T. (1995) Free sphingosines of human skin include 6-hydroxysphingosine and unusually long-chain dihydrosphingosines. *J Invest Dermatol*, **105**, 613–618.
21. Farwanah,H., Pierstorff,B., Schmelzer,C.E.H., Raith,K., Neubert,R.H.H., Kolter,T. and Sandhoff,K. (2007) Separation and mass spectrometric characterization of covalently bound skin ceramides using LC/APCI-MS and Nano-ESI-MS/MS. *Journal of Chromatography B*, **852**, 562–570.
22. Pruett,S.T., Bushnev,A., Hagedorn,K., Adiga,M., Haynes,C.A., Sullards,M.C., Liotta,D.C. and Merrill,A.H. (2008) Biodiversity of sphingoid bases (“sphingosines”) and related amino alcohols. *Journal of Lipid Research*, **49**, 1621–1639.
23. Penno,A., Reilly,M.M., Houlden,H., Laurá,M., Rentsch,K., Niederkofler,V., Stoeckli,E.T., Nicholson,G., Eichler,F., Brown,R.H., *et al.* (2010) Hereditary sensory neuropathy type 1 is caused by the accumulation of two neurotoxic sphingolipids. *Journal of Biological Chemistry*, **285**, 11178–11187.
24. Lone,M.A., Santos,T., Alecu,I., Silva,L.C. and Hornemann,T. (2019) 1-Deoxysphingolipids. *Biochimica et Biophysica Acta (BBA) - Molecular and Cell Biology of Lipids*, **1864**, 512–521.
25. Stoffel,W., LeKim,D. and Sticht,G. (1968) Stereospecificity of the N ADPH-dependent Reduction Reaction of 3-Oxodihydrosphingosine (2-Amino-l-hydroxyoctadecane-3-one). *Hoppe-Seyler’s Zeitschrift fur Physiologische Chemie*, **349**, 1637–1644.
26. Rother,J., Echten,G. van, Schwarzmann,G. and Sandhoff,K. (1992) Biosynthesis of sphingolipids: Dihydroceramide and not sphinganine is desaturated by cultured cells. *Biochemical and Biophysical Research Communications*, **189**, 14–20.

27. Merrill,A.H. and Wang,E. (1986) Biosynthesis of long-chain (sphingoid) bases from serine by LM cells. Evidence for introduction of the 4-trans-double bond after de novo biosynthesis of N-acylsphinganine(s). *Journal of Biological Chemistry*, **261**, 3764–3769.
28. Michel,C., van Echten-Deckert,G., Rother,J., Sandhoff,K., Wang,E. and Merrill,A.H. (1997) Characterization of ceramide synthesis. A dihydroceramide desaturase introduces the 4,5-trans-double bond of sphingosine at the level of dihydroceramide. *J Biol Chem*, **272**, 22432–7.
29. Geeraert,L., Mannaerts,G.P. and van Veldhoven,P.P. (1997) Conversion of dihydroceramide into ceramide: involvement of a desaturase. *Biochemical Journal*, **327**, 125–132.
30. Omae,F., Miyazaki,M., Enomoto,A., Suzuki,M., Suzuki,Y. and Suzuki,A. (2004) DES2 protein is responsible for phytoceramide biosynthesis in the mouse small intestine. *Biochemical Journal*, **379**, 687–695.
31. Enomoto,A., Omae,F., Miyazaki,M., Kozutsumi,Y., Yubisui,T. and Suzuki,A. (2006) Dihydroceramide:sphinganine C-4-hydroxylation requires Des2 hydroxylase and the membrane form of cytochrome b5. *Biochemical Journal*, **397**, 289–295.
32. Ternes,P., Franke,S., Zähringer,U., Sperling,P. and Heinz,E. (2002) Identification and Characterization of a Sphingolipid Δ4-Desaturase Family *. *Journal of Biological Chemistry*, **277**, 25512–25518.
33. Mizutani,Y., Kihara,A., letters,Y.I.-F. and 2004, undefined (2004) Identification of the human sphingolipid C4-hydroxylase, hDES2, and its up-regulation during keratinocyte differentiation. *Wiley Online Library*, **563**, 93–97.
34. Rabionet,M., Gorgas,K. and Sandhoff,R. (2014) Ceramide synthesis in the epidermis. *Biochimica et Biophysica Acta - Molecular and Cell Biology of Lipids*, **1841**, 422–434.
35. Futerman,A.H. and Riezman,H. (2005) The ins and outs of sphingolipid synthesis. *Trends in Cell Biology*, **15**, 312–318.
36. Schulze,H. and Sandhoff,K. (2014) Sphingolipids and lysosomal pathologies. *Biochimica et Biophysica Acta (BBA) - Molecular and Cell Biology of Lipids*, **1841**, 799–810.
37. Stoffel,W., Lekim,D. and Sticht,G. (1969) Distribution and Properties of Dihydrosphingosine-1-phosphate Aldolase (Sphinganine-1-phosphate alkanal-lyase). *Hoppe-Seyler's Zeitschrift fur Physiologische Chemie*, **350**, 1233–1241.
38. Fyrst,H. and Saba,J.D. (2008) Sphingosine-1-phosphate lyase in development and disease: Sphingolipid metabolism takes flight. *Biochimica et Biophysica Acta (BBA) - Molecular and Cell Biology of Lipids*, **1781**, 448–458.
39. Nakahara,K., Ohkuni,A., Kitamura,T., Abe,K., Naganuma,T., Ohno,Y., Zoeller,R.A. and Kihara,A. (2012) The Sjögren-Larsson Syndrome Gene Encodes a Hexadecenal Dehydrogenase of the Sphingosine 1-Phosphate Degradation Pathway. *Molecular Cell*, **46**, 461–471.
40. Venkataraman,K., Riebeling,C., Bodennec,J., Riezman,H., Allegood,J.C., Cameron Sullards,M., Merrill,A.H. and Futerman,A.H. (2002) Upstream of Growth and Differentiation Factor 1 (uog1), a Mammalian Homolog of the Yeast Longevity Assurance Gene 1 (LAG1),

RegulatesN-Stearoyl-sphinganine (C18-(Dihydro)ceramide) Synthesis in a Fumonisin B1-independent Manner in Mammalian Cells *. *Journal of Biological Chemistry*, **277**, 35642–35649.

41. Laviad,E.L., Albee,L., Pankova-Kholmyansky,I., Epstein,S., Park,H., Merrill,A.H. and Futerman,A.H. (2008) Characterization of ceramide synthase 2: Tissue distribution, substrate specificity, and inhibition by sphingosine 1-phosphate. *Journal of Biological Chemistry*, **283**, 5677–5684.
42. Mizutani,Y., Kihara,A. and Igarashi,Y. (2006) LASS3 (longevity assurance homologue 3) is a mainly testis-specific (dihydro)ceramide synthase with relatively broad substrate specificity. *Biochemical Journal*, **398**, 531–538.
43. Jennemann,R., Rabionet,M., Gorgas,K., Epstein,S., Dalpke,A., Rothermel,U., Bayerle,A., van der hoeven,F., Imgrund,S., Kirsch,J., *et al.* (2012) Loss of ceramide synthase 3 causes lethal skin barrier disruption. *Human Molecular Genetics*, **21**, 586–608.
44. Rabionet,M., Bayerle,A., Jennemann,R., Heid,H., Fuchser,J., Marsching,C., Porubsky,S., Bolenz,C., Guillou,F., Gröne,H.J., *et al.* (2015) Male meiotic cytokinesis requires ceramide synthase 3-dependent sphingolipids with unique membrane anchors. *Human Molecular Genetics*, **24**, 4792–4808.
45. Riebeling,C., Allegood,J.C., Wang,E., Merrill,A.H. and Futerman,A.H. (2003) Two Mammalian Longevity Assurance Gene (LAG1) Family Members, trh1 and trh4, Regulate Dihydroceramide Synthesis Using Different Fatty Acyl-CoA Donors *. *Journal of Biological Chemistry*, **278**, 43452–43459.
46. Mizutani,Y., Kihara,A. and Igarashi,Y. (2005) Mammalian Lass6 and its related family members regulate synthesis of specific ceramides. *Biochemical Journal*, **390**, 263–271.
47. Kihara,A. (2016) Synthesis and degradation pathways, functions, and pathology of ceramides and epidermal acylceramides. *Progress in Lipid Research*, **63**, 50–69.
48. D'Angelo,G., Capasso,S., Sticco,L. and Russo,D. (2013) Glycosphingolipids: Synthesis and functions. *FEBS Journal*, **280**, 6338–6353.
49. Yamashita,T., Wada,R., Sasaki,T., Deng,C., Bierfreund,U., Sandhoff,K. and Proia,R.L. (1999) A vital role for glycosphingolipid synthesis during development and differentiation. *National Acad Sciences*, **96**, 9142–9147.
50. Futerman,A.H. and Pagano,R.E. (1991) Determination of the intracellular sites and topology of glucosylceramide synthesis in rat liver. *Biochemical Journal*, **280**, 295–302.
51. Gault,C.R., Obeid,L.M. and Hannun,Y.A. (2010) An Overview of Sphingolipid Metabolism: From Synthesis to Breakdown. In *Advances in Experimental Medicine and Biology*.pp. 1–23.
52. Hanada,K., Kumagai,K., Yasuda,S., Miura,Y., Kawano,M., Fukasawa,M. and Nishijima,M. (2003) Molecular machinery for non-vesicular trafficking of ceramide. *Nature 2004 426:6968*, **426**, 803–809.
53. Buton,X., Hervé,P., Kubelt,J., Tannert,A., Burger,K.N.J., Fellmann,P., Müller,P., Herrmann,A., Seigneuret,M. and Devaux,P.F. (2002) Transbilayer movement of monohexosylsphingolipids in endoplasmic reticulum and Golgi membranes. *Biochemistry*, **41**, 13106–13115.

54. D'Angelo,G., Rega,L.R. and de Matteis,M.A. (2012) Connecting vesicular transport with lipid synthesis: FAPP2. *Biochim Biophys Acta*, **1821**, 1089–95.

55. D'Angelo,G., Polishchuk,E., Tullio,G. di, Santoro,M., Campli,A. di, Godi,A., West,G., Bielawski,J., Chuang,C.-C., van der Spoel,A.C., *et al.* (2007) Glycosphingolipid synthesis requires FAPP2 transfer of glucosylceramide. *Nature*, **449**, 62–67.

56. Budani,M., Auray-Blais,C. and Lingwood,C. (2021) ATP-binding cassette transporters mediate differential biosynthesis of glycosphingolipid species. *Journal of Lipid Research*, **62**, 100128.

57. Yamaji,T. and Hanada,K. (2015) Sphingolipid Metabolism and Interorganellar Transport: Localization of Sphingolipid Enzymes and Lipid Transfer Proteins. *Traffic*, **16**, 101–122.

58. Kojima,Y., Fukumoto,S., Furukawa,K., Okajima,T., Wiels,J., Yokoyama,K., Suzuki,Y., Urano,T., Ohta,M. and Furukawa,K. (2000) Molecular Cloning of Globotriaosylceramide/CD77 Synthase, a Glycosyltransferase That Initiates the Synthesis of Globo Series Glycosphingolipids. *Journal of Biological Chemistry*, **275**, 15152–15156.

59. Yamaji,T., Sekizuka,T., Tachida,Y., Sakuma,C., Morimoto,K., Kuroda,M. and Hanada,K. (2019) A CRISPR Screen Identifies LAPTM4A and TM9SF Proteins as Glycolipid-Regulating Factors. *iScience*, **11**, 409–424.

60. Tian,S., Muneeruddin,K., Choi,M.Y., Tao,L., Bhuiyan,R.H., Ohmi,Y., Furukawa,K., Furukawa,K., Boland,S., Shaffer,S.A., *et al.* (2018) Genome-wide CRISPR screens for Shiga toxins and ricin reveal Golgi proteins critical for glycosylation. *PLOS Biology*, **16**, e2006951.

61. Pacheco,A.R., Lazarus,J.E., Sit,B., Schmieder,S., Lencer,W.I., Blondel,C.J., Doench,J.G., Davis,B.M. and Waldor,M.K. (2018) CRISPR screen reveals that EHEC's T3SS and Shiga toxin rely on shared host factors for infection. *Am Soc Microbiol*, **9**.

62. Kok,K., Zwiers,K.C., Boot,R.G., Overkleeft,H.S., Aerts,J.M.F.G. and Artola,M. (2021) Fabry Disease: Molecular Basis, Pathophysiology, Diagnostics and Potential Therapeutic Directions. *Biomolecules 2021, Vol. 11, Page 271*, **11**, 271.

63. Aerts,J.M., Groener,J.E., Kuiper,S., Donker-Koopman,W.E., Strijland,A., Ottenhoff,R., van Roomen,C., Mirzaian,M., Wijburg,F.A., Linthorst,G.E., *et al.* (2008) Elevated globotriaosylsphingosine is a hallmark of Fabry disease. *Proc Natl Acad Sci U S A*, **105**, 2812–2817.

64. Kint,J.A. (1970) Fabry's disease: Alpha-galactosidase deficiency. *Science (1979)*, **167**, 1268–1269.

65. Mathow,D., Chessa,F., Rabionet,M., Kaden,S., Jennemann,R., Sandhoff,R., Gröne,H.-J. and Feuerborn,A. (2015) Zeb1 affects epithelial cell adhesion by diverting glycosphingolipid metabolism. *EMBO Rep*, **16**, 321–331.

66. Lopez,P.H. and Schnaar,R.L. (2009) Gangliosides in cell recognition and membrane protein regulation. *Current Opinion in Structural Biology*, **19**, 549–557.

67. Herzer,S., Meldner,S., Rehder,K., Gröne,H.J. and Nordström,V. (2016) Lipid microdomain modification sustains neuronal viability in models of Alzheimer's disease. *Acta Neuropathologica Communications*, **4**, 1–20.

68. Yu,R.K., Tsai,Y.T. and Ariga,T. (2012) Functional roles of gangliosides in Neurodevelopment: An overview of recent advances. *Neurochemical Research*, **37**, 1230–1244.

69. Tagami,S., Inokuchi,J.I., Kabayama,K., Yoshimura,H., Kitamura,F., Uemura,S., Ogawa,C., Ishii,A., Saito,M., Ohtsuka,Y., *et al.* (2002) Ganglioside GM3 Participates in the Pathological Conditions of Insulin Resistance *. *Journal of Biological Chemistry*, **277**, 3085–3092.

70. Hakomori,S.I., Handa,K., Iwabuchi,K., Yamamura,S. and Prinetti,A. (1998) New insights in glycosphingolipid function: “Glycosignaling domain,” a cell surface assembly of glycosphingolipids with signal transducer molecules, involved in cell adhesion coupled with signaling [1]. *Glycobiology*, **8**, xi–xviii.

71. Hakomori,S., biochemistry,Y.I.-T. journal of and 1995, undefined (1995) Functional role of glycosphingolipids in cell recognition and signaling. *academic.oup.com*, **118**, 1091–1103.

72. Yamashita,T., Wada,R., Sasaki,T., Deng,C., Bierfreund,U., Sandhoff,K. and Proia,R.L. (1999) A vital role for glycosphingolipid synthesis during development and differentiation. *Proc Natl Acad Sci U S A*, **96**, 9142–9147.

73. Kumagai,T., Tanaka,M., Yokoyama,M., Sato,T., Shinkai,T. and Furukawa,K. (2009) Early lethality of β-1,4-galactosyltransferase V-mutant mice by growth retardation. *Biochemical and Biophysical Research Communications*, **379**, 456–459.

74. Yoshihara,T., Satake,H., Nishie,T., Okino,N., Hatta,T., Otani,H., Naruse,C., Suzuki,H., Sugihara,K., Kamimura,E., *et al.* (2018) Lactosylceramide synthases encoded by B4galt5 and 6 genes are pivotal for neuronal generation and myelin formation in mice. *PLOS Genetics*, **14**, e1007545.

75. Yamashita,T., Hashiramoto,A., Haluzik,M., Mizukami,H., Beck,S., Norton,A., Kono,M., Tsuji,S., Daniotti,J.L., Werth,N., *et al.* (2003) Enhanced insulin sensitivity in mice lacking ganglioside GM3. *Proceedings of the National Academy of Sciences*, **100**, 3445–3449.

76. Coetzee,T., Fujita,N., Dupree,J., Shi,R., Blight,A., Suzuki,K., Suzuki,K. and Popko,B. (1996) Myelination in the Absence of Galactocerebroside and Sulfatide: Normal Structure with Abnormal Function and Regional Instability. *Cell*, **86**, 209–219.

77. Kuan,C.T., Chang,J., Mansson,J.E., Li,J., Pegram,C., Fredman,P., McLendon,R.E. and Bigner,D.D. (2010) Multiple phenotypic changes in mice after knockout of the B3gnt5 gene, encoding Lc3 synthase - A key enzyme in lacto-neolacto ganglioside synthesis. *BMC Developmental Biology*, **10**, 1–20.

78. Okuda,T., Tokuda,N., Numata,S., Ito,M., Ohta,M., Kawamura,K., Wiels,J., Urano,T., Tajima,O., Furukawa,K., *et al.* (2006) Targeted Disruption of Gb3/CD77 Synthase Gene Resulted in the Complete Deletion of Globo-series Glycosphingolipids and Loss of Sensitivity to Verotoxins. *Journal of Biological Chemistry*, **281**, 10230–10235.

79. Hamamura,K., Hamajima,K., Yo,S., Mishima,Y., Furukawa,K., Uchikawa,M., Kondo,Y., Mori,H., Kondo,H., Tanaka,K., *et al.* (2019) Deletion of Gb3 Synthase in Mice Resulted in the Attenuation of Bone Formation via Decrease in Osteoblasts. *International Journal of Molecular Sciences 2019, Vol. 20, Page 4619*, **20**, 4619.

80. Race,R., Sanger,R. and Fisher,R. (1968) Blood groups in man.

81. Miwa,S., Matuhasi,T. and Yasuda,J. (1974) p Phenotype in Two Successive Generations of a Japanese Family. *Vox Sanguinis*, **26**, 565–567.

82. Cantin,G. and Lyonnais,J. (1983) Anti-PP1Pk and early abortion. *Transfusion (Paris)*, **23**, 350–351.

83. Furukawa,K., Iwamura,K., Uchikawa,M., Sojka,B.N., Wiels,J., Okajima,T., Urano,T. and Furukawa,K. (2000) Molecular Basis for the p Phenotype: IDENTIFICATION OF DISTINCT AND MULTIPLE MUTATIONS IN THE α1,4-GALACTOSYLTRANSFERASE GENE IN SWEDISH AND JAPANESE INDIVIDUALS *. *Journal of Biological Chemistry*, **275**, 37752–37756.

84. Ojima,T., Shibata,E., Saito,S., Toyoda,M., Nakajima,H., Yamazaki-Inoue,M., Miyagawa,Y., Kiyokawa,N., Fujimoto,J.I., Sato,T., *et al.* (2015) Glycolipid dynamics in generation and differentiation of induced pluripotent stem cells. *Scientific Reports 2015 5:1*, **5**, 1–13.

85. Liang,Y.J., Kuo,H.H., Lin,C.H., Chen,Y.Y., Yang,B.C., Cheng,Y.Y., Yu,A.L., Khoo,K.H. and Yu,J. (2010) Switching of the core structures of glycosphingolipids from globo- and lacto- to ganglio-series upon human embryonic stem cell differentiation. *Proc Natl Acad Sci U S A*, **107**, 22564–22569.

86. Liang,Y.J., Yang,B.C., Chen,J.M., Lin,Y.H., Huang,C.L., Cheng,Y.Y., Hsu,C.Y., Khoo,K.H., Shen,C.N. and Yu,J. (2011) Changes in Glycosphingolipid Composition During Differentiation of Human Embryonic Stem Cells to Ectodermal or Endodermal Lineages. *Stem Cells*, **29**, 1995–2004.

87. Russo,D., della Ragione,F., Rizzo,R., Sugiyama,E., Scalabrì,F., Hori,K., Capasso,S., Sticco,L., Fioriniello,S., de Gregorio,R., *et al.* (2018) Glycosphingolipid metabolic reprogramming drives neural differentiation. *EMBO J*, **37**.

88. Capolupo,L., Khven,I., Lederer,A.R., Mazzeo,L., Glousker,G., Ho,S., Russo,F., Montoya,J.P., Bhandari,D.R., Bowman,A.P., *et al.* (2022) Sphingolipids control dermal fibroblast heterogeneity. *Science (1979)*, **376**.

89. Park,S.Y., Kwak,C.Y., Shayman,J.A. and Kim,J.H. (2012) Globoside promotes activation of ERK by interaction with the epidermal growth factor receptor. *Biochim Biophys Acta*, **1820**, 1141–1148.

90. Chuang,P.K., Hsiao,M., Hsu,T.L., Chang,C.F., Wu,C.Y., Chen,B.R., Huang,H.W., Liao,K.S., Chen,C.C., Chen,C.L., *et al.* (2019) Signaling pathway of globo-series glycosphingolipids and β1,3-galactosyltransferase V (β3GalT5) in breast cancer. *Proc Natl Acad Sci U S A*, **116**, 3518–3523.

91. Jacob,F., Alam,S., Konantz,M., Liang,C.Y., Kohler,R.S., Everest-Dass,A. v., Huang,Y.L., Rimmer,N., Fedier,A., Schotzau,A., *et al.* (2018) Transition of Mesenchymal and Epithelial Cancer Cells Depends on α1-4 Galactosyltransferase-Mediated Glycosphingolipids. *Cancer Research*, **78**, 2952–2965.

92. Nitta,T., Kanoh,H., Inamori,K.I., Suzuki,A., Takahashi,T. and Inokuchi,J.I. (2019) Globo-series glycosphingolipids enhance Toll-like receptor 4-mediated inflammation and play a pathophysiological role in diabetic nephropathy. *Glycobiology*, **29**, 260–268.

93. Kondo,Y., Ikeda,K., Tokuda,N., Nishitani,C., Ohto,U., Akashi-Takamura,S., Ito,Y., Uchikawa,M., Kuroki,Y., Taguchi,R., *et al.* (2013) TLR4-MD-2 complex is negatively regulated by an endogenous ligand, globotetraosylceramide. *Proc Natl Acad Sci U S A*, **110**, 4714–4719.

94. Distler,U., Souady,J., Hülsewig,M., Drmić-Hofman,I., Haier,J., Friedrich,A.W., Karch,H., Senninger,N., Dreisewerd,K., Berkenkamp,S., *et al.* (2009) Shiga Toxin Receptor Gb3Cer/CD77: Tumor-Association and Promising Therapeutic Target in Pancreas and Colon Cancer. *PLOS ONE*, **4**, e6813.

95. Stults,C.L.M., Larsen,R.D. and Macher,B.A. (1995) α1,4Galactosyltransferase activity and Gb3Cer expression in human leukaemia/lymphoma cell lines. *Glycoconjugate Journal 1995 12:5*, **12**, 680–689.

96. Sigal,D.S., Hermel,D.J., Hsu,P. and Pearce,T. (2022) The role of Globo H and SSEA-4 in the development and progression of cancer, and their potential as therapeutic targets. *Future Oncology*, **18**, 117–134.

97. Morace,I., Pilz,R., Federico,G., Jennemann,R., Krunic,D., Nordström,V., von Gerichten,J., Marsching,C., Schießl,I.M., Müthing,J., *et al.* (2019) Renal globotriaosylceramide facilitates tubular albumin absorption and its inhibition protects against acute kidney injury. *Kidney International*, **96**, 327–341.

98. Lakshminarayan,R., Wunder,C., Becken,U., Howes,M.T., Benzing,C., Arumugam,S., Sales,S., Ariotti,N., Chambon,V., Lamaze,C., *et al.* (2014) Galectin-3 drives glycosphingolipid-dependent biogenesis of clathrin-independent carriers. *Nature Cell Biology*, **16**, 595–606.

99. Weisz,O.A. (2021) Endocytic adaptation to functional demand by the kidney proximal tubule. *The Journal of Physiology*, **599**, 3437–3446.

100. Festa,B.P., Berquez,M., Nieri,D. and Luciani,A. (2021) Endolysosomal Disorders Affecting the Proximal Tubule of the Kidney: New Mechanistic Insights and Therapeutics. In. Springer, Berlin, Heidelberg, pp. 1–25.

101. Schuh,C.D., Polesel,M., Platonova,E., Haenni,D., Gassama,A., Tokonami,N., Ghazi,S., Bugarski,M., Devuyst,O., Ziegler,U., *et al.* (2018) Combined structural and functional imaging of the kidney reveals major axial differences in proximal tubule endocytosis. *Journal of the American Society of Nephrology*, **29**, 2696–2712.

102. Limbutara,K., Chou,C.L. and Knepper,M.A. (2020) Quantitative proteomics of all 14 renal tubule segments in rat. *Journal of the American Society of Nephrology*, **31**, 1255–1266.

103. Eshbach,M.L. and Weisz,O.A. (2017) Receptor-Mediated Endocytosis in the Proximal Tubule. *Annu Rev Physiol*, **79**, 425–448.

104. Christensen,E.I., Verroust,P.J. and Nielsen,R. (2009) Receptor-mediated endocytosis in renal proximal tubule. *Pflugers Archiv European Journal of Physiology*, **458**, 1039–1048.

105. Fyfe,J.C., Madsen,M., Højrup,P., Christensen,E.I., Tanner,S.M., de La Chapelle,A., He,Q. and Moestrup,S.K. (2004) The functional cobalamin (vitamin B12)–intrinsic factor receptor is a novel complex of cubilin and amnionless. *Blood*, **103**, 1573–1579.

106. Nagai,J., Christensen,E.I., Morris,S.M., Willnow,T.E., Cooper,J.A. and Nielsen,R. (2005) Mutually dependent localization of megalin and Dab2 in the renal proximal tubule. *American Journal of Physiology - Renal Physiology*, **289**, 569–576.
107. Abbas,Y.M., Wu,D., Bueler,S.A., Robinson,C. v. and Rubinstein,J.L. (2020) Structure of V-ATPase from the mammalian brain. *Science (1979)*, **367**, 1240–1246.
108. Breton,S. and Brown,D. (2013) Regulation of luminal acidification by the V-ATPase. *Physiology*, **28**, 318–329.
109. Perez Bay,A.E., Schreiner,R., Benedicto,I., Paz Marzolo,M., Banfelder,J., Weinstein,A.M. and Rodriguez-Boulan,E.J. (2016) The fast-recycling receptor Megalin defines the apical recycling pathway of epithelial cells. *Nature Communications 2016 7:1*, **7**, 1–15.
110. Devuyst,O. and Luciani,A. (2015) Chloride transporters and receptor-mediated endocytosis in the renal proximal tubule. *The Journal of Physiology*, **593**, 4151–4164.
111. Raghavan,V., Rbaibi,Y., Pastor-Soler,N.M., Carattino,M.D. and Weisz,O.A. (2014) Shear stress-dependent regulation of apical endocytosis in renal proximal tubule cells mediated by primary cilia. *Proc Natl Acad Sci U S A*, **111**, 8506–8511.
112. Christensen,E.I., Kristoffersen,I.B., Grann,B., Thomsen,J.S., Andreasen,A. and Nielsen,R. (2021) A well-developed endolysosomal system reflects protein reabsorption in segment 1 and 2 of rat proximal tubules. *Kidney International*, **99**, 841–853.
113. Simpson,C.L., Patel,D.M. and Green,K.J. (2011) Deconstructing the skin: cytoarchitectural determinants of epidermal morphogenesis. *Nature Reviews Molecular Cell Biology 2011 12:9*, **12**, 565–580.
114. Fuchs,E. and Raghavan,S. (2002) Getting under the skin of epidermal morphogenesis. *Nature Reviews Genetics 2002 3:3*, **3**, 199–209.
115. Watt,F.M. (2002) Role of integrins in regulating epidermal adhesion, growth and differentiation. *The EMBO Journal*, **21**, 3919–3926.
116. Barrandon,Y. and Green,H. (1987) Three clonal types of keratinocyte with different capacities for multiplication. *Proc Natl Acad Sci U S A*, **84**, 2302–2306.
117. Koster,M.I. (2009) Making an Epidermis. *Ann N Y Acad Sci*, **1170**, 7–10.
118. Gallala,H., Macheleidt,O., Doering,T., Schreiner,V. and Sandhoff,K. (2004) Nitric oxide regulates synthesis of gene products involved in keratinocyte differentiation and ceramide metabolism. *European Journal of Cell Biology*, **83**, 667–679.
119. Feingold,K.R. (2007) Thematic review series: Skin Lipids. The role of epidermal lipids in cutaneous permeability barrier homeostasis. *Journal of Lipid Research*, **48**, 2531–2546.
120. Menon,G.K., Feingold,K.R. and Elias,P.M. (1992) Lamellar Body Secretory Response to Barrier Disruption. *Journal of Investigative Dermatology*, **98**, 279–289.
121. Wolff,K. and Holubar,K. (1967) Odland-Körper (Membrane Coating Granules, Keratinosomen) als epidermale Lysosomen. *Archiv für klinische und experimentelle Dermatologie 1967 231:1*, **231**, 1–19.
122. Oren,A., Ganz,T., Liu,L. and Meerloo,T. (2003) In human epidermis, β-defensin 2 is packaged in lamellar bodies. *Experimental and Molecular Pathology*, **74**, 180–182.

123. Candi,E., Schmidt,R. and Melino,G. (2005) The cornified envelope: a model of cell death in the skin. *Nature Reviews Molecular Cell Biology 2005 6:4*, **6**, 328–340.

124. Michel,S., Schmidt,R., Shroot,B. and Reichert,U. (1988) Morphological and Biochemical Characterization of the Cornified Envelopes from Human Epidermal Keratinocytes of Different Origin. *Journal of Investigative Dermatology*, **91**, 11–15.

125. Halprin,K.M. (1972) Epidermal “turnover time”--a re-examination. *Br J Dermatol*, **86**, 14–9.

126. Gelfant,S. (1976) The cell cycle in psoriasis: a reappraisal. *Br J Dermatol*, **95**, 577–90.

127. Denecker,G., Ovaere,P., Vandenabeele,P. and Declercq,W. (2008) Caspase-14 reveals its secrets. *Journal of Cell Biology*, **180**, 451–458.

128. Lampe,M.A., Burlingame,A.L., Whitney,J.A., Williams,M.L., Brown,B.E., Roitman,E. and Elias,P.M. (1983) Human stratum corneum lipids: characterization and regional variations. *Journal of Lipid Research*, **24**, 120–130.

129. Geilen,C.C., Barz,S. and Bektas,M. (2001) Sphingolipid Signaling in Epidermal Homeostasis. *Skin Pharmacology and Physiology*, **14**, 261–271.

130. Masukawa,Y., Narita,H., Shimizu,E., Kondo,N., Sugai,Y., Oba,T., Homma,R., Ishikawa,J., Takagi,Y., Kitahara,T., *et al.* (2008) Characterization of overall ceramide species in human stratum corneum. *Journal of Lipid Research*, **49**, 1466–1476.

131. Pons,A., Timmerman,P., Leroy,Y. and Zanetta,J.P. (2002) Gas-chromatography/mass-spectrometry analysis of human skin constituents as heptafluorobutyrate derivatives with special reference to long-chain bases. *Journal of Lipid Research*, **43**, 794–804.

132. Farwanah,H., Kolter,T. and Sandhoff,K. (2011) Mass spectrometric analysis of neutral sphingolipids: Methods, applications, and limitations. *Biochimica et Biophysica Acta (BBA) - Molecular and Cell Biology of Lipids*, **1811**, 854–860.

133. Hornemann,T., Penno,A., Rütti,M.F., Ernst,D., Kivrak-Pfiffner,F., Rohrer,L. and von Eckardstein,A. (2009) The SPTLC3 Subunit of Serine Palmitoyltransferase Generates Short Chain Sphingoid Bases. *The Journal of Biological Chemistry*, **284**, 26322.

134. Vasireddy,V., Uchida,Y., Salem,N., Kim,S.Y., Mandal,M.N.A., Reddy,G.B., Bodepudi,R., Alderson,N.L., Brown,J.C., Hama,H., *et al.* (2007) Loss of functional ELOVL4 depletes very long-chain fatty acids (≥C28) and the unique ω-O-acylceramides in skin leading to neonatal death. *Hum Mol Genet*, **16**, 471.

135. Sassa,T., Ohno,Y., Suzuki,S., Nomura,T., Nishioka,C., Kashiwagi,T., Hirayama,T., Akiyama,M., Taguchi,R., Shimizu,H., *et al.* (2013) Impaired epidermal permeability barrier in mice lacking elovl1, the gene responsible for very-long-chain fatty acid production. *Mol Cell Biol*, **33**, 2787–2796.

136. Wertz,P.W. and Downing,D.T. (1983) Ceramides of pig epidermis: structure determination. *Journal of Lipid Research*, **24**, 759–765.

137. Ohno,Y., Nakamichi,S., Ohkuni,A., Kamiyama,N., Naoe,A., Tsujimura,H., Yokose,U., Sugiura,K., Ishikawa,J., Akiyama,M., *et al.* (2015) Essential role of the cytochrome P450 CYP4F22 in the production of acylceramide, the key lipid for skin permeability barrier formation. *Proc Natl Acad Sci U S A*, **112**, 7707–12.

138. Ohno,Y., Kamiyama,N., Nakamichi,S. and Kihara,A. (2017) PNPLA1 is a transacylase essential for the generation of the skin barrier lipid ω-O-acylceramide. *Nature Communications*, **8**, 14610.

139. Marekov,L.N. and Steinert,P.M. (1998) Ceramides Are Bound to Structural Proteins of the Human Foreskin Epidermal Cornified Cell Envelope *. *Journal of Biological Chemistry*, **273**, 17763–17770.

140. Rabionet,M., Bayerle,A., Marsching,C., Jennemann,R., Gröne,H.J., Yildiz,Y., Wachten,D., Shaw,W., Shayman,J.A. and Sandhoff,R. (2013) 1-O-acylceramides are natural components of human and mouse epidermis. *Journal of Lipid Research*, **54**, 3312–3321.

141. Motta,S., Monti,M., Sesana,S., Caputo,R., Carelli,S. and Ghidoni,R. (1993) Ceramide composition of the psoriatic scale. *Biochimica et Biophysica Acta (BBA) - Molecular Basis of Disease*, **1182**, 147–151.

142. Mizutani,Y., Mitsutake,S., Tsuji,K., Kihara,A. and Igarashi,Y. (2009) Ceramide biosynthesis in keratinocyte and its role in skin function. *Biochimie*, **91**, 784–790.

143. Holleran,W.M., Takagi,Y. and Uchida,Y. (2006) Epidermal sphingolipids: Metabolism, function, and roles in skin disorders. *FEBS Letters*, **580**, 5456–5466.

144. Wilkening,G., Linke,T. and Sandhoff,K. (1998) Lysosomal degradation on vesicular membrane surfaces. Enhanced glucosylceramide degradation by lysosomal anionic lipids and activators. *J Biol Chem*, **273**, 30271–30278.

145. Feingold,K.R. and Elias,P.M. (2014) Role of lipids in the formation and maintenance of the cutaneous permeability barrier. *Biochimica et Biophysica Acta (BBA) - Molecular and Cell Biology of Lipids*, **1841**, 280–294.

146. Uchida,Y. and Holleran,W.M. (2008) Omega-O-acylceramide, a lipid essential for mammalian survival. *Journal of Dermatological Science*, **51**, 77–87.

147. Hamanaka,S., Hara,M., Nishio,H., Otsuka,F., Suzuki,A. and Uchida,Y. (2002) Human Epidermal Glucosylceramides are Major Precursors of Stratum Corneum Ceramides. *Journal of Investigative Dermatology*, **119**, 416–423.

148. Uchida,Y., Hara,M., Nishio,H., Sidransky,E., Inoue,S., Otsuka,F., Suzuki,A., Elias,P.M., Holleran,W.M., Hamanaka,S., *et al.* (2000) Epidermal sphingomyelins are precursors for selected stratum corneum ceramides. *Journal of Lipid Research*, **41**, 2071–2082.

149. Mizutani,Y., Kihara,A., Chiba,H., Tojo,H. and Igarashi,Y. (2008) 2-Hydroxy-ceramide synthesis by ceramide synthase family: enzymatic basis for the preference of FA chain length. *J Lipid Res*, **49**, 2356–2364.

150. Mizutani,Y., Sun,H., Ohno,Y., Sassa,T., Wakashima,T., Obara,M., Yuyama,K., Kihara,A. and Igarashi,Y. (2013) Cooperative Synthesis of Ultra Long-Chain Fatty Acid and Ceramide during Keratinocyte Differentiation. *PLOS ONE*, **8**, e67317.

151. Kien,B., Grond,S., Haemmerle,G., Lass,A., Eichmann,T.O. and Radner,F.P.W. (2018) ABHD5 stimulates PNPLA1-mediated ω-O-acylceramide biosynthesis essential for a functional skin permeability barrier. *Journal of Lipid Research*, **59**, 2360.

152. Takeichi,T., Hirabayashi,T., Miyasaka,Y., Kawamoto,A., Okuno,Y., Taguchi,S., Tanahashi,K., Murase,C., Takama,H., Tanaka,K., *et al.* (2020) SDR9C7 catalyzes critical dehydrogenation of acylceramides for skin barrier formation. *Journal of Clinical Investigation*, **130**, 890–903.

153. Jobard,F., Lefèvre,C., Karaduman,A., Blanchet-Bardon,C., Emre,S., Weissenbach,J., Özgüc,M., Lathrop,M., Prud'Homme,J.F. and Fischer,J. (2002) Lipoxygenase-3 (ALOXE3) and 12(R)-lipoxygenase (ALOX12B) are mutated in non-bullous congenital ichthyosiform erythroderma (NCIE) linked to chromosome 17p13.1. *Human Molecular Genetics*, **11**, 107–113.

154. Wertz,P.W., Madison,K.C. and Downing,D.T. (1989) Covalently Bound Lipids of Human Stratum Corneum. *Journal of Investigative Dermatology*, **92**, 109–111.

155. Jennemann,R., Sandhoff,R., Langbein,L., Kaden,S., Rothermel,U., Gallala,H., Sandhoff,K., Wiegandt,H. and Gröne,H.-J. (2007) Integrity and Barrier Function of the Epidermis Critically Depend on Glucosylceramide Synthesis. *Journal of Biological Chemistry*, **282**, 3083–3094.

156. Tybulewicz,V.L.J., Tremblay,M.L., Lamarca,M.E., Willemsen,R., Stubblefield,B.K., Winfield,S., Zablocka,B., Sidransky,E., Martin,B.M., Huang,S.P., *et al.* (1992) Animal model of Gaucher's disease from targeted disruption of the mouse glucocerebrosidase gene. *Nature 1992 357:6377*, **357**, 407–410.

157. Amen,N., Mathow,D., Rabionet,M., Sandhoff,R., Langbein,L., Gretz,N., Jäckel,C., Gröne,H.J. and Jennemann,R. (2013) Differentiation of epidermal keratinocytes is dependent on glucosylceramide:ceramide processing. *Human Molecular Genetics*, **22**, 4164–4179.

158. Schmuth,M., Elias,P.M. and Williams,M. (2005) Pathogenesis of the Barrier Abnormalities in Disorders of Cornification. In *Skin Barrier*. CRC Press, pp. 489–530.

159. Doering,T., Holleran,W.M., Potratzt,A., Vielhaber,G., Elias,P.M., Suzuki,K. and Sandhoff,K. (1999) Sphingolipid Activator Proteins Are Required for Epidermal Permeability Barrier Formation *. *Journal of Biological Chemistry*, **274**, 11038–11045.

160. Nakajima,K., Terao,M., Takaishi,M., Kataoka,S., Goto-Inoue,N., Setou,M., Horie,K., Sakamoto,F., Ito,M., Azukizawa,H., *et al.* (2013) Barrier Abnormality Due to Ceramide Deficiency Leads to Psoriasiform Inflammation in a Mouse Model. *Journal of Investigative Dermatology*, **133**, 2555–2565.

161. Eckl,K.M., Tidhar,R., Thiele,H., Oji,V., Hausser,I., Brodesser,S., Preil,M.L., Önal-Akan,A., Stock,F., Müller,D., *et al.* (2013) Impaired Epidermal Ceramide Synthesis Causes Autosomal Recessive Congenital Ichthyosis and Reveals the Importance of Ceramide Acyl Chain Length. *Journal of Investigative Dermatology*, **133**, 2202–2211.

162. Zhang,K., Kniazeva,M., Han,M., Li,W., Yu,Z., Yang,Z., Li,Y., Metzker,M.L., Allikmets,R., Zack,D.J., *et al.* (2001) A 5-bp deletion in ELOVL4 is associated with two related forms of autosomal dominant macular dystrophy. *Nature Genetics 2001 27:1*, **27**, 89–93.

163. Sugiura,K., Takeichi,T., Tanahashi,K., Ito,Y., Kosho,T., Saida,K., Uhara,H., Okuyama,R. and Akiyama,M. (2013) Lamellar ichthyosis in a collodion baby caused by CYP4F22 mutations in

a non-consanguineous family outside the Mediterranean. *Journal of Dermatological Science*, **72**, 193–195.

164. Lefèvre,C., Bouadjar,B., Ferrand,V., Tadini,G., Mégarbané,A., Lathrop,M., Prud'homme,J.F. and Fischer,J. (2006) Mutations in a new cytochrome P450 gene in lamellar ichthyosis type 3. *Human Molecular Genetics*, **15**, 767–776.
165. Stone,S.J., Myers,H.M., Watkins,S.M., Brown,B.E., Feingold,K.R., Elias,P.M. and Farese,R. v. (2004) Lipopenia and Skin Barrier Abnormalities in DGAT2-deficient Mice *. *Journal of Biological Chemistry*, **279**, 11767–11776.
166. Akiyama,M., Sugiyama-Nakagiri,Y., Sakai,K., McMillan,J.R., Goto,M., Arita,K., Tsuji-Abe,Y., Tabata,N., Matsuoka,K., Sasaki,R., *et al.* (2005) Mutations in lipid transporter ABCA12 in harlequin ichthyosis and functional recovery by corrective gene transfer. *The Journal of Clinical Investigation*, **115**, 1777–1784.
167. Kelsell,D.P., Norgett,E.E., Unsworth,H., Teh,M.T., Cullup,T., Mein,C.A., Dopping-Hepenstal,P.J., Dale,B.A., Tadini,G., Fleckman,P., *et al.* (2005) Mutations in ABCA12 Underlie the Severe Congenital Skin Disease Harlequin Ichthyosis. *The American Journal of Human Genetics*, **76**, 794–803.
168. Epp,N., Fürstenberger,G., Müller,K., de Juanes,S., Leitges,M., Hausser,I., Thieme,F., Liebisch,G., Schmitz,G. and Krieg,P. (2007) 12R-lipoxygenase deficiency disrupts epidermal barrier function. *Journal of Cell Biology*, **177**, 173–182.
169. Moran,J.L., Qiu,H., Turbe-Doan,A., Yun,Y., Boeglin,W.E., Brash,A.R. and Beier,D.R. (2007) A Mouse Mutation in the 12R-Lipoxygenase, Alox12b, Disrupts Formation of the Epidermal Permeability Barrier. *Journal of Investigative Dermatology*, **127**, 1893–1897.
170. Krieg,P., Rosenberger,S., de Juanes,S., Latzko,S., Hou,J., Dick,A., Kloz,U., van der Hoeven,F., Hausser,I., Esposito,I., *et al.* (2013) Aloxe3 Knockout Mice Reveal a Function of Epidermal Lipoxygenase-3 as Hepoxilin Synthase and Its Pivotal Role in Barrier Formation. *Journal of Investigative Dermatology*, **133**, 172–180.
171. Uchida,Y. and Park,K. (2021) Ceramides in Skin Health and Disease: An Update. *American Journal of Clinical Dermatology 2021 22:6*, **22**, 853–866.
172. Leung,D.Y.M. (2000) Atopic dermatitis: New insights and opportunities for therapeutic intervention. *Journal of Allergy and Clinical Immunology*, **105**, 860–876.
173. Chamlin,S.L., Kao,J., Frieden,I.J., Sheu,M.Y., Fowler,A.J., Fluhr,J.W., Williams,M.L. and Elias,P.M. (2002) Ceramide-dominant barrier repair lipids alleviate childhood atopic dermatitis: Changes in barrier function provide a sensitive indicator of disease activity. *J Am Acad Dermatol*, **47**, 198–208.
174. Elias,P.M., Hatano,Y. and Williams,M.L. (2008) Basis for the barrier abnormality in atopic dermatitis: Outside-inside-outside pathogenic mechanisms. *Journal of Allergy and Clinical Immunology*, **121**, 1337–1343.
175. Imokawa,G., Abe,A., Jin,K., Higaki,Y., Kawashima,M. and Hidano,A. (1991) Decreased Level of Ceramides in Stratum Corneum of Atopic Dermatitis: An Etiologic Factor in Atopic Dry Skin? *Journal of Investigative Dermatology*, **96**, 523–526.

176. di Nardo,A., Wertz,P., Giannetti,A. and Seidenari,S. (1998) Ceramide and cholesterol composition of the skin of patients with atopic dermatitis. *Acta Derm Venereol (Stockh)*, **78**, 27–30.

177. Ishikawa,J., Narita,H., Kondo,N., Hotta,M., Takagi,Y., Masukawa,Y., Kitahara,T., Takema,Y., Koyano,S., Yamazaki,S., *et al.* (2010) Changes in the Ceramide Profile of Atopic Dermatitis Patients. *Journal of Investigative Dermatology*, **130**, 2511–2514.

178. van Smeden,J., Janssens,M., Kaye,E.C.J., Caspers,P.J., Lavrijsen,A.P., Vreeken,R.J. and Bouwstra,J.A. (2014) The importance of free fatty acid chain length for the skin barrier function in atopic eczema patients. *Experimental Dermatology*, **23**, 45–52.

179. Janssens,M., van Smeden,J., Gooris,G.S., Bras,W., Portale,G., Caspers,P.J., Vreeken,R.J., Hankemeier,T., Kezic,S., Wolterbeek,R., *et al.* (2012) Increase in short-chain ceramides correlates with an altered lipid organization and decreased barrier function in atopic eczema patients [S]. *Journal of Lipid Research*, **53**, 2755–2766.

180. Ito,S., Ishikawa,J., Naoe,A., Yoshida,H., Hachiya,A., Fujimura,T., Kitahara,T. and Takema,Y. (2017) Ceramide synthase 4 is highly expressed in involved skin of patients with atopic dermatitis. *Journal of the European Academy of Dermatology and Venereology*, **31**, 135–141.

181. Koyano,S., Hatamochi,A., Yamazaki,S., Ishikawa,J., Kitahara,T., Narita,H., Kondo,N. and Masukawa,Y. (2010) Psoriasis Patients Have Abnormal Ceramide Profile in Stratum Corneum. *Nishi Nihon Hifuka*, **72**, 494–499.

182. Boyden,L.M., Vincent,N.G., Zhou,J., Hu,R., Craiglow,B.G., Bayliss,S.J., Rosman,I.S., Lucky,A.W., Diaz,L.A., Goldsmith,L.A., *et al.* (2017) Mutations in KDSR Cause Recessive Progressive Symmetric Erythrokeratoderma. *The American Journal of Human Genetics*, **100**, 978–984.

183. Takeichi,T., Torrelo,A., Lee,J.Y.W., Ohno,Y., Lozano,M.L., Kihara,A., Liu,L., Yasuda,Y., Ishikawa,J., Murase,T., *et al.* (2017) Biallelic Mutations in KDSR Disrupt Ceramide Synthesis and Result in a Spectrum of Keratinization Disorders Associated with Thrombocytopenia. *Journal of Investigative Dermatology*, **137**, 2344–2353.

184. Bariana,T.K., Labarque,V., Heremans,J., Thys,C., de Reys,M., Greene,D., Jenkins,B., Grassi,L., Seyres,D., Burden,F., *et al.* (2019) Sphingolipid dysregulation due to lack of functional KDSR impairs proplatelet formation causing thrombocytopenia. *Haematologica*, **104**, 1036.

185. Ryan,M.J., Johnson,G., Kirk,J., Fuerstenberg,S.M., Zager,R.A. and Torok-Storb,B. (1994) HK-2: An immortalized proximal tubule epithelial cell line from normal adult human kidney. *Kidney International*, **45**, 48–57.

186. Gerl,M.J., Bittl,V., Kirchner,S., Sachsenheimer,T., Brunner,H.L., Lüchtenborg,C., Özbalci,C., Wiedemann,H., Wegehingel,S., Nickel,W., *et al.* (2016) Sphingosine-1-Phosphate Lyase Deficient Cells as a Tool to Study Protein Lipid Interactions. *PLoS One*, **11**, e0153009.

187. Schwab,S.R., Pereira,J.P., Matloubian,M., Xu,Y., Huang,Y. and Cyster,J.G. (2005) Lymphocyte Sequestration Through S1P Lyase Inhibition and Disruption of S1P Gradients. *Science (1979)*, **309**, 1735–1739.

188. Weiler,S., Braendlin,N., Beerli,C., Bergsdorf,C., Schubart,A., Srinivas,H., Oberhauser,B. and Billich,A. (2014) Orally Active 7-Substituted (4-Benzyl-phthalazin-1-yl)-2-methyl-piperazin-1-yl]-nicotinonitriles as Active-site Inhibitors of Sphingosine-1-Phosphate Lyase for the Treatment of Multiple Sclerosis. *J Med Chem*, **57**, 5074–5084.

189. Harris,C.M., Mittelstadt,S., Banfor,P., Bousquet,P., Duignan,D.B., Gintant,G., Hart,M., Kim,Y. and Segreti,J. (2016) Sphingosine-1-phosphate Lyase Inhibition Causes Increased Cardiac S1P Levels and Bradycardia in Rats. *J Pharmacol Exp Ther*, **359**, 151–158.

190. Ran,F.A., Hsu,P.D., Wright,J., Agarwala,V., Scott,D.A. and Zhang,F. (2013) Genome engineering using the CRISPR-Cas9 system. *Nature Protocols 2013 8:11*, **8**, 2281–2308.

191. Concordet,J.P. and Haeussler,M. (2018) CRISPOR: intuitive guide selection for CRISPR/Cas9 genome editing experiments and screens. *Nucleic Acids Research*, **46**, W242–W245.

192. Haeussler,M., Schönig,K., Eckert,H., Eschstruth,A., Mianné,J., Renaud,J.-B., Schneider-Maunoury,S., Shkumatava,A., Teboul,L., Kent,J., *et al.* (2016) Evaluation of off-target and on-target scoring algorithms and integration into the guide RNA selection tool CRISPOR. *Genome Biology*, **17**, 148.

193. Hsu,P.D., Scott,D.A., Weinstein,J.A., Ran,F.A., Konermann,S., Agarwala,V., Li,Y., Fine,E.J., Wu,X., Shalem,O., *et al.* (2013) DNA targeting specificity of RNA-guided Cas9 nucleases. *Nature Biotechnology*, **31**, 827–832.

194. Tycko,J., Wainberg,M., Marinov,G.K., Ursu,O., Hess,G.T., Ego,B.K., Aradhana, Li,A., Truong,A., Trevino,A.E., *et al.* (2019) Mitigation of off-target toxicity in CRISPR-Cas9 screens for essential non-coding elements. *Nature Communications 2019 10:1*, **10**, 1–14.

195. Doench,J.G., Fusi,N., Sullender,M., Hegde,M., Vaimberg,E.W., Donovan,K.F., Smith,I., Tothova,Z., Wilen,C., Orchard,R., *et al.* (2016) Optimized sgRNA design to maximize activity and minimize off-target effects of CRISPR-Cas9. *Nature Biotechnology 2015 34:2*, **34**, 184–191.

196. Brinkman,E.K., Chen,T., Amendola,M. and van Steensel,B. (2014) Easy quantitative assessment of genome editing by sequence trace decomposition. *Nucleic Acids Res*, **42**, e168.

197. Presolski,S.I., Hong,V.P. and Finn,M.G. (2011) Copper-Catalyzed Azide-Alkyne Click Chemistry for Bioconjugation. *Curr Protoc Chem Biol*, **3**, 153–162.

198. Besanceney-Webler,C., Jiang,H., Zheng,T., Feng,L., Soriano Del Amo,D., Wang,W., Klivansky,L.M., Marlow,F.L., Liu,Y. and Wu,P. (2011) Raising the Efficacy of Bioorthogonal Click Reactions for Bioconjugation: A Comparative Study. *Angew Chem Int Ed Engl*, **50**, 8051.

199. Li,L. and Zhang,Z. (2016) Development and Applications of the Copper-Catalyzed Azide-Alkyne Cycloaddition (CuAAC) as a Bioorthogonal Reaction. *Molecules 2016, Vol. 21, Page 1393*, **21**, 1393.

200. Hong,V., Presolski,S.I., Ma,C. and Finn,M.G. (2009) Analysis and optimization of copper-catalyzed azide-alkyne cycloaddition for bioconjugation. *Angew Chem Int Ed Engl*, **48**, 9879–9883.

201. Renard,H.F., Tyckaert,F., lo Giudice,C., Hirsch,T., Valades-Cruz,C.A., Lemaigre,C., Shafaq-Zadah,M., Wunder,C., Wattiez,R., Johannes,L., *et al.* (2020) Endophilin-A3 and Galectin-8 control the clathrin-independent endocytosis of CD166. *Nature Communications*, **11**, 1–13.

202. Haberkant,P., Stein,F., Höglinger,D., Gerl,M.J., Brügger,B., van Veldhoven,P.P., Krijgsveld,J., Gavin,A.-C. and Schultz,C. (2016) Bifunctional Sphingosine for Cell-Based Analysis of Protein-Sphingolipid Interactions. *ACS Chemical Biology*, **11**, 222–230.

203. Roxlau,T.J. (2019) Investigation of the lipid environment of the mammalian transamidase complex. 10.11588/heidok.00027099.

204. Deng,Y., You,L., Lu,Y., Han,S., Wang,J., Vicas,N., Chen,C. and Ye,J. (2021) Identification of TRAMs as sphingolipid-binding proteins using a photoactivatable and clickable short-chain ceramide analog. 10.1016/j.jbc.2021.101415.

205. Schweinfurth,D. (2020) Characterisation of Protein-Very Long Chain Fatty Acid-Containing Sphingolipid Interactions.

206. Förster,L.-C. (2019) Analysis of protein-sphingolipid interactions in Influenza A-infected cells.

207. Shimomura,T., Denda,K., Kitamura,A., Kawaguchi,T., Kito,M., Kondo,J., Kagaya,S., Qin,L., Takata,H., Miyazawa,K., *et al.* (1997) Hepatocyte Growth Factor Activator Inhibitor, a Novel Kunitz-type Serine Protease Inhibitor. *Journal of Biological Chemistry*, **272**, 6370–6376.

208. Szabo,R., Molinolo,A., List,K. and Bugge,T.H. (2006) Matriptase inhibition by hepatocyte growth factor activator inhibitor-1 is essential for placental development. *Oncogene 2007 26:11*, **26**, 1546–1556.

209. Kaitu'u-Lino,T.J., MacDonald,T.M., Cannon,P., Nguyen,T.V., Hiscock,R.J., Haan,N., Myers,J.E., Hastie,R., Dane,K.M., Middleton,A.L., *et al.* (2020) Circulating SPINT1 is a biomarker of pregnancies with poor placental function and fetal growth restriction. *Nature Communications 2020 11:1*, **11**, 1–10.

210. Nagaike,K., Kawaguchi,M., Takeda,N., Fukushima,T., Sawaguchi,A., Kohama,K., Setoyama,M. and Kataoka,H. (2008) Defect of Hepatocyte Growth Factor Activator Inhibitor Type 1/Serine Protease Inhibitor, Kunitz Type 1 (Hai-1/Spint1) Leads to Ichthyosis-Like Condition and Abnormal Hair Development in Mice. *The American Journal of Pathology*, **173**, 1464–1475.

211. Kataoka,H., Kawaguchi,M., Fukushima,T. and Shimomura,T. (2018) Hepatocyte growth factor activator inhibitors (HAI-1 and HAI-2): Emerging key players in epithelial integrity and cancer. *Pathology International*, **68**, 145–158.

212. Kataoka,H., Suganuma,T., Shimomura,T., Itoh,H., Kitamura,N., Nabeshima,K. and Koono,M. (1999) Distribution of Hepatocyte Growth Factor Activator Inhibitor Type 1 (HAI-1) in Human

Tissues: Cellular Surface Localization of HAI-1 in Simple Columnar Epithelium and Its Modulated Expression in Injured and Regenerative Tissues. *The Journal of Histochemistry & Cytochemistry*, **47**, 673–682.

213. Kawaguchi,M., Takeda,N., Hoshiko,S., Yorita,K., Baba,T., Sawaguchi,A., Nezu,Y., Yoshikawa,T., Fukushima,T. and Kataoka,H. (2011) Membrane-Bound Serine Protease Inhibitor HAI-1 Is Required for Maintenance of Intestinal Epithelial Integrity. *The American Journal of Pathology*, **179**, 1815–1826.
214. Porubsky,S., Federico,G., Müthing,J., Jennemann,R., Gretz,N., Büttner,S., Obermüller,N., Jung,O., Hauser,I.A., Gröne,E., *et al.* (2014) Direct acute tubular damage contributes to Shigatoxin-mediated kidney failure. *The Journal of Pathology*, **234**, 120–133.
215. Elisabeth Grimm (2022) Generation of a Clathrin light chain - A reporter mouse model for in vivo imaging of endocytosis.
216. Fan,B., Wu,T.D., Li,W. and Kirchhofer,D. (2005) Identification of Hepatocyte Growth Factor Activator Inhibitor-1B as a Potential Physiological Inhibitor of Prostasin. *Journal of Biological Chemistry*, **280**, 34513–34520.
217. List,K., Bugge,T.H. and Szabo,R. (2006) Matriptase: Potent Proteolysis on the Cell Surface. *Molecular Medicine*, **12**, 1–7.
218. Uhland,K. (2006) Matriptase and its putative role in cancer. *Cellular and Molecular Life Sciences CMLS 2006 63:24*, **63**, 2968–2978.
219. Kirchhofer,D., Peek,M., Li,W., Stamos,J., Eigenbrot,C., Kadkhodayan,S., Elliott,J.M., Corpuz,R.T., Lazarus,R.A. and Moran,P. (2003) Tissue Expression, Protease Specificity, and Kunitz Domain Functions of Hepatocyte Growth Factor Activator Inhibitor-1B (HAI-1B), a New Splice Variant of HAI-1. *Journal of Biological Chemistry*, **278**, 36341–36349.
220. Denda,K., Shimomura,T., Kawaguchi,T., Miyazawa,K. and Kitamura,N. (2002) Functional Characterization of Kunitz Domains in Hepatocyte Growth Factor Activator Inhibitor Type 1. *Journal of Biological Chemistry*, **277**, 14053–14059.
221. Kataoka,H., Shimomura,T., Kawaguchi,T., Hamasuna,R., Itoh,H., Kitamura,N., Miyazawa,K. and Koono,M. (2000) Hepatocyte Growth Factor Activator Inhibitor Type 1 Is a Specific Cell Surface Binding Protein of Hepatocyte Growth Factor Activator (HGFA) and Regulates HGFA Activity in the Pericellular Microenvironment. *Journal of Biological Chemistry*, **275**, 40453–40462.
222. Comoglio,P.M., Giordano,S. and Trusolino,L. (2008) Drug development of MET inhibitors: targeting oncogene addiction and expedience. *Nature Reviews Drug Discovery 2008 7:6*, **7**, 504–516.
223. Igawa,T., Kanda,S., Kanetake,H., Saitoh,Y., Ichihara,A., Tomita,Y. and Nakamura,T. (1991) Hepatocyte growth factor is a potent mitogen for cultured rabbit renal tubular epithelial cells. *Biochemical and Biophysical Research Communications*, **174**, 831–838.
224. Naka,D., Ishii,T., Yoshiyama,Y., Miyazawa,K., Hara,H., Hishida,T. and Kitamura,N. (1992) Activation of hepatocyte growth factor by proteolytic conversion of a single chain form to a heterodimer. *Journal of Biological Chemistry*, **267**, 20114–20119.

225. Naldini,L., Tamagnone,L., Vigna,E., Sachs,M., Hartmann,G., Birchmeier,W., Daikuhara,Y., Tsubouchi,H., Blasi,F. and Comoglio,P.M. (1992) Extracellular proteolytic cleavage by urokinase is required for activation of hepatocyte growth factor/scatter factor. *The EMBO Journal*, **11**, 4825–4833.

226. Gak,E., Taylor,W.G., Chan,A.M.L. and Rubin,J.S. (1992) Processing of hepatocyte growth factor to the heterodimeric form is required for biological activity. *FEBS Letters*, **311**, 17–21.

227. Miyazawa,K., Shimomura,T., Naka,D. and Kitamura,N. (1994) Proteolytic activation of hepatocyte growth factor in response to tissue injury. *Journal of Biological Chemistry*, **269**, 8966–8970.

228. Zhou,D., Tan,R.J., Lin,L., Zhou,L. and Liu,Y. (2013) Activation of hepatocyte growth factor receptor, c-met, in renal tubules is required for renoprotection after acute kidney injury. *Kidney International*, **84**, 509–520.

229. Nagano,T., Mori-Kudo,I., Tsuchida,A., Kawamura,T., Taiji,M. and Noguchi,H. (2002) Ameliorative effect of hepatocyte growth factor on glycerol-induced acute renal failure with acute tubular necrosis. *Nephron*, **91**, 730–738.

230. Nagano,T., Mori-Kudo,I., Kawamura,T., Taiji,M. and Noguchi,H. (2009) Pre- or Post-treatment with Hepatocyte Growth Factor Prevents Glycerol-Induced Acute Renal Failure. *http://dx.doi.org/10.1081/JDI-120028537*, **26**, 5–11.

231. Homsi,E., Janino,P., Amano,M. and Saraiva Camara,N.O. (2009) Endogenous Hepatocyte Growth Factor Attenuates Inflammatory Response in Glycerol-Induced Acute Kidney Injury. *American Journal of Nephrology*, **29**, 283–291.

232. Miyazawa,K., Shimomura,T. and Kitamura,N. (1996) Activation of Hepatocyte Growth Factor in the Injured Tissues Is Mediated by Hepatocyte Growth Factor Activator (∗). *Journal of Biological Chemistry*, **271**, 3615–3618.

233. Shimomura,T., Kondo,J., Ochiai,M., Naka,D., Miyazawa,K., Morimoto,Y. and Kitamura,N. (1993) Activation of the zymogen of hepatocyte growth factor activator by thrombin. *Journal of Biological Chemistry*, **268**, 22927–22932.

234. Godiksen,S., Selzer-Plon,J., Pedersen,E.D.K., Abell,K., Rasmussen,H.B., Szabo,R., Bugge,T.H. and Vogel,L.K. (2008) Hepatocyte growth factor activator inhibitor-1 has a complex subcellular itinerary. *Biochemical Journal*, **413**, 251–259.

235. Hakomori,S. and Handa,K. (2016) Regulation of Growth Factor Receptors by Glycosphingolipids. In *Glycosignals in Cancer: Mechanisms of Malignant Phenotypes*. Springer Japan, Tokyo, pp. 77–93.

236. Liang,Y.J., Wang,C.Y., Wang,I.A., Chen,Y.W., Li,L.T., Lin,C.Y., Ho,M.Y., Chou,T.L., Wang,Y.H., Chiou,S.P., *et al.* (2017) Interaction of glycosphingolipids GD3 and GD2 with growth factor receptors maintains breast cancer stem cell phenotype. *Oncotarget*, **8**, 47454.

237. Zhuo,D. and Guan,F. (2019) Ganglioside GM1 promotes contact inhibition of growth by regulating the localization of epidermal growth factor receptor from glycosphingolipid-enriched microdomain to caveolae. *Cell Proliferation*, **52**, e12639.

238. Bremer,E.G. and Hakomori,S. itiroh (1982) GM3 ganglioside induces hamster fibroblast growth inhibition in chemically-defined medium: ganglioside may regulate growth factor receptor function. *Biochem Biophys Res Commun*, **106**, 711–718.

239. Todeschini,A.R., dos Santos,J.N., Handa,K. and Hakomori,S.I. (2007) Ganglioside GM2-tetraspanin CD82 complex inhibits met and its cross-talk with integrins, providing a basis for control of cell motility through glycosynapse. *J Biol Chem*, **282**, 8123–8133.

240. Regina Todeschini,A. and Hakomori,S. itiroh (2008) Functional role of glycosphingolipids and gangliosides in control of cell adhesion, motility, and growth, through glycosynaptic microdomains. *Biochimica et Biophysica Acta (BBA) - General Subjects*, **1780**, 421–433.

241. Myrdal,S.E., Johnson,K.C. and Steyger,P.S. (2005) Cytoplasmic and intra-nuclear binding of gentamicin does not require endocytosis. *Hear Res*, **204**, 156.

242. Dai,C.F., Mangiardi,D., Cotanche,D.A. and Steyger,P.S. (2006) Uptake of fluorescent gentamicin by vertebrate sensory cells in vivo. *Hear Res*, **213**, 64.

243. Lee,J.H., Park,C., Kim,S.J., Kim,H.J., Oh,G.S., Shen,A., So,H.S. and Park,R. (2013) Different uptake of gentamicin through TRPV1 and TRPV4 channels determines cochlear hair cell vulnerability. *Experimental & Molecular Medicine 2013 45:3*, **45**, e12–e12.

244. Sandoval,R.M. and Molitoris,B.A. (2004) Gentamicin traffics retrograde through the secretory pathway and is released in the cytosol via the endoplasmic reticulum. *American Journal of Physiology - Renal Physiology*, **286**, 617–624.

245. Quiros,Y., Vicente-Vicente,L., Morales,A.I., López-Novoa,J.M. and López-Hernández,F.J. (2011) An Integrative Overview on the Mechanisms Underlying the Renal Tubular Cytotoxicity of Gentamicin. *Toxicological Sciences*, **119**, 245–256.

246. Kaneko,T., Tsubakihara,Y., Fushimi,H., Yamaguchi,S., Takabatake,Y., Rakugi,H., Kawakami,H. and Isaka,Y. (2015) Histochemical and immunoelectron microscopic analysis of ganglioside GM3 in human kidney. *Clinical and Experimental Nephrology*, **19**, 403–410.

247. Halleck,M.S., Lawler,J.F., Blackshaw,S., Gao,L., Nagarajan,P., Hacker,C., Pyle,S., Newman,J.T., Nakanishi,Y., Ando,H., *et al.* (1999) Differential expression of putative transbilayer amphipath transporters. *Physiological Genomics*, **1999**, 139–150.

248. Tanaka,Y., Ono,N., Shima,T., Tanaka,G., Katoh,Y., Nakayama,K., Takatsu,H. and Shin,H.W. (2016) The phospholipid flippase ATP9A is required for the recycling pathway from the endosomes to the plasma membrane. *Molecular Biology of the Cell*, **27**, 3883–3893.

249. Naik,J., Hau,C.M., ten Bloemendaal,L., Mok,K.S., Hajji,N., Wehman,A.M., Meisner,S., Muncan,V., Paauw,N.J., de Vries,H.E., *et al.* (2019) The P4-ATPase ATP9A is a novel determinant of exosome release. *PLOS ONE*, **14**, e0213069.

250. ATP9A protein expression summary - The Human Protein Atlas.

251. Vogt,G., Verheyen,S., Schwartzmann,S., Ehmke,N., Potratz,C., Schwerin-Nagel,A., Plecko,B., Holtgrewe,M., Seelow,D., Blatterer,J., *et al.* (2021) Biallelic truncating variants in ATP9A cause a novel neurodevelopmental disorder involving postnatal microcephaly and failure to thrive. *J Med Genet*, **0**, jmedgenet-2021-107843.

252. Wicky,S., Schwarz,H. and Singer-Krüger,B. (2004) Molecular Interactions of Yeast Neo1p, an Essential Member of the Drs2 Family of Aminophospholipid Translocases, and Its Role in Membrane Trafficking within the Endomembrane System. *Molecular and Cellular Biology*, **24**, 7402–7418.

253. Pomorski,T., Lombardi,R., Riezman,H., Devaux,P.F., van Meer,G. and Holthuis,J.C.M. (2003) Drs2p-related P-type ATPases Dnflp and Dnf2p are required for phospholipid translocation across the yeast plasma membrane and serve a role in endocytosis. *Molecular Biology of the Cell*, **14**, 1240–1254.

254. Daleke,D.L. (2007) Phospholipid flippases. *Journal of Biological Chemistry*, **282**, 821–825.

255. Coleman,J.A., Kwok,M.C.M. and Molday,R.S. (2009) Localization, purification, and functional reconstitution of the P4-ATPase Atp8a2, a phosphatidylserine Flippase in photoreceptor disc membranes. *Journal of Biological Chemistry*, **284**, 32670–32679.

256. Muthusamy,B.P., Natarajan,P., Zhou,X. and Graham,T.R. (2009) Linking phospholipid flippases to vesicle-mediated protein transport. *Biochimica et Biophysica Acta (BBA) - Molecular and Cell Biology of Lipids*, **1791**, 612–619.

257. Graham,T.R. (2004) Flippases and vesicle-mediated protein transport. *Trends in Cell Biology*, **14**, 670–677.

258. Graham,T.R. and Kozlov,M.M. (2010) Interplay of proteins and lipids in generating membrane curvature. *Current Opinion in Cell Biology*, **22**, 430–436.

259. Sebastian,T.T., Baldridge,R.D., Xu,P. and Graham,T.R. (2012) Phospholipid flippases: Building asymmetric membranes and transport vesicles. *Biochimica et Biophysica Acta (BBA) - Molecular and Cell Biology of Lipids*, **1821**, 1068–1077.

260. van der Mark,V.A., Oude Elferink,R.P.J. and Paulusma,C.C. (2013) P4 ATPases: Flippases in Health and Disease. *International Journal of Molecular Sciences 2013, Vol. 14, Pages 7897-7922*, **14**, 7897–7922.

261. Takada,N., Takatsu,H., Miyano,R., Nakayama,K. and Shin,H.W. (2015) ATP11C mutation is responsible for the defect in phosphatidylserine uptake in UPS-1 cells. *Journal of Lipid Research*, **56**, 2151–2157.

262. Naito,T., Takatsu,H., Miyano,R., Takada,N., Nakayama,K. and Shin,H.W. (2015) Phospholipid Flippase ATP10A Translocates Phosphatidylcholine and Is Involved in Plasma Membrane Dynamics *. *Journal of Biological Chemistry*, **290**, 15004–15017.

263. Takatsu,H., Tanaka,G., Segawa,K., Suzuki,J., Nagata,S., Nakayama,K. and Shin,H.W. (2014) Phospholipid Flippase Activities and Substrate Specificities of Human Type IV P-type ATPases Localized to the Plasma Membrane *. *Journal of Biological Chemistry*, **289**, 33543–33556.

264. Roland,B.P., Naito,T., Best,J.T., Arnaiz-Yépez,C., Takatsu,H., Yu,R.J., Shin,H.W. and Graham,T.R. (2019) Yeast and human P4-ATPases transport glycosphingolipids using conserved structural motifs. *The Journal of Biological Chemistry*, **294**, 1794.

265. McGough,I.J., de Groot,R.E.A., Jellett,A.P., Betist,M.C., Varandas,K.C., Danson,C.M., Heesom,K.J., Korswagen,H.C. and Cullen,P.J. (2018) SNX3-retromer requires an

evolutionary conserved MON2:DOPEY2:ATP9A complex to mediate Wntless sorting and Wnt secretion. *Nature Communications 2018 9:1*, **9**, 1–13.

266. Grant,B.D. and Donaldson,J.G. (2009) Pathways and mechanisms of endocytic recycling. *Nature Reviews Molecular Cell Biology 2009 10:9*, **10**, 597–608.
267. Johannes,L.I., Barbier,J. and Gillet,D. (2017) Shiga Toxin-A Model for Glycolipid-Dependent and Lectin-Driven Endocytosis. *Toxins (Basel)*, **9**.
268. Röhrborn,D., Wronkowitz,N. and Eckel,J. (2015) DPP4 in diabetes. *Frontiers in Immunology*, **6**, 386.
269. Aroor,A., Zuberek,M., Duta,C., Meuth,A., Sowers,J.R., Whaley-Connell,A. and Nistala,R. (2016) Angiotensin II Stimulation of DPP4 Activity Regulates Megalin in the Proximal Tubules. *International Journal of Molecular Sciences 2016, Vol. 17, Page 780*, **17**, 780.
270. Tanaka,Y., Kume,S., Chin-Kanasaki,M., Araki,H., Araki,S.I., Ugi,S., Sugaya,T., Uzu,T. and Maegawa,H. (2016) Renoprotective effect of DPP-4 inhibitors against free fatty acid-bound albumin-induced renal proximal tubular cell injury. *Biochemical and Biophysical Research Communications*, **470**, 539–545.
271. Delacour,D., Gouyer,V., Zanetta,J.P., Drobecq,H., Leteurtre,E., Grard,G., Moreau-Hannedouche,O., Maes,E., Pons,A., André,S., *et al.* (2005) Galectin-4 and sulfatides in apical membrane trafficking in enterocyte-like cells. *Journal of Cell Biology*, **169**, 491–501.
272. Stechly,L., Morelle,W., Dessein,A.F., André,S., Grard,G., Trinel,D., Dejonghe,M.J., Leteurtre,E., Drobecq,H., Trugnan,G., *et al.* (2009) Galectin-4-Regulated Delivery of Glycoproteins to the Brush Border Membrane of Enterocyte-Like Cells. *Traffic*, **10**, 438–450.
273. Schuck,S. and Simons,K. (2004) Polarized sorting in epithelial cells: raft clustering and the biogenesis of the apical membrane. *J Cell Sci*, **117**, 5955–5964.
274. Lakshminarayan,R., Wunder,C., Becken,U., Howes,M.T., Benzing,C., Arumugam,S., Sales,S., Ariotti,N., Chambon,V., Lamaze,C., *et al.* (2014) Galectin-3 drives glycosphingolipid-dependent biogenesis of clathrin-independent carriers. *Nat Cell Biol*, **16**, 592–603.
275. Iwakura,T., Zhao,Z., Marschner,J.A., Devarapu,S.K., Yasuda,H. and Anders,H.J. (2019) Dipeptidyl peptidase-4 inhibitor teneligliptin accelerates recovery from cisplatin-induced acute kidney injury by attenuating inflammation and promoting tubular regeneration. *Nephrology Dialysis Transplantation*, **34**, 1669–1680.
276. Dupre,T. v. and Siskind,L.J. (2018) The role of sphingolipids in acute kidney injury. *Advances in Biological Regulation*, **70**, 31–39.
277. Dupre,T. v., Doll,M.A., Shah,P.P., Sharp,C.N., Siow,D., Megyesi,J., Shayman,J., Bielawska,A., Bielawski,J., Beverly,L.J., *et al.* (2017) Inhibiting glucosylceramide synthase exacerbates cisplatin-induced acute kidney injury. *Journal of Lipid Research*, **58**, 1439–1452.
278. Contreras,F.-X., Ernst,A.M., Haberkant,P., Björkholm,P., Lindahl,E., Gönen,B., Tischer,C., Elofsson,A., von Heijne,G., Thiele,C., *et al.* (2012) Molecular recognition of a single sphingolipid species by a protein's transmembrane domain. *Nature*, **481**, 525–529.

279. Hammerschmidt,P., Ostkotte,D., Nolte,H., Gerl,M.J., Jais,A., Brunner,H.L., Sprenger,H.-G., Awazawa,M., Nicholls,H.T., Turpin-Nolan,S.M., *et al.* (2019) CerS6-Derived Sphingolipids Interact with Mff and Promote Mitochondrial Fragmentation in Obesity. *Cell*, **177**, 1536-1552.e23.

280. Waldek,S. and Feriozzi,S. (2014) Fabry nephropathy: A review - How can we optimize the management of Fabry nephropathy? *BMC Nephrology*, **15**, 1–13.

281. Chévrier,M., Brakch,N., Lesueur,C., Genty,D., Ramdani,Y., Moll,S., Djavaheri-Mergny,M., Brasse-Lagnel,C., Laquerrière,A., Barbey,F., *et al.* (2010) Autophagosome maturation is impaired in Fabry disease. *http://dx.doi.org/10.4161/auto.6.5.11943*, **6**, 589–599.

282. Russo,D., Capolupo,L., Loomba,J.S., Sticco,L. and D'Angelo,G. (2018) Glycosphingolipid metabolism in cell fate specification. *Journal of Cell Science*, **131**.

283. Cheng,H., Fukushima,T., Takahashi,N., Tanaka,H. and Kataoka,H. (2009) Hepatocyte growth factor activator inhibitor type 1 regulates epithelial to mesenchymal transition through membrane-bound serine proteinases. *Cancer Research*, **69**, 1828–1835.

284. Stoker,M. and Perryman,M. (1985) An epithelial scatter factor released by embryo fibroblasts. *J Cell Sci*, **77**, 209–223.

285. Lamouille,S., Xu,J. and Derynck,R. (2014) Molecular mechanisms of epithelial–mesenchymal transition. *Nature Reviews Molecular Cell Biology 2014 15:3*, **15**, 178–196.

286. Cazet,A., Bobowski,M., Rombouts,Y., Lefebvre,J., Steenackers,A., Popa,I., Guérardel,Y., le Bourhis,X., Tulasne,D. and Delannoy,P. (2012) The ganglioside GD2 induces the constitutive activation of c-Met in MDA-MB-231 breast cancer cells expressing the GD3 synthase. *Glycobiology*, **22**, 806–816.

287. Namdar,M., Gebhard,C., Studiger,R., Shi,Y., Mocharla,P., Schmied,C., Brugada,P., Lüscher,T.F. and Camici,G.G. (2012) Globotriaosylsphingosine Accumulation and Not Alpha-Galactosidase-A Deficiency Causes Endothelial Dysfunction in Fabry Disease. *PLOS ONE*, **7**, e36373.

288. Mizuguchi,K., Aoki,H., Aoyama,M., Kawaguchi,Y., Waguri-Nagaya,Y., Ohte,N. and Asai,K. (2021) Three-dimensional spheroid culture induces apical-basal polarity and the original characteristics of immortalized human renal proximal tubule epithelial cells. *Experimental Cell Research*, **404**, 112630.

289. Xu,Y., Qin,S., Niu,Y., Gong,T., Zhang,Z. and Fu,Y. (2020) Effect of fluid shear stress on the internalization of kidney-targeted delivery systems in renal tubular epithelial cells. *Acta Pharmaceutica Sinica B*, **10**, 680–692.

290. Whitin,J.C., Bhamre,S., Tham,D.M. and Cohen,H.J. (2002) Extracellular glutathione peroxidase is secreted basolaterally by human renal proximal tubule cells. *American Journal of Physiology-Renal Physiology*, **283**, F20–F28.

291. Huang,X., Schurman,N., Handa,K. and Hakomori,S. (2017) Functional role of glycosphingolipids in contact inhibition of growth in a human mammary epithelial cell line. *FEBS Letters*, **591**, 1918–1928.

292. Bursztejn,A.-C., Happle,R., Charbit,L., Küsel,J., Leclerc-Mercier,S., Hadj-Rabia,S., Fraitag,S., Zimmer,A. and Fischer,J. (2019) The PERIOPTER syndrome (periorificial and ptychotropic erythrokeratoderma): a new Mendelian disorder of cornification. *J Eur Acad Dermatol Venereol*, **33**, e1–e3.

293. Pilz,R., Opálka,L., Majcher,A., Grimm,E., van Maldergem,L., Mihalceanu,S., Schäkel,K., Enk,A., Aubin,F., Bursztejn,A.-C., *et al.* (2022) Formation of keto-type ceramides in palmoplantar keratoderma based on biallelic KDSR mutations in patients. *Human Molecular Genetics*, **31**, 1105–1114.

294. Liu,Q., Chan,A.K.N., Chang,W.H., Yang,L., Pokharel,S.P., Miyashita,K., Mattson,N., Xu,X., Li,M., Lu,W., *et al.* (2021) 3-Ketodihydrosphingosine reductase maintains ER homeostasis and unfolded protein response in leukemia. *Leukemia 2021 36:1*, **36**, 100–110.

295. Gaver,R.C. and Sweeley,C.C. (1965) Methods for methanolysis of sphingolipids and direct determination of long-chain bases by gas chromatography. *J Am Oil Chem Soc*, **42**, 294–298.

296. Morell,P. and Radin,N.S. (1970) Specificity in Ceramide Biosynthesis from Long Chain Bases and Various Fatty Acyl Coenzyme A's by Brain Microsomes. *Journal of Biological Chemistry*, **245**, 342–350.

297. Li,Q., Fang,H., Dang,E. and Wang,G. (2020) The role of ceramides in skin homeostasis and inflammatory skin diseases. *Journal of Dermatological Science*, **97**, 2–8.

298. Yokose,U., Ishikawa,J., Morokuma,Y., Naoe,A., Inoue,Y., Yasuda,Y., Tsujimura,H., Fujimura,T., Murase,T. and Hatamochi,A. (2020) The ceramide [NP]/[NS] ratio in the stratum corneum is a potential marker for skin properties and epidermal differentiation. *BMC Dermatology*, **20**.

299. Kishimoto,Y. and Mitry,M.T. (1974) A new procedure for synthesis of 3-keto derivatives of sphingolipids and its application for study of fatty acid composition of brain ceramides and cerebrosides containing dihydrosphingosine or sphingosine. *Archives of Biochemistry and Biophysics*, **161**, 426–434.

300. Kishimoto,Y. and Costello (1975) Rearrangement of 3-ketoceramide. *Chem Phys Lipids*, **15**, 27–32.

301. Breiden,B. and Sandhoff,K. (2014) The role of sphingolipid metabolism in cutaneous permeability barrier formation. *Biochim Biophys Acta*, **1841**, 441–452.

302. Kishimoto,Y. and Mitry,M.T. (1974) A new procedure for synthesis of 3-keto derivatives of sphingolipids and its application for study of fatty acid composition of brain ceramides and cerebrosides containing dihydrosphingosine or sphingosine. *Archives of Biochemistry and Biophysics*, **161**, 426–434.

303. Hsu,F.F. and Turk,J. (2000) Structural determination of sphingomyelin by tandem mass spectrometry with electrospray ionization. *J Am Soc Mass Spectrom*, **11**, 437–449.

304. Školová,B., Januìššová,B., Zbytovská,J., Gooris,G., Bouwstra,J., Slepička,P., Berka,P., Roh,J., Palát,K., Hrabálek,A., *et al.* (2013) Ceramides in the skin lipid membranes: Length matters. *Langmuir*, **29**, 15624–15633.

305. Merrill,A.H., Sullards,M.C., Allegood,J.C., Kelly,S. and Wang,E. (2005) Sphingolipidomics: High-throughput, structure-specific, and quantitative analysis of sphingolipids by liquid chromatography tandem mass spectrometry. *Methods*, **36**, 207–224.
306. Momin,A.A. (2010) Application of bioinformatics in studies of sphingolipid biosynthesis.
307. Zhou,Y., Kato,H., Asanoma,K., Kondo,H., Arima,T., Kato,K., Matsuda,T. and Wake,N. (2002) Identification of FOXC1 as a TGF-β1 Responsive Gene and Its Involvement in Negative Regulation of Cell Growth. *Genomics*, **80**, 465–472.
308. Tamimi,Y., Lines,M., Coca-Prados,M. and Walter,M.A. (2004) Identification of target genes regulated by FOXC1 using nickel agarose-based chromatin enrichment. *Investigative Ophthalmology and Visual Science*, **45**, 3904–3913.
309. Ardail,D., Popa,I., Alcantara,K., Pons,A., Zanetta,J.P., Louisot,P., Thomas,L. and Portoukalian,J. (2001) Occurrence of ceramides and neutral glycolipids with unusual long-chain base composition in purified rat liver mitochondria. *FEBS Lett*, **488**, 160–4.
310. Nakano,M. and Fujino,Y. (1973) Enzymatic conversion of labeled ketodihydrosphingosine to sphingosine. *Biochimica et Biophysica Acta (BBA) - Lipids and Lipid Metabolism*, **296**, 457–460.
311. Fujino,Y. and Nakano,M. (1973) Enzymatic Formation of Sphingenine from Ketosphinganine in Rat Liver Particulates. *Agricultural and Biological Chemistry*, **37**, 2429–2430.
312. Fujino,Y. and Nakano,M. (1971) Enzymatic conversion of labeled ketodihydrosphingosine to ketosphingosine in rat liver particulates. *Biochim Biophys Acta*, **239**, 273–9.
313. Kishimoto,Y. and Kawamura,N. (1979) Ceramide metabolism in brain. *Mol Cell Biochem*, **23**, 17–25.
314. Shoyama,Y. and Kishimoto,Y. (1976) Invivo conversion of 3-ketoceramide to ceramide in rat liver. *Biochemical and Biophysical Research Communications*, **70**, 1035–1041.
315. Shoyama,Y. and Kishimoto,Y. (1978) In vivo metabolism of 3-ketoceramide in rat brain. *J Neurochem*, **30**, 377–82.
316. Laviad,E.L., Albee,L., Pankova-Kholmyansky,I., Epstein,S., Park,H., Merrill,A.H. and Futerman,A.H. (2008) Characterization of ceramide synthase 2: tissue distribution, substrate specificity, and inhibition by sphingosine 1-phosphate. *J Biol Chem*, **283**, 5677–5684.
317. Mullen,T.D., Hannun,Y.A. and Obeid,L.M. (2012) Ceramide synthases at the centre of sphingolipid metabolism and biology. *Biochem J*, **441**, 789.
318. Mizutani,Y., Mitsutake,S., Tsuji,K., Kihara,A. and Igarashi,Y. (2009) Ceramide biosynthesis in keratinocyte and its role in skin function. *Biochimie*, **91**, 784–790.
319. Eckl,K.M., Tidhar,R., Thiele,H., Oji,V., Hausser,I., Brodesser,S., Preil,M.L., Önal-Akan,A., Stock,F., Müller,D., *et al.* (2013) Impaired Epidermal Ceramide Synthesis Causes Autosomal Recessive Congenital Ichthyosis and Reveals the Importance of Ceramide Acyl Chain Length. *Journal of Investigative Dermatology*, **133**, 2202–2211.
320. Radner,F.P.W., Marrakchi,S., Kirchmeier,P., Kim,G.J., Ribierre,F., Kamoun,B., Abid,L., Leipoldt,M., Turki,H., Schempp,W., *et al.* (2013) Mutations in CERS3 Cause Autosomal Recessive Congenital Ichthyosis in Humans. *PLOS Genetics*, **9**, e1003536.

321. Kaylor,J.J., Yuan,Q., Cook,J., Sarfare,S., Makshanoff,J., Miu,A., Kim,A., Kim,P., Habib,S., Roybal,C.N., *et al.* (2013) Identification of DES1 as a vitamin A isomerase in Müller glial cells of the retina. *Nature Chemical Biology*, **9**, 30–36.

322. Mizutani,Y., Kihara,A. and Igarashi,Y. (2004) Identification of the human sphingolipid C4-hydroxylase, hDES2, and its up-regulation during keratinocyte differentiation. *FEBS Letters*, **563**, 93–97.

323. Stankeviciute,G., Tang,P., Ashley,B., Chamberlain,J.D., Hansen,M.E.B., Coleman,A., D'Emilia,R., Fu,L., Mohan,E.C., Nguyen,H., *et al.* (2022) Convergent evolution of bacterial ceramide synthesis. *Nat Chem Biol*, **18**, 305–312.

324. Sarmientos,F., Schwarzmann,G. and Sandhoff,K. (1986) Specificity of Human Glucosylceramide ß-Glucosidase Towards Structurally Modified Glucosylceramides in a Liposomal Assay-System. In *Enzymes of Lipid Metabolism II*. Springer US, Boston, MA, pp. 299–304.

325. Sarmientos,F., Schwarzmann,G., Sandhoff,K., Furbish,[, Blair,F.S., Brady,P.G.& and Sandhoff,K. (1986) Specificity of human glucosylceramide β-glucosidase towards synthetic glucosylsphingolipids inserted into liposomes. *European Journal of Biochemistry*, **160**, 527–535.

326. Usta,J., el Bawab,S., Roddy,P., Szulc,Z.M., Hannun,Y.A. and Bielawska,A. (2001) Structural Requirements of Ceramide and Sphingosine Based Inhibitors of Mitochondrial Ceramidase†. *Biochemistry*, **40**, 9657–9668.

327. Kanfer,J.N. and Gal,A.E. (1966) In,vivo conversion of erythro and threo DL-sphingosine-3H to ceramide and sphingomyelin. *Biochemical and Biophysical Research Communications*, **22**, 442–446.

328. Fujino,Y., Nakano,M., Negishi,T. and Ito,S. (1968) Substrate Specificity for Ceramide in the Enzymatic Formation of Sphingomyelin. *Journal of Biological Chemistry*, **243**, 4650–4651.

329. Fujino,Y., Negishi,T. and Ito,S. (1968) Enzymic synthesis of sphingosylphosphorylcholine. *Biochemical Journal*, **109**, 310.

330. Holleran,W.M., Ginns,E.I., Menon,G.K., Grundmann,J.U., Fartasch,M., McKinney,C.E., Elias,P.M. and Sidransky,E. (1994) Consequences of beta-glucocerebrosidase deficiency in epidermis. Ultrastructure and permeability barrier alterations in Gaucher disease. *The Journal of Clinical Investigation*, **93**, 1756–1764.

331. Iwamori,M. and Nagai,Y. (1977) Beta-eliminative cleavage of 3-ketocerebroside and 3-ketosphingomyelin. *Chemistry and Physics of Lipids*, **20**, 193–203.

332. Proksch,E. (2018) pH in nature, humans and skin. *The Journal of Dermatology*, **45**, 1044–1052.

333. Ali,S.M. and Yosipovitch,G. (2013) Skin pH: From basic science to basic skin care. *Acta Dermato-Venereologica*, **93**, 261–267.

334. Radin,N.S. (2003) Designing anticancer drugs via the achilles heel: ceramide, allylic ketones, and mitochondria. *Bioorganic & Medicinal Chemistry*, **11**, 2123–2142.

335. Radin,N.S. (2001) Apoptotic death by ceramide: will the real killer please stand up? *Medical Hypotheses*, **57**, 96–100.

336. Azuma,H., Yoshida,Y., Paul,D., Shinoda,S., Tsukube,H. and Nagasaki,T. (2009) Cytochrome c-binding “proteo-dendrimers” as new types of apoptosis inhibitors working in HeLa cell systems. *Organic & Biomolecular Chemistry*, **7**, 1700.

337. Azuma,H., Ijichi,S., Kataoka,M., Masuda,A., Izumi,T., Yoshimoto,T. and Tachibana,T. (2007) Short-chain 3-ketoceramides, strong apoptosis inducers against human leukemia HL-60 cells. *Bioorganic & Medicinal Chemistry*, **15**, 2860–2867.

338. Park,K.H., Ye,Z. wei, Zhang,J., Hammad,S.M., Townsend,D.M., Rockey,D.C. and Kim,S.H. (2019) 3-ketodihydrosphingosine reductase mutation induces steatosis and hepatic injury in zebrafish. *Scientific Reports 2019 9:1*, **9**, 1–13.

339. Trombetti,S., Cesaro,E., Catapano,R., Sessa,R., Bianco,A. lo, Izzo,P. and Grosso,M. (2021) Oxidative Stress and ROS-Mediated Signaling in Leukemia: Novel Promising Perspectives to Eradicate Chemoresistant Cells in Myeloid Leukemia. *International Journal of Molecular Sciences*, **22**, 1–19.

340. Uchida,Y. (2014) Ceramide signaling in mammalian epidermis. *Biochimica et Biophysica Acta (BBA) - Molecular and Cell Biology of Lipids*, **1841**, 453–462.

341. Williams,R.D., Wang,E. and Merrill,A.H. (1984) Enzymology of long-chain base synthesis by liver: Characterization of serine palmitoyltransferase in rat liver microsomes. *Archives of Biochemistry and Biophysics*, **228**, 282–291.

342. Machlus,K.R. and Italiano,J.E. (2013) The incredible journey: From megakaryocyte development to platelet formation. *The Journal of Cell Biology*, **201**, 785.

343. Patel,S.R., Hartwig,J.H. and Italiano,J.E. (2005) The biogenesis of platelets from megakaryocyte proplatelets. *Journal of Clinical Investigation*, **115**, 3348.

344. Raza,Y., Salman,H. and Luberto,C. (2021) Sphingolipids in Hematopoiesis: Exploring Their Role in Lineage Commitment. *Cells*, **10**.

345. Tani,M., Sano,T., Ito,M. and Igarashi,Y. (2005) Mechanisms of sphingosine and sphingosine 1-phosphate generation in human platelets. *Journal of Lipid Research*, **46**, 2458–2467.

346. Vermeij,W.P., Alia,A. and Backendorf,C. (2011) ROS Quenching Potential of the Epidermal Cornified Cell Envelope. *Journal of Investigative Dermatology*, **131**, 1435–1441.

347. Ishitsuka,Y. and Roop,D.R. (2021) The Epidermis: Redox Governor of Health and Diseases. *Antioxidants 2022, Vol. 11, Page 47*, **11**, 47.

348. Schäfer,M. and Werner,S. (2011) The Cornified Envelope: A First Line of Defense against Reactive Oxygen Species. *Journal of Investigative Dermatology*, **131**, 1409–1411.

349. Zaki,T. and Choate,K. (2018) Recent advances in understanding inherited disorders of keratinization. *F1000Res*, **7**.

350. Yano,S., Komine,M., Fujimoto,M., Okochi,H. and Tamaki,K. (2004) Mechanical Stretching In Vitro Regulates Signal Transduction Pathways and Cellular Proliferation in Human Epidermal Keratinocytes. *Journal of Investigative Dermatology*, **122**, 783–790.

351. Qiao,P., Guo,W., Ke,Y., Fang,H., Zhuang,Y., Jiang,M., Zhang,J., Shen,S., Qiao,H., Dang,E., *et al.* (2019) Mechanical Stretch Exacerbates Psoriasis by Stimulating Keratinocyte Proliferation and Cytokine Production. *Journal of Investigative Dermatology*, **139**, 1470–1479.

352. Kováčik,A., Pullmannová,P., Maixner,J. and Vávrová,K. (2018) Effects of Ceramide and Dihydroceramide Stereochemistry at C-3 on the Phase Behavior and Permeability of Skin Lipid Membranes. *Langmuir*, **34**, 521–529.

353. Školová,B., Jandovská,K., Pullmannová,P., Tesař,O., Roh,J., Hrabálek,A. and Vávrová,K. (2014) The role of the trans double bond in skin barrier sphingolipids: Permeability and infrared spectroscopic study of model ceramide and dihydroceramide membranes. *Langmuir*, **30**, 5527–5535.

354. Stahlberg,S., Školová,B., Madhu,P.K., Vogel,A., Vávrová,K. and Huster,D. (2015) Probing the role of the ceramide acyl chain length and sphingosine unsaturation in model skin barrier lipid mixtures by 2H solid-state NMR spectroscopy. *Langmuir*, **31**, 4906–4915.

355. Holleran,W.M., Gao,W.N., Feingold,K.R. and Elias,P.M. (1995) Localization of epidermal sphingolipid synthesis and serine palmitoyl transferase activity: alterations imposed by permeability barrier requirements. *Archives of Dermatological Research*, **287**, 254–258.

356. Mahanty,S. and Setty,S.R.G. (2021) Epidermal Lamellar Body Biogenesis: Insight Into the Roles of Golgi and Lysosomes. *Frontiers in Cell and Developmental Biology*, **9**, 2068.

357. Ishikawa,J., Shimotoyodome,Y., Ito,S., Miyauchi,Y., Fujimura,T., Kitahara,T. and Hase,T. (2013) Variations in the ceramide profile in different seasons and regions of the body contribute to stratum corneum functions. *Archives of Dermatological Research*, **305**, 151–162.

358. J,A., M,I., M,K., Y,T., Y,I. and G,I. (2002) Decreased levels of sphingosine, a natural antimicrobial agent, may be associated with vulnerability of the stratum corneum from patients with atopic dermatitis to colonization by Staphylococcus aureus. *J Invest Dermatol*, **119**, 433–439.

359. Bibel,D.J., Aly,R. and Shinefield,H.R. (1995) Topical sphingolipids in antisepsis and antifungal therapy. *Clinical and Experimental Dermatology*, **20**, 395–400.

360. Bibel,D.J., Aly,R. and Shinefield,H.R. (2011) Inhibition of microbial adherence by sphinganine. *https://doi.org/10.1139/m92-158*, **38**, 983–985.

361. Sigruener,A., Tarabin,V., Paragh,G., Liebisch,G., Koehler,T., Farwick,M. and Schmitz,G. (2013) Effects of sphingoid bases on the sphingolipidome in early keratinocyte differentiation. *Experimental Dermatology*, **22**, 677–679.

362. Merrill,A.H. and Jones,D.D. (1990) An update of the enzymology and regulation of sphingomyelin metabolism. *Biochimica et Biophysica Acta (BBA) - Lipids and Lipid Metabolism*, **1044**, 1–12.

363. Stoffel,W., Lekim,D. and Sticht,G. (1968) Metabolism of Sphingosine Bases, VIII. Distribution, Isolation and Properties of D-3-Oxosphinganine Reductase. Stereospecificity of the NADPH-dependent Reduction Reaction of 3-Oxodihydrosphingosine(2-Amino-1-

hydroxyoctadecane-3-one). *Hoppe-Seyler´s Zeitschrift für physiologische Chemie*, **349**, 1637–1644.

364. Pettus,B.J., Chalfant,C.E. and Hannun,Y.A. (2002) Ceramide in apoptosis: an overview and current perspectives. *Biochimica et Biophysica Acta (BBA) - Molecular and Cell Biology of Lipids*, **1585**, 114–125.
365. Huber,M., Chiticariu,E., Bachmann,D., Flatz,L. and Hohl,D. (2020) Palmoplantar Keratoderma with Leukokeratosis Anogenitalis Caused by KDSR Mutations. *J Invest Dermatol*, **140**, 1662-1665.e1.
366. Liu,C., Chen,X., Wu,W. and Zhu,X. (2020) A Homozygotic Mutation in KDSR may Cause Keratinization Disorders and Thrombocytopenia: A Case Report. *Chinese Medical Sciences Journal*, **35**, 278–282.
367. Tsuji,K., Mitsutake,S., Ishikawa,J., Takagi,Y., Akiyama,M., Shimizu,H., Tomiyama,T. and Igarashi,Y. (2006) Dietary glucosylceramide improves skin barrier function in hairless mice. *Journal of Dermatological Science*, **44**, 101–107.
368. Zweerink,M.M., Edison,A.M., Wells,G.B., Pinto,W. and Lester,R.L. (1992) Characterization of a novel, potent, and specific inhibitor of serine palmitoyltransferase. *Journal of Biological Chemistry*, **267**, 25032–25038.
369. Chen,Y. (2012) Calcium Phosphate Transfection of Eukaryotic Cells. *BIO-PROTOCOL*, **2**.
370. Jordan,M., Schallhorn,A. and Wurm,F.M. (1996) Transfecting mammalian cells: optimization of critical parameters affecting calcium-phosphate precipitate formation. *Nucleic Acids Research*, **24**, 596.
371. Cunningham,F., Allen,J.E., Allen,J., Alvarez-Jarreta,J., Amode,M.R., Armean,I.M., Austine-Orimoloye,O., Azov,A.G., Barnes,I., Bennett,R., *et al.* (2022) Ensembl 2022. *Nucleic Acids Research*, **50**, D988–D995.
372. Woiwode,U., Sievers-Engler,A. and Lämmerhofer,M. (2016) Preparation of fluorescent labeled gentamicin as biological tracer and its characterization by liquid chromatography and high resolution mass spectrometry. *Journal of Pharmaceutical and Biomedical Analysis*, **121**, 307–315.
373. Keller,L., Werner,S. and Pantel,K. (2019) Biology and clinical relevance of EpCAM. *Cell Stress*, **3**, 165.
374. Deiteren,K., Hendriks,D., Scharpé,S. and Lambeir,A.M. (2009) Carboxypeptidase M: Multiple alliances and unknown partners. *Clinica Chimica Acta*, **399**, 24–39.
375. Oberst,M.D., Chen,L.Y.L., Kiyomiya,K.I., Williams,C.A., Lee,M.S., Johnson,M.D., Dickson,R.B. and Lin,C.Y. (2005) HAI-1 regulates activation and expression of matriptase, a membrane-bound serine protease. *American Journal of Physiology - Cell Physiology*, **289**.
376. Bowen,M.A., Patel,D.D., Li,X., Modrell,B., Malacko,A.R., Wang,W.C., Marquardt,H., Neubauer,M., Pesando,J.M., Francke,U., *et al.* (1995) Cloning, mapping, and characterization of activated leukocyte-cell adhesion molecule (ALCAM), a CD6 ligand. *Journal of Experimental Medicine*, **181**, 2213–2220.

377. van Kempen,L.C.L.T., Nelissen,J.M.D.T., Degen,W.G.J., Torensma,R., Weidle,U.H., Bloemers,H.P.J., Figdor,C.G. and Swart,G.W.M. (2001) Molecular Basis for the Homophilic Activated Leukocyte Cell Adhesion Molecule (ALCAM)-ALCAM Interaction *. *Journal of Biological Chemistry*, **276**, 25783–25790.

378. Blemings,K.P., Crenshaw,T.D., Swick,R.W. and Benevenga,N.J. (1994) Lysine-α-Ketoglutarate Reductase and Saccharopine Dehydrogenase Are Located Only in the Mitochondrial Matrix in Rat Liver. *The Journal of Nutrition*, **124**, 1215–1221.

379. Klemann,C., Wagner,L., Stephan,M. and von Hörsten,S. (2016) Cut to the chase: a review of CD26/dipeptidyl peptidase-4's (DPP4) entanglement in the immune system. *Clinical and Experimental Immunology*, **185**, 1–21.

8 Supplement

Table 35 Pull-down (Exp2) protein candidates for ΔS1PL/ΔGb3S vs ΔS1PL.

Table shows hits and candidates from pacSph pull-down screening that are depleted or enriched in ΔS1PL/ΔGb3S with FDR < 20%, FC > 50%.

Gene Name	Protein Name	log_2FC	$-log_{10}P$
Depleted Proteins			
EPCAM	Epithelial cell adhesion molecule	-1.40	5.55
CPM	Carboxypeptidase M	-1.01	4.88
SPINT1	Kunitz-type protease inhibitor 1	-0.97	4.28
ATP9A	Probable phospholipid-transporting ATPase IIA	-0.84	4.57
PLCB4	1-phosphatidylinositol 4,5-bisphosphate phosphodiesterase beta-4	-0.80	4.09
PTK7	Inactive tyrosine-protein kinase 7	-0.75	4.46
ALCAM	CD166 antigen	-0.74	4.92
MOXD1	DBH-like monooxygenase protein 1	-0.71	3.82
GAA	Lysosomal alpha-glucosidase	-0.69	4.79
SCCPDH	Saccharopine dehydrogenase-like oxidoreductase	-0.69	3.41
DPP4	Dipeptidyl peptidase 4	-0.68	4.71
MET	Hepatocyte growth factor receptor	-0.68	4.00
AXL	Tyrosine-protein kinase receptor UFO	-0.66	2.45
CGNL1	Cingulin-like protein 1	-0.64	2.35
ACSF2	Acyl-CoA synthetase family member 2, mitochondrial	-0.63	4.18
ITGA3	Integrin alpha-3	-0.62	2.92
FAM171A2	Protein FAM171A2	-0.60	2.95
SLC6A8	Sodium- and chloride-dependent creatine transporter 1	-0.60	3.44
KDELC1	KDEL motif-containing protein 1	-0.59	3.75
Enriched Proteins			
VCAM1	Vascular cell adhesion protein 1	1.54	6.46
CNN3	Calponin	1.40	5.50
TGFBI	Transforming growth factor-beta-induced protein	1.16	3.64
CALD1	Caldesmon	1.02	6.02
F3	Tissue factor	0.92	3.99
EPRS	Bifunctional glutamate/proline--tRNA ligase	0.86	4.37
EPPK1	Epiplakin	0.85	3.17
SDC2	Syndecan	0.82	2.11
SLC2A3	Solute carrier family 2, facilitated glucose transporter member 3	0.77	3.93
TAGLN	Transgelin	0.76	4.98
VASN	Vasorin	0.76	2.40
TGM2	Protein-glutamine gamma-glutamyltransferase 2	0.74	4.17
QARS	Glutamine--tRNA ligase	0.72	4.90
PAPSS2	Bifunctional 3'-phosphoadenosine 5'-phosphosulfate synthase 2	0.72	2.55
EEF1B2	Elongation factor 1-beta	0.69	4.80
LARS	Leucine--tRNA ligase, cytoplasmic	0.69	4.63

SEMA3C	Semaphorin-3C	0.67	4.68
IARS	Isoleucine--tRNA ligase, cytoplasmic	0.67	4.67
IFI16	Gamma-interferon-inducible protein 16	0.66	1.82
THBS1	Thrombospondin-1	0.66	3.13
SLC38A1	Sodium-coupled neutral amino acid transporter 1	0.65	2.81
RECQL	ATP-dependent DNA helicase Q1	0.63	1.89
RARS	Arginine--tRNA ligase, cytoplasmic	0.63	4.51
CNN2	Calponin	0.61	3.69
SAR1A	GTP-binding protein SAR1a	0.59	2.13

Table 36 Pull-down (Exp2) protein candidates for ΔS1PL vs no UV control.

Table shows hits and candidates from pacSph pull-down screening with FDR < 5%, $log_2FC > 4$.

Gene Name	Protein Name	log_2FC	$-log_{10}P$
Enriched Proteins			
TMEM19	Transmembrane protein 19 (Fragment)	6.07	6.13
KCT2	Keratinocyte-associated transmembrane protein 2	5.97	7.22
SPPL2A	Signal peptide peptidase-like 2A (Fragment)	5.68	5.96
CD47	Leukocyte surface antigen CD47	5.28	8.48
PON2	Paraoxonase 2, isoform CRA_a	5.25	7.15
SLC29A1	Equilibrative nucleoside transporter 1	5.24	5.74
SLC44A2	Choline transporter-like protein 2	5.18	7.86
SLC15A4	Solute carrier family 15 member 4	5.17	7.28
SSR1	Translocon-associated protein subunit alpha	5.11	10.03
SLC43A3	Solute carrier family 43 member 3 (Fragment)	4.92	5.90
ATP2B3	Plasma membrane calcium-transporting ATPase 3	4.92	8.44
LAMP1	Lysosome-associated membrane glycoprotein 1	4.78	9.70
SCCPDH	Saccharopine dehydrogenase-like oxidoreductase	4.75	9.50
TGOLN2	Trans-Golgi network integral membrane protein 2	4.72	8.90
SLC39A6	Zinc transporter ZIP6 (Fragment)	4.68	9.25
SLC12A4	Solute carrier family 12 member 4	4.63	9.36
SLC43A2	Large neutral amino acids transporter small subunit 4	4.60	8.82
STX7	Syntaxin-7	4.60	9.12
ARL6IP5	PRA1 family protein 3	4.51	5.56
CD46	Isoform K of Membrane cofactor protein	4.49	10.52
PODXL	Podocalyxin	4.44	9.77
VDAC1	Voltage-dependent anion-selective channel protein 1	4.44	9.70
SLC26A2	Sulfate transporter	4.43	8.67
APLP2	Amyloid-like protein 2	4.43	9.22
SRPRB	Signal recognition particle receptor subunit beta	4.43	10.74
RAB11B	Ras-related protein Rab-11B	4.39	8.39
SLC16A1	Monocarboxylate transporter 1	4.38	10.59
ITGB3	Integrin beta-3	4.35	9.84
F2R	Proteinase-activated receptor 1	4.32	8.86
SPNS1	Protein spinster homolog 1	4.29	9.37
TTYH3	Protein tweety homolog 3	4.27	6.58

SIRPA	Tyrosine-protein phosphatase non-receptor type substrate 1	4.27	9.27
SPINT1	Kunitz-type protease inhibitor 1 (Fragment)	4.27	9.01
ENTPD7	Ectonucleoside triphosphate diphosphohydrolase 7	4.25	7.21
SLC17A5	Sialin	4.22	5.56
TM9SF3	Transmembrane 9 superfamily member 3	4.21	9.38
ITM2C	Integral membrane protein 2C (Fragment)	4.20	8.83
APOB	Apolipoprotein B-100	4.19	8.90
CD276	CD276 antigen	4.18	9.28
ATP2B4	Isoform XB of Plasma membrane calcium-transporting ATPase 4	4.18	10.30
TMEM192	Transmembrane protein 192	4.18	10.40
STX6	Syntaxin-6	4.17	9.03
SCARB1	SCARB1 protein	4.15	8.81
STX4	Syntaxin-4	4.15	9.09
SLC19A1	Folate transporter 1	4.13	7.04
TMBIM6	Bax inhibitor 1 (Fragment)	4.12	5.92
SLC7A11	Cystine/glutamate transporter	4.12	8.23
CERS2	Ceramide synthase 2 (Fragment)	4.12	8.17
FZD2	Frizzled-2	4.11	6.91
NPTN	Neuroplastin	4.10	9.71
GPRC5C	G-protein-coupled receptor family C group 5 member C	4.10	8.21
ICAM1	Intercellular adhesion molecule 1	4.09	9.41
TFRC	Transferrin receptor protein 1	4.09	10.40
ATP1A1	Sodium/potassium-transporting ATPase subunit alpha-1	4.09	10.80
NECTIN3	Nectin-3	4.07	9.27
ITGB1	Integrin beta-1	4.07	9.67
CADM1	Cell adhesion molecule 1	4.05	10.43
GPR108	Protein GPR108	4.04	8.06
SLC35B2	Adenosine 3'-phospho 5'-phosphosulfate transporter 1	4.03	9.07
UGCG	Ceramide glucosyltransferase	4.01	9.38
CD44	CD44 antigen	4.01	9.95

Table 37 Full Proteome depleted hits and candidates for ΔS1PL/ΔGb3S vs ΔS1PL.

Table shows hits and candidates from full proteome screening that are depleted in ΔS1PL/ΔGb3S with FDR < 20%, FC > 50%.

Gene Name	Protein Name	log_2FC	$-log_{10}P$
Depleted Proteins			
MEIOC	Meiosis-specific coiled-coil domain-containing protein MEIOC	-1.39	7.02
CTSH	Pro-cathepsin H	-1.26	5.25
CLDN11	Claudin	-1.22	6.69
GPAT3	Glycerol-3-phosphate acyltransferase 3	-1.17	4.58
SEMA7A	Semaphorin-7A	-1.13	6.31
BNIP3	BCL2/adenovirus E1B 19 kDa protein-interacting protein 3	-1.03	3.79
CRISPLD2	Cysteine-rich secretory protein LCCL domain-containing 2	-1.02	3.61
SHISA2	Protein shisa-2 homolog	-1.01	4.39
MYO1D	Unconventional myosin-Id	-0.98	5.96
FUT8	Alpha-(1,6)-fucosyltransferase	-0.96	7.08
GAA	Lysosomal alpha-glucosidase	-0.93	7.14
NUDT11	Diphosphoinositol polyphosphate phosphohydrolase 3-beta	-0.93	6.22
GDAP1	Ganglioside-induced differentiation-associated protein 1	-0.89	6.35
GEM	GTP-binding protein GEM	-0.88	3.75
SCPEP1	Retinoid-inducible serine carboxypeptidase	-0.87	5.83
DPYSL4	Dihydropyrimidinase-related protein 4	-0.86	6.02
RUNX2	Runt-related transcription factor 2	-0.86	4.07
ACSL5	Long-chain-fatty-acid--CoA ligase 5	-0.80	5.26
GCNT1	Beta-1,3-galactosyl-O-glycosyl-glycoprotein beta-1,6-N-acetylglucosaminyltransferase	-0.79	7.15
PLCB4	Isoform 3 of 1-phosphatidylinositol 4,5-bisphosphate phosphodiesterase beta-4	-0.78	4.29
NRK	Nik-related protein kinase	-0.77	4.72
MELTF	Melanotransferrin	-0.76	6.04
FAM49A	Protein FAM49A	-0.75	4.63
PITPNM3	Membrane-associated phosphatidylinositol transfer protein 3	-0.73	2.33
SARG	Specifically androgen-regulated gene protein	-0.72	6.10
PDK3	[Pyruvate dehydrogenase (acetyl-transferring)] kinase isozyme 3, mitochondrial	-0.72	6.10
DKK1	Dickkopf-related protein 1	-0.71	3.10
KHDRBS3	KH domain-containing, RNA-binding, signal transduction-associated protein 3	-0.68	4.93
CPM	Carboxypeptidase M	-0.65	2.85
DPYSL3	Isoform LCRMP-4 of Dihydropyrimidinase-related protein 3	-0.65	4.05
ANKRD13A	Ankyrin repeat domain-containing protein 13A	-0.64	4.57
ARID3B	AT-rich interactive domain-containing protein 3B	-0.64	4.08
NXN	Nucleoredoxin	-0.64	4.89
CEP250	Centrosome-associated protein CEP250	-0.63	5.99
MYLK	Myosin light chain kinase, smooth muscle	-0.63	6.29
LHPP	Phospholysine phosphohistidine inorganic pyrophosphate phosphatase	-0.62	3.57

TSTD1	Thiosulfate sulfurtransferase/rhodanese-like domain-containing protein 1	-0.61	3.68
PEG10	Retrotransposon-derived protein PEG10	-0.60	3.46
ZNF512B	Zinc finger protein 512B	-0.59	6.54

Table 38 Full Proteome enriched hits and candidates for ΔS1PL/ΔGb3S vs ΔS1PL.

Table shows hits and candidates from full proteome screening that are enriched in ΔS1PL/ΔGb3S with FDR < 20%, FC > 50%.

Gene Name	Protein Name	log_2FC	$-log_{10}P$
Enriched Proteins			
VCAM1	Vascular cell adhesion protein 1	3.30	7.39
SDPR	Serum deprivation-response protein	1.61	5.54
MT1X	Metallothionein-1X	1.35	3.08
TRIM2	Tripartite motif-containing protein 2	1.30	7.17
SLCO2A1	Solute carrier organic anion transporter family member 2A1	1.28	5.08
NPNT	Nephronectin	1.27	5.57
THBS1	Thrombospondin-1	1.27	4.86
SERPINE2	Glia-derived nexin	1.26	7.91
FAM107B	Protein FAM107B (Fragment)	1.23	7.26
ASS1	Argininosuccinate synthase	1.19	4.90
IGFBP7	Insulin-like growth factor-binding protein 7	1.19	7.27
PRODH	Proline dehydrogenase 1, mitochondrial	1.17	5.81
HGFAC	Hepatocyte growth factor activator	1.09	4.89
PSAT1	Phosphoserine aminotransferase	1.08	6.40
HPGD	15-hydroxyprostaglandin dehydrogenase [NAD(+)]	1.07	7.26
IVNS1ABP	Influenza virus NS1A-binding protein	1.07	8.07
ALDH1L2	Mitochondrial 10-formyltetrahydrofolate dehydrogenase	1.05	6.40
ENG	Endoglin	1.05	6.35
JAG1	Protein jagged-1	1.04	6.17
IFIT1	Interferon-induced protein with tetratricopeptide repeats 1	1.00	6.00
LIMCH1	LIM and calponin homology domains-containing protein 1	0.98	5.99
ARHGDIB	Rho GDP-dissociation inhibitor 2 (Fragment)	0.97	5.52
FN1	Fibronectin	0.96	4.08
IFIT3	Interferon-induced protein with tetratricopeptide repeats 3	0.95	5.82
ACSL1	Long-chain-fatty-acid--CoA ligase 1	0.95	6.03
COL7A1	Collagen alpha-1(VII) chain	0.94	6.55
TFAP2A	Transcription factor AP-2-alpha	0.94	6.16
DDX60	Probable ATP-dependent RNA helicase DDX60	0.93	6.88
GGT1	Gamma-glutamyltranspeptidase 1	0.92	4.25
IFIT2	Interferon-induced protein with tetratricopeptide repeats 2	0.92	4.92
FBLN1	Fibulin-1	0.87	5.48
DSP	Desmoplakin	0.86	6.40
COL18A1	Collagen alpha-1(XVIII) chain	0.86	4.95
ADGRG1	Adhesion G-protein coupled receptor G1	0.82	3.78
SLC38A2	Sodium-coupled neutral amino acid transporter 2	0.80	6.21

ISG15	Ubiquitin-like protein ISG15 (Fragment)	0.77	5.23
L1CAM	Isoform 2 of Neural cell adhesion molecule L1	0.77	5.98
DHTKD1	Probable 2-oxoglutarate dehydrogenase E1 component DHKTD1, mitochondrial	0.76	3.95
BCHE	Cholinesterase	0.76	4.14
CTGF	Connective tissue growth factor	0.74	5.61
ARRB1	Isoform 1B of Beta-arrestin-1	0.74	5.83
NDUFA6	NADH dehydrogenase [ubiquinone] 1 alpha subcomplex subunit 6	0.73	3.03
EPPK1	Epiplakin	0.73	6.39
NIF3L1	NIF3-like protein 1	0.72	1.02
NFIB	Nuclear factor 1	0.71	5.25
CHRDL1	Isoform 2 of Chordin-like protein 1	0.70	3.88
HMGA2	Isoform 2 of High mobility group protein HMGI-C	0.70	4.22
CAMK4	Calcium/calmodulin-dependent protein kinase type IV	0.69	6.76
CLDN1	Claudin-1	0.69	3.88
SCEL	Sciellin	0.69	4.13
CRYAB	Alpha-crystallin B chain	0.68	4.74
SLC2A3	Solute carrier family 2, facilitated glucose transporter member 3	0.68	3.76
DPYD	Dihydropyrimidine dehydrogenase [NADP(+)]	0.67	4.42
TTYH3	Protein tweety homolog 3	0.67	2.87
AIM1	Absent in melanoma 1 protein	0.67	4.90
TIA1	Nucleolysin TIA-1 isoform p40	0.67	4.40
TMEM2	Transmembrane protein 2	0.66	6.10
EML1	Echinoderm microtubule-associated protein-like 1	0.66	4.84
CSRP1	Cysteine and glycine-rich protein 1	0.65	5.50
TNFRSF21	Tumor necrosis factor receptor superfamily member 21	0.65	3.65
SET	Protein SET	0.64	3.27
BAK1	Bcl-2 homologous antagonist/killer	0.64	4.12
SLC38A1	Sodium-coupled neutral amino acid transporter 1	0.64	4.74
CD63	CD63 antigen	0.64	3.08
COX7C	Cytochrome c oxidase subunit 7C, mitochondrial	0.63	2.44
CDKN2AIPNL	CDKN2AIP N-terminal-like protein	0.63	3.40
CALD1	Caldesmon	0.63	3.72
ADGRL2	Adhesion G protein-coupled receptor L2	0.62	1.79
ANXA1	Annexin A1	0.62	5.10
MMAB	Cob(I)yrinic acid a,c-diamide adenosyltransferase, mitochondrial	0.62	5.05
TFPI2	Tissue factor pathway inhibitor 2	0.62	3.25
FAS	Tumor necrosis factor receptor superfamily member 6	0.60	5.17
PDZK1	Na(+)/H(+) exchange regulatory cofactor NHE-RF3	0.60	5.15
COL11A1	Collagen alpha-1(XI) chain	0.60	4.72
GREM1	Gremlin-1	0.59	1.88
TNFSF10	Tumor necrosis factor ligand superfamily member 10	0.59	2.50
CES2	Carboxylic ester hydrolase	0.59	4.60

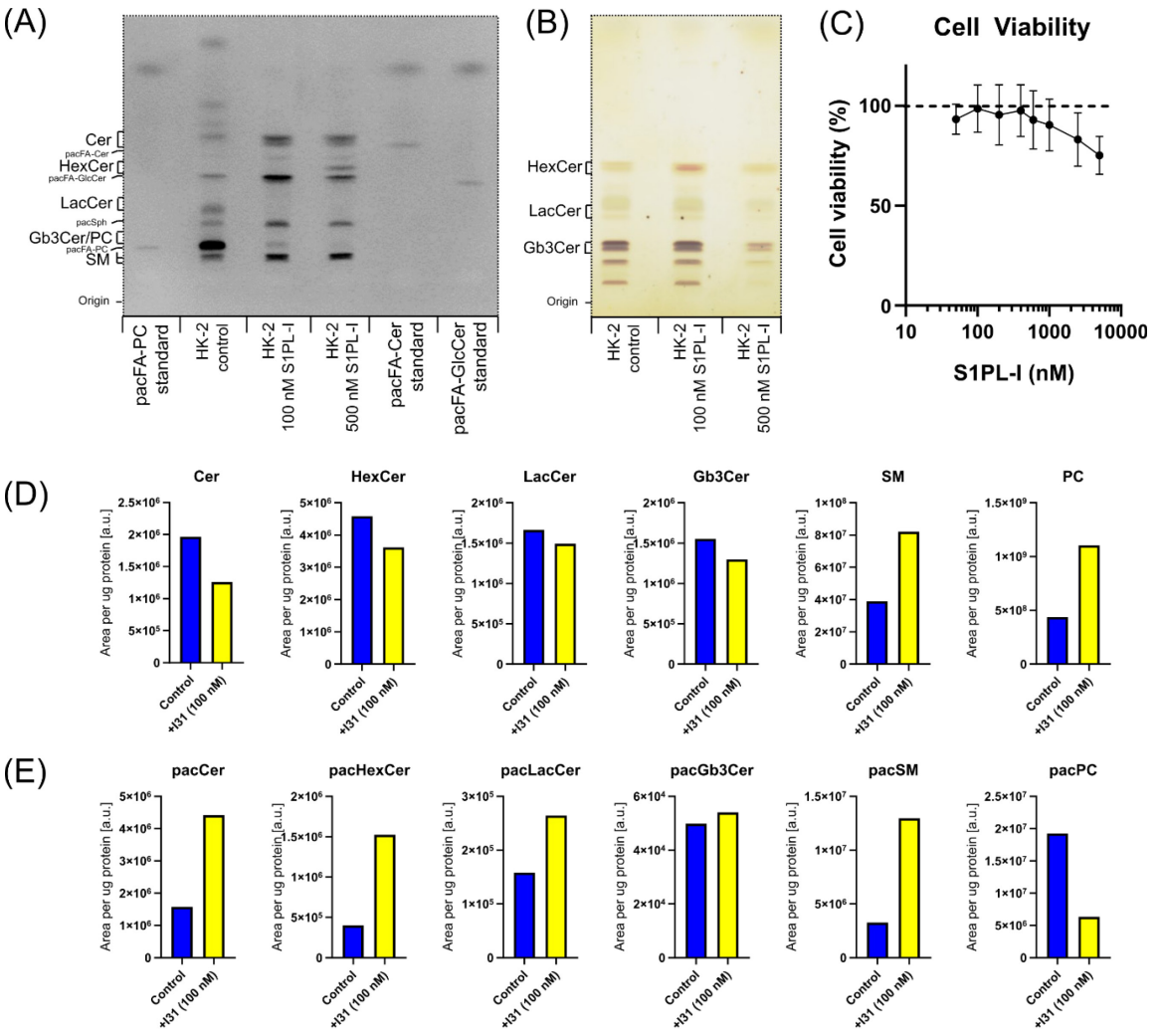

Supplementary Figure 1 Metabolic effects of S1PL inhibition.

Evaluation of S1PL inhibitors as a strategy to avoid glycerolipid labelling by pacSph. (A) Visualization of labelled lipids on a HPTLC by UV fluorescence after CuAAC-click reaction with coumarin-azide. (B) Visualization of glycosphingolipids (GSL) on a HPTLC by derivatization with orcinol reagent. (C) Cell viability with different concentrations of S1PL-I as determined by MTT assay. (D) Relative quantification of steady state lipid levels by LC-MS/MS. (E) Relative quantification of labelled lipids by LC-MS/MS.

To evaluate the applicability of an S1PL inhibitor (S1PL-I) for the prevention of glycerolipid labelling, I labelled HK-2 cells with pacSph (6 µM, 4h) pre-treated with and cultured the cells in the presence of varying concentrations of S1PL-I (100 nM and 500 nM). With inhibition of S1PL a clear change in the pacSph labelling pattern can be observed. Labelling of glycerolipid as seen without S1PL inhibition is strongly reduced and the amount of labelled sphingolipids (including ceramide, sphingomyelin, hexosylceramide and pacSph) is increased. Although reduced, glycerolipids still account for a major fraction of the labelled lipids. With higher S1PL-I concentration this effect seems to be reduced. After orcinol staining to visualize GSL, I found no difference between control and 100 nM S1PL-I condition, but the amount of GSL appears to be reduced with higher concentrations of the inhibitor. LC-MS evaluation of control and 100 nM S1PL-I samples indicates a reduction in ceramides and GSL, while sphingomyelin and phosphatidylcholine is increased.

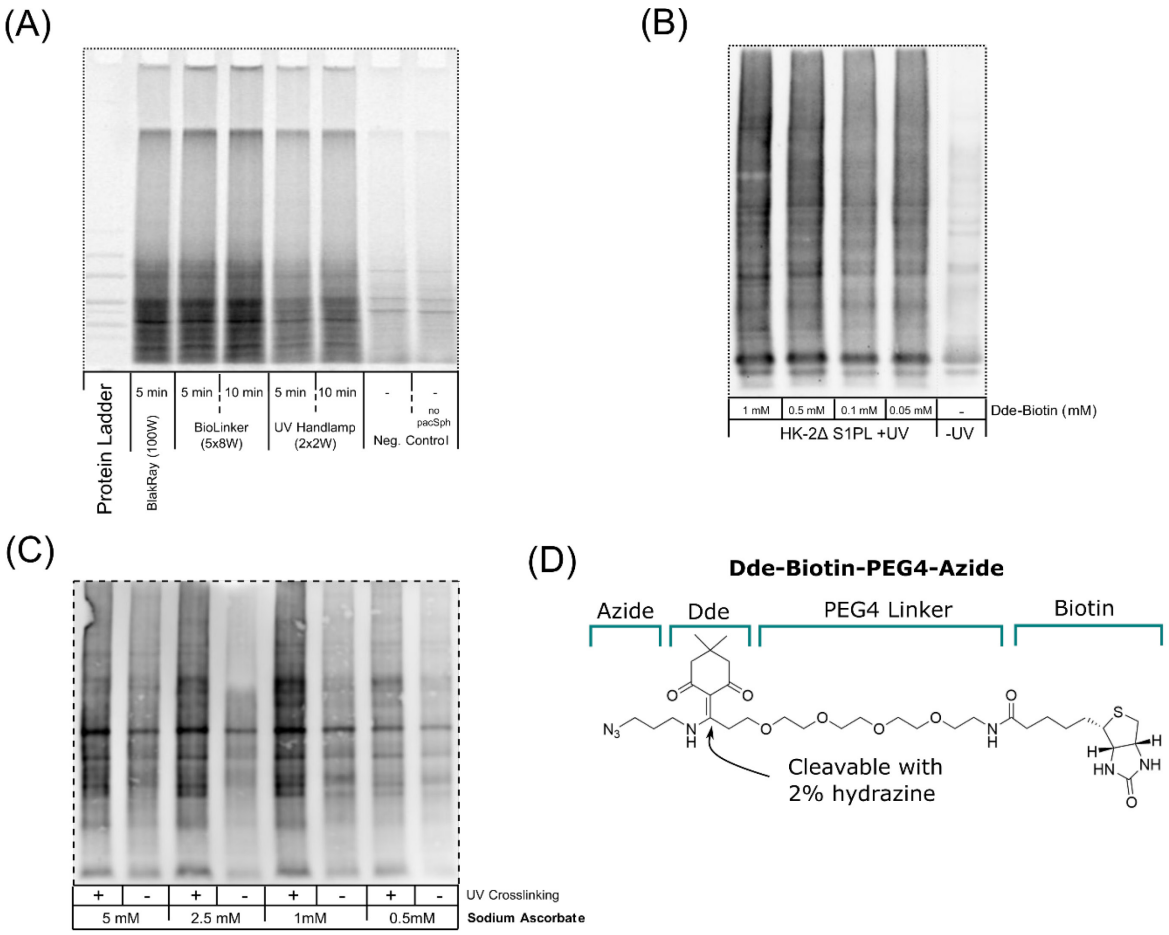

Supplementary Figure 2 Optimization of protein enrichment procedure

Optimization of UV crosslinking and CuAAC-based click chemistry conditions. HK-2 ΔS1PL cells were labelled with pacSph (6 µM, 4h). (A) Several lamps were tested for UV crosslinking. Proteins were extracted and click reaction was performed with Cy5-azide. Cy5-conjugated protein-sphingolipid conjugates were visualized by in-gel fluorescence after separation by SDS-PAGE. (B) HK-2 ΔS1PL cells were labelled with pacSph (6 µM, 4h). After UV crosslinking (365 nm, 5 min) proteins were extracted and subjected to CuAAC-based click reaction with Dde-biotin-azide in varying concentrations. Biotinylated proteins were separated by SDS-PAGE, transferred onto nitrocellulose membrane, and visualized using Neutravidin-HRP. (C) HK-2 ΔS1PL cells were labelled with pacSph (6 µM, 4h). After UV crosslinking (365 nm, 5 min) proteins were extracted and subjected to CuAAC-based click reaction with sodium ascorbate in varying concentrations and with or without UV crosslinking. Biotinylated proteins were separated by SDS-PAGE, transferred onto nitrocellulose membrane, and visualized using Neutravidin-HRP. (D) Structure of hydrazine-cleavable Dde-biotin-azide. (E) Workflow for the enrichment of protein-sphingolipid conjugates from cells.

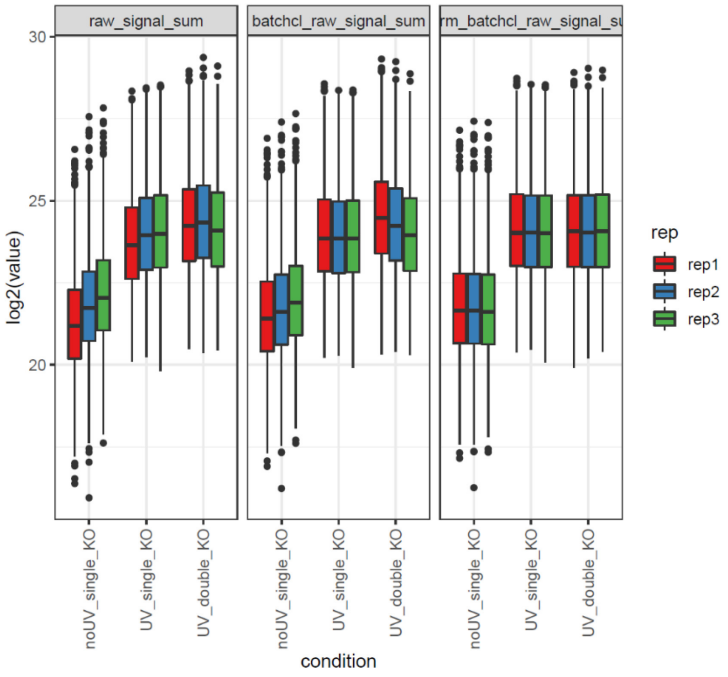

Supplementary Figure 3 Raw signal sum of all measured proteins by sample and replicate

Significant enrichment of proteins was observed in UV irradiated samples indicating a crosslinking dependent pull-down.

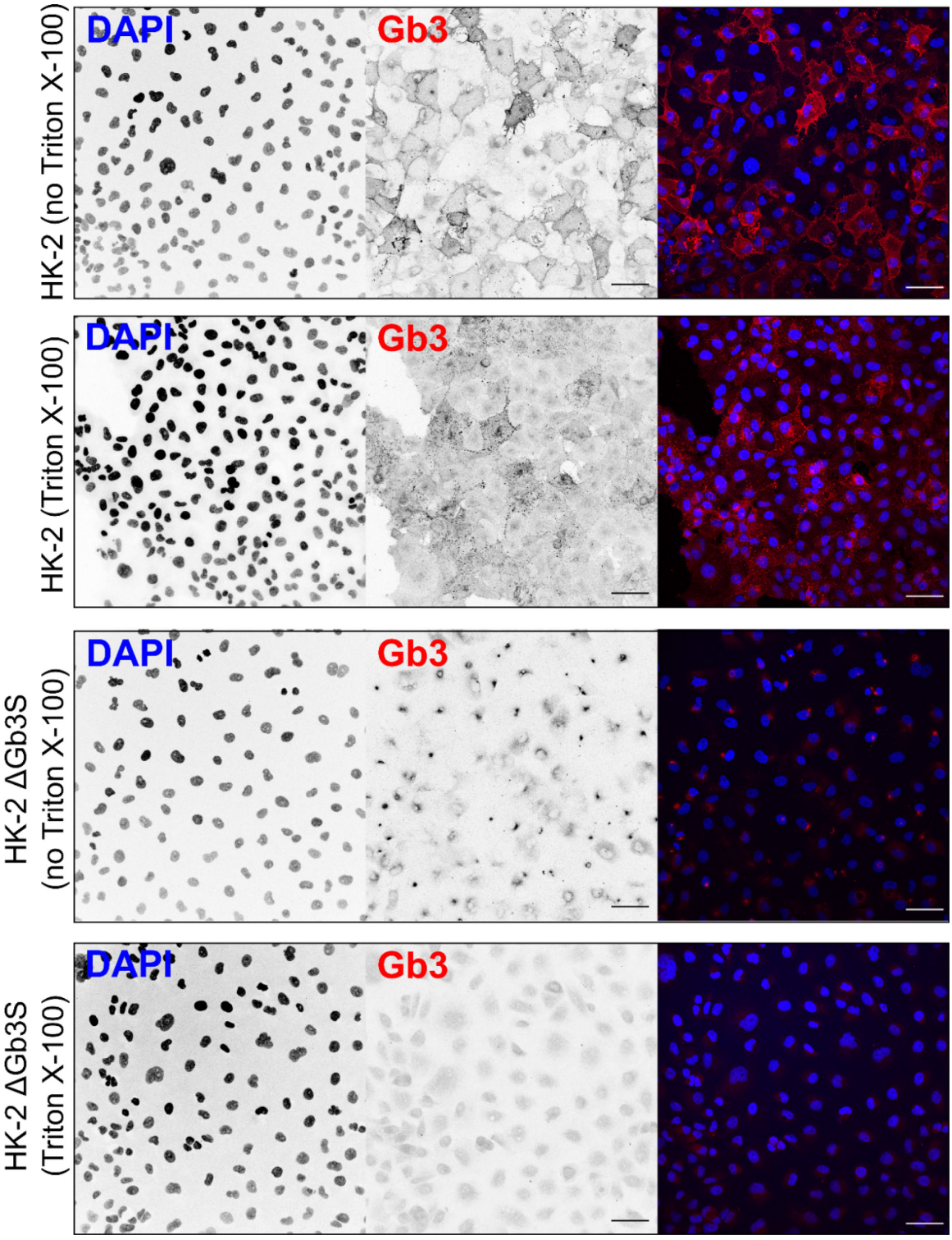

Supplementary Figure 4 Immunostaining of Gb3Cer in HK-2 wild type and ΔGb3S

HK-2 cells were grown on coverslips and immunostaining was performed with anti-Gb3Cer antibody (1:100) with or without using Triton X-100 as a detergent. ΔGb3S cells were stained as a negative control. The antibody is specific for Gb3Cer, as seen by the drop in signal in ΔGb3S cells, but gives rise to a faint background staining.

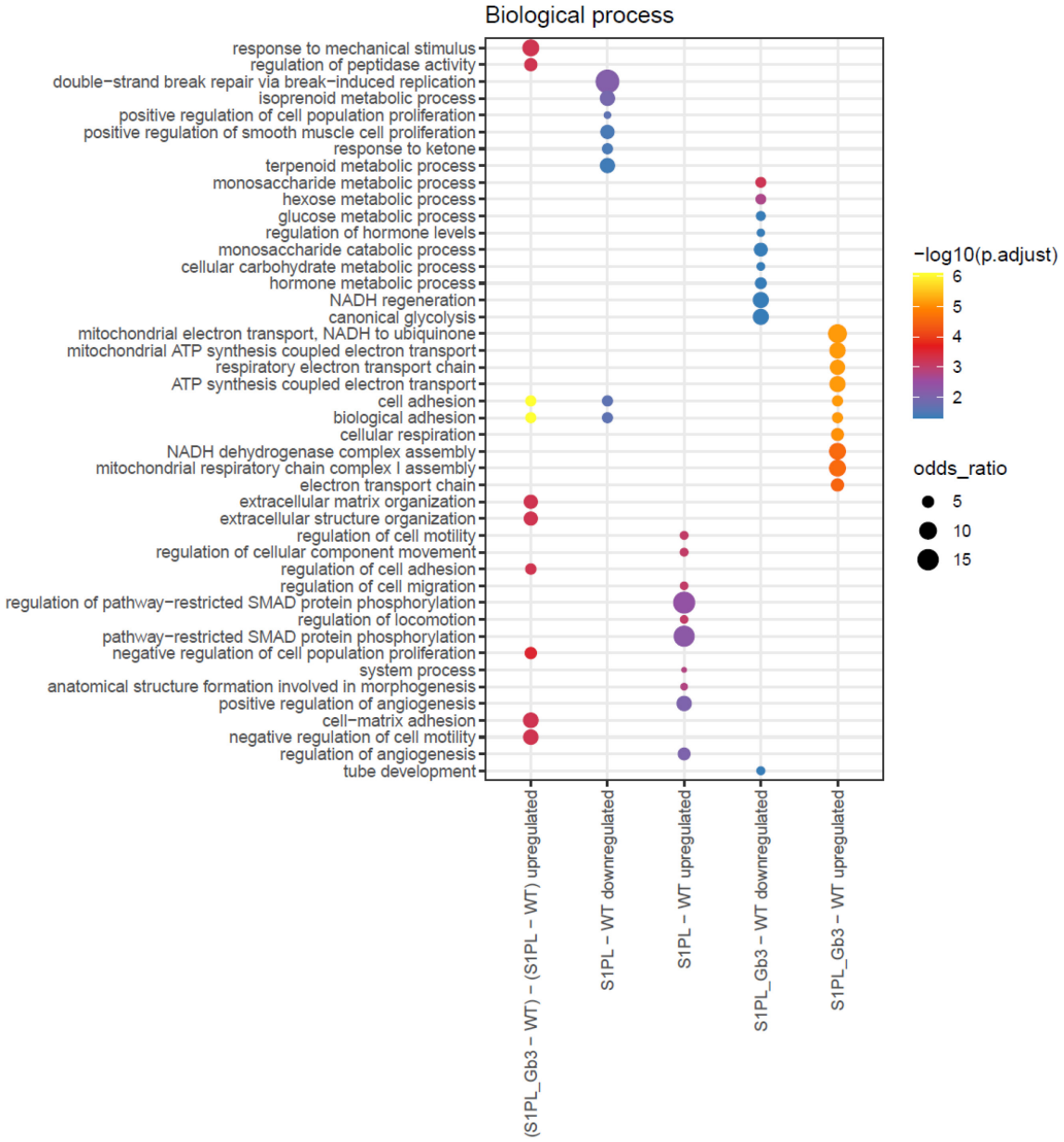

Supplementary Figure 5 GO:Biological Process enrichment of full proteome data

GO enrichment based on GO:Biological Process for full proteome analysis of HK-2 wild type, ΔS1PL and ΔS1PL/ΔGb3S.

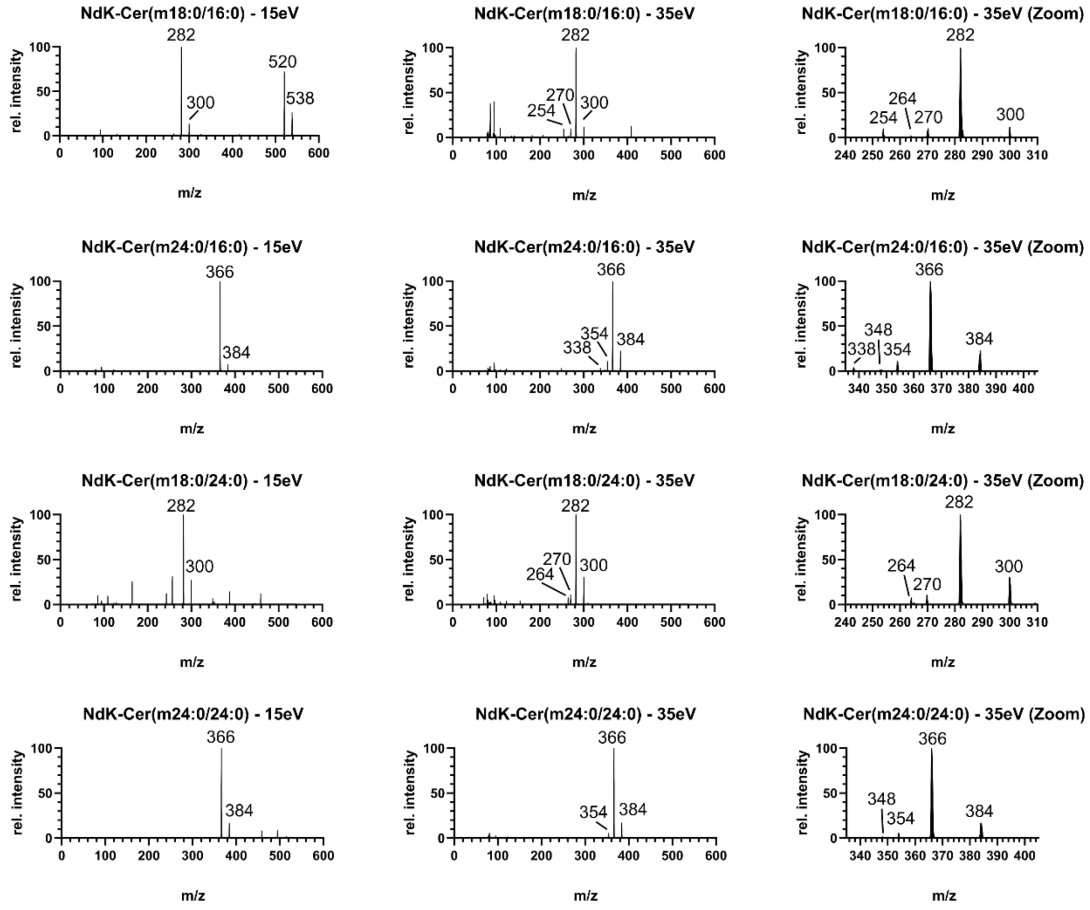

Supplementary Figure 6 Fragmentation of synthetic NdK-ceramide standards with different collision energies.

Table 39 Transmembrane domains of selected candidate proteins.

Protein	#TMD	Length	Sequence (+/- 4 AA)
EPCAM	1	23	QGLK**AGVIAVIVVVVIAVVAGIVVLVI**SRKK
CPM	0		GPI-anchored
SPINT1	1	23	GSVE**MAVAVFLVICIVVVVAILGYCFF**KNQR
ATP9A	1	22	FTFL**PGVLFNQFKYFFNLYFLLLACS**QFVP
	2	23	FVPE**MRLGALYTYWVPLGFVLAVTVIR**EAVE
	3	22	VNCL**TKILFGALVVVSLVMVALQHFA**GRWY
	4	22	YLQI**IRFLLLFSNIIPISLRVNLDMG**KIVY
	5	21	RSAA**LSQFVIHRSLCISTMQAVFSS**VFYF
	6	19	LYQG**FLIIGYSTIYTMFPVFSLV**LDKD
	7	19	SYKT**FLIWVLISIYQGSTIMYGA**LLLF
	8	23	FESE**FVHIVAISFTSLILTELLMVALT**IQTW
	9	21	TWHW**LMTVAELLSLACYIASLVFLH**EFID
	10	24	DVYF**IATLSFLWKVSVITLVSCLPLYVL**KYLR
ALCAM	1	22	DQAK**LIVGIVVGLLLAALVAGVVYWL**YMK
SCCPDH	1	27	SPVQ**YAAYVTVGGITSVIKLMFAGLFFLFFV**RFGI
DPP4	1	22	TPWK**VLLGLLGAAALVTIITVPVVLL**NKGT
MET	1	23	QNFT**GLIAGVVSISTALLLLLGFFLWL**KKRK
ITGA3	1	23	AEIE**LWLVLVAVGAGLLLLGLIILLLW**KCGF
SLC6A8	1	21	RQMD**FIMSCVGFAVGLGNVWRFPYL**CYKN
	2	21	KNGG**GVFLIPYVLIALVGGIPIFFL**EISL
	3	21	YASM**VIVFYCNTYYIMVLAWGFYYL**VKSF
	4	21	VPGA**LNWEVTLCLLACWVLVYFCVW**KGVK
	5	21	TFPY**VVLVVLLVRGVLLPGALDGII**YYLK
	6	21	GSPQ**VWIDAGTQIFFSYAIGLGALT**ALGS
	7	21	YKDA**IILALINSGTSFFAGFVVFSI**LGFM
	8	21	RAVT**LMPVAPLWAALFFFMLLLLGL**DSQF
	9	21	FQRE**ISVALCCALCFVIDLSMVTDG**GMYV
	10	21	YSAS**GTTLLWQAFWECVVVAWVYGA**DRFM
	11	21	PWMK**WCWSFFTPLVCMGIFIFNVVY**YEPL
	12	21	GEAM**GWAFALSSMLCVPLHLLGCLL**RAKG

Acknowledgment

Ich möchte mich zuallererst bei Roger Sandhoff dafür bedanken, dass er mich mit seiner Begeisterung für Wissenschaft und Sphingolipide angesteckt hat. Ich habe viel von dir gelernt und unsere Diskussionen immer genossen. Vielen Dank für das Vertrauen, dass du in mich hattest und natürlich auch die vielen kleinen spannenden, mal mehr und mal weniger erfolgreichen Projekte.

Danke an Per Haberkant und Frank Stein. Ohne euch wäre dieses Projekt so nicht möglich gewesen und ich weiß eure Erfahrung und Hilfe sehr zu schätzen. Danke auch an Lukas Opalka und Adam Majcher für die große Unterstützung bei der Synthese von Keto-Sphingolipiden. Ich freue mich schon euch bei der nächsten Konferenz wiederzusehen.

Mein Dank geht auch an mein Prüfungskomitee und die Mitglieder meiner TAC Kommission, Prof. Dr. Britta Brügger, Prof. Dr. Ana Martin-Villalba, Dr. Wilhelm Palm und Dr. Steeve Boulant, für viele hilfreiche Kommentare und Vorschläge.

Ich danke außerdem allen jetzigen und ehemaligen Freunden im Labor. Ohne eure Unterstützung wäre diese Doktorarbeit nicht möglich gewesen. Vielen Dank an Richard Jennemann, du hast mit deiner Expertise dazu beitragen, dass ich Sackgassen rechtzeitig erkennen und umfahren konnte. Elisabeth Grimm, danke, dass du da warst und wir viele schwierige und schöne Momente teilen konnten. Danke Benita, dass du mir, als ich frisch in Labor kam, gezeigt hast, wie man Lipide richtig extrahiert. Danke Martina für die Zuarbeit, wenn 24 Stunden am Tag einfach nicht genug waren. Danke auch an Aysu Basak-Kök und Mariona Rabionet, die es immer geschafft haben mir eine andere Perspektive zu vermitteln. Ganz besonders möchte ich meinen Dank an Emily Steffke hervorheben. Wir hatten nicht viel Zeit zusammen, aber mit deiner frohen Art und Motivation hast du mich immer wieder begeistert. Danke für die großartige Zeit und deine Unterstützung bei der Herstellung der ΔS1PL Zelllinie.

Und natürlich Danke ich meiner Familie, einschließlich aller neuen Familienmitglieder die ich in den letzten Jahren gewonnen habe.

Ganz besonderen Dank schulde ich aber meiner Frau Ronja Engel. Du hast es immer geschafft mir zu zeigen, dass sich das Leben nicht nur im Labor abspielt. Danke, dass du mir den Rücken freigehalten hast, als ich diese Arbeit zusammengeschrieben habe. Unsere kleine Familie macht mich unendlich glücklich und hat mir auch in schwierigen Momenten die Kraft gegeben weiterzumachen. Danke auch an dich Elliot für dein ansteckendes Lachen.